MICROMECHANICAL ANALYSIS OF INDUCED ANISOTROPY IN GRANULAR MATERIALS

MICROMECHANICAL ANALYSIS OF INDUCED ANISOTROPY IN GRANULAR MATERIALS

By

JINGSHAN SHI, B.Sc., M.Sc.

A THESIS

SUBMITTED TO THE DEPARTMENT OF CIVIL ENGINEERING AND THE SCHOOL OF GRADUATE STUDIES OF MCMASTER UNIVERSITY IN PARTIAL FULFILMENT TO THE REQUIREMENTS FOR THE DEGREE OF

DOCTOR OF PHILOSOPHY

Descriptive Note

DOCTOR OF PHILOSOPHY (2018) McMaster University

(Civil Engineering) Hamilton, Ontario

TITLE: Micromechanical Analysis of Induced Anisotropy in Granular Materials

AUTHOR: Jingshan Shi

B. Eng. (Wuhan Polytechnic University, China)

M. Sc. (Tongji University, China)

SUPERVISOR: Dr. Peijun Guo

NUMBER OF PAGES: XXV 233

Lay Abstract

In civil engineering, granular materials are ubiquitous, such as sand, gravel, rock, and concrete. Due to the discrete nature of microstructure, this type of material usually displays exceedingly complicated behaviours under shear, for example, dilatancy, non-coaxiality, critical state, instability, and anisotropy. These mechanical responses are notoriously difficult to model and most existing models are phenomenological and lack a clear physical meaning. To provide a clear physical meaning for the constitutive model of granular material, the current study explored the evolution of the microstructure within the granular material subjected to quasi-static shear and the micromechanical origins of those macroscopic behaviours such as critical state, non-coaxiality, and instability. Both micromechanical analysis and discrete element method were applied. Results showed that the evolution of the whole microstructure depended on the loading condition. However, the evolution of the microstructure joined by the ‘strong contacts’ was independent of the loading path. At critical state, the microstructure was highly anisotropic, not unique and depended on the stress paths. The rearrangement of the microstructure helped to maintain the stability of a granular material. The instability of the granular material was triggered by the failure of the microstructure joined by the ‘weak contacts’.

Abstract

Granular materials, such as sand, are systems consisting of huge numbers of particles that interact with each other through inter-particle contacts. Different from continuum materials, a granular material displays distinctive features due to the discrete nature of the microstructure, characterized by a spatial arrangement of inter-particle connection as well as a force-chain network. With a consideration of the contact force, the overall contact network is divided into a strong sub-network and a weak sub-network that carry contacts with normal contact forces larger and lower than the average normal contact force, respectively. Thus, the fabric anisotropy for different contact networks, are employed to characterize the microstructure of the granular material.

In this research, the behavior of granular materials subjected to quasi-static shear was extensively investigated in terms of the fabric evolution including the magnitude and direction of anisotropy for different contact networks. Both statistical and micromechanical approaches were adopted to obtain the macroscopic properties, such as the fabric tensor, Cauchy stress tensor and the second-order work, in terms of the micro-scale variables. The discrete element method (DEM) was employed to simulate laboratory tests along fixed loading paths; for example, 2D tests along proportional strain paths, 2D simple shear tests and 3D tests along radial stress paths on the π-plane.

Results demonstrated that the induced fabric anisotropy for the overall contact network can be related to the deviatoric stress ratio for both two-dimensional and three-dimensional conditions. The relation was found to be not unique, depending on the loading paths as well as the stress state. Nevertheless, a unique linear fabric-stress relation was presented between the stress tensor and fabric tensor for the strong sub-network. Specifically, the obliquity of this linear relation was found to be a function of the mean stress. This description held true for initially isotropic specimens

subjected to proportional and non-proportional loading paths. On the other hand, for the initially anisotropic specimen, this correspondence only worked at the critical stress state.

According to Nicot and Darve (2006), the macro second-order work cannot be interpreted as a summation of the local second-order work from the contact plane. The second-order work induced by the fabric evolution and the volumetric change must also be taken into account. The second-order work induced by the fabric evolution cannot be neglected in 2D analysis along proportional strain paths. Moreover, the vanishing of the second-order work is related to the fabric anisotropy in contact sub-networks that the decrease of fabric anisotropy for the weak sub-network or the degradation of weak sub-network was observed to be an indicator of deformation instability even though the strong sub-network dominants the shear resistance. The degradation of strong sub-network was a necessary but not a sufficient condition of instability.

The direction of the fabric anisotropy for the strong sub-network was observed to be coaxial with the orientation of the principal stress. The principal direction of fabric anisotropy for the weak sub-network was always perpendicular to that of the strong sub-network, regardless of whether the principal stress rotated or not. For the overall contact network, however, the direction of the fabric anisotropy was not necessarily in line with the major principal stress direction, even for an initial isotropic granular assembly. Therefore, the finding by Radjaï *et al.*(1998) that the direction of the fabric anisotropy for the weak sub-network is perpendicular to that for the overall contact network only held true for the loadings in which the critical stress could be approached no matter if the principal stress orientation rotated or not. Under this circumstance, the fabric anisotropy for the overall contact network could be interpreted as a function of sub-networks' anisotropy weighted by the ratio of contact number in each sub-network over the total number of contacts.

At critical state, both the strong sub-network and the overall contact network

developed high fabric anisotropy with the weak sub-network being mostly isotropic. When plotted on the π-plane, both the fabric anisotropy for the strong sub-network and the fabric anisotropy for the overall contact network depended on the stress paths but were independent of the mean stress level. The response surface of the former could be expressed as a Lade's surface. The response envelope of the latter was an inverted Lade's surface.

Acknowledgements

There is a set of people I wish to express my sincere appreciation here. To start with, I want to give my special thanks to my supervisor, Dr. Peijun Guo, for his constant support, guidance, and patience throughout my graduate study. I have been extremely lucky to have a knowledgeable and professional supervisor, who always responds my queries promptly. Special thanks are also expressed to my supervisory committee member, Dr. Dietor Stolle, for his help with the write-up and paper revise, and to Dr. Michael Thompson for dedicating time to better my work.

Of my fellow graduate students, I give many thanks to Dr. Yaqian Liu for his help in my settling down in this city. I wish to thank Dr. Sina Moallemi and Ph.D. student Hojjat Mohammadi for valuable discussions. I would extend my appreciation to Hui Guo, Wei Liu, Xing Li, Jun Wang and all graduate students in JHE-331 for their friendship which makes the graduate student lab a cheerful place. I am also grateful to my other friends who have supported me along the way.

But most of all, I give my specialist gratitude to my wife, Dr. Xiaojing Quan, who always stands beside me, encourages me and supports me. Without her none of this could have been achieved. I thank her for her sacrifice and her willingness to take on this adventure with me. I express my deepest gratitude and love to my parents, my sisters and my brother for their dedication and support for so many years.

Table of Contents

List of Figures

List of Tables

List of Symbols

D_{REV}	the diameter of the Representative Volume Element (*REV*)
V	the volume of REV
D_{min}, D, D_{50}, D_{max}	the minimum, average, median and maximum diameters of the particle
$\bar{r}$	the average radius of the particle
N_c, N_p	the numbers of the contact and particle
N_c^s, N_c^w	the numbers of contact in strong sub-network and the weak sub-network
α	the ratio of the number of strong contacts $\alpha = N_c^s / N_c$
$\phi_{ij}, \phi_{ij}^s, \phi_{ij}^w$	the fabric tensor for the overall contact network (ϕ_{ij}), the strong sub-network (ϕ_{ij}^s) and weak sub-network (ϕ_{ij}^w)
ϕ_{ij}' , $\phi_{ij}'^s$, $\phi_{ij}'^w$	the deviatoric fabric tensor of ϕ_{ij}, ϕ_{ij}^s and ϕ_{ij}^w: $\phi_{ij}' = \phi_{ij} - \delta_{ij}/2$ (2D) or $\phi_{ij}' = \phi_{ij} - \delta_{ij}/3$ (3D)
$I_{1\phi}, I_{2\phi}, I_{3\phi}$	the first, second and third invariants of the fabric tensor ϕ_{ij}: $I_{1\phi} = \phi_{ii}$, $I_{2\phi} = (\phi_{ii}\phi_{jj} - \phi_{ij}\phi_{ji})/2$ and $I_{3\phi} = \det(\phi_{ij})$
$J_{2\phi}, J_{3\phi}$	the second and the third invariants of the deviatoric stress tensor ϕ_{ij}' : $J_{2\phi} = \phi_{ij}'\,\phi_{ij}'/2$, $J_{3\phi} = \det(\phi_{ij}')$
q_ϕ, p_ϕ	the deviatoric stress and mean fabric for the overall contact network, $q_\phi = \sqrt{3\phi_{ij}'\phi_{ij}'/2}$, $p_\phi = 1/3(3D)\ 1/2(2D)$
q_ϕ^s, p_ϕ^s	the deviatoric stress and mean fabric for the strong contact network
q_ϕ^w, p_ϕ^w	the deviatoric stress and mean fabric for the weak contact network
$q_{\phi,cr}, q_{\phi,cr}^s, q_{\phi,cr}^w$	the critical values of $q_\phi, q_\phi^s, q_\phi^w$
$q_{\phi,\max}, q_{\phi,\max}^s, q_{\phi,\max}^w$	the maximum values of $q_\phi, q_\phi^s, q_\phi^w$

$q_{\phi,ult}, q^s_{\phi,ult}, q^w_{\phi,ult}$	the ultimate values of the $q_\phi, q^s_\phi, q^w_\phi$
a_c, θ_c	the degree and direction of the fabric anisotropy for the directional distribution of contact normals in the whole contact network
a^s_c, θ^s_c	the degree and direction of the fabric anisotropy for the directional distribution of contact normals in the strong subnetwork
a^w_c, θ^w_c	the degree and direction of the fabric anisotropy for the directional distribution of contact normals in the weak contact network
a_l, θ_l	the degree and direction of the anisotropy for the directional distribution of branch vectors
a_n, θ_n	the degree and direction of the anisotropy of directional distribution of normal contact forces
a_t, θ_t	the degree and direction of the fabric anisotropy using tangential contact forces
$\theta_\sigma, \theta_{d\varepsilon}$	the orientation of the principal stress and strain increment
k^n, k^s, k^r	the normal, tangential contact stiffness and stiffness of rolling resistance on the contact
μ	the frictional coefficient
σ_{ij}	the Cauchy stress tensor
σ_m	the mean stress: $\sigma_m = \sigma_{ii}/2$ (2D) and $\sigma_m = \sigma_{ii}/3$ (3D)
s_{ij}	the deviatoric stress tensor $s_{ij} = \sigma_{ij} - \sigma_m \delta_{ij}$
t, s	the deviatoric stress and mean stress for 2D conditions $t = (\sigma_1 - \sigma_2)/2$, $s = (\sigma_1 + \sigma_2)/2$
q, p	the deviatoric stress and mean stress for 3D conditions: $q = \sqrt{3 s_{ij} s_{ij}/2}$, $p = \sigma_{ii}/3$
I_1, I_2, I_3	the first, the second and the third invariants of the stress tensor σ_{ij}, $I_1 = \sigma_{ii}$, $I_2 = (\sigma_{ii}\sigma_{jj} - \sigma_{ij}\sigma_{ji})/2$ and $I_3 = \det(\sigma_{ij})$

J_2, J_3	the second and the third invariants of the deviatoric stress tensor s_{ij}, $J_2 = \frac{1}{2} s_{ij} s_{ji}$, $J_3 = \det(s_{ij})$
b	the intermediate stress ratio $b = \sigma_2 - \sigma_3 \,/\, \sigma_1 - \sigma_3$
χ_{LD}	the parameter for Lade-Duncan relation for the Cauchy stress
χ_{MN}	the parameter for Matsuoka-Nakai relation for the Cauchy stress
$\overline{e}_{ij}$	the deformation gradient tensor
ε_{ij}	the strain tensor $\left(\partial u_i / \partial x_j + \partial u_j / \partial x_i\right) / 2$
e'_{ij}	the deviatoric strain tensor: $e'_{ij} = \varepsilon_{ij} - \frac{\varepsilon_{kk}}{3}\delta_{ij}$ or $e'_{ij} = \varepsilon_{ij} - \frac{\varepsilon_{kk}}{2}\delta_{ij}$
$\gamma, \varepsilon_q, \varepsilon_v$	the shear strain, the equivalent deviatoric strain and the volumetric strain: $\varepsilon_v = \varepsilon_{ii}$, $\gamma = \sqrt{3 e'_{ij} e'_{ij} / 2}$, $\varepsilon_q = \sqrt{2 e'_{ij} e'_{ij} / 3}$
$\boldsymbol{l}$	the branch vector joining the centroids of two connected particles
$\boldsymbol{n}$	the contact normal vector
$\boldsymbol{t}$	the tangential vector
$\boldsymbol{s}$	the tangential vector in 3D
$\boldsymbol{m}$	the normal branch vector
$\boldsymbol{b}$	the orientation vector paralleling the longest axis of the ellipsoid particle
$\boldsymbol{f}$	the contact force vector: $\boldsymbol{f} = f^n \boldsymbol{n} + f^t \boldsymbol{t} + f^s \boldsymbol{s}$
f^n	the normal contact force
f^t	the tangential contact force
f^s	the tangential contact force (3D)

f_0^n	the directional average of the normal contact force distribution $f_0^n = \oint f_n^c(\theta) d\theta$
$\langle f^n \rangle$	the average normal contact force
$\hat{l}_0$	the average length of the branch vector
m_v	the volumetric density of contact $m_v = N_c / V$
e_0	the initial void ratio
H, W	the height and the width of a specimen (2D)
Δt	the length of a time step
$\mathfrak{R}$	the parameter defined as $-\dot{\varepsilon}_{11}/\dot{\varepsilon}_{22}$
$\mathfrak{g}$	the parameter defined as $(\mathfrak{R}-1)/(\mathfrak{R}+1)$
δ	the initial stress ratio $\delta = \left(\sigma_{x0} - \sigma_{y0}\right) \Big/ \left(\sigma_{x0} + \sigma_{y0}\right)$
φ_{cv}, φ_p	the critical state friction angle and the peak state friction angle
$\bar{\theta}$	the lode angle of the Cauchy stress tensor
$\bar{\theta}_\phi$	the lode angle of the fabric tensor
δ_{ij}	the Kronecker delta
Γ_{ij}	the traceless symmetric second-rank tensor
ϕ_m	the mobilized friction angle and the mobilized dilation angle $\sin\phi_m = t/s$
ψ_m	the mobilized dilation angle $\sin\psi_m = -\dot{\varepsilon}_v^p / \dot{\gamma}^p$
σ_{ij}^*	the true stress tensor: $\sigma_{ij}^* = \phi_{ik}^{-1}\sigma_{kj}$
σ_{ij}^{s*}	the fictitious stress tensor: $\sigma_{ij}^{s*} = (\phi_{ik}^s)^{-1}\sigma_{kj}$
q^*, p^*	the deviatoric and mean values of the stress tensor σ_{ij}^*

χ_{LD}^{*}	the parameter for Lade-Duncan relation of the true stress
χ_{MN}^{*}	the parameter for Matsuoka-Nakai relation of the true stress
$\hat{\sigma}_i$	a measure of principal stress components: $\hat{\sigma}_i = (\sigma_i)^m \phi_i^{-1}$ (i is not in summation here)
$\hat{q}, \hat{p}$	the deviatoric and mean values of $\hat{\sigma}_i$
σ_{ij}^{f}	the fabric stress tensor: $\sigma_{ij}^{f} = \sigma_{ik}\phi_{kj}$
χ_{LD}^{f}	the parameter of Lade-Duncan relation for the fabric stress
χ_{MN}^{f}	the parameter of Matsuoka-Nakai relation for the fabric stress
A, n	the parameters defined for the stress fabric relation before peak stress state in 2D
B, z	the parameters defined for the stress fabric relation before peak stress state in 3D
κ^{w}	the obliquity for the stress and fabric for weak sub-network in 2D
κ	the obliquity for the stress and fabric for strong sub-network in 2D
κ_p	the obliquity for the stress and fabric overall contact network after peak stress in 2D
η^{*}	the parameter of fabric response surface description
a^{*}, b^{*}	the coefficients for the fabric response surface description
$S(\boldsymbol{l})$	the PDF of the branch vector
$E(\mathbf{m})$	the PDF of the orientation of the branch vector
$P(l\|\boldsymbol{m})$	the conditional length distribution of the branch vector
$E(\mathbf{n})$	the PDF of the contact normal vector
a_2, b_2	the coefficient of the second-order component of the Flourier function for $E(\theta)$
a_2^s, b_2^s	the coefficient of the second-order component of the Flourier function for $E^s(\theta)$

a_2^w, b_2^w	the coefficient of the second-order component of the Flourier function for $E^w(\theta)$
μ_r	the coefficient of the rolling friction
d^2W	the second-order work
$(\mathrm{d}^2W)_{\mathrm{I}}$	the second-order work induced by stress from the normal contact force
$(\mathrm{d}^2W)_{\mathrm{II}}$	the second-order work induced by stress from the tangential contact force
$(\mathrm{d}^2W)_{\mathrm{I}}^{fabric}$	the part of $(\mathrm{d}^2W)_{\mathrm{I}}$ computed from fabric change
$(\mathrm{d}^2W)_{\mathrm{I}}^{micro}$	the part of $(\mathrm{d}^2W)_{\mathrm{I}}$ computed from the local directional second-order work
$(\mathrm{d}^2W)_{\mathrm{I}}^{volume}$	the part of $(\mathrm{d}^2W)_{\mathrm{I}}$ computed from volume change
$(\mathrm{d}^2W)_{\mathrm{II}}^{fabric}$	the part of $(\mathrm{d}^2W)_{\mathrm{II}}$ computed from fabric change
$(\mathrm{d}^2W)_{\mathrm{II}}^{fabric}$	the part of $(\mathrm{d}^2W)_{\mathrm{II}}$ computed from the local directional second-order work
$(\mathrm{d}^2W)_{\mathrm{II}}^{volume}$	the part of $(\mathrm{d}^2W)_{\mathrm{II}}$ computed from volume change
$\bar{\mathbf{J}}^{\mathbf{s}}$	the diagonal matrix of ϕ_{ij}^s
$\bar{\boldsymbol{\sigma}}$	the diagonal matrix of the stress σ_{ij}
$\mathbf{T}, \mathbf{Q}$	the transformation matrixes
ρ_0	the initial density of the sample
ρ_g	the density of the particle

List of Abbreviations

2D	two dimensional
3D	three dimensional
ACST	the anisotropic critical state theory
CSL	the critical state lLine
DEM	the discrete element method
PDF	the properbility density function
PFC	the particle flow code
PSL	the peak state line
SFF	the stress-force-fabric relation
SMP	the spacially mobilized plane
VCC	the volumetric compression test along imposed paths of horizontal compression $\mathfrak{R}<-1$
VEC	the volumetric compression test along imposed paths of horizontal extension $\mathfrak{R}>1$
VED	the volumetric dilation test along imposed paths of horizontal extension $1>\mathfrak{R}>0$
VEI	the isochonic compression test along imposed paths of horizontal extension $\mathfrak{R}=1$
VP200	the biaxial compression test under confining pressure of 200 kPa
VP300	the biaxial compression test under confining pressure of 300 kPa
VP400	the biaxial compression test under confining pressure of 300 kPa

Chapter 1 Introduction

1.1 Background

Granular materials, such as sand and gravel, are commonly encountered in civil engineering. Different from a continuum mass, the granular material can be pictured as a collection of individual particles that interact with each other through inter-particle contacts which portray a geometric topology of the internal structure specifically. Upon loading, the mechanical and hydrological behaviors of granular material can be interpreted as an aggregation of the grain-scale actions over the topology of the microstructure. Thus, some microstructure based parameters are employed in the continuum modeling of granular material to achieve more physically profound explanations of macro-behaviour. The fabric tensor, characterizing the geometric microstructure, is commonly used to characterize microstructure.

As a measure of the microstructural alignment, the fabric anisotropy of a granular material can have an either inherent or induced origin. Inherent anisotropy is produced during the sedimentation of the particles. Induced anisotropy, is the result of the non-elastic deformation (Oda, 1993). Both experimental and theoretical studies suggest that fabric anisotropy and its evolution contribute to some key features of granular material behaviour, including dilation (i.e. shear-induced volume change), and non-coaxiality between stress and strain rate, as well as failure and instability during deformation (Cai *et al.*, 2013; Collins and Muhunthan, 2003; Fu and Dafalias, 2011; Li and Yu, 2009; Oda, 1993; Ohkawa *et al.*, 2011; Radjaï *et al.*, 2012; Wan and Guo, 2004).

Shear-induced dilatancy

The shear-induced dilatancy was first noted by Reynolds (1885) to describe the

remarkable phenomenon that the volume of a dense-packed granulate assembly increases when it is subjected to shear. The topic of shear-induced dilatancy was not in the mainstream interest in soil mechanics until the work of Taylor (1948), who presented a link between the shear strength and dilation properties. He adopted an energy principle where the total work done during shear equals to the dissipated energy at zero volume change and the work of volume change under constant stress. Thereafter, various theoretical models of shear-induced dilatancy have been established. Generally, these models can be categorized into two major trends. One is the microscopic analysis that considers a granular mass as a collection of particles. A stress-dilatancy relation based on a minimum energy principle was presented by Rowe (1962), which has become a fundamental conceptual idea in geomechanics. Following this line, different stress-dilatancy equations were developed (Collins and Muhunthan, 2003; Matsuoka, 1974; Tokue, 1979; Ueng and Lee, 1990; Wan and Guo, 1998). The physical significance of these approaches is profound since micromechanical aspects were incorporated. However, the geometric connectivities of the individual particles, was not explicitly considered for these approaches. The second trend is to obtain the stress-dilation relation by directly assuming the internal energy dissipation function, for example the famous Cam-Clay model by Roscoe *et al*. (1963). Similar research can also be found in Modaressi *et al.* (1994) and Dafalias (1986). For this type of approach, possible origins of the dilatancy are neglected. For example, the physical origin behind shear-induced dilatancy could be either the geometrical constraint including the grain-level behaviours and the microstructure (Wan *et al.*, 2007) or the kinematic constraint as the coupling between the shape and the volume of the assembly of rigid particles (Goddard, 1999). Therefore, in addition to the constraints of confining pressure and packing density, the fabric structure as well as its evolution must be properly incorporated into the stress-dilation equations. However, only a few dilatancy models considered the effect of fabric structure.

It is worth to note that Wan and Guo (2004) embedded a second-order tensor, obtained from a microscopic analysis of an ensemble of rigid particles, into their stress-induced dilatancy equation. More recently, Li and Dafalias (2011) related the fabric tensor based on the void space to the dilatancy state line using a dilatancy state parameter. Thereafer, Gao *et al.* (2014) proposed a fabric-dependent dilatancy function. Yin and Chang (2013) derived a relation between stress increment, strain increment and fabric tensor by considering the slips at contacts in all orientations. Kruyt and Rothenburg (2016) demonstrated a fabric-based expression of the dilatancy rate. To provide strong support for mechanisms of shear-induced dilatancy, more research must be dedicated to investigate the evolution of the fabric structure along various loading paths.

Critical state

The concept of critical state, in which a granular soil undergoes continuous shear deformation without volume change under constant stress, plays an important role in geomechanics. The necessary and sufficient conditions for critical state have been proposed. Schofield and Wroth (1968) originally developed the critical state soil mechanics, in which the granular soil at critical state reaches a constant stress ratio and a unique critical void ratio. The theory includes the microstructure parameter, void ratio, which is a homogeneous scaler thus does not characterize any anisotropic details of the internal structure. Thus, at critical state, the internal structure must be isotropic no matter the structure at initial state. However, experimental and numerical studies have indicated that the internal structure is of high anisotropy instead of being isotropic before approaching the critical state (Dafalias and Li, 2004; Hardin, 1989; Nakata *et al.*, 1998; Masanobu Oda, 1972; Yoshimine *et al.*, 1998). Such fabric has been measured in various ways, including preferred orientations of the contact normal, via branch vectors and the void space.

One question is how to add fabric to the necessary and sufficient condition for a critical state to occur. Li and Dafalias (2011) presented an Anisotropic Critical State Theory (ACST) for granular material by introducing a normalized fabric parameter that evolves toward a critical state value norm-wise and direction-wise. The fabric is computed according to the geometry of the void cells (Li and Li, 2009). A sufficient characterization of fabric structure usually includes two terms, the fabric tensor based on void shape and the fabric tensor based on the inter-particle contact normal (Fu and Dafalias, 2015). The latter, known as the geometric fabric, is believed to be more sensitive to the stress-strain relation in granular materials (Kuhn *et al.* 2015). Hence, geometric fabric should be incorporated into the critical state conditions. The notable work of Zhao and Guo (2013) introduced the effect of the geometric fabric to the critical state parameters, by including a fabric anisotropic parameter K, defined as the first joint invariant of the deviatoric stress tensor and the deviatoric fabric tensor. A unique relation between the mean stress level and the parameter K was obtained. However, this unique relationship is not profound physically, since the parameters, K and confining stress are not independent and actually K already includes the stress component.

It is emphasized that the natural process from the initial state to the critical state is associated with the evolution of fabric anisotropy which should be carefully integrated in critical state theory of granular soils. Hence, a microstructural sufficient and necessary condition with regard to the fabric tensor for critical state, as well as the evolution of the fabric tensor deserves more attention. One possible approach is to define a modified stress tensor based on the Cauchy stress tensor and fabric tensor and then achieve an identical state at the critical state.

Instability of granular materials

A theoretical basis for stability in granular materials is the Drucker's postulate of

non-negative second-order plastic work, i.e., $\mathrm{d}^2W = \mathrm{d}\sigma_{ij}\mathrm{d}\varepsilon_{ij}^{p} > 0$ for stability (Drucker, 1957). This postulate was extended to the total work by Hill (1958) as $\mathrm{d}^2W = \mathrm{d}\sigma_{ij}\mathrm{d}\varepsilon_{ij} > 0$, in which $\mathrm{d}\sigma_{ij}$ and $\mathrm{d}\varepsilon_{ij}$ are incremental stress and strain, respectively, using upper script "p" implying plastic component. It is essential to note that the second-order criterion by itself provides a sufficient but not necessary condition of stability. Correspondingly, the material may be unstable when $\mathrm{d}^2W \le 0$. The effective collapse of a homogeneous sample depends on the loading direction and the controlled loading variables (François Nicot *et al.*, 2013; Prunier *et al.*, 2009). Various experimental studies have been conducted to explore the instability of granular soils in terms of the postulate (Castro, 1969; Lade, 1988; Misra and Poorsolhjouy, 2015; Nicot *et al.*, 2015; Wan *et al.*, 2007; Zhu *et al.*, 2016). As put forward by Nicot and Darve (2009), Hill's second-order work criterion lacks physical insight and misses the physical link between the macro instability and vanishing of the second-order work. Since the apparent stress and strain are functions of the contact forces and particle displacements on the grain-scale; respectively. It is believed that the fabric structure of granular material evolves during the deformation history and that the fabric is inevitably linked with the macroscopic material instability. In this respect, multi-scale approaches of modeling instability may be applied in order to investigate physical origins of the instability in granular materials. This issue has been extensively studied, for example by Misra and Poorsolhjouy (2013), F. Nicot *et al.* (2013), Nicot and Darve (2005) , Zhu *et al.* (2016) and among other. However, the macroscopic second-order work cannot be understood as a simple summation of the all local second-order works in each contact orientations. The challenge lies in the unilateral contract interactions allowing for rearrangements of the fabric structure and the change of volume. In another word, the fabric structure and its evolution must be properly considered. However, an understanding of the relation between the vanishing

of the second-order work and micro-variables is far from achieved.

Non-coaxiality within granular material

The conventional elastic-plastic constitutive models generally assume that the directions of the principal stress coincide with these of the principal strain rate. However, both experimental studies and numerical simulations show that, for example in simple shear tests, the direction of the principal strain rate does not follow the rotation of principal stress direction in granular soils, which is known as non-coaxiality (Ai *et al.*, 2014; Cai *et al.*, 2013; Gutierrez and Ishihara, 2000; Joer *et al.*, 1992; Li and Yu, 2009; Matsuoka *et al.*, 1988; Roscoe *et al.*, 1967). Roscoe (1970) is among the first to observe the inconsistency of the principal axes of the plastic strain increment and those for the stress. This non-coaxiality is greatest at lower shear strain levels and generally decreases as the shear strain increases. At the critical state, they become coaxial. Since both the stress tensor and the strain increment tensor can be computed through contact forces and relative displacements acting through inter-particle contacts (Bagi, 1996; Bathurst and Rothenburg, 1988; Chang and Liao, 1990; Christoffersen *et al.*, 1981). Hence, non-coaxiality is inevitably related to the internal structure, characterized by fabric anisotropy. For example, a higher degree of non-coaxiality is observed in more anisotropic samples, and it gradually diminishes as the stress ratio approaches the critical state (Gao and Zhao, 2017, 2013; Gutierrezl *et al.*, 1991; Miura *et al.*, 1986; Yang *et al.*, 2007). Therefore, the micromechanical study of fabric and its evolution during principal stress rotation can be of great theoretical and practical importance for the understanding of the non-coaxial behaviour in granular materials.

1.2 Objectives

The primary objectives of this research are to determine the evolutionary relation

between the internal structure, as characterized by fabric, and the stress state during various loading paths. DEM simulations are employed to obtain the detailed information on the microstructure in numerically simulated laboratory tests. The statistic approach is adopted to investigate the non-coaxial behaviour within the granular material. Some specific objectives are:

- To characterize the internal structure using fabric anisotropy in both the overall contact network and the strong and weak sub-networks, and explore their physical relation under the statistic framework.
- To determine fabric evolution in different contact networks (i.e., the overall contact network, the strong and weak sub-networks) during proportional and non-proportional shearing of granular materials.
- To examine the fabric anisotropy at critical state and quantify the response surface of the fabric for different contact networks on the π-plane and then obtain a unique stress-fabric relation for the critical state.
- To investigate the major principal direction of the fabric tensors for different contact networks during the rotating and of the principal orientation of the stress tensor and examine non-coaxiality between the orientations of principal stress and the principal fabric components along various loading paths with an expectation of better understanding the non-coaxial behaviour of granular materials.
- To interpret the origin of material instability from a microscopic point of view using a micromechanical analysis and statistic approach, and then to verify the relation between the degradation of different contact networks and the vanishing of the second-order work.

1.3 Outline of the thesis

An extensive investigation on the research objectives gives a dissertation, which is

organized into eight chapters. A brief outline of these chapters is provided as follows.

Chapter 2 presented an exclusive review of the microscopic modeling of granular materials and discrete element method. The significance of the micro-macro correspondence between stress state and microstructural evolution was highlighted.

Chapter 3 demonstrated series of two-dimensional and three-dimensional tests using the discrete element method (DEM). Stress-strain responses from numerical tests were investigated by comparing them with data from laboratory tests.

Chapter 4 explored the fabric evolution within granular materials which were subjected to general loading conditions in two-dimensional and three-dimensional conditions. The evolution of fabric anisotropy for the overall contact network and sub-networks were investigated based on the numberical tests results. Typically, the fabric-stress relation was established in different contact networks.

Chapter 5 examined the fabric and its evolution at the critical state. The fabric-stress relation was established using the fabric tensor for the strong sub-network or the overall contact network. The fabric response surfaces on the octahedral plane were determined for fabric tensor in different contact networks.

Chapter 6 examined the coaxiality between the direction of the principal component of the fabric tensor and that of the stress tensor micromechanically. This coaxiality was further verified using numerical tests results involving in shearing under both fixed and rotating of the principal stress orientation.

Chapter 7 investigated fabric in different contact networks and its relation to the vanishing of the macroscopic second-order work. Micromechanically, the second-order work was derived using local level parameters which made it possible to interpret the origin of material instability from a microscopic point of view.

Chapter 8 summarized the main conclusions of the current study and highlighted the future work.

Chapter 2 Literature Reviews

A literature review on various important aspects about the micromechanical analysis of granular materials including the characterization of fabric, stress-fabric relations, the fabric at critical state and material instability, as well as discrete element method is provided in this chapter.

2.1 Homogenization

In granular materials, the load-deformation behaviour is usually described within a continuum mechanics framework, in terms of stress and strain. Micromechanically, the mechanical behaviour is dominated by the inter-particle interaction and the geometric arrangement of particles, known as the microstructure. The inter-particle contact forces, i.e., normal force, tangential force and bounded force, produce motions on the contact plane, such as relative displacement, particle rotation and contact sliding. Hence, the microscopic interpretation of the stress tensor and strain tensor, as well as the geometric microstructure is a fundamental step for constitutively modeling of granular material.

Among the earliest works, Cundall and Strack (1979) highlighted the significance of involving particulate details into the continuum parameters and presented the interpretation of the average stress tensor, the average moment tensor and average displacement gradient tensor within an assembly of disks. For example, the stress tensor and strain tensor can be related to the contact force and particle displacement on the particle scale. A key assumption of this process is homogenization within a Representative Volume Element (RVE) (see Nemat-Nasser *et al.* 1996). The RVE is considered as a statistically representative of the material. It must be sufficiently large and include enough particles. Nemat-Nasser (1999) suggested a relative size of the

RVE in the heterogeneous material such that $D_{RVE} > D_{50} \times 10^3$, where D_{RVE}, D_{50} are the diameter of the RVE and the mean particle diameter, respectively. Lower ratios of D_{RVE} / D_{50} tend to be applied in the DEM simulations due to the limitations associated with the computer technology.

Stress in granular materials

Among the definitions of the stress tensor in terms of contact forces using averaging approaches, Christoffersen *et al.* (1981) derived the symmetric stress tensor by applying the principle of virtual work considering the time rate as $\sigma_{ij} = \frac{1}{2} N_c \hat{l}_0 \left\langle f_i n_j + f_j n_i \right\rangle$, where N_c, f_i, n_j and $\hat{l}_0$ are the number of total contact within the unit volume of granular mass, the *i*-th component of contact force vector including the normal force and tangential force, the *j* component of contact normal vector and the average length over all branch vectors, respectively. A branch vector, ***l***, is the vector joining the centroids of two contacting particles. $\langle \bullet \rangle$ denotes averaging which takes place over all N_c contacts within the unit volume of granular assembly. Mehrabadi *et al.* (1982) obtained the same formulation of the macroscopic stress tensor using average tractions. Emeriault and Chang (1997) employed the stress tensor of principal virtual work and derived the incremental form such that $\Delta\sigma_{ij} = \frac{1}{2} N_c \hat{l}_0 \left\langle \Delta f_i n_j + \Delta f_j n_i \right\rangle$. According to these definitions, the stress tensor is symmetric.

Rothenburg (1980) analyzed the static equilibrium and obtained an expression for the boundary stress tensor in term of the average contact forces and branch vectors as $\sigma_{ij} = \frac{N_c}{V} < f_i l_j >$ with V being the volume of REV, which was verified using three-dimensional idealized granular assemblies. Rothenburg and Selvadurai (1981)

proposed a continuum expression of the stress tensor using a probability density function $E(\boldsymbol{n})$ as $\sigma_{ij} = m_v \hat{l}_0 \int_V f(\boldsymbol{n}) n_i n_j E(\boldsymbol{n}) \boldsymbol{dn}$, where $m_v = N_c / V$ is also known as the volumetric density of the contact and $f(\boldsymbol{n})$ is the contact force in the direction of $\boldsymbol{n}$.

Chang and Ma (1991) proposed a definition of stress based on the principle of energy equivalence referring to the particle point rather than to a local element. The basic idea is that the energy at all contacts of a particle equals to the energy calculated using the stress and strain on the local scale. Accordingly, the Cauchy stress tensor can be given as $\sigma_{ij} = \frac{N_c}{2V} < f_i l_j >$.

Various stress formulations have been proposed either using statistical averaging over the sample volume of contact forces and branch vector or defining the overall tractions transformed across an interior imaged plane as the sum of the contact forces that represent the mechanical effect on one side of the unit area of this plane (see Mehrabadi *et al.* 1982). Regarding statistical averaging methods, three approaches have been developed (a) from boundaries (Drescher *et al.* 1972); (b) from particle stress (Christoffersen *et al.*, 1981; Potyondy and Cundall, 2004) and (c) from local stress (Bagi, 1996). Nevertheless, all these methods arrive at a similar expression for the stress, i.e.

$$\sigma_{ij} = \frac{1}{V} \sum_{k=1}^{N_c} f_i^k l_j^k \tag{2-1}$$

where V is the volume of REV; f^k and l^k represent the contact force and branch vector of the *k-th* contact, respectively.

Strain in granular materials

The volumetric homogenization of the contact forces and branch vectors can be used to physically interpret the stress tensor in terms of geometrical considerations and

equilibrium. On the other hand, to relate the strain tensor to the microscopic details is not straightforward. Many efforts have been dedicated to derive the strain tensor for granular materials. Initially, the strain tensor is defined kinematically at the local level. Research along this line can be found, for example, in Walton (1987), Jenkins (1987), Chang (1993) and Bathurst and Rothenburg (1988). An important assumption for these local strain formulations is that the strain field is uniform and that there is no particle rotation. Chang and Liao (1990) derived local strain by considering a non-uniform strain field and the effect of particle rotation. The local level strain definition can help to build the micro constitutive law of granular materials. However, the global strain cannot be derived from the local level strain directly using homogenization since there are too many unknown parameters.

Compared with the local definition of strain, it is more complicated to obtain a strain definition in terms of the relative displacement of neighboring grains. Generally, two categories of strain homogenization have been developed in granular materials. One is the spatial discretization approach or equivalent continuum method that describes the assembly as a continuum geometric system such as Voronoi network, Dirichlet network, and Delaunay network. Then the displacement gradient tensor becomes an expression of the discrete micro-variables only. Using this approach, Bagi (1996) arrived the deformation gradient tensor as

$$\bar{e}_{ij} = \frac{1}{V} \sum_{m>n}^{m,n \in N_c} \triangle u_i^{mn} d_j^{mn} \tag{2-2}$$

where $\triangle u_i^{mn} = u_i^m - u_i^n$ and u^m, u^n are the relative displacements of node pair m and n. d^{mn} is an area complementary vector. Similarly, Li and Li (2009) applied the volumetric averaging on the sub-cell displacement gradient into the total displacement gradient.

Another approach is the best fit method based on the premise that the mean field

of displacement rate, the mean displacement rate gradient multiplying the branch vector of the contact, is the best fit of actual particle displacement rate (Liao *et al.*, 1997, Potyondy and Cundall, 2004). A best fit is achieved by minimizing the summation of least squares of differences between the actual displacement gradient and the approximate displacement gradients over all particles. Once the best fit curve is found, the strain can be obtained through integrating the mean displacement rate gradient over time. This approach works well in a material with a homogeneous strain field. Shear band or localization may not be picked up in a heterogeneous strain field.

2.2 Fabric tensor

The concept of the fabric was originally defined to present the directional arrangement of particles and associated voids (Brewer, 1964). Thereafter, it was widely used to define the internal structure of the granular material. Experimental results have shown that fabric is significant for the understanding various properties of a granular mass, especially dilatancy and anisotropy (Oda, 1972b; Wan *et al.*, 2007). According to Oda (1972b), the fabric of granular mass should include at least two main sub-concepts; i.e., (1) orientation of individual particles, and (2) position of the particle and their relationships. According to Kuhn *et al.* (2015), various measures can be used to describe the fabric structure of a granular material: particle orientation, particle surfaces, contacts between particles, and void space.

Fabric based on particle orientations

The simplest measures of fabric are those based on the orientations of the particles (Kuhn *et al.*, 2015), especially for the non-spherical particles. Oda (1972b) characterized the internal structure using an inclination angle, which is defined as the angle from the long or short axis of the grain to a fixed direction. Then the distribution of particle orientations, or orientation vectors, is described using a directional

distribution function $E(\beta)$. The fabric is defined as a ratio of the normalized contact area in the minor principal stress direction over that in the major principal stress direction.

Oda and Nakayama (1988) proposed a fabric definition based on preferred orientations of non-spherical particles. They presented the definition of the fabric tensor in an assembly with non-spherical particles as that $\phi_{ij} = \int_{\Theta} n_i n_j E(\mathbf{b}) d\Theta$ where $\mathbf{b}$ is the orientation vector which is parallel to the longest axis of the ellipsoid particle. $E(\mathbf{b})$ and Θ are the density function of $\mathbf{b}$ and the solid angle corresponding to the entire surface of a unit sphere.

Kuhn *et al.* (2015) employed a matrix $\mathbf{J}^{p,i} = [\mathbf{q}_1^{p,i}, \mathbf{q}_2^{p,i}, \mathbf{q}_3^{p,i}]$ and a diagonal matrix $\mathbf{A}^{p,i}$ to represent the principal axes and widths of the i-th particle, respectively. For the ellipsoidal particles, $\mathbf{q}_1^{p,i}$ is the orthogonal direction of the particle principal axis. For the oval particles, $\mathbf{q}_1^{p,i}$ is oriented along a particle's central axis and $\mathbf{q}_2^{p,i}$, $\mathbf{q}_3^{p,i}$ are oriented in arbitrary transverse directions. When averaged among all particles in an assembly, a tensor-valued measure of the average particle orientations gives:

$$\bar{\mathbf{J}}^p = \left\langle \frac{3}{tr(\mathbf{A}^{p,i})} J_{jm}^{p,i} A_{ml}^{p,i} J_{lk}^{p,i} \right\rangle \mathbf{e}_j \otimes \mathbf{e}_k \tag{2-3}$$

where $\langle \bullet \rangle$ denotes an average over all particles and $\mathbf{e}$ is the Cartesian basis vector. As a second-order tensor $\bar{\mathbf{J}}^p$ gives clear indication of the particle arrangement. The anisotropy of particle orientation is characterized by $(\bar{J}_{11}^p - \bar{J}_{33}^p)/(tr(\bar{\mathbf{J}}^p)/3)$. According to this definition, the fabric anisotropy is always zero for an assembly of spherical particle.

Fabric based on measures of particle connectivity: contact orientation and

branch vector

For both non-spherical and spherical particulate assemblies, particles and their connected neighbors can intensively affect the mechanical behaviour of granular materials. The inter-particle connection can be qualified with a branch vector or a contact normal vector. The branch vector joins the centroids of the contacting particles. The contact normal vector is a unit vector that is perpendicular to the contact plane. Fabric tensors based on branch vectors or contact normal vectors have been proposed in various forms.

Among the earliest researchers, Satake (1978) defines the fabric tensor using the contact normal vector. The contact orientation gives a basic interpretation of the internal structure in both spherical and non-spherical particulate assemblies. This definition is the most commonly used expression for the fabric tensor, which is given by

$$\phi_{ij} = \frac{1}{N_c} \sum_{k=1}^{N_c} n_i^k n_j^k \tag{2-4}$$

where N_c is the total number of the contacts in the system with n_i^k and n_i^k being components of the kth contact normal vector in the i and j-directions, respectively. The fabric tensor can also be defined in terms of particle as $\phi_{ij} = \frac{2}{N_p} \sum_{k=1}^{N_p} n_i^k n_j^k$ (Kruyt and Rothenburg, 2014).

Oda and Nemat-Nasser (1982) adopted a statistic method to describe the distribution of the contact normal vector and branch vector. Let $E(\boldsymbol{n})$ and Θ represent the density function of $\boldsymbol{n}$ and the solid angle corresponding to the entire surface of a unit sphere. The probability density function of the contact normal $\boldsymbol{n}$ is defined as $E(\boldsymbol{n})$. The mean value of the $f(\boldsymbol{n})$ can be obtained by applying $\overline{f} = \int_{\Theta} f(\boldsymbol{n}) E(\boldsymbol{n}) d\Theta$. They define a second-order fabric tensor as

$$F_{ij} = \frac{N_c}{V}\hat{l}_0 \iint_{\Theta} n_i n_j E(\boldsymbol{n}) d\Theta = \frac{\hat{l}_0}{V}\sum_{k=1}^{N_c} n_i^k n_j^k \tag{2-5}$$

in which $\hat{l}_0$ and V are the mean length of the branch vector and volume of the assembly. Instead of considering the contact nature only in Eq. (2-4), both the volumetric contact density and the average length of the branch vector are involved according to the definition in Eq. (2-5). These two definitions are related by $F_{ij} = \frac{N_c}{V}\hat{l}_0\phi_{ij}$. Actually, the fabric tensor defined by Oda and Nemat-Nasser (1982) emphasizes the connection between fabric tensor and the macro stress tensor. The fabric surface can be developed similar to the stress response surface. For the non-spherical granules, a natural modification of the fabric tensor Eq. (2-5) becomes $F_{ij} = \frac{\hat{l}_0}{V}\sum_{k=1}^{N_c} m_i^k m_j^k$ with $\boldsymbol{m}^k$ being the unit vector of the branch vector at contact k (Mehrabadi and Nemat-Nasser, 1983).

Similar to the stress tensor, the fabric tensor can be converted into a diagonal form characterized by its principal components. Oda (1982) introduced fabric space using a coordinate system with the three axes corresponding to the principal components of the fabric tensor. Then a fabric state can be described as a vector in the fabric space where the mean and deviator values are the isotropic and anisotropic parts of the fabric tensor.

Besides defining a fabric tensor quantity using the average length of the branch vector, Satake (1982) also proposed a fabric tensor quantity that contains both the contact orientations and the branch vectors.

-branch vector

$$H_{ij}^{'} = \int_{\Theta} E(\mathbf{n}) l_i l_j d\Theta = \left\langle l_i l_j \right\rangle \tag{2-6}$$

-combined fabric tensor

$$H_{ij}^{"} = \int_{\Theta} E(\mathbf{n}) n_i l_j d\Theta = \left\langle n_i l_j \right\rangle \tag{2-7}$$

Mehrabadi and Nemat-Nasser (1983) proposed a fabric tensor, which includes both the contact normal vector and branch vector. The length of the branch vector and the contact area are also considered. The fabric tensor is of the form

$$\overline{H}_{ij} = \frac{1}{V} \sum_{k=1}^{N_c} a^k m_i^k n_j^k l^k \tag{2-8}$$

Under the static hypothesis, Liao *et al.* (1997) derived the relationship between global strain and inter-particle displacement using a term related to the fabric tensor. An inverse form of the fabric tensor is employed to describe the stress localization in granular material. The fabric tensor is defined using the branch vector as well as the volume of the assembly $B_{ij} = \frac{1}{V} \sum_{k=1}^{N_c} l_i^k l_j^k$. Thereafter, Hicher and Chang (2005) introduced a simpler expression of the fabric tensor as $B_{ij} = \sum_{k=1}^{N_c} l_i^k l_j^k$.

Similarly, Emeriault and Chang (1997) suggested a definition of the fabric tensor for the homogenization of the global strain, where the fabric is defined using branch vector and contact normal vector, as well as the volume of the representative element, as $F_{ij}^{"} = \frac{1}{V} \sum_{k=1}^{N_c} l_i^k n_j^k$. For an assembly with N_c contacts and identical particle radius R, the fabric tensor can be decomposed into an isotropic part and anisotropy part as

$$F_{ij}^{"} = \frac{RN_c}{V} (\delta_{ij} + \frac{1}{2} \varphi_{ij}) \tag{2-9}$$

in which φ_{ij} is a second-order tensor with $tr(\varphi) = 0$ and δ_{ij} is the Kronecker delta.

Radjaï et al. (2012) evaluated the geometrical state of the granular material using a combined definition involving both of the coordination number *Z* and the fabric anisotropy. As lowest-order descriptors of the contact network, the combined tensor is

defined as

$$G_{ij} = \frac{Z}{2}\left\langle n_i n_j \right\rangle = \frac{Z}{2}\int_{\Theta} E(\mathbf{n}) n_i n_j d\Theta \tag{2-10}$$

According to this definition, the mean value of G_{ij} becomes $G_P = \frac{G_{11}+G_{22}}{2} = \frac{Z}{4}$ in 2D and $G_P = \frac{Z}{6}$ in 3D.

Fabric based on surface area

Surface texture provides critical information in the stereology granular assembly. The anisotropy of the surface texture influences both the permeability of the sample and the mechanic characters such as dilation and critical state (Kuhn *et al.*, 2015). Kuo *et al.* (1998) defined fabric tensors based on the principles of stereology, including the surface area tensor, mean free path tensor and porosity tensor. They introduced an orientation distribution function of $S(\mathbf{u})$ to quantify the anisotropy of surface area, which is defined as the fraction of surface area per unit volume with a unit normal vector in the direction of $\mathbf{u}$, as

$$S(\mathbf{u}) = \frac{S_v}{4\pi V}(1 + S_{ij} u_i u_j) \tag{2-11}$$

where, S_{ij} is the surface area tensor, and S_v is the total surface area of the particles in volume V, with $S_v = \oint_{\Theta} S(\mathbf{u}) d\Theta$

Kuhn *et al.* (2015) defined the orientation of a particle surface using an inertia tensor, $\mathbf{I}^{s,i}$, for each particle. Then the preferential distribution of the particle surface within the assembly is described with the mean of the inertia tensor among all particles.

$$\mathbf{I}^{s,i} = \int_{\partial S^i} \mathbf{x} \otimes \mathbf{x} dA^i \qquad \bar{\mathbf{I}}^{s} = \left\langle \frac{3}{tr(\mathbf{I}^{s,i})} \mathbf{I}^{s,i} \right\rangle \tag{2-12}$$

where $\mathbf{x}$ is the vector from the centroid of the particle surface ∂S^i to points on this

surface, and $\mathbf{x} \otimes \mathbf{x}$ is the dyad $x_i x_j$.

Fabric based on the void

It is widely accepted that the fabric tensor based on the contact normal is the most important measure in connection with the mechanical behaviour of the granular material. It is expected that the void might be an alternative or a complementary measure of fabric since the particle contact and void are the two fundamental elements of the internal structure of granular materials. The hydraulic properties of the granular material are affected by the size, shape, orientation, and connectivity of internal voids. The proper characterization of the void has been conducted in varies approaches.

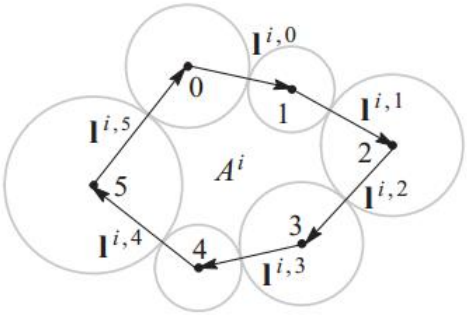

Figure 2-1: A void with associated particle and a replaced polygon

Given a void domain enclosed by connected particles, the geometry of the domain is described by a polygon with every chord being a vector connecting the adjacent contact points. Konishi and Naruse (1988) suggested a mean void tensor v_{ij} to characterize the void system in terms of the local void within the system. An intermediate tensor p_{ij}^k is defined using the edges of the polygon as:

$$p_{ij}^k = \frac{1}{2} \sum_{l=1}^{2n_v^k} v_i^l v_j^l \tag{2-13}$$

where n_v^k is the number of associated chord vector $\boldsymbol{v}$ of the k domain. The local void tensor can be described using the difference of the principal values $(p_1^k - p_2^k)$ and the major principal axis ς^k of the intermediate tensor p_{ij}^k. Let $\mathbf{h}$ be the unit vector of the principal axis of ς^k and N^p be the number of the local void. The mean void tensor for the while void system can be given as:

$$V_{ij} = \frac{1}{2N^p} \frac{1}{\sum_{k=1}^{2N^p} D^k} \sum_{k=1}^{2N^p} D^k h_i h_j \tag{2-14}$$

Instead of using the local void tensor, Tsuchikura and Satake (1998) present a loop tensor for describing the local void cell. The loop tensor F_L^k for the kth void domain with m^k branch vectors $\mathbf{l}^m$ is defined as

$$F_L^k = \frac{1}{2} \sum_{m=0}^{m^k-1} \mathbf{l}^m \otimes \mathbf{l}^m \tag{2-15}$$

According to Li and Li (2009), the geometry of a spatial object can be described with the polar spherical coordinates, (r, **n**), in which **n** is a unit vector representing directions, and r is the length of from the center of the object boundary. Therefore, for the void cells, the geometry is described by the void vector, **v**, which is a vector connecting the void cell center and the contact points on the boundary. The anisotropy of the granular material can be quantified based on an average void cell. The length of the void vector in the direction of **n** is the average length of all the void vectors along that direction. This allow us to define

$$G_{ij} = E_0 \oint_{\Theta} \bar{v}(\mathbf{n}) n_i n_j d\Theta \tag{2-16}$$

The integration is taken over the entire domain of solid angle in space. E_0 is the normalization factor which is equal to 2π and 4π in 2D and 3D space, respectively.

Fabric in strong and weak sub-networks

Traditional attempts to mathematically characterize the internal structure are based on the geometrical description of contact normal or branch vector in the whole contact network. However, both experimental and numerical results indicate that the majority of the contacts carry the force less than the average contact force and the contacts with contact forces larger than the average contact force dominate the shear resistance (Radjaï *et al.*,1998; Thornton and Antony, 2000; Peters *et al.*, 2005; Wan *et al.*, 2007).

Generally, the contact force distribution is inhomogeneous even among spherical particles since the internal structure affects force chains during a loading process. Radjaï *et al.* (1996) evaluated contact network of a granular assembly by defining a "ξ-network" which consists of all contacts with normal contact forces lower than a given cutoff ξ. The value of ξ may vary from 0 to the maximum contact force in the system. The "ξ-network" corresponding to $\xi = f_{\max}^{n}$ and $\xi = \langle f^{n} \rangle$ are the overall and the weak sub-network, respectively. $\langle f^{n} \rangle$ and $f_{\max}^{n}$ are the average and maximum values of the normal contact force.

Radjaï *et al.* (1998) discussed the correlation between contact forces and the texture of a granular assembly subjected to biaxial compression test using numerical simulations. According to the test results, almost all sliding dissipation occurs within weak sub-network, and all contacts within the strong sub-network are non-sliding. Moreover, referring to the strong and weak contacts, the contact network is divided into a load-bearing network or strong sub-network and a dissipative network or weak sub-network corresponding to the normal contact force larger or smaller than the average normal contact force. The load-bearing carries the shear-induced anisotropy and all contacts are non-sliding. Meanwhile, the orientation of induced structural anisotropy in the weak sub-network is orthogonal to that of the overall contact network.

Thornton and Antony (1998) derived the relation between the fabric tensor in overall contact network, ϕ_{ij}, and the fabric tensors in the strong (ϕ_{ij}^{s}) and the weak sub-network (ϕ_{ij}^{w}) as $\phi_{ij} = (1-\alpha)\phi_{ij}^{w} + \alpha\phi_{ij}^{s}$ where α is the proportion of contact number in strong sub-network. Under quasi-static shear deformation, they observed that the fabric anisotropy in weak sub-network is much lower than that in strong sub-network. Moreover, the fabric tensor for the weak sub-network was found to be coaxial with that of the stress tensor. Thornton and Zhang (2010) obtained the equation of $\phi_{ij} = 2\phi_{ij}^{w}/3 + \phi_{ij}^{s}/3$ which is independent of the radial strain direction and magnitude of the deviatoric strain.

Radjaï *et al.* (1998) investigated the force distribution within both two-dimensional and three-dimensional systems through a set of numerical observations. They found that the weak forces do not contribute to the shear stress; the stress computed from the weak sub-network is analogous to the mean stress. It is the strong forces that support the whole shear stress of the medium. Even for a granular packing with elongated particles, the shear stress is totally sustained by the strong sub-network (Radjaï *et al.,* 2012).

Peters *et al.* (2005) conducted numerical simulations on a 2D granular assembly consisting of polydisperse particles which were subjected to indentation by a rigid flat punch. They found that only half of the particles in the strong sub-network were actually working in the force-chain. In other words, the weak sub-network might play a significant role during resisting external loads.

García and Medina (2008) observed a switch between the orientation of structural fabric tensor in strong sub-network and that in weak sub-network. After a series loading-unloading cycles, they found that induced anisotropies remained for both contact networks.

By adopting a statistical framework, Kruyt (2016) proposed an alternative

definition of weak and strong contacts based on the comparison of the forces at contacts with the average force within the specific contact orientation. Under this definition, both the pressure and the shear stress were found to be equally carried by the weak and strong sub-networks.

Thornton and Zhang (2010) explored stress and fabric responses to general three-dimensional compression tests along radial strain paths which corresponds to straight lines on the π-plane of principal strain components. The fabric response envelope was found to be similar to the stress response surface, which could be described with Lade surfaces. The anisotropy corresponding to the weak sub-network at critical state was relatively small, but depending on the stress paths.

Based on three-dimensional DEM simulations, Zhao and Guo (2013) investigated the shear-induced anisotropy during drained/undrained shearing. They concluded that the weak sub-network always showed isotropic features, while the nature of the overall contact network was dominated by that of the strong sub-network.

2.3 The stress-fabric relation

As mentioned previously, the internal structure or fabric can influence the macroscopic behaviour of a granular assembly significantly. The fabric can be quantified by various measures that characterize microscopic features such as the distribution of contact normals or branch vectors that describe inter-particle connectivity (Mehrabadi *et al.*, 1983; Mehrabadi *et al.*,1982; Oda *et al.*,1985; Satake,1978), the distribution of void size or orientation (Fu and Dafalias, 2015; Konishi and Naruse, 1988; Kuhn, 1999; Li and Li, 2009), the distribution of longer axis for non-spherical particles (Oda *et al.*,1985) or the orientation of particle surfaces (Kuo *et al.*,1998). The measure of the contact orientations is the most responsive to loading than the other measures (Kuhn *et al.*,2015). As shown in Figure 2-2, the quasi-static loading-deformation responses of a particulate assembly are governed by

a contact law that describes the correspondence between contact force and relative displacement at the local level. Macroscopically, the stress-strain response follows constitutive laws. One practical approach to bridge the gap between local and global behavior is to add the fabric evolution into the constitutive laws. Following this approach, various fabric evolution models have been established using either stress or strain rate (Kruyt, 2012; Maeda *et al.*, 2006; Ng, 2001; Oda *et al.*, 1982; Satake, 1987; Subhash *et al.*, 1991; Zhao and Guo, 2013). The fabric evolution within these models employs the fabric tensor for the overall contact network. Not all contacts play the same role during the deformation of a granular assembly. Moreover, the load-bearing strong sub-network carries a direct geometrical anisotropy induced by shear. It gives rise via buckling to an indirect anisotropy inside the dissipative weak sub-network with a preferred direction orthogonal to the major principal direction of the stress tensor (Radjai et al., 1998).

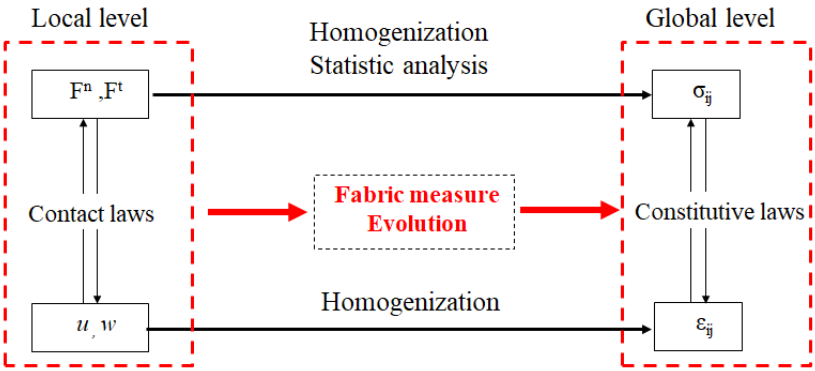

Figure 2-2: Skeleton of micro-macro transition in granular material

The preferential distribution of the contact force network describes the mechanical anisotropy and that of the contact network is the geometric anisotropy. The shear-induced anisotropy of contact network in an initially isotropic specimen can be interpreted as a result of the interaction between the contact force-chain and the contact network. According to Eq. (2-1), the macro stress tensor is developed using

the contact force vector and the branch vector. Therefore, the relation between the fabric anisotropy and stress parameters, such as the shear strength, can be thoroughly investigated. Generally, research in this area follows two trends: (1) decomposition of the stress tensor into components related to characteristics of contact force and parameters reflecting the microscopic geometry or the fabric, i.e., the stress-force-fabric relation; (2) observation or derivation of the relation between fabric tensor and stress tensor directly.

Stress-force-fabric(SFF) relation

On the basis of static equilibrium, Rothenburg and Selvadurai (1981) derived the expression of the stress using the microscopic characterization of a contact force network and a contact normal network. A Stress-Force-Fabric (SFF) relation in a two-dimensional case can be obtained in the form of $\frac{\sigma_t}{\sigma_n} = \frac{a_c + a_n + a_t}{2}$. Herein, $\sigma_t = (\sigma_1 - \sigma_2)/2$ and $\sigma_n = (\sigma_1 + \sigma_2)/2$, respectively. The three components on the right-hand side are the degree of anisotropy for contact normal (a_c), the normal contact force (a_n), and tangential contact force (a_t). It is clear that the ability of the specimen to resist an external load depends on the anisotropies in the distribution of the contact, normal contact force and tangential contact force, which equally contribute to the shear strength of an assembly. It is notable that this SFF relation is based on two assumptions: (a) the distributions of the contact normal, the normal contact force and tangential contact force are independent of each other and (b) the major principal axes of these directional distributions are coaxial. Chantawarungal (1993) developed a SFF equation for three-dimensional cases using spherical particle and then verified the equation with numerical results from true triaxial tests. Following these assumptions, Voivret *et al.* (2009) considered the effect of anisotropy

in the distribution of branch vector (a_l) and obtained a stress-force-fabric equation as of the form $\frac{\sigma_t}{\sigma_n} = \frac{a_c + a_n + a_l + a_t}{2}$ for two-dimensional cases. Here, σ_t and σ_n are the deviatoric and effective mean stresses. Similarly, Zhao and Guo (2013) added anisotropy of the distribution of the branch vector. Then the stress-force-fabric relation becomes $\frac{q}{p'} = \frac{2}{5}(a_c + a_l + a_n + \frac{3}{2}a_t)$ where cross products between two degrees of fabric anisotropy are neglected. Moreover, Ouadfel and Rothenburg (2001) concluded that a_l can give a negative contribution to the overall shear strength if the particle shape is non-spherical.

Instead of adopting the assumption that the distribution of the contact force vector is independent of that of the contact normal vector, Kruyt (2016) described the probability density function of both contact force and contact normal vectors under a statistic framework. A joint probability density function and a conditional probability density function were employed. An assumption that the contact force and contact normal within a certain angle are self-similar to the whole system was made. A stress-force-fabric relation was obtained for both overall contact network and weak sub-network without considering the tangential contact force. For the overall contact network, the SFF relation coincided with the conclusion made by Rothenburg and Selvadurai (1981) without considering a_t.

Li and Yu (2013) applied the theory of directional statistics in exploring the directional dependence between contact vectors and contact forces. The directional dependence between the contact vectors and contact forces was described by a scalar, which is independent of direction. They proved that the assumption made by Rothenburg and Selvadurai (1981), the directional distribution of contact vectors is independent with that of the contact forces, which does not hold true for the

non-proportional loadings. Meanwhile, their orientations were not coaxial neither during the non-proportional loadings.

Hosseininia (2015) decomposed the branch vector into a normal and a tangential component according to the contact plane and then derived the stress-force-fabric equation for planar granular materials. He found that assumptions made by Rothenburg and Selvadurai (1981) are not applicable since the branch vector did not coincide with the contact force vector.

Fabric evolution- numerical findings

Mehrabadi et al. (1982) provided a relation between the stress tensor and the fabric tensor in terms a fourth-order tensor as $\sigma_{ij} = A_{ijkl} F_{kl}$ where the $F_{kl} = N_c \hat{l}_0 \left\langle m_i m_j \right\rangle$, $\sigma_{ij} = N_c \hat{l}_0 \left\langle \bar{\sigma} m_i m_j \right\rangle$, and A_{ijkl} is a function of the contact normal vector and Kronecker delta δ_{ij}. Furthermore, Mehrabadi and Nemat-Nasser (1983) proposed a stress expression based on the local stress tensor on the contact scale. This leads to the average stress being connected with the fabric tensor in an inherent nonlinear equation such that $\sigma_{ij} = a_0^{'} F_{ij} + a_1^{'} F_{ik} F_{kj}$. Here $a_0^{'}$ and $a_1^{'}$ are the functions of the stress invariants. Since the fabric tensor and the stress tensor are coaxial according to their definition above, Oda *et al.* (1982) presented a stress-fabric relation of the form $\sigma_1/\sigma_2 = A^{'} F_1/F_2 + B^{'}(F_1/F_2)^2$ in which the parameter $A^{'}$ and $B^{'}$ are -1.0 and 2 .0 based on results from biaxial compression tests on assemblies of oval cross-section rod. Results of biaxial tests on photo-elastic rods demonstrate that the ratio of principal values of fabric tensor was approximately proportional to the square roots of the corresponding principal stress ratio as $\sigma_1 / \sigma_2 \approx (\phi_1/\phi_2)^{1/2}$ (Satake, 1984). A similar relation was obtained by Maeda et al. (2006)

Antony (2004) conducted biaxial compression tests on the assembly of oval

particles. They obtained a relation between shear stress ratio and the square root of $(\phi_{22}^s/\phi_{11}^s)$ for strong sub-network as $(\sigma_1-\sigma_2)/(\sigma_1+\sigma_2)\approx(1/2)(\phi_{22}^s/\phi_{11}^s)^{1/2}$ where ϕ_{11}^s and ϕ_{22}^s are the components of fabric tensor defined in Eq. (2-8). By carrying out drained triaxial compression tests on an assembly of ellipsoidal particles, Ng (2001) observed that the principal stress ratio (σ_1/σ_3) is proportional to $\ln(\phi_1/\phi_3)$ where ϕ_1 and ϕ_3 are the major and minor principal components of the fabric tensor for overall contact network defined according to Eq. (2-8).

Various fabric evolution laws have been proposed through either theoretical approaches or experimental tests. The application of fabric evolution laws in a continuum modeling of granular material is far from satisfactory. Wan and Guo (2004) proposed a stress dilatancy model with embedded microstructural information by assuming a fabric evolution law. They assumed that the rate of change of fabric tensor components is proportional to the rate of change of the deviatoric stress ratio which is defined as the increment of deviatoric stress over that of the mean stress. Their principal orientations were assumed to be coaxial with each other. Similarly, Yu (2008) assumed that the increment of the fabric tensor is related to the deviatoric stress and the stress rate.

2.4 Fabric at critical state

The existence and uniqueness of the critical state fabric has been a controversial topic in soil mechanics. Even laboratory tests with simple and controllable boundaries often give opposite findings. For example, the critical state strength of sand has been found to be stress-path dependent, which means the critical state line may be not unique (Riemer and Seed, 1997; Vaid and Chern, 1985; Vaid and Sivathayalan, 1996; Yoshimine *et al.*, 1998). Yoshimine *et al.* (1998) demonstrated non-uniqueness due to

an anisotropic fabric structure. The fabric anisotropy could be either inherent or induced. By conducting a series of hollow cylinder undrained torsional tests on Toyoura sand, Nakata *et al.* (1998) and Yoshimine *et al.*(1998) found that the orientation of fabric structure within a soil specimen has a considerable effect on the critical state failure. Some research also indicates that shearing processes can totally destroy all previous memory of granular media, including initial anisotropy, such that the critical state will not be affected by the initial fabric structure (Ng, 2009; Soga and Yimsiri, 2010).

In general, as pointed out by Been and Jefferies (1985), a state is a description of physical conditions, as opposed to properties of a material or substance. The behaviour of sand may be characterized in term of two variables: a state parameter combining the influence of void ratio and stress, and a fabric parameter characterizing the arrangement of the sand grains. Hence, the fabric should be properly considered when describing the critical state. Moreover, microstructural studies without exception reveal that the fabric anisotropy at critical state is considerable (Li and Li, 2009; Masson and Martinez, 2001; Masanobu Oda, 1972). A uniqueness of void ratio-confining stress-fabric relation is extensively pursued. Li and Dafalias (2002) employed a joint invariant of the fabric tensor and the stress tensor, as a state parameter of the critical state. Therefore, the critical state line in the *e-p* space was made a function of the joint invariant. It is noted that only inherent anisotropy was considered as a characterization of the contact orientations. Zhao and Guo (2013) incorporated a fabric anisotropic parameter K, defined as the first joint invariant of the deviatoric stress tensor and the deviatoric fabric tensor, into the critical state conditions. A unique relationship between the mean stress level and the parameter K was obtained, with the fabric anisotropy being induced by shearing. Li and Dafalias (2011) presented an Anisotropic Critical State Theory (ACST) for granular material by introducing a normalized fabric parameter that evolves toward a critical state value

norm-wisely and direction-wisely. The fabric tensor is defined based on the concept of void cell (Li and Li, 2009). According to Fu and Dafalias (2015), a strong linear correlation between contact-normal-based fabric tensor and void-vector-based fabric tensor was obtained for granular material composed of non-elongated particles. The fabric tensor based on contact normal can be easily incorporated into the ACST for assembly of non-elongated particles. Furthermore, Gao et al. (2014) developed a critical state plastic model expressed by the direct and joint isotropic invariants of the stress tensor and fabric tensor.

By adopting the fabric space defined by Oda (1982), Thornton and Zhang (2010) found that the response surface of the induced structural anisotropy was a small inverted Lade surface using triaxial tests with fixed strain paths at the critical state. A new parameter η_f^* was introduced to define the fabric response envelopes, thereby providing a general measure of the induced structural anisotropy. At critical state, the value of η_f^* was found to be a constant for all strain paths. Similar fabric envelopes were obtained by Zhao and Guo (2013) using triaxial tests along fixed stress paths.

2.5 Material instability and contact network

Strain softening and instability of geomaterials may lead to catastrophic deformation including failure. In granular material, various bifurcations and their related failure modes coexist, such as plastic limit, strain localization and instability. In mechanical terms, stability is obtained if a small load increment yields a small strain increment, while instability is defined as a phenomenon that a large plastic strain develops quickly due to the inability of a soil element to sustain a given stress or load (Guo and Su 2007). The theoretical basis for stability is Drucker's postulate of non-negative second order plastic work, i.e., $\mathrm{d}^2W = \mathrm{d}\sigma_{ij}\mathrm{d}\varepsilon_{ij}^p > 0$ (Drucker, 1957) This postulate was extended to include the total work by Hill (1958) that $\mathrm{d}^2W > 0$. Positive

second-order work constitutes is a sufficient, but not a necessary condition of stability. When $d^2W \leq 0$, the effective collapse of a homogeneous sample depends on the loading direction and the controlled loading variables (François Nicot *et al.*, 2013; Prunier *et al.*, 2009). It can be interpreted as a bifurcation criterion. At a bifurcation point, the response path can be unique or non-unique (undetermined) and stable or unstable. For example, in tests along proportional strain paths, the failure corresponding to the vanishing of the second-order work is thought to be non-effective (François Nicot *et al.*, 2013).

Based on this postulate, various experimental studies have been conducted to explore the instability of granular sand (Castro, 1969; Chu *et al.*, 1993; Daouadji *et al.*, 2013; Lade, 2002; Lade *et al.*, 1988; Wan *et al.*, 2007). Lade (1988) proposed the existence of an instability line above which the instability occurs. Later on, this instability line was found to be void ratio and stress history dependent. As put forward by Nicot and Darve (2009), Hill's second-order work criterion lacks physical insight and misses physical links between the instability and vanishing of the second-order work. Matiotti *et al.* (1995) found that the initial anisotropic consolidation is an important factor in the Lade's instability line. Notably, Wan *et al.* (2007) conducted series of controlled strain path tests using photoelastic disks. They found that strong force-chains in the core play a critical role in the instability of assembly. Sibille *et al.* (2007) presented the micromechanical detail for the vanishing of the second-order work, which does not work profoundly with DEM results.

Nicot and Darve (2006) inspected the physical origins of the Hill's instability condition for frictional materials using the micro-directional model and demonstrated that the macro-scale instability could be directly related to the constitutive nature of the local contact model between neighboring particles. The micro-directional model was proposed to relate to models at two different scales (Nicot, 2004, 2003). However, decomposing the macroscopic second-order work has highlighted that, as far as

granular materials are concerned, the macroscopic second-order work could not be understood as the single summation of all the local second-order works on each contact direction; other terms account for the change in volume and fabric must be considered. The specific effect of fabric structure on the macro-scale instability was not verified. Furthermore, for each incremental step, the generating and deleting of the contacts were ignored.

A major challenge is to understand the micromechanical mechanisms that govern the vanishing the second-order work. To continue work along this line, Nicot *et al.* (2014) found that global potential instability occurs only after several contact planes become potentially unstable. After vanishing of the summation of all the local second-order works, global potential instability occurs and the overall stress-strain response shows a decrease of the deviatoric stress. More inter-particle contact planes become potentially unstable. Misra and Poorsolhjouy (2015) investigated the instability micromechanically for a 2D assembly of cylindrical particle by using both a kinematic method and a least squares method. Along with the principal virtual work, the work done by microscopic force-displacement conjugates equated to that of the macroscopic stress and strain tensor conjugates. They found that the macroscopic instability coincided with instabilities of the inter-particle contacts. But, the micro-scale mechanisms for these two methods were not identical when the information of fabric structure was not properly considered.

It is believed that the microstructure or fabric of granular material evolves during the deformation history and the fabric is inevitably linked with the macroscopic behaviour related to the stress path, such as material strength and stability. Thus, fabric structure must be incorporated into the macroscopic instability of granular soil.

2.6 Coaxiality between fabric tensor and stress tensor

In geotechnical engineering, principal stress rotation is inevitable in responding to

loading conditions such as cyclic loading, excavation, earthquakes etc. Upon cyclic rotation of the stress, permanent strain can grow continuously even when the magnitudes of principal stresses are kept constant (Ishihara, 1983). The experimental studies by Roscoe *et al.* (1967) and Roscoe (1970) shows that the principal stress direction changes in simple shearing tests for which the direction of the principal strain rate does not follow. This phenomenon is also known as the non-coaxiality. Moreover, the difference between the principal stress orientation and principal strain rate orientation is the largest when the shear strain is small and decreases with the shear strain (Roscoe, 1970; Matsuoka *et al.*, 1988). Oda and Konishi (1974) found that the principal axes of the stress and strain increments did not generally coincide with each other, at least up to the peak stress ratio. A similar conclusion was obtained by Arthur *et al.* (1977) and Hight *et al.* (1983).

In granular materials, both the stress and strain are originated from the inter-particle actions, the contact force, and relative displacement, in the microscopic scale as shown in Eqs. (2-1) and (2-2). Therefore, the non-coaxiality between the directions of the principal stress and strain rate is inevitably related to the internal structure at the particle scale. The coaxiality assumption is actually only valid for isotropic media according to Hill (1950) and along proportional loading paths (Li and Yu, 2011).

Among the earliest studies, Matsuoka *et al.* (1988) connected the non-coaxiality between the orientation of the principal stress and the direction of the principal strain rate with the internal structure and the fabric, during the simple shearing tests using the photoelastic rod mass. The principal direction of the directional distribution of the contact normal also rotates during the rotation of the maximum shear stress, which indicated that the induced anisotropy is a natural consequence of the external loading involving principal stress rotation. Similar work has been conducted by Wong and Arthur (1986) by using a directional shear cell apparatus. They observed

non-coaxiality between the directions of the stress and strain rate along planes other than the bedding plane. Generally, the non-coaxiality is found to be dependent on the fabric anisotropy, that defines the preference of the directional distribution of particle contacts (Cai *et al.*, 2013; Li and Yu, 2009; Miura *et al.*, 1986; Ohkawa *et al.*, 2011; Pradel *et al.*, 1990). The evolution of fabric anisotropy and its direction are indispensable for modeling the non-coaxial behavior of granular material (Gao and Zhao, 2017; Yu, 2008).

The Discrete Element Method (DEM), proposed by Cundall and Strack (1979), enables monitoring of the internal structure during the numerical experimental tests and provides an ideal methodology for studying non-coaxiality. Among those first using two-dimensional DEM to investigate the behavior of granular material, Arthur *et al.* (1977) conducted biaxial tests (2D) along stress paths that included a chosen sudden change in the major principal stress direction. Thornton and Zhang (2006) examined shear banding and non-coaxial flow rules for simple shear tests using a 2D numerical model. Dabeet *et al.* (2015) investigated the non-coaxial stress-strain behavior by performing 3D DEM simulations to mimic the direct simple shear test. Li and Yu (2009) studied the influence of inherent anisotropy on the stress-strain behavior on continuously sheared 2D tests using two-particle bounded disks. They found that the non-coaxiality depends on the relative direction and magnitude of the contact fabric anisotropy and contact force anisotropy. Ai *et al.* (2014) conducted a series of simple shear tests using a discrete element method. The degree of fabric anisotropy, as well as its orientation, was investigated. They concluded that the evolution of the principal fabric direction resembled that of the principal stress direction. In other words, the orientation of the principal fabric rotated during the rotation of the principal stress direction.

The micromechanical study of the non-coaxial behavior of granular material mostly starts from the fabric-stress relation. The Stress-Force-Fabric (SFF) proposed

by Rothenburg and Selvadurai (1981) is based on the assumption that the distribution of contact normal is independent with that of the contact force or $\theta_c = \theta_n = \theta_t$. Based on this assumption, we can easily obtain that the orientation of the principal stress is coaxial with that of the principal fabric tensor or $\theta_c = \theta_\sigma$. Here, $\theta_c, \theta_n, \theta_t, \theta_\sigma$ are the directions of a_c, a_n, a_t and the principal stress, respectively. However, little effort has been conducted to verify the conclusion that $\theta_c = \theta_\sigma$. Based on the SFF relation obtained by Rothenburg and Selvadurai (1981), Hosseininia (2015) derived the expression of $\theta_\sigma = \frac{1}{2}\tan^{-1}(\frac{a_i \sin 2\theta_i}{a_i \cos 2\theta_i})(i = c, n, t)$. The assumption of $\theta_c \approx \theta_n \approx \theta_t$ was verified using a 2D biaxial compression test. It is worth to mention that, the principal stress direction is not monotonically rotated during the test. Li and Yu (2013) derived the SFF function based on directional statistical theory and considered the effect of statistic dependence between the contact vectors and the contact forces. They concluded that the assumption of $\theta_c \approx \theta_n \approx \theta_t$ was invalid for non-proportional loading.

2.7 Discrete element method

As noted previously, particulate systems are quite common in nature. Their dynamic behavior is very complicated due to the discrete nature induced by the interaction between contact particles. Owing to their heterogeneous structure, classical continuum mechanics cannot completely capture the mechanical behaviour of granular material because of the fundamental assumptions regarding continuity, homogeneity, and isotropy. The discrete particle simulation technique rapidly flourished with the advent of computing technology. A well-known modeling framework is the discrete element method (DEM) which was initially developed by Cundall (1971) for the analysis of

rock mass problems. Cundall and Strack (1979) adopted this method in describing the mechanical behaviour of particulate assemblies.

Generally, the discrete element method is based on dynamic or transient analysis using an explicit numerical scheme in which the particle interaction is monitored for each individual contact and the motion of the particles is modeled from particle to particle. The interaction between contacting particles is viewed as a transient problem that the state of equilibrium developed whenever the internal force balances. Two fundamental calculations are adopted in a DEM analysis. One is Newton's second law describing the motion of the individual particle. The other is a force-displacement law acting on the contact. One basic assumption for the explicit numerical scheme lies in that the disturbances cannot propagate from any particle further than its neighbors in a single time step (Cundall and Strack 1979).

DEM has been extensively used to study various geomechanical problems which can be categorized into two main motivations. In the first case, the DEM can be applied to simulate physical laboratory tests in which the evolution of the contact forces, the particle and contact orientations, the particle rotations etc., can be easily measured. While it is incredibly difficult to access all those details in a physical laboratory test. As far as the laboratory test is concerned, the most common modeling of the granular matter is based on the quasi-static condition in which, the loading rate is slow enough to ensure the inertial forces is much smaller than typical contact forces (Cundall and Strack 1979). Thereafter, DEM simulation has been extensively used to study the quasi-static behaviour of granular matter for different shearing flows: a) direct shear test, e.g. Cui and O'Sullivan (2006), Masson and Martinez (2001), Thornton and Zhang (2006) and Liu and Matsuoka (2003); b) biaxial compression test, e.g. Oda and Iwashita (2000), Kuhn (1999), O'Sullivan et al. (2002), David *et al.* (2007), Potyondy and Cundall (2004), Rothenburg and Kruyt (2004) and *Antony et al.* (2004); c) triaxial compression test, e.g. O'Sullivan *et al.* (2007), Ishibashi and Capar

(2003), Belheine *et al.* (2009), Thornton and Zhang (2010), Zhao and Guo (2013), Yoshimine *et al.* (1998) and Nicot *et al.* (2014). Validation of the results from DEM simulated tests has been conducted extensively. For example, Cheng *et al.* (2003) showed that the macroscopic behaviour of triaxial tests obtained in their DEM simulations is similar to those from laboratory tests on sands/silica. Powrie *et al.* (2005) conducted biaxial tests and found that effective angles of friction at peak strength and critical state are similar to those obtained from test results in the lab.

A second, more applied, motivation for the used of DEM is that it allows analysis of the mechanisms involved in large-displacement problems in geomechanics, e.g. rock cracking, rock fill, slope stability, fluid-solid coupling, soil-machine interaction, which can not easily be modeled using continuum approaches. Since the real boundary value problem will include millions of particles with highly complex and varying geometries, DEM simulation could be applied within a simplified physical system and provide good insights into the development of mechanisms (O'Sullivan, 2011).

Disks and spheres are currently the most popular types of particle considered in 2D and 3D DEM simulations; respectively. This is because the contact detection and the contact force computing are much easier conducted than those of irregular particles. However, due to the complex geometries of real soil particle, one drawback associated with using disk or sphere particles is that the rotation of the particles experience greatly exceeds the rotation particles has in real soil under equivalent loading conditions (O'Sullivan, 2011). Elliptical particles (2D) for two-dimensional analyses were proposed by Rothenburg and Bathurst (1991) and Ting (1992). More cases can be found in Azéma and Radjaï (2012), Bathurst and Rothenburg (1992) and Fu *et al.* (2012) The ellipsoid particle (3D) was introduced by Lin and Ng (1995) and Ng and Lin (1997). Vu-Quoc *et al.* (2000) applied ellipsoidal particles to simulate the dry granular material. The ellipsoidal particles were represented by clusters of

spheres for contact detection and for contact-force calculation. The method of cluster, gluing several spherical particles into one element through overlapping, provides an efficient tool for generating non-smooth, non-convex and non-spherical geometries. Various authors have proposed algorithms to create cluster particles, for example, Favier *et al.*(1999), O'Sullivan (2002) and Vu-Quoc *et al.* (2000). Even using circular and spherical particles, DEM simulation can capture mechanical behaviors observed in the laboratory tests.

As a powerful tool of investigating the microscopic behaviour of the granular material, the DEM simulation has been extensively employed to bridge the gap between micro-macro responses of the granular material, for example, the evolution of fabric structure in various loading paths. Rothenburg and Bathurst (1989) characterized the directional distribution of the contact normal and contact forces based on the data from DEM simulated biaxial tests using disc-shaped particle conduced by Bathurst (1985) and validated the Stress-Force-Fabric relation, originally proposed by Rothenburg (1980) based on micromechanics approach. Thereafter, Bathurst and Rothenburg (1992) explored the fabric evolution with stress and strain terms using DEM simulated tests on assemblies of 2D ellipse particles. Ouadfel and Rothenburg (2001) studied the fabric evolution in DEM simulated triaxial tests on assemblies of ellipsoid particles. Antony *et al.* (2004) analyzed the effect of the particle shape on the fabric evolution during DEM simulated biaxial compression tests where oval and circular particle was employed. By applying DEM simulation, Kuhn *et al.* (2015) explored the evolution of fabric structure in response to biaxial compression using assemblies of ovoid particles. More than fourteen measures of the fabric structure are investigated and can be categorized into four types: particles, particle surface, interparticle contact, the void space. The evolution of the fabric structures for the strong and weak sub-networks was also investigated. Hosseininia (2015) carried 2D biaxial compression tests on aggregates consisting circular particles or elongated

polygon-shaped particles using DEM simulation. The evolution of the fabric anisotropy, as well as its direction, was investigated. Zhao and Guo (2013) studied the characteristics of shear-induced anisotropy in granular material based on three-dimensional discrete element method simulation. In their research, the distinct features associated with the evolution of internal granular structure and different anisotropy sources during drained/undrained shearing of granular samples were carefully examined. Zhao and Guo (2014) considered rotational resistance among spherical particles in the DEM code as an approximate way to account for the effect of particle shape. The internal structure was divided into a strong force-chain network and a weak force-chain network. The 3D test results indicated that the critical state can be uniquely characterized by two linear relations between $e - p'$ and $a_c - \ln p'$, where p' and a_c are the mean effective stress and the fabric anisotropy.

2.8 Summary

A brief literature review has demonstrated the characterization of internal structure and its relation to the macroscopic response of granular materials. The microstructural definition of fabric tensor, stress tensor and strain, the fabric-stress relation, coaxiality between directions of the fabric tensor and stress were presented. Generally, the following statements can be concluded :

a) The fabric tensor which is defined using the contact orientations, characterized by the branch vector or contact normal, is one of the most apparent and effective measures associated with the mechanical response of the granular material. Therefore, one possible approach of microstructure based continuum model is to introduce the fabric tensor into the constitutive equations. A fabric evolution law in terms of the fabric-stress relation is a necessary prerequisite.

b) Several fabric-stress relations have been obtained under either statistical

framework or numerical simulations. However, a unique equation that could be introduced into the constitutive model, has not been proposed.

c) The weak and strong sub-networks behave individually during the shear deformation. The weak sub-network behaves much like the mean stress while the strong sub-network contributes to most of the shear strength. The evolution of fabric anisotropies in these sub-networks with stress deserves more effort.

d) At critical state, the overall contact network develops a high degree of fabric anisotropy depending on the loading path, which is similar to the critical state stress ratio. Hence, the fabric and its evolution at critical state have been intensively investigated with an expectation of achieving an anisotropic critical state theory.

e) The micromechanical study of the second-order work within a granular assembly gives the conclusion that the macro second-order work can be decomposed into three terms, the summation of the all local second-order work, the term induced by fabric evolution and the term induced by volume change. Therefore the fabric evolution corresponding to the vanishing of the second-order work might reveal the physical motivation of the macro instability.

Chapter 3 Numerically Simulated Laboratory Tests

3.1 Introduction

The discrete element method makes use of dynamic or transient analysis that considering the dynamic interaction of a system of interacting particles based on explicit time-marching schemes. The particle interaction is monitored for each individual contact and physical motion is modeled for individual particles. A contact constitutive model is employed to describe force-displacement on the contact scale. A dynamic equilibrium is always fulfilled for the individual particle. Hence, DEM simulations can provide dynamic information of micro-scale, such as the trajectories of particle connections and transient forces acting on individual particles, which are difficult to obtain in physical experiments. Moreover, numerical tests can be a supplement of real tests in investigating the mechanical behaviour of granular materials since various states can be easily handled using DEM approaches, which may not be applicable in real tests.

A brief outline of the discrete element approach is firstly demonstrated followed by an introduction of the contact model and parameter selection for numerical simulations. By adopting the selected DEM properties, a series of biaxial tests along proportional strain paths, simple shear tests and three-dimensional test along radial stress paths on the π-plane will be conducted to simulate the mechanical responses of granular material in the experimental tests.

3.2 Numerical tool-Discrete Element Approach

Following Cundall and Strack (1979), a single calculation step for interacting and potentially interacting particles can be divided into two stages: finding the contact force corresponding to the relative displacement between two contacting particles;

determining accelerations of individual particle based on the dynamic equilibrium. Owning to the particle motion, springs are introduced or removed as contacts are formed or broken. The continuous removal and introduction of contact springs result in a change in the overall system stiffness.

Description of motion of particles

To illustrate the mechanisms of the discrete approach during a calculation cycle, a simple contact integration procedure is assumed, as shown in Figure 3-1. Two initially isolated particles, A and B with the radius and mass r_A, r_B and m_A, m_B, respectively, move together motivated by the initial boundary conditions. The particle centers corresponding to A and B are (x_A, y_A) and (x_B, y_B); respectively. The velocity vectors for translational motion of A and B are $(\dot{x}_A, \dot{y}_A)$ and $(\dot{x}_B, \dot{y}_B)$. The acceleration vectors for translational motion of A and B are $(\ddot{x}_A, \ddot{y}_A)$ and $(\ddot{x}_B, \ddot{y}_B)$. At time step t_0, each particle has an independent velocity in the x-direction, $\dot{x}_{A,t_0}$ and $\dot{x}_{B,t_0}$, respectively. At time step t_i, two particles are detected to be in contact at point C with the velocities being $\dot{x}_{A,t_i}$ and $\dot{x}_{B,t_i}$ in the x-direction. The contact detection is conducted by the condition that the distance between two particle centers is less than the sum of their radii, i.e. $d_{AB} < r_A + r_B$, where $d_{AB} = \sqrt{(\dot{x}_{A,t_i} - \dot{x}_{B,t_i})^2 + (\dot{y}_{A,t_i} - \dot{y}_{B,t_i})^2}$. Once in contact, an overlap between two particles develops and during the time step, the overlap becomes $\Delta\delta_{t_i}^x = (\dot{x}_{A,t_i} - \dot{x}_{B,t_i})\Delta t$ in the x-direction. An incremental force-displacement law at contact C during the step yields

$$\Delta f_{n,t_i}^{x,A} = -k^n \Delta\delta_{t_i}^x, \quad \Delta f_{n,t_i}^{x,B} = k^n \Delta\delta_{t_i}^x \tag{3-1}$$

where k^n is the normal stiffness; $\Delta f_{n,t_i}^{x,A}, \Delta f_{n,t_i}^{x,B}$ represent the x-components of normal

force increment within the time step for particle A and B, respectively. Therefore, the resultant x- components of the normal contact force increments for particle A, $\Delta F_{n,t_i}^{x,A}$, is summations of contact forces over all $N_{t_i}^{A}$ contacts regards to particles A at this time step. Therefore, $\Delta F_{n,t_i}^{x,A}$ and $\Delta F_{n,t_i}^{x,B}$ can be expressed as

$$\Delta F_{n,t_i}^{x,A} = \sum_{j=1}^{N_{t_i}^{A}} \Delta f_{n,t_i}^{x,A,j} \; ; \quad \Delta F_{n,t_i}^{x,B} = \sum_{j=1}^{N_{t_i}^{B}} \Delta f_{n,t_i}^{x,B,j} \tag{3-2}$$

The x-components of the acceleration increment for particle A and B within this time step can be derived using Newton's second law as

$$\Delta \ddot{x}_A = \Delta F_{n,t_i}^{x,A} / m_A ; \quad \Delta \ddot{x}_B = \Delta F_{n,t_i}^{x,B} / m_B \tag{3-3}$$

The new accelerations for time step t_i can be updated as $\ddot{x}_{A,t_{i+1}} = \ddot{x}_{A,t_i} + \Delta \ddot{x}_A$ and $\ddot{x}_{B,t_{i+1}} = \ddot{x}_{B,t_i} + \Delta \ddot{x}_B$ for particles A and B, respectively. $\ddot{x}_{A,t_i}$ and $\ddot{x}_{B,t_i}$ are the accelerations for particle A and B in the positive x-direction for the time step t_i. By assuming that these accelerations are constant during the time period Δt, the updated velocities for particle A and B at the end of this time step (t_i) become

$$\dot{x}_{A,t_{i+1}} = \dot{x}_{A,t_i} + \ddot{x}_{A,t_{i+1}} \Delta t \quad \dot{x}_{B,t_{i+1}} = \dot{x}_{B,t_i} + \ddot{x}_{B,t_{i+1}} \Delta t \tag{3-4}$$

Similarly, during the subsequent time step, the incremental overlap at contact C in the x positive direction becomes $\Delta \delta_{t_{i+1}}^{x} = (\dot{x}_{A,t_{i+1}} - \dot{x}_{B,t_{i+1}}) \Delta t$. The incremental normal contact force and the accelerations of particles can be obtained using Eqs. (3-1) to (3-4). For simplification purposes, only one inter-particle contact is presented in Figure 3-1. It is worth mentioning that the particle acceleration is governed by all contacts forces related to the specific particle and the tangential contact force together with the particle rotation must also be considered for actual cases.

Figure 3-2 shows a schematic diagram of contact information between two disc

particles where both the contact vector and the contact force vector have a normal component and a tangential component. The rotation of the particle is also considered with the rotation angles of the particle A and B being θ_A and θ_B, respectively.

The relative velocity at the contact can be decomposed into a translation of the particle center and a part of the angle rotation. The relative velocity vector ($[\dot{x}_C \quad \dot{y}_C]^T$), with respect to the contact plane in Figure 3-2, becomes

$$\begin{bmatrix} \dot{x}_C \\ \dot{y}_C \end{bmatrix} = \begin{bmatrix} \dot{x}_A - \dot{x}_B \\ \dot{y}_A - \dot{y}_B \end{bmatrix} + \begin{bmatrix} (\dot{\theta}_A r_A + \dot{\theta}_B r_B) & 0 \\ 0 & (\dot{\theta}_B r_B + \dot{\theta}_A r_A) \end{bmatrix} \begin{bmatrix} t_1 \\ t_2 \end{bmatrix} \tag{3-5}$$

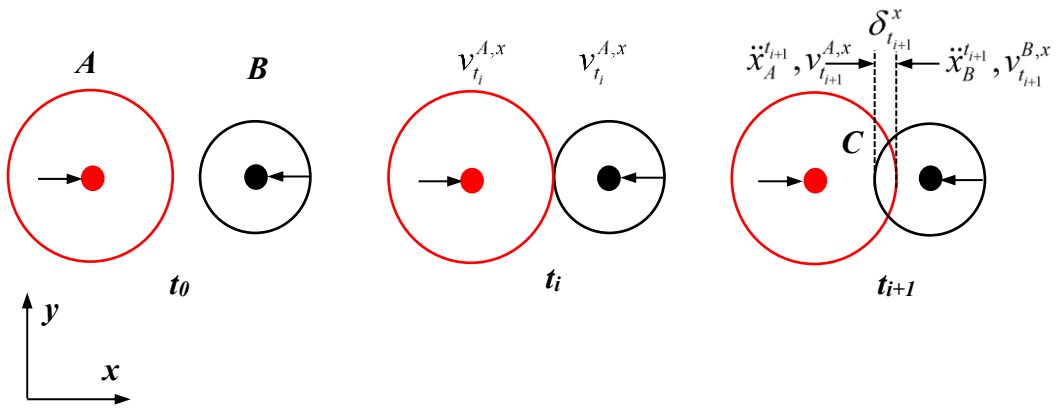

Figure 3-1: Schematic illustration of particle motion and inter-particle contact

Instead of using the (x, y) coordinate system, the relative velocity is projected on the plane of (**n**, **t**) as

$$\begin{bmatrix} \dot{n}_C \\ \dot{t}_C \end{bmatrix} = [\mathbf{n} \quad \mathbf{t}]^T \begin{bmatrix} \dot{x}_C \\ \dot{y}_C \end{bmatrix} \tag{3-6}$$

Therefore, the relatively incremental displacements in the normal and tangential directions within the time step Δt are

$$\begin{bmatrix} \Delta\delta_n \\ \Delta\delta_t \end{bmatrix} = \begin{bmatrix} \dot{n}_C \\ \dot{t}_C \end{bmatrix} \Delta t \tag{3-7}$$

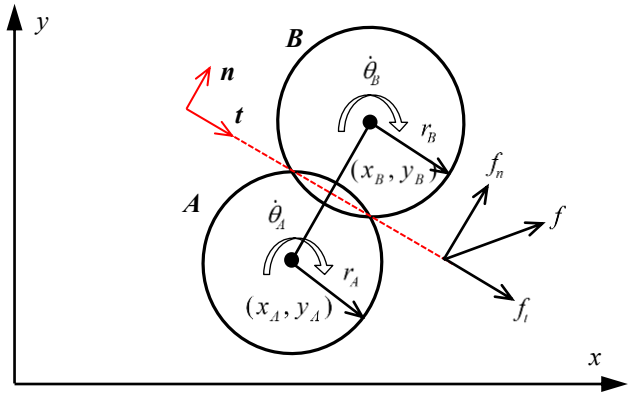

Figure 3-2: Illustration of a contact scheme between two particles

Description of contact law

In geomechanics, the particle forces may be induced by activities such as normal and tangential displacements, particle rotation, contact cohesion, contact damping, parallel bond, liquid bridge, surface tension, et al. Correspondingly, numerical contact models have been developed to describe these interactions, such as normal contact models, tangential models, bond models, rotational resistance models et al. When the mechanical behaviour of frictional material in laboratory tests is concerned, normal contact overlap, particle sliding, and particle rotation are most commonly considered.

Among various contact laws, there are two popular ones that are widely applied in simulating granular soils. The first one is based on a linear contact model introducing three input parameters: the normal contact stiffness k^n, the tangential contact stiffness k^s and the frictional coefficient μ. The corresponding increments of normal contact force and tangential contact are described as

$$\Delta f_n = k^n \Delta\delta_n, \quad \Delta f_t = k^s \Delta\delta_t \tag{3-8}$$

Here, the contact stiffness is only related to the stiffness of the particles. In other words, k^n and k^s are the equivalent contact stiffnesses. Given k_A^n, k_A^s and k_B^n, k_B^s being the normal and tangential contact stiffness for particle A and particle B, respectively, the equivalent stiffness is expressed as $k^n = k_A^n k_B^n / (k_A^n + k_B^n)$, $k^s = k_A^s k_B^s / (k_A^s + k_B^s)$.

The Coulomb friction model is employed to describe the relation between the tangential and normal contact forces as

$$\left| f_t^c \right| < \mu f_n^c \tag{3-9}$$

where μ is the inter-particle friction coefficient. When $\left| f_t^c \right| = \mu f_n^c$, sliding occurs and the tangential force acts opposite to the direction of slip. In some cases, a cohesion term, C', may be added to the failure criterion for the tangential force as $\left| f_t^c \right| < \mu f_n^c + C'$.

The other is the nonlinear Hertz-Mindlin formulation. This normal contact force-displacement model was developed by Hertz (1882) (also reported in Johnson, 1985). The tangential contact force-displacement model was reported by Mindlin (1949) where the tangential stiffness is constant for no-slip contact. A series of loading conditions were identified in the work of Mindlin and Deresiewicz (1953) who developed a set of rules for the generation from simple cases to the oblique impact problem using an incremental procedure. For spherical particles, when neglecting the plastic deformation of particles, the normal and tangential stiffnesses can be estimated as:

$$k^n = 2E^* \sqrt{r^* \delta_n}\ ,\ \ k^s = 8G^* \sqrt{r^* \delta_n} * \left(1 - \frac{f_t}{\mu f_n} \right)^{1/3} \tag{3-10}$$

where r^* and E^* are the equivalent particle radius and the elastic modulus,

$r^* = r_A r_B / (r_A + r_B)$ and $1/E^* = (1-\nu_A^2)/E_A + (1-\nu_B^2)/E_B$. G^* is the equivalent elastic shear modulus such that $1/G^* = (2-\nu_A)/G_A + (2-\nu_B)/G_B$. ν_A, E_A and G_A are Poisson's ratio, the elastic modulus and the elastic shear modulus of particle A. δ_n is the relative approach of the centroids of the two spheres in contact $\delta_n = r_A + r_B - d_{AB}$.

Rolling resistance

The shape and the roughness of the contact surface between soil particles can produce a rolling resistance or rolling friction that has a significant influence on the overall material response. Iwashita and Oda (1998) employed a combined sprint-dashpot-slider system that transferred a moment to the contacting particles as

$$M_r = -k^r \theta_r - C_r \dot{\theta}_r \tag{3-11}$$

where k^r is the stiffness of rotation resistance; C_r is the rational viscosity coefficient and θ_r is the relative rotation of the two particles, "-" implies the negative effect or in opposite direction with the rolling. Within the context of modeling the effect of particle shape, a rolling stiffness was defined by Iwashita and Oda (1998) as $k^r \approx k^s r^2$.

It is assumed that perfectly plastic rolling will occur if M_r exceeds a threshold value, $M_{r\max}$, which is related to normal contact force as

$$M_{r\max} = \mu_r f_n^c \tag{3-12}$$

where μ_r is the coefficient of rolling friction. It should be noted that the total moment increment during a time step contains the part resulted from tangential contact force increments for all contacts regarding to the specific particle and the

increment of movement from rolling resistance.

Damping

For the real inter-particle contact, particle damage and plastic yielding will happen and dissipate the accumulated kinetic energy within the system. In DEM simulation, as far as the elastic model is concerned, the energy dissipation could only happen during frictional sliding between particles. If the frictional sliding is small, the particle will vibrate constantly like a highly complex system of connected elastic springs without approaching a steady state. Therefore, the artificial damping is usually introduced to overcome the non-physical nature of the contact constitutive models used in DEM simulations, especially for the quasi-static conditions. Moreover, the damping is critical to the numerical stability in DEM simulation.

There are two most common types of damping, viscous damping and "non-viscous" damping. The viscous damping is proposed by Cundall and Strack (1979) and then was implemented in DEM analysis as (Bardet, 1998)

$$Ma^t + Cv^t = F^t \tag{3-13}$$

where M is the mass matrix, a^t is the acceleration vector at time t, C is the damping matrix, v^t is the velocity vector at time t and F^t is the force vector. Since the viscous damping force on each particle is proportional to its mass, it is sometimes called mass-damping. Cundall (1987) proposed an alternative damping system, in which the damping force at each node is proportional to the magnitude of the out-of-balance force with a sign that ensures that the vibrational modes are damped, rather than steady motion. Here the "out-of-balance force" is the non-zero resultant force that acts on a particle to cause acceleration. According to Cundall (2004), the damping force is given by

$$\boldsymbol{F}_d^p = -\alpha^* \left| \boldsymbol{F}^p \right| sign\left(\boldsymbol{v}^p \right) \tag{3-14}$$

in which $\boldsymbol{F}_d^p$ is the damping force for particle p, α^* is the damping constant, $\boldsymbol{F}^p$ is the resultant or out-of-balance force acting on the particle p, and $\boldsymbol{v}^p$ is the velocity vector for particle p. According to this definition, only accelerating motion is damped, therefore no erroneous damping force arise from steady-state motion.

3.3 Parameter selection

Owing to the complexity of natural granular materials, including the randomness in particle shape and particle size distribution, it is generally difficult to reproduce a real granular assembly and its corresponding mechanical behaviour by DEM simulations. Nevertheless, the models with circular or spherical particles enable us to investigate the micromechanics of granular material in a way that cannot be achieved in continuum methods. In the following sections, the linear contact model in Eq. (3-8) and the Coulomb friction model in Eq. (3-9) are employed to describe the activities on the contact plane.

Properties for two-dimensional tests

The selection of the contact stiffness and the inter-particle friction coefficient μ has a direct influence on the results of DEM simulations. In general, both the elastic modulus and the Poisson's ratio of the bulk material are intensively affected by the stiffness ratio k^s/k^n. According to Mohamed and Gutierrez (2010), $k^s/k^n = 1.0$ gives a Poisson's ratio of 0.25 while $k^s/k^n = 0.5$ corresponds to a Poisson's ratio of 0.28 in two-dimensional cases. Both of them are realistic for most granular materials. Consequently, the assumption $k^s/k^n = 1.0$ has been adopted in DEM simulations (Antony *et al.*, 2004; Nguyen *et al.*, 2009; Zhu *et al.*, 2016). Similarly, $k^s/k^n = 0.5$ is also widely adopted, for example, Kruyt (2012).

Various studies have revealed that the inter-particle friction can influence the

critical state and the stress-dilatancy relation. According to Huang et al.(2014), when $\mu < 0.5$, the dilatancy tends to increase with an increase of μ. On the other hand, the behaviour of granular material at the critical state seems to be insensitive to further increases in μ when $\mu \geqslant 0.5$. Moreover, a high friction coefficient can cause a negative Poisson's ratio ($\mu \to \infty$) (Rothenburg and Kruyt, 2004). Hence, $\mu = 0.5$ has been widely adopted by Kruyt (2012), Rothenburg and Kruyt (2004) and Jiang *et al.* (2006); see, e.g., Figure 3-3.

In two-dimensional tests, a linear elastic contact law is employed in this research and the inter-particle friction coefficient is selected as 0.5. In the biaxial tests along proportional strain paths, the normal and tangential stiffness are chosen based on $k^s / k^n = 1.0$ and $k^n / \bar{r} = 5.4 \times 10^9 Pa$ where $\bar{r}$ is the mean value of the particle radius. For the simple shear test, the normal and tangential stiffness are valued according to $k^s / k^n = 0.5$ and $k^n / \bar{r} = 2.6 \times 10^{10} Pa$. The ratio of p_0 / k^n in both tests is lower enough (10^{-3}) to guarantee the rigid particle assumption.

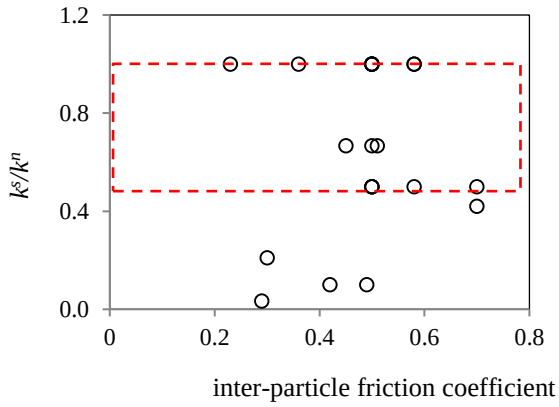

Figure 3-3: A summary of numerical properties k^s / k^n *vs.* friction coefficient in 2D DEM simulations

Properties for three-dimensional tests

For three-dimensional DEM simulations, Goldenberg and Goldhirsch (2005)

suggested that $2/3 < k^s/k^n < 1$. $k^s/k^n = 1$ was adopted by, for example, Zhao and Guo (2013) and Yoshimine *et al.* (1998). The ratio of normal contact stiffness over average particle radius should be larger than $k^n/\bar{r} > 10^8$Pa to guarantee the assumption of rigid particles according to Nicot *et al.* (2014). In 3D tests along radial stress paths on the π-plane, a linear elastic model is employed with the friction coefficient being 0.5. The contact stiffness in all three-dimensional tests are selected as on $k^s/k^n = 1.0$ and $k^n/\bar{r} = k^s/\bar{r} = 2\times10^8$Pa.

3.4 2D tests along proportional strain paths

According to Wan *et al.* (2007) and Guo and Su (2007), strain softening and material instability for granular materials are dominated by the rate of forced volume change, as well as the inherent potential of dilation. From a kinematical point of view, the collapse of a specimen can be illustrated as a larger imposed dilatancy rate than the intrinsic dilatancy rate of the granular assembly. Comparing with tests along selected stress paths, controlled proportional strain path tests can provide in-depth observations towards the mechanism of strain-softening and deformation instability of a granular material. As a result, DEM simulations for biaxial tests along proportional strain paths were carried out.

3.4.1 Test setup

A rectangle packing of polydisperse disks was considered as the 2D DEM model that was constrained by four frictionless rigid sidewalls. The normal contact stiffness at the walls was chosen to be sufficiently high, and the tangential contact stiffness at the walls is set to zero. A linear force-displacement contact law was employed with the contact behavior being governed by the normal stiffness k^n, tangential stiffness k^s and the frictional coefficient μ. The following assumptions were made: $k^s/k^n = 1$ and

$\mu = 0.5$. The basic characteristics of the initial assembly are given in Table 3-1.

The initial packing of the assembly for each test was generated by filling the box with randomly generated particles after which the specimen was slowly consolidated up to an initial isotropic confining pressure, as illustrated in Figure 3-4 (a). A total of nineteen numerical tests were conducted that can be divided into two categories: tests along proportional strain paths with a constant strain increment ratio $\Re = -\dot{\varepsilon}_{11}/\dot{\varepsilon}_{22}$ and tests with constant horizontal stress, which was achieved by controlling the movement of the vertical and horizontal walls (Figure 3-4 b).

Table 3-1: DEM parameters and material properties

Parameter	Value
Number of particles	≈ 26000
Particle density	2000 kg/m^3
Smallest particle diameter D_{min}	1.6 cm
Largest particle diameter D_{max}	2.0 cm
Average particle diameter D	1.8 cm
Initial porosity/Void ratio (e_0)	0.14~0.22/0.16~0.28
Inter-particle friction coefficient μ	0.5
Particle-wall friction coefficient μ	0.0
Height (H), width (W) of sample	H/D= 212, W/D=110
Initial axial stress σ_{11}	170 to 400 kPa
Initial confining stress σ_{22}	170 to 400 kPa
Normal spring stiffness k^n	k^n/D=2800MPa
Tangential spring stiffness k^s	k^s/D=2800MPa

In this study, the average macroscopic strain was determined according to the displacement gradient, e.g., $\varepsilon_{ij} = \frac{1}{2}\left(\partial u_i/\partial x_j + \partial u_j/\partial x_i\right)$. The strain rates in the vertical ($\dot{\varepsilon}_{11}$) and horizontal ($\dot{\varepsilon}_{22}$) direction are kept constant. Referring to Suiker and Chang (2004) and Christoffersen *et al.* (1981), the uniform strain field ε_{ij} in the granular assembly is the best fit for describing the actual contact displacements and can be

considered as a plausible assumption. The macroscopic strain rates in the assembly are related to the relative velocities of the boundary walls as $v_{1-1}^t = -v_{1-2}^t = \frac{1}{2}\dot{\varepsilon}_{11} \cdot H^t$ and $v_{2-1}^t = -v_{2-2}^t = \frac{1}{2}\dot{\varepsilon}_{22} \cdot W^t$ with H^t and W^t being the height and width of the specimen at time t. Similar treatments can be found in Thornton (2000) as well as Suiker and Chang(2004). The vertical strain rate $\dot{\varepsilon}_{11}$ is always positive (compression), while the lateral strain rate $\dot{\varepsilon}_{22} = -\dot{\varepsilon}_{11}/\Re$ can be positive or negative depending on the selected $\Re$ value. Since $\Re \notin (-1,0)$ and the boundary walls are frictionless, directions of the major principal stress and strain are always in the vertical direction, $\dot{\varepsilon}_{11} = \dot{\varepsilon}_1$ and $\sigma_{11} = \sigma_1$. Generally, the major and minor principal strain can be calculated as $\varepsilon_1 = \sum \dot{\varepsilon}_1 \Delta t$ and $\varepsilon_2 = \sum \dot{\varepsilon}_2 \Delta t$. Here Δt is the length of time within a step. It should be noted that for initially isotropic specimens, the strain paths with $-1<\Re< 0$ are the same as those with that belongs to a subgroup of tests with $\Re > 1$.

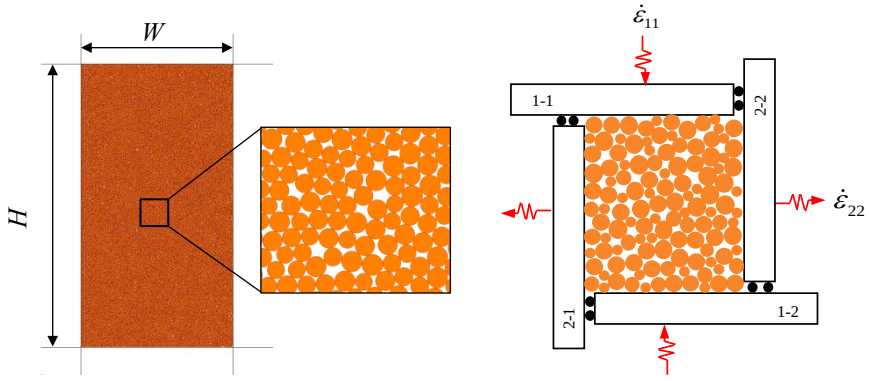

(a) (b)

Figure 3-4: Schematics of the specimen (a) and associated loading boundaries (b) in a 2D test

In all DEM simulations, the velocities of the boundary walls are slow enough (e.g., $\dot{\varepsilon}_1 = 10^5$/s) to maintain a quasi-static condition throughout the entire loading

history. We introduce the parameter $\vartheta = \dot{\varepsilon}_v / \dot{\gamma}$, which is the ratio of volumetric strain rate ($\dot{\varepsilon}_v = \dot{\varepsilon}_1 + \dot{\varepsilon}_2$) to the shear strain rate ($\dot{\gamma} = \dot{\varepsilon}_1 - \dot{\varepsilon}_2$). It is related to the strain ratio $\Re$ as $\vartheta = (\Re - 1)/(\Re + 1)$. Hence, all proportional strain paths can be categorized into forced dilation with $\vartheta < 0$ (or $0 < \Re < 1$) and forced contraction $\vartheta > 0$ (or $|\Re| > 1$), respectively. Hereby, a value of $\vartheta = 0$ (or $\Re = 1$) is associated with the isochoric deformation condition, while the hydrostatic compression and K_0-compression conditions are obtained when $\vartheta \to \infty$ ($\Re = -1$) and $\vartheta = 1$ ($\Re \to \pm\infty$).

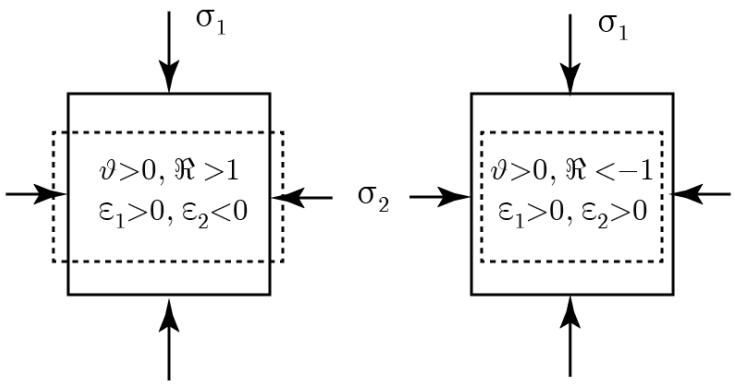

Figure 3-5: Two types of forced contractant tests (a) the VEC test and (b) the VCC test

For the sake of convenience, a test along an imposed strain path is described according to the following conventions: (a) the first letter, V stands for vertical compression; (b) the second letter, C or E means horizontal compression or horizontal extension; (c) the third letter, C, I or D, refers to volumetric contraction, isochoric deformation or volumetric dilation. For example, VEI represents a test in which the specimen has vertical compression, horizontal extension with the volume being a constant ($\Re = 1.0$). For tests with constant confining pressure, the second letter P stands for constant confining pressure. VP200 is used to describe a test in which the

specimen undergoes vertical compression with σ_2=200 kPa. Details of the tests are listed in Table 3-2.

It is worth to mention that for the two-dimensional cases, the principal stresses are calculated as

$$\sigma_{1,2} = \frac{\sigma_x + \sigma_y}{2} \pm \sqrt{(\frac{\sigma_x - \sigma_y}{2})^2 + \tau_{xy}{}^2} \tag{3-15}$$

where σ_x and σ_y are normal stresses in the x and y directions, and τ_{xy} is the shear stress. The corresponding mean and deviatoric stresses are readily obtained as $s = (\sigma_1 + \sigma_2)/2$ and $t = (\sigma_1 - \sigma_2)/2$.

Table 3-2: Details about tests

Test type	Test label	Initial stresses	Macroscopic boundary conditions
$\sigma_2 =$ constant	VP200	$\sigma_1 = \sigma_2 = 200kPa$	$\dot{\varepsilon}_1 > 0,\ \sigma_2 = 200kPa$
	VP300	$\sigma_1 = \sigma_2 = 300kPa$	$\dot{\varepsilon}_1 > 0,\ \sigma_2 = 300kPa$
	VP400	$\sigma_1 = \sigma_2 = 400kPa$	$\dot{\varepsilon}_1 > 0,\ \sigma_2 = 400kPa$
Controlled strain paths	VED	$\sigma_1 = \sigma_2 = 170kPa$	$\dot{\varepsilon}_1 > 0,\ \dot{\varepsilon}_2 < 0,\ \lvert\dot{\varepsilon}_1\rvert < \lvert\dot{\varepsilon}_2\rvert$
	VEI		$\dot{\varepsilon}_1 > 0,\ \dot{\varepsilon}_2 < 0,\ \lvert\dot{\varepsilon}_1\rvert = \lvert\dot{\varepsilon}_2\rvert$
	VEC		$\dot{\varepsilon}_1 > 0,\ \dot{\varepsilon}_2 < 0,\ \lvert\dot{\varepsilon}_1\rvert > \lvert\dot{\varepsilon}_2\rvert$
	VCC		$\dot{\varepsilon}_1 > 0,\ \dot{\varepsilon}_2 > 0,\ \lvert\dot{\varepsilon}_1\rvert > \lvert\dot{\varepsilon}_2\rvert$

Note: The sign convention for strain and strain increment is positive for compression.

3.3.2 Stress-strain responses

Figure 3-6 presents the stress paths in the s-t space along a variety of imposed strain

paths ranging from extreme dilation $\Re = 0.43$ ($\vartheta = -0.40$) to extreme contraction, $\Re = -1.1$ ($\vartheta = 21$). The initial consolidation pressure was 170 kPa. The critical state line (CSL) and the failure envelope corresponding to the peak state line (PSL) on the stress-strain curves obtained from drained compression tests under the constant confining pressure are also presented in Figure 3-6. The peak and critical state friction angles were determined as $\varphi_p = 23.6°$ and $\varphi_{cv} = 16°$, respectively. A similar critical friction angle was reported by Jiang *et al.* (2006). Such small values of peak and critical friction angle are normal when the particle rolling resistance is ignored according to the Thornton (2000). Moreover, the stress path patterns were similar to the test results obtained by Wan *et al.*(2007). The stress-strain responses in different tests are presented in Figure 3-7.

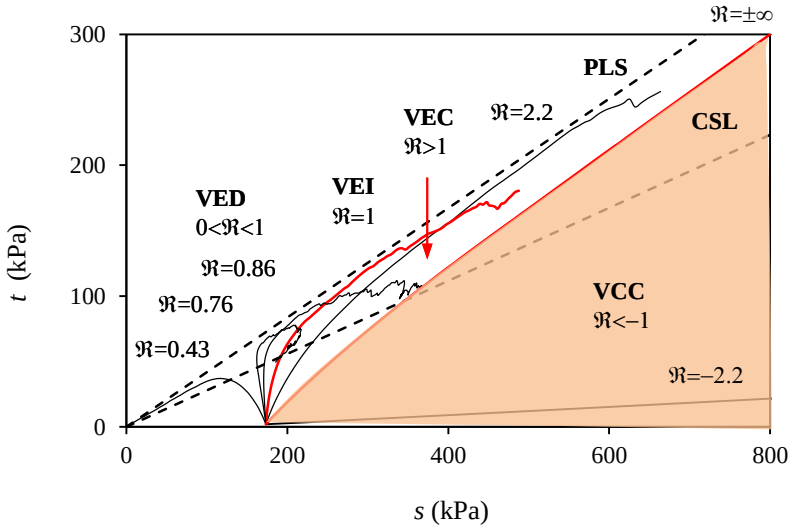

Figure 3-6: Stress path response for tests along proportional strain paths

One immediately observes that the material response was not bounded by the stress paths in the constant lateral confining pressure (akin to a drained test) and the isochoric (akin to an undrained test of a saturated specimen) conditions. As the imposed strain ratio changes, the response of the material changed from a stable

behaviour (hardening) in VEC and VCC tests corresponding to forced contraction ($\vartheta > 0$), to an unstable one (strain softening) in VED tests with $\vartheta < 0$. More specifically, for the highly dilative strain path (i.e., $\Re = 0.43$), shearing induced a continuous decrease in the mean effective stress. The deviator stress first increases and then decreased until "flow" failure occurred, as if the specimen were a saturated loose sand subjected to undrained shearing. For the moderate dilative strain path with $\Re = 0.76$, the mean effective stress first decreased while the deviator stress increases at the beginning of shearing. Then the effective stress path changed direction with all stress components increasing with axial strain, which reflects typical strain hardening. Nevertheless, the effective stress path snaped back shortly after the maximum friction angle $(t/s)_{max}$ ratio was mobilized. The effective stress paths along low dilative strain paths with $\Re = 0.86 \sim 2.2$ had the same feature as a saturated dense sand subjected to undrained shear: the mobilized friction angle (or the t/s ratio) gradually increased to its peak value and then tended to approach the critical state, while the mean effective stress and the deviator stress increased monotonically. For VED tests ($\vartheta < 0$ or $0 < \Re < 1$), the effective stress paths at large shear strain were bounded by the peak state line (PSL) and the critical state line (CSL). These observations are consistent with those of Guo and Su (2007), Wan *et al.*(2007) and Wan and Guo (2004) based on laboratory test results and constitutive simulations. It should be noted that the limiting case with $\vartheta \to \infty$ is isotropic compression. The stress-strain responses along different dilative strain paths are presented in Figure 3-7 (a).

The deformation states corresponding to the two types of contraction strain paths, the VEC tests with $\vartheta > 0$ and $\Re > 1$, and the VCC tests with $\vartheta > 0$ and $\Re < -1$, are illustrated in Figure 3-5. On the s-t plane, the strain paths in the VEC and VCC tests are separated by the stress path of K_0-compression at $\vartheta = 1$ and $\Re \to \pm\infty$, as shown in Figure 3-6. The stress-strain responses, presented in Figure 3-7 (b) and (c)

for VEC and VCC groups, are very distinctive depending on the deformation. For VEC tests with $\vartheta > 0$ and $\Re > 1$, a peak value of t/s is obtained, with ultimate deformation state being different from the critical state. One observes that the value of $\Re$ increased, the lateral strain tended to decrease and gradually approaches the (biaxial) K_0-condition with $\varepsilon_2 = 0$. For strain paths for VCC with $\vartheta > 0$ and $\Re < -1$, the t/s ratio increased monotonically with shear strain, gradually approaching a constant that is smaller than $\sin\varphi_{cv}$ which depended on the strain ratio $\Re$. These observations are generally consistent with the findings of Wan *et al.*(2007).

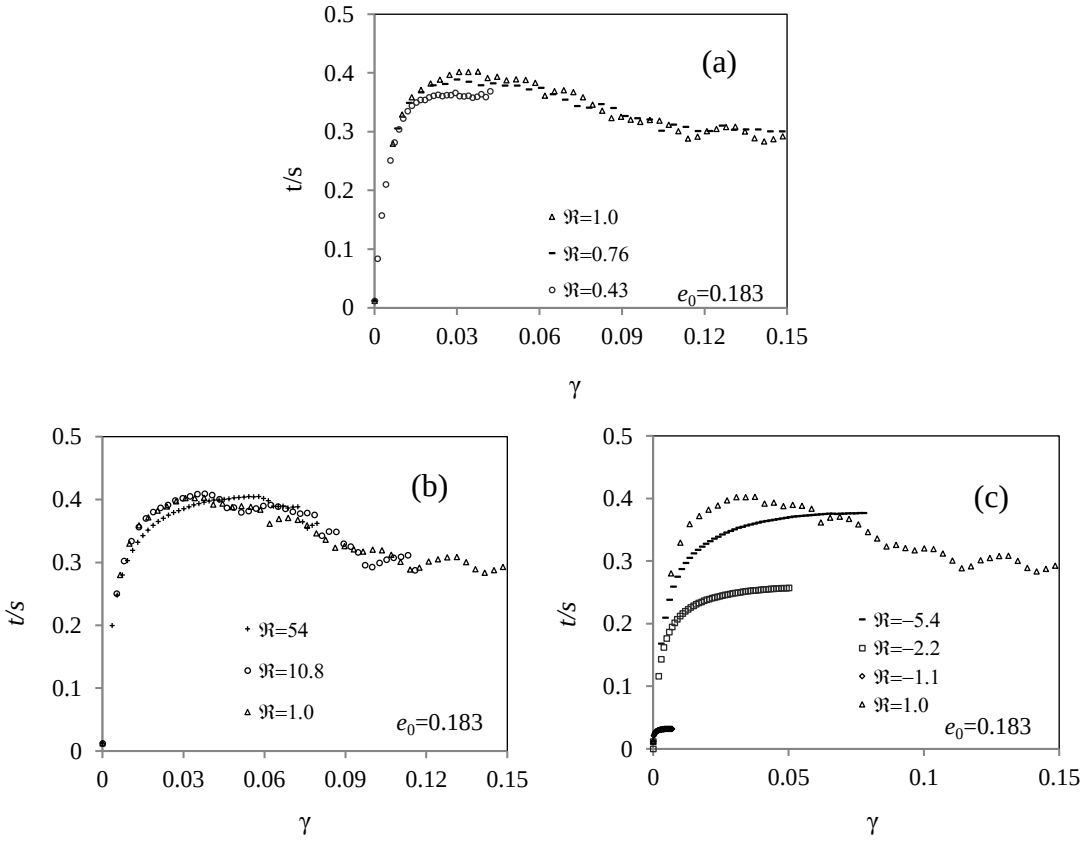

Figure 3-7: Stress strain responses in:(a) VED tests with $0 < \Re < 1$; (b) VEC tests with $\Re > 1$; (c) VCC tests with $\Re < -1$

The stress-strain curves obtained from drained compression tests under the constant confining pressure are presented in Figure 3-8. Here, $\varepsilon_v > 0$ represents volumetric compression. Unique peak shear strength was obtained for tests under different confining pressures. After the peak, the shear strength underwent softening until a constant value was approached that coincided with that of the biaxial tests on a dense sand. An initial contraction was observed for all cases after which the specimen underwent dilation. The specimen with lower confining pressure tended to be less contractive but more dilatant than a specimen with higher confining pressure.

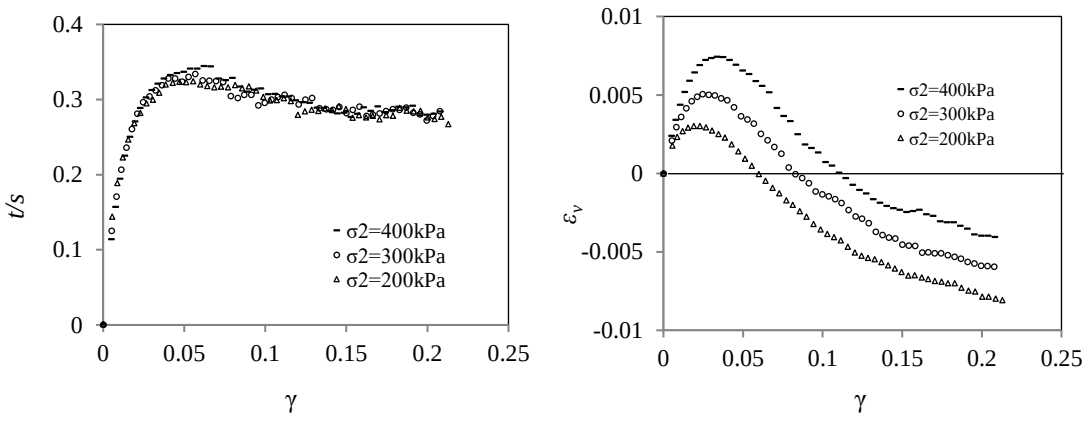

Figure 3-8 Stress strain responses of biaxial compression under different confining stresses: (a) t/s *vs.* shear strain; (b) volumetric strain *vs.* shear strain

3.5 2D simple shear tests

3.5.1 Test setup

A simple shear test can be mimicked by a discrete wall system as shown in Figure 3-9. According to Ai *et al.* (2014), the discrete wall system encloses the granular sample by individual rigid points with the inter-point gaps being much smaller than any particle diameter. The motion of each boundary point is governed by a target strain

rate and its location. In Figure 3-9, two horizontal discrete walls maintain a constant shear strain rate according to $\dot{x}_i = \dot{\varepsilon}_{ij} x_j$ where x_i is the coordinate of point i on the boundary and $\dot{\varepsilon}_{ij}$ is the target strain rate tensor. The vertical solid walls maintain a constant confining pressure via a servo-controlled system.

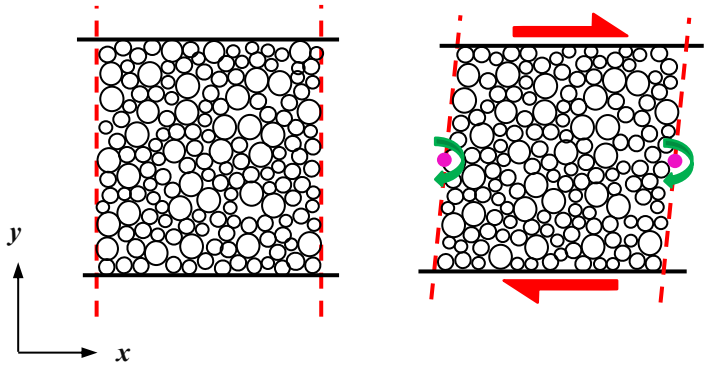

(a) (b)

Figure 3-9: Sketches of simple shear tests using discretized wall system: (a) before shearing and (b) after shearing

DEM simulations were carried out on rectangle specimens consisting of approximately 4700 elastic disks with the radii ranging from 0.75 cm to 2.25 cm. A linear force-displacement contact law was employed where the contact behavior was governed by the normal stiffness k^n, tangential stiffness k^s, and the friction coefficient μ. The normal and tangential contact stiffnesses satisfied $k^n / D = 6.7$ GPa and k^s/k^n=0.5, with D being the mean particle radius. As a comparison, biaxial tests along proportional strain paths were also conducted using the arrangement shown in Figure 3-4. The details of initial assembly are summarized in Table 3-3.

The specimens were generated with an initial porosity 0.175 following the method described in Section 3.4. Once generated, these specimens were subjected to either isotropic consolidation or anisotropic consolidation to selected initial stress states between 300 kPa and 900 kPa. The initial stress ratio δ was defined as

$\delta = (\sigma_x - \sigma_y)/(\sigma_x + \sigma_y)$ to characterize the initial stress states. When $\delta > 0$, the orientation of initial major principal stress is coaxial with the horizontal axis (x+). Then $\delta < 0$ is corresponding to the major principal stress orientation coincides with the vertical axis (y+). Figure 3-10 summarizes the initial stress states prior to simple shear, with the initial mean stress $s_0 = \frac{1}{2}\left(\sigma_{x0} + \sigma_{y0}\right)$ being 300 kPa, 500 kPa, 700 kPa and 900 kPa respectively. The initial stress ratio δ ranged from highly vertical bias of $\delta = -0.3$ to highly horizontal bias of $\delta = 0.3$ for each mean stress level.

Table 3-3: DEM parameters and material properties in 2D tests

Parameter	Value
Number of particles	≈ 4700
Particle density	2550 kg/m^2
Smallest particle diameter D_{min}	1.5cm
Largest particle diameter D_{max}	4.5cm
Average particle diameter D	3 cm
Initial porosity/Void ratio (e_0)	0.17/0.205
Inter-particle friction coefficient μ	0.5
Particle-wall friction coefficient μ	0.0
Height (H), width (W) of sample	H/D=67, W/D=67
Initial axial stress σ_{11}	500 kPa
Initial confining stress σ_{22}	500 kPa
Normal spring stiffness k^n	k^n/D=6.7GPa
Tangential spring stiffness k^s	k^s/D=3.35GPa

When performing the simple shear test simulations, the vertical stress σ_y on the specimen was kept constant and the specimen had zero lateral extension (i.e., $\varepsilon_x = 0$). The accumulated shear strain was calculated by

$$\gamma = 2\sum\nolimits_{\Delta t} (\dot{\varepsilon}_{yx} \Delta t) \tag{3-16}$$

where $\dot{\varepsilon}_{yx}$ is the strain rate with respect to the x-axis, Δt is the size of the time step.

The value of $\dot{\varepsilon}_{yx}$ was low enough ($\dot{\varepsilon}_{yx} < 10^{-4}$) to ensure quasi-static deformation in all simulations. The orientation of principal strain rate relative to the x-axis was calculated by

$$\tan(2\theta_{d\varepsilon}) = \frac{2\dot{\varepsilon}_{yx}}{\dot{\varepsilon}_x - \dot{\varepsilon}_y} = -\frac{2\dot{\varepsilon}_{yx}}{\dot{\varepsilon}_y} \tag{3-17}$$

where $\theta_{d\varepsilon}$ refers to the angle of the principal axis of strain increment relative to the horizontal direction.

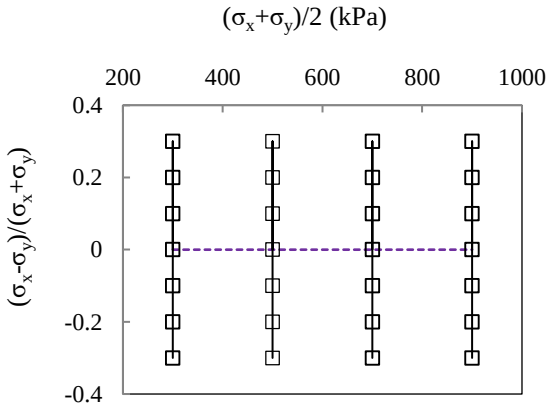

Figure 3-10: Initial stress states in simple shear tests

3.5.2 Stress-strain responses

Simple shear tests

Figure 3-11 presents the normalized stress-strain curves for specimens subjected to different initial isotropic consolidation stresses and the corresponding stress paths are presented in Figure 3-11 (b). A master curve was obtained for all tests under different initial mean stress level in Figure 3-11 (a). Thus, a peak and critical state lines could be represented in the stress space (*t*-*s*) with peak and critical friction angles being 17.5° and 15° as shown in Figure 3-11 (b). All specimens, with different initial mean stress, initially experienced volumetric compression and then dilation upon shearing, as shown in Figure 3-11 (c). The stage of volumetric contraction stage was relatively

short with $\gamma < 5\%$. The volumetric dilation depended on the mean stress level, in which higher initial mean stress levels induced lower volumetric dilation.

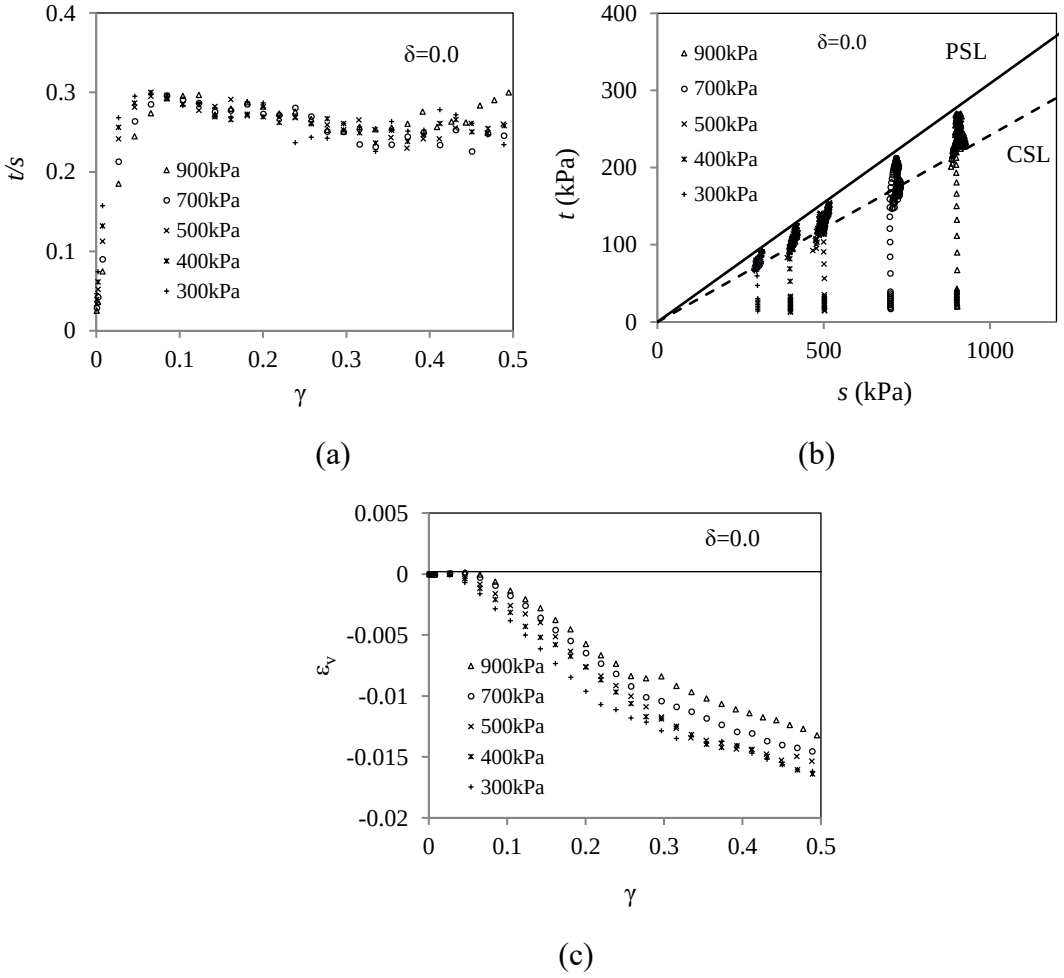

Figure 3-11: Evolution of (a) stress ratio with shear strain, (b) stress paths and (c) the volumetric strain vs shear strain in simple shear tests under different confining pressure with $\delta = 0$

Figure 3-12 (a) show the normalized stress-strain curves for specimens with initial stress state $\delta \neq 0$ at an initial mean stress of $s_0 = (\sigma_x + \sigma_y)/2 = 500kPa$. One observed that the peak and critical stress ratios were approximately the same as those obtained in tests with isotropic initial conditions, as shown in Figure 3-12 (a). In other

words, the peak and the critical friction angles were independent of the initial stress ratio. But the initial consolidation stress rate δ could influence the volumetric strain significantly since the initial mean stress was identical for different δ values. With an increase of δ value, the vertical confining pressure decreased gradually, which in turns induced more dilation, as exhibited in Figure 3-12 (b).

Upon shearing, the horizontal stress decreased for tests with an initial stress ratio $\delta > 0$ due to lower confining stress in the vertical direction. Correspondingly, the horizontal stress increased for tests with an initial stress ratio $\delta < 0$ due to higher confining stress in the vertical direction. As exhibited in Figure 3-13 (a), the horizontal stress increased or decreased monotonically until to an identical ultimate value in which $\sigma_x = \sigma_y$. Meanwhile, the shear stress gradually increased in all tests. The peak and critical values of σ_{xy} / σ_y approximately equaled the peak and critical stress ratios in Figure 3-12 (a).

It is notable that the peak frictional angle corresponded to $\delta = \pm 0.3$ ($\sin^{-1}(0.3) = 17.5°$). Therefore in Figure 3-12 (c), the stress paths for tests with $\delta = \pm 0.3$ originated from the peak state line. Upon shearing, the stress path of the test with $\delta = -0.3$ evolved upward and migrated away from the peak state line until the critical state was reached due to the increase of the horizontal stress and the shear stress. According to Eq. (3-15), the rise of σ_x increased the mean stress level. When $\delta = 0.3$, the horizontal stress decreased upon shear and the mean stress declined. According to Eq. (3-15), both tests with an increase of the horizontal stress with $\delta < 0$ and a decrease of vertical stress with $\delta > 0$ had a negative influence on the deviatoric stress. However, the increase of the shear stress had a positive effect on the deviatoric stress. This is because the shear stresses in tests with $\delta < 0$ were larger

than those with $\delta > 0$ and the positive influence of the shear stress on the deviatoric stress dominated the variation of the deviatoric stress. Therefore, when $\delta = 0.3$, the stress path just followed the peak state line and evolved downward in the (t-s) stress space, in Figure 3-12 (c). On the other hand, the stress path evolved upward and gradually approached the critical state line (*t*-*s*) stress space.

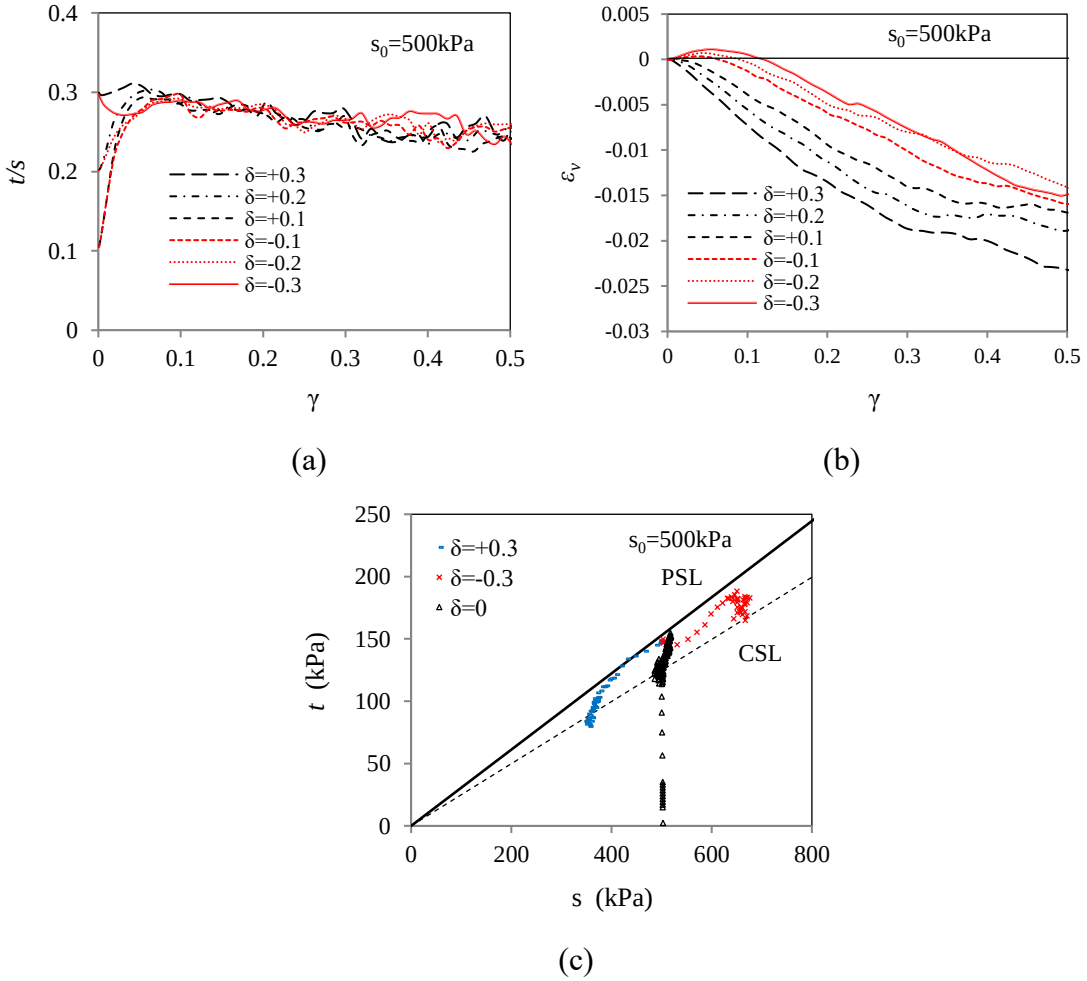

Figure 3-12: (a) Evolution of stress ratio and (b) volumetric strain with shear strain and (c) the stress paths with initial stress $s_0 = (\sigma_x + \sigma_y)/2 = 500kPa$

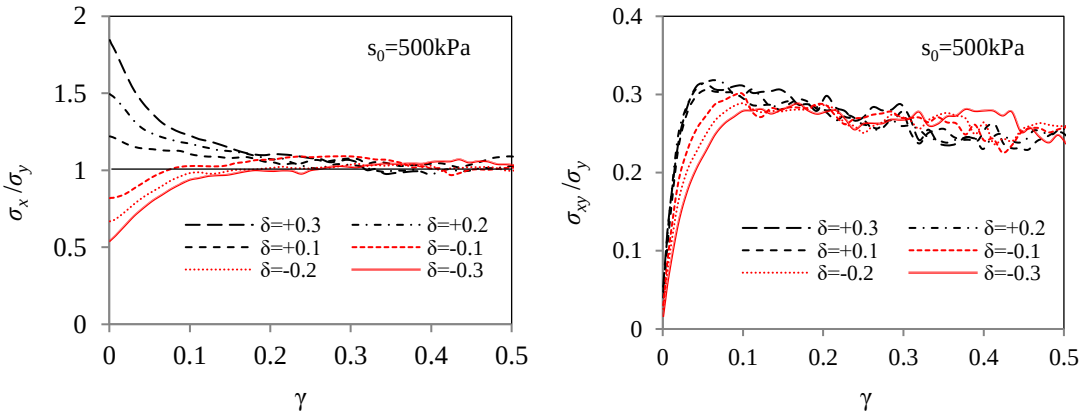

Figure 3-13: Effect of initial stress ratio δ on (a) the evolution of stress ratio σ_x / σ_y and (b) shear stress ratio τ_{xy} / σ_y against shear strain in simple shear tests

Figure 3-14 (a) presents the variation of major principal stress direction with shear strain under different initial stress ratios. As expected, the major principal stress direction rotated during the simple shear tests, from its initial orientation to $45°$. Depending on the initial stress ratio, the initial principal stress direction was either horizontal ($\theta_\sigma = 0°$) for $\delta > 0$ or vertical ($\theta_\sigma = 90°$) for $\delta < 0$. The angle between the directions of the principal stress and the principal strain increment is presented in Figure 3-14 (b) for different initial stress ratios. It should be noted that the principal strain increment always made a $45°$ angle with the horizontal; i.e., $\theta_{d\varepsilon} = 45°$. One observes a period of non-coaxiality (when $\gamma < 10\%$) between the major principal orientation of the stress and that of the strain rate for all cases at the beginning of shearing. When $\gamma < 10\%$, $\theta_\sigma \to \theta_{d\varepsilon} = 45°$. The stress-strain curves for different initial stress ratio followed a master curve after the stress and strain ratio became coaxial.

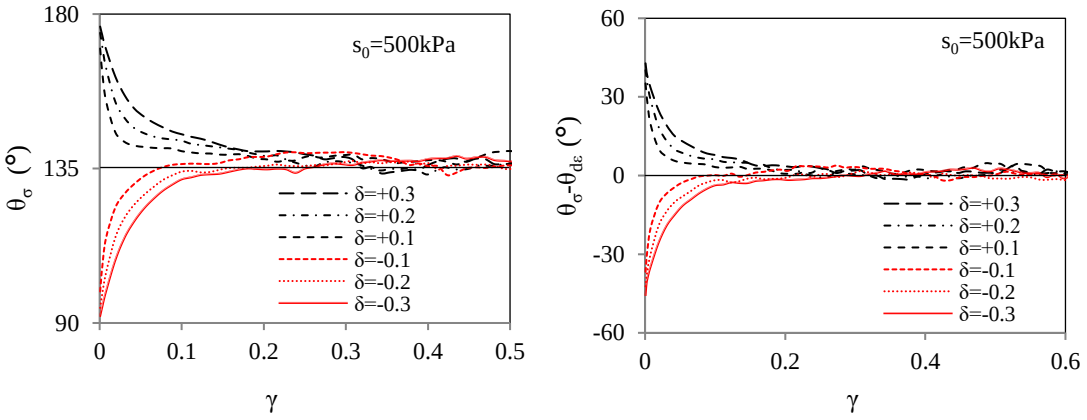

Figure 3-14: Effect of initial stress ratio δ on the evolution of (a) principal stress orientation, (b) non-coaxiality between principal orientations of stress and strain rate

3.6 3D tests along radial stress paths on the π-plane

3.6.1 Test setup

The traditional triaxial compression test in the laboratory is usually conducted on a cylindrical specimen that is compressed axially with the $\sigma_2 = \sigma_3$. This type of test is also known as 'standard triaxial test'. For most geotechnical problems, the second principal stress is not identical with the third principal stress, $\sigma_1 \neq \sigma_2 \neq \sigma_3$. Tests applying three individual principal stress are referred as 'true' triaxial tests. Herein, laboratory tests under true triaxial stress state were simulated using the discrete element method. The 'true' triaxial test was performed on a cubic representative volumetric element enclosed by six frictionless walls. More than 20000 spheres were employed with the radius ranging from 0.1 mm~0.3 mm. A linear force-displacement contact law is employed where the contact behavior was governed by the normal stiffness k^n, tangential stiffness k^s and the frictional coefficient μ. The tangential contact stiffness was assumed to equal to the normal contact stiffness; i.e., k^n=k^s. The basic characteristics of the initial assembly are given in Table 3-4. The ratio of k^n / D

was selected as 10^8 N/m which was large enough to guarantee the rigid particles assumption. Here D denotes the average diameter of the particle.

Table 3-4: DEM parameters and material properties

Parameter	Value
Specimen dimension	20× 20× 20 mm^3
Number of particles	≈ 20000
Particle density	2000kg/m^3
Particle diameter r_{min} ~r_{max}	0.1mm ~0.3mm
Initial porosity	0.40
Inter-particle friction coefficient μ	0.5
Particle-wall friction coefficient μ	0.0
Initial confining pressure	300~900 kPa
Normal spring stiffness k^n	$k^n / D = 10^8 Pa$
Tangential spring stiffness k^s	$k^s / D = 10^8 Pa$

The initial packing specimen was generated by filling the cubic cell with randomly generated spheres according to the initial porosity. Once the specimen was generated, the system was subjected to an isotropic consolidation to the initial stress state with the mean stress ranging from 300 kPa to 900 kPa. The inter-particle frictional coefficient was 0.5. After consolidation, the specimen was subjected to loading along select stress paths during which the Lode angle and the mean stress were constant. This corresponded to a straight line on the π-plane. As shown in Figure 3-15, a stress state can be expressed in the Lode coordinate system using radial coordinate r and Lode angle $\bar{\theta}$, as

$$r = \sqrt{2J_2} = \frac{\sqrt{6}}{3} q, \quad \bar{\theta} = -\frac{1}{3}\sin^{-1}\left(\frac{3\sqrt{3}J_3}{2J_2^{3/2}}\right) \tag{3-18}$$

in which J_2 and J_3 are the second and the third invariants of the deviatoric stress tensor $s_{ij} = \sigma_{ij} - \sigma_m \delta_{ij}$ with $\sigma_m = \sigma_{ii}/3$. The deviatoric stress is defined as $q = \sqrt{\frac{3}{2} s_{ij} s_{ij}}$.

According to this definition, the Lode angle takes value in the range of $-\pi/6 \le \bar{\theta} \le \pi/6$ and the point with $\bar{\theta} = -\pi/6$ representing an axisymmetric compression stress state (i.e. a conventional triaxial compression stress state). Introducing the intermediate stress ratio $b = (\sigma_2 - \sigma_3)/(\sigma_1 - \sigma_3)$, the relation between the Lode angle and the intermediate stress ratio is provided in Table 3-5 where b ranges from 0.0 to 1.0.

Table 3-5: Conversion between the stress ratio and the Lode angle

	From compression to dilation				
b	0.000	0.280	0.500	0.732	1.000
$\bar{\theta}$	-π/6 (comp)	-π/12	0.0	π/12	π/6 (ext)

A simulation was conducted by applying a constant strain rate ($\dot{\varepsilon}_1 < 10^{-5}$/s) in the major principal direction (σ_1). Meanwhile, the other two principal stresses (σ_2, σ_3) were adjusted using the servo-controlled systems to maintain the constant mean stress and stress path. It is easy to obtain the expression of the principal stress, where both the mean stress and the Lode angle are constants:

$$\sigma_2 = \frac{(1-b)3p + (2b-1)\sigma_1}{2-b}, \quad \sigma_3 = \frac{3p - (b+1)\sigma_1}{2-b} \tag{3-19}$$

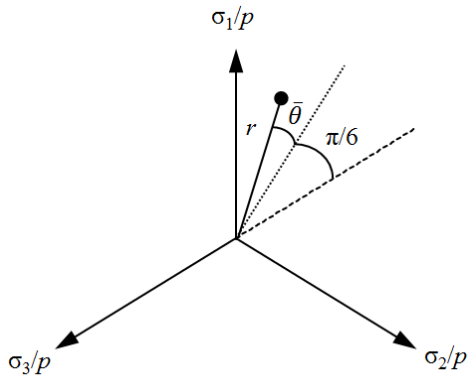

Figure 3-15: Loading paths in the Lode coordinate system

3.6.2 Stress-strain responses

Figure 3-16 presents the variation of deviator stress ratio q/p and volumetric strain ε_v with respect to the deviatoric strain ε_q along different stress paths for an initial consolidation pressure of 300 kPa when $k^n = k^s = 4\times10^4$ N/m. Herein the volume strain and deviatoric strain are defined as $\varepsilon_v = \varepsilon_{ii}$ and $\varepsilon_q = \sqrt{\frac{2}{3}e_{ij}^{'}e_{ij}^{'}}$ with $e_{ij}^{'} = \varepsilon_{ij} - \frac{\varepsilon_v}{3}\delta_{ij}$. Referring to Figure 3-16 (a), all specimens initially experienced compression and then dilation upon shearing. The $\varepsilon_v \sim \varepsilon_q$ curves were not sensitive to the stress paths, particularly at small shear strains. However, the stress-strain responses and the maximum deviatoric stress ratios are stress path dependent, as shown in Figure 3-16 (b). In general, the peak shear resistance in axisymmetric extension when $\bar{\theta} = \pi/6$ (or b=1) is the smallest and in axisymmetric compression test at $\bar{\theta} = -\pi/6$ (or b=0), it is the largest for all stress paths examined.

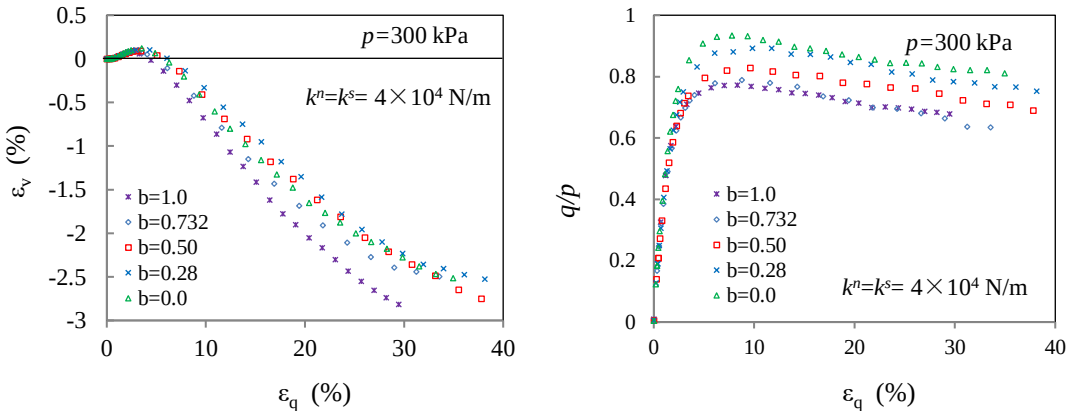

Figure 3-16: Stress-strain responses (a) volumetric strain *vs.* shear strain and (b) stress ratio *vs.* shear strain with $k^n = k^s = 4\times10^4$ N/m, p=300 kPa

In comparison, Figure 3-17 provides stress-strain responses along different stress paths at an initial consolidation pressure of 500kPa. The normal and tangential contact stiffnesses were $k^n = k^s = 10^6$ N/m. The volumetric contraction stage was very short and then all samples dilated upon shearing along different stress paths, as shown in Figure 3-17 (a).

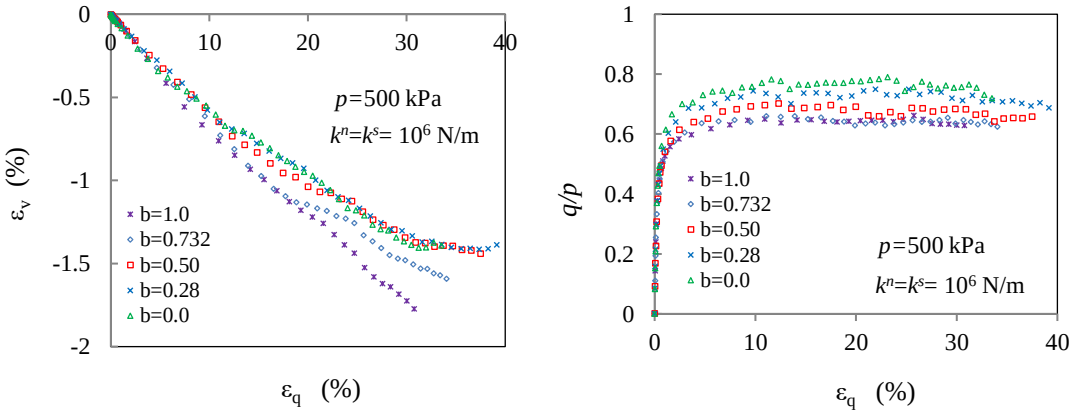

(a) (b)

Figure 3-17: Stress-strain responses (a) volumetric strain *vs.* shear strain and (b) stress ratio *vs.* shear strain with k^n=k^s= 10^6 N/m, p=500 kPa

3.7 Summary

This chapter briefly introduced numerically simulated tests including biaxial compression tests, two-dimensional tests along proportional strain paths, two-dimensional simple shear tests, and three-dimensional tests using discrete element method. To begin with, a brief introduction of the discrete element approach and the selection of material properties.

For two-dimensional conditions, a series of biaxial tests were conducted along proportional strain paths. The results of biaxial tests qualitatively coincided with the results from laboratory experiments, for example, identical critical stress state for the

dense and loose sample, strain softening and shear-induced dilation for dense sand. Meanwhile, simple shear tests were simulated for both isotropic and anisotropic consolidated specimens using point wall system. The orientation of the major principal stress rotated with the orientation of the major strain rate being constant during the shearing. The numerically simulated simple shear tests generally reproduced the stress-strain responses of the simple shear tests in laboratory tests. For the three-dimensional conditions, 'true' triaxial tests were performed along certain stress paths that were in straight lines in the Lode coordinate system. The stress and strain responses of tests along different stress paths were found to be reasonable when compare these results with those from real tests, e.g., the significance of the intermediate principal stress.

Generally, the DEM simulated experimental tests qualitatively reproduced the macro response of the granular matter in both 2D and 3D cases. Moreover, the configuration of the microstructure became visible when using the discrete element method. Correspondingly the evolution of the microstructure could be monitored and might be related with the macro-mechanical behaviour of granular materials.

Chapter 4 Evolution of Induced Anisotropy of Granular Materials

4.1 Introduction

The mechanical behavior of a natural granular material can be inherently anisotropic as a consequence of the deposition process and the following stress history. Such anisotropy is easily altered when the granular material is subjected to shear distortion, because of the rearrangement of particles via relative particle movements, including rolling and sliding at particle contacts. The spatial arrangement or inter-connectivity of discrete particles subjected to stress change is known as the stress-induced anisotropy (Oda, 1993). Both experimental and theoretical studies suggest that the induced anisotropy and its evolution contribute to key aspects of granular soil behaviours, including dilation (i.e. shear-induced volume change), failure and instability during deformation (Collins and Muhunthan, 2003; Fu and Dafalias, 2011; Oda 1993; Radjaï *et al.*, 2012; Wan *et al.*, 2007; Wan and Guo, 2004; Richard Wan and Pouragha, 2015). Research incorporating anisotropy into the constitutive model has been conducted by Gao *et al.* (2014), Lade (2008), Li and Dafalias (2011). Yet, one challenge of micromechanically formulated constitutive laws lies in how to mathematically describe the anisotropy and its evolution with the deformation history.

This chapter explores the evolution of fabric and its correlation with stress states of granular materials sheared along proportional strain and different stress paths using DEM. The evolution of fabric for different contact networks (i.e., the overall contact network, the strong and weak sub-networks) is traced in all simulations. The results reveal that the deviator of fabric tensor based on the strong sub-network shows a unique relation with the deviatoric stress ratio, particularly for specimens along proportional strain paths corresponding to forced dilation. The maximum value of the

deviator of fabric tensor varies with the applied strain ratio or the maximum dilatancy rate in stress-controlled tests. The strong sub-network plays the primary role in shear resistance, while the weak sub-network and its evolution are significantly affected by the imposed dilatancy rate.

4.2 Macroscopic stress and fabric tensor of granular materials

4.2.1 Quantification of micromechanics

A number of measures for fabric anisotropy have been developed, which can be classified in four categories as preferred orientations of the particle body, the particle surface, the contact normal and the void space (Kuhn *et al.*, 2015). Among these measures, the most apparent and efficient measure associated with the mechanical response of granular materials is based on the orientation of contact normal. The fabric tensor quantifying the contact normal orientation of the overall contact network is defined as (Satake, 1978):

$$\phi_{ij} = \frac{1}{N_c}\sum_{k=1}^{N_c} n_i^k n_j^k \,, \quad \phi_{ii} = 1 \tag{4-1}$$

where n_i^k is the *i*-th component of the unit vector representing the contact normal at the *k*-th contact. When using polar coordinate systems as shown in Figure 4-1, $\boldsymbol{n} = (\cos\theta, \sin\theta)^T$ for 2D and $\boldsymbol{n} = (\cos\theta, \sin\theta\cos\varphi, \sin\theta\sin\varphi)^T$ with $\theta \subset [0, \pi]$, $\varphi \subset [0, 2\pi]$ for 3D cases, respectively.

Let V be the volume of a representative element, which has N_p particles and N_c contacts. By introducing the probability density function (PDF) of the contact orientation $E(\boldsymbol{n})$, the number of contact vectors within the range of solid angle $[\Theta - d\Theta/2, \Theta + d\Theta/2]$ is $N_c E(\boldsymbol{n}) d\Theta$. The fabric tensor in Eq.(4-1) can be rewritten as

$$\phi_{ij} = \frac{1}{N_c}\sum_{k=1}^{N_c} n_i^k n_j^k = \int_\Theta E(\boldsymbol{n}) n_i n_j d\Theta \tag{4-2}$$

It should be noted that the probability density function $E(\boldsymbol{n})$ satisfies $\int_\Theta E(n)d\Theta = 1.0$ and $E(\boldsymbol{n}) = E(-\boldsymbol{n})$.

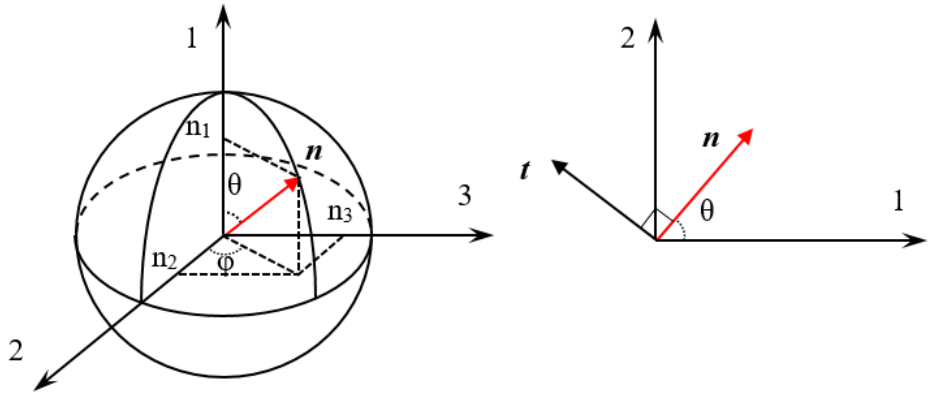

(a) (b)

Figure 4-1: Contact normal in (a) 3D and (b) 2D spaces

For 2D cases, the unit vector of contact normal $\boldsymbol{n}$ can be expressed as $(n_1, n_2) = (\cos\theta, \sin\theta)$ with θ being the inclination of the angle of $\boldsymbol{n}$ with respect to the reference axis 1. Since $E(\theta)$ is a periodic function of 2π, it can be expanded with the Fourier function as

$$E(\theta) = \frac{1}{2\pi}\{a_0 + \sum_{n=1}^{\infty}(a_k \cos k\theta + b_k \sin k\theta)\} \tag{4-3}$$

where a_k and b_k are both zeroes if k is an odd number (Oda,1999).

$$a_k = 2\int_0^{2\pi} E(x)\cos(kx)dx \qquad b_k = 2\int_0^{2\pi} E(x)\sin(kx)dx \tag{4-4}$$

By considering $E(\boldsymbol{n}) = E(-\boldsymbol{n})$, when taking k=2, the Flourier expansion of $E(\theta)$ is simplified as

$$E(\theta) = \frac{1}{2\pi}\left[1 + a_c \cos 2(\theta - \theta_c)\right] \tag{4-5}$$

The second-order fabric tensor in Eq. (4-2) becomes

$$\phi_{ij} = \int_{\Theta} E(\boldsymbol{n}) n_i n_j d\Theta = \frac{1}{4}\begin{pmatrix} a_2 + 2 & b_2 \\ b_2 & -a_2 + 2 \end{pmatrix} \tag{4-6}$$

It can be shown that θ_c defines the major principal direction of the fabric tensor and a_c is a measure of the degree of fabric anisotropy $\tan 2\theta_c = b_2 / a_2$ and $a_c = \sqrt{(a_2)^2 + (b_2)^2}$.

In 3D cases, the probability density function $E(\boldsymbol{n}) = E(\theta, \beta)$ that satisfies $\iint E(\theta, \beta) \sin\theta d\theta d\beta = 1.0$. According to Chang *et al.* (2011), when applying the Flourier expansion of the $E(\theta, \beta)$ and taking the second-order term only, the contract orientation distribution can be expressed as:

$$E(\theta, \beta) = \frac{1}{4\pi}\left[1 + \frac{a_0}{4}(2\cos 2\theta + 1) + 3\sin^2\theta(a_{22}\cos 2\beta + b_{22}\sin 2\beta)\right] \tag{4-7}$$

The probability density function of contact normal can also be written in a combination of an isotropic part and a deviatoric part in both 2D and 3D cases.

$$E(\boldsymbol{n}) = \frac{1}{2\pi}(\delta_{ij} + \Gamma_{ij}) n_i n_j \quad \text{(2D)} \qquad E(\boldsymbol{n}) = \frac{1}{4\pi}(\delta_{ij} + \Gamma_{ij}) n_i n_j \quad \text{(3D)} \tag{4-8}$$

where δ_{ij} is the Kronecker delta and Γ_{ij} is a traceless symmetric second-rank tensor. Then the fabric tensor can be decomposed into an isotropic part and a deviatoric part as

$$\phi_{ij} = \frac{1}{2}\delta_{ij} + \frac{1}{4}\Gamma_{ij} \quad \text{(2D)} \quad \phi_{ij} = \frac{1}{3}\delta_{ij} + \frac{2}{15}\Gamma_{ij} \quad \text{(3D)} \tag{4-9}$$

Following Radjaï *et al.* (1996), we evaluate the geometrical anisotropy of granular assemblies by determining the fabric tensor for both the network of all contacts and subsets of contacts that carry forces lower or higher than a given cutoff ξ that may vary from 0 to the maximum contact force in the system. The subset that carries forces lower than ξ is referred to as the "ξ-network", which is the same as

the overall contact network when $\xi = F_{\max}$. The contacts in the network supplementary to the "ξ -network" carry normal contact forces higher than ξ . For simplicity, the ξ -network and its supplementary sub-network corresponding to $\xi = \langle f^n \rangle$ with $\langle f^n \rangle$ being the average contact force in the system are referred to as the weak sub-network and strong sub-network, respectively. The fabric tensors associated with the strong and weak networks are expressed as

$$\phi_{ij}^w = \frac{1}{N_c^w} \sum_{k=1}^{N_c^w} n_i^k n_j^k , \quad \phi_{ij}^s = \frac{1}{N_c^s} \sum_{k=1}^{N_c^s} n_i^k n_j^k \tag{4-10}$$

where N_c^s and N_c^w are the number of contacts in the strong and weak contact networks, respectively. The total number of contacts N_c in the granular assembly is $N_c = N_c^s + N_c^w$. By introducing the relative proportion of the strong contacts in the system $\alpha = N_c^s / N_c$, the relation between the fabric tensor ϕ_{ij} of the overall contact network and those of the sub-networks can be expressed as

$$\phi_{ij} = (1-\alpha)\phi_{ij}^w + \alpha\phi_{ij}^s \tag{4-11}$$

For a two-dimensional case, similar to Eq. (4-6), the fabric tensors in different sub-networks can be expressed as

$$\phi_{ij}^s = \frac{1}{4}\begin{pmatrix} a_2^s + 2 & b_2^s \\ b_2^s & -a_2^s + 2 \end{pmatrix} \quad \phi_{ij}^w = \frac{1}{4}\begin{pmatrix} a_2^w + 2 & b_2^w \\ b_2^w & -a_2^w + 2 \end{pmatrix} \tag{4-12}$$

where (a_2^s, b_2^s) and (a_2^w, b_2^w) are the coefficients of the second-order components in Flourier functions of $E^s(\theta)$ and $E^w(\theta)$, which are the PDFs of the strong and weak sub-network, respectively. Accordingly, the magnitude and the direction of anisotropy in strong sub-network are $a_c^s = \sqrt{(a_2^s)^2 + (b_2^s)^2}$ and $b_2^s / a_2^s = \tan 2\theta_c^s$. In weak sub-network, they are $a_c^w = \sqrt{(a_2^w)^2 + (b_2^w)^2}$ and $b_2^w / a_2^w = \tan 2\theta_c^w$ correspondingly.

By employing $\alpha = N_c^s / N_c$, the fabric anisotropy within the overall contact network can be expressed with that in the sub-networks as

$$a_c \cos 2\theta_c = (1-\alpha) a_c^w \cos 2\theta_c^w + \alpha a_c^s \cos 2\theta_c^s \tag{4-13}$$

For 2D analysis, the degree of anisotropy of different contact networks can be characterized by the corresponding fabric deviator as

$$q_\phi^* = \phi_1^* - \phi_2^* = 2\sqrt{\left(\frac{\phi_{xx}^* - \phi_{yy}^*}{2}\right)^2 + \phi_{xy}^{*\,2}} \tag{4-14}$$

where * represents the overall contact network, strong sub-network and weak sub-network with ϕ_1^*, ϕ_2^* being the major and minor principal fabric components of different contact networks, with $\phi_{1,2}^* = \frac{\phi_{xx}^* + \phi_{yy}^*}{2} \pm \sqrt{(\frac{\phi_{xx}^* - \phi_{yy}^*}{2})^2 + (\phi_{xy}^*)^2}$. The mean value of fabric tensor is $p_\phi^* = (\phi_1^* + \phi_2^*)/2 = 1/2$ for all contact networks. q_ϕ^* can be related to the degree of fabric anisotropy a_c^* via $q_\phi^* = \frac{1}{2} a_c^*$.

Under 3D stress conditions, the fabric deviator of different contact networks is expressed as

$$q_\phi^* = \sqrt{\frac{3}{2} \phi_{ij}'^* \phi_{ij}'^*} \tag{4-15}$$

where * represents the overall contact network, strong sub-network and weak sub-network and $\phi_{ij}'^* = \phi_{ij}^* - \frac{1}{3}\delta_{ij}$. Similarly, $p_\phi^* = \phi_{ii}^*/3 = 1/3$ holds true for all contact networks.

4.2.2 Macroscopic stresses and strains

(1) Macroscopic strains

In the DEM simulations carried out in this study, the strain of a specimen was obtained from the boundary displacement in both two-dimensional and

three-dimensional cases. The average macroscopic strain was determined according to the displacement gradient, e.g., $\varepsilon_{ij} = \frac{1}{2}\left(\partial u_i/\partial x_j + \partial u_j/\partial x_i\right)$. Referring to Suiker and Chang (2004) and Christoffersen *et al.* (1981), the uniform strain field ε_{ij} in a granular assembly is the best fit for describing the actual contact displacements. Under biaxial conditions, the following quantities with i, j =1 and 2 were used: $\varepsilon_v = \varepsilon_{ii}$, $\gamma = \varepsilon_1 - \varepsilon_2$, $\sin\phi_m = t/s$, $\sin\psi_m = -\dot{\varepsilon}_v^p / \dot{\gamma}^p$. Here $\dot{\varepsilon}_v^p$ and $\dot{\gamma}^p$ are the volumetric and shear plastic strain increments. The angles φ_m and ψ_m are the mobilized friction angle and the mobilized dilation angle, respectively. $\varepsilon_1, \varepsilon_2$ are the principal components of ε_{ij}. In biaxial tests along proportional strain paths, for example, the macroscopic strain rates in the assembly were related to the relative velocities of the boundary walls as $v_{1-1}^t = -v_{1-2}^t = \frac{1}{2}\dot{\varepsilon}_{11} \cdot H^t$ and $v_{2-1}^t = -v_{2-2}^t = \frac{1}{2}\dot{\varepsilon}_{22} \cdot W^t$ with H^t and W^t being the height and width of the specimen at time t, as shown in Figure 3-4 (a). Similar methods can be found in Thornton (2000) as well as Suiker and Chang (2004).

In 3D tests along radial stress paths on the π-plane, three principal strain components were calculated from the average displacement gradient. The volumetric strain and the deviatoric strain ε_q were

$$\varepsilon_v = \varepsilon_1 + \varepsilon_2 + \varepsilon_3, \quad \varepsilon_q = \sqrt{\frac{1}{2}\left[\left(\varepsilon_1 - \varepsilon_2\right)^2 + \left(\varepsilon_1 - \varepsilon_3\right)^2 + \left(\varepsilon_2 - \varepsilon_3\right)^2\right]} \tag{4-16}$$

(2) Macroscopic stresses

The micromechanical description of the stress tensor within a representative elementary volume (REV) with volume V can be related to the contact forces and branch vectors according to Eq. (2-1). For a two-dimensional assembly composed of circular disks, the contact force $\boldsymbol{f}^k$ and the branch vector $\boldsymbol{l}^k$ at the k^{th} contact can be

expressed as

$$\boldsymbol{f}^k = f^{nk}\boldsymbol{n}^k + f^{tk}\boldsymbol{t}^k, \quad \boldsymbol{l}^k = l^k\boldsymbol{m}^k \tag{4-17}$$

in which $\boldsymbol{n}^k$=(cosθ^k, sinθ^k) and $\boldsymbol{t}^k$=(-sinθ^k, cosθ^k) are the normal and tangential direction of the contact plane, with θ^k representing the orientation of the branch vector. l^k is the length of the branch vector at the k^{th} contact, f^{nk} and f^{tk} are the normal and tangential components of the contact force, respectively; as shown in Figure 4-2. Therefore, the stress tensor can be expressed as

$$\sigma_{ij} = \frac{1}{V}\sum_{k=1}^{N_c} f^{nk} l^k n_i^k n_j^k + \frac{1}{V}\sum_{k=1}^{N_c} f^{tk} l^k t_i^k n_j^k \tag{4-18}$$

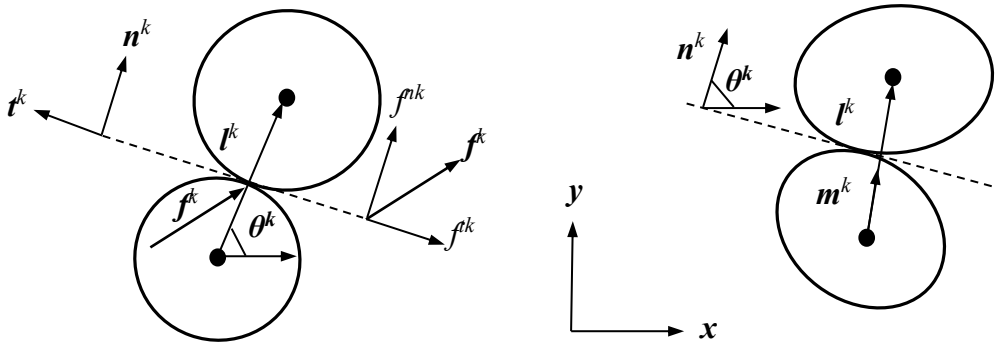

(a) (b)

Figure 4-2: Sketches of a contact between two (a) circular particles and (b) elongated particles

Branch vector

The branch vector $\boldsymbol{l}$ is defined as a vector connecting the centroids of two particles in contact. A probability density function $S(\boldsymbol{l})$ can be used to describe the distribution of the length and orientation of the branch vectors. Therefore $S(\boldsymbol{l})d\boldsymbol{l}$

gives the proportion of the branch vector ranging from $\boldsymbol{l}$ to $\boldsymbol{l}+d\boldsymbol{l}$. It is noted that $S(\boldsymbol{l})$ is a joint distribution of the length and orientation, as $S(\boldsymbol{l})=S(l,\boldsymbol{m})$. Rothenburg and Bathurst (1989) assumed that the length of a branch vector is independent of its orientation $\boldsymbol{m}$. Therefore, $S(\boldsymbol{l})$ can be decomposed into a conditional length distribution $P(l|\boldsymbol{m})$ and an orientation distribution $E(\boldsymbol{m})$ as $S(\boldsymbol{l})=P(l|\boldsymbol{m})E(\boldsymbol{m})$. It should be noted that the orientation of a branch vector $\boldsymbol{m}$ is the same as the associated contact normal $\boldsymbol{n}$ only for circular disks or spherical particles.

Without loss of generality, one may assume that the distribution of particle radius r follows a normal distribution within the ranges of [$r_{\min}$, $r_{\max}$] with the mean value being $\bar{r}=(r_{\min}+r_{\max})/2$. We further make the following assumptions:

- all particles are randomly arranged, the length of branch vector $l=r_1+r_2$ of two particles in contact follows a normal distribution with the expected mean value being $\hat{l}_0=2\bar{r}$.
- within the range $[\theta-\Delta\theta/2,\theta+\Delta\theta/2]$, the length of l exhibits a self-similarity with that in the whole domain and $P(l|\boldsymbol{m})=P(l)$

The average length of branch vectors in a given direction is

$$l(\theta)=\int_{l_{\min}}^{l_{\max}} lP(l|\boldsymbol{m})dl=\int_{l_{\min}}^{l_{\max}} lP(l)dl=\frac{\sum_{k\in N(\theta)} l^k}{N(\theta)}=\hat{l}_0 \tag{4-19}$$

in which $N(\theta)$ is the number of contacts within the range $[\theta-\Delta\theta/2,\theta+\Delta\theta/2]$. $l_{\min}=2r_{\min}$ and $l_{\max}=2r_{\max}$ are the maximum and minimum length of the branch vectors.

Contact forces

Referring to Figure 4-2, the contact force $\boldsymbol{f}^c$ can be decomposed into a normal and a

tangential component as $\boldsymbol{f}^c = f^{nc}\boldsymbol{n} + f^{nc}\boldsymbol{t}$ in 2D problems. The directional distributions of the normal and tangential contact forces can be described as (Rothenburg and Bathurst, 1989)

$$f^n(\theta) = f_0^n\ 1 + a_n \cos 2(\theta - \theta_n)\ ,\quad f^t(\theta) = -f_0^n a_t \sin 2(\theta - \theta_t) \tag{4-20}$$

where $f_0^n = \frac{1}{2\pi}\oint f^n(\theta)d\theta$ is the directional average normal contact force, a_n and a_t describe the degree of anisotropies for the distributions of f^n and f^t, θ_n and θ_t define the directions of the anisotropy for the distributions of f^n and f^t.

By substituting Eqs. (4-20) and (4-19) into the Eq. (4-18), the stress tensor becomes

$$\sigma_{ij} = \frac{N_c \hat{l}_0}{V}\int_\Theta E(\theta) f^n(\theta) n_i n_j d\theta + \frac{N_c \hat{l}_0}{V}\int_\Theta E(\theta) f^t(\theta) t_i n_j d\theta \tag{4-21}$$

For 2D cases, the stress components are explicitly expressed as

$$\sigma_{11} = m_v^0\ 2 + a_c \cos 2\theta_c + a_n \cos 2\theta_n + a_n a_c \cos 2(\theta_n - \theta_c) + a_t \cos 2\theta_t \tag{4-22a}$$

$$\sigma_{22} = m_v^0\ 2 - a_c \cos 2\theta_c - a_n \cos 2\theta_n + a_n a_c \cos 2(\theta_n - \theta_c) - a_t \cos 2\theta_t \tag{4-22b}$$

$$\sigma_{12} = \sigma_{21} = m_v^0\ a_c \sin 2\theta_c + a_n \sin 2\theta_n + a_n a_t (\sin 2\theta_t - \cos 2\theta_t) + a_t \sin 2\theta_t \tag{4-22c}$$

where $m_v^0 = \frac{N_c \hat{l}_0 f_0^n}{4V}$.

When the macroscopic variables can be obtained from the microscopic variables via averaging operations, the local contact forces and relative particle displacements can be obtained from corresponding macroscopic variables through localization or projections (Chang and Gao, 1996; Emeriault and Cambou, 1996). More specifically, the projection rule is derived from the mean field value (MFV) theorem (Jenkins and Strack, 1993), which gives the local microscopic variable attached to a pair of particles as the projection of the macroscopic variable gradient along the branch

vector characterizing the connectivity of particles. The contact force can be related to the Cauchy stress tensor and the fabric tensor ϕ_{ij} via

$$f_i^c = \sigma_{ij}^* l_j^c \tag{4-23}$$

in which $\sigma_{ij}^* = \frac{1}{3}\phi_{ik}^{-1}\sigma_{kj}$ is defined as the true stress tensor (Oda, 1993). Here we use the definition that $\sigma_{ij}^* = \phi_{ik}^{-1}\sigma_{kj}$. When ϕ_{ij} and σ_{ij} are coaxial, the principal components of σ_{ij}^*, σ_{ij} and ϕ_{ij} can be related by

$$\sigma_i^* = \sigma_i / (\phi_i) \qquad \text{(i is not in summation here)} \tag{4-24}$$

Similarly, one may define the true stress tensor or fictitious stress tensor based on the fabric tensor for the strong sub-network as $\sigma_{ij}^{s*} = (\phi_{ik}^s)^{-1}\sigma_{kj}$. When ϕ_{ij}^s and σ_{ij} are coaxial, the principal components of σ_{ij}^{s*}, σ_{ij} and ϕ_{ij}^s can be related by $\sigma_i^{s*} = \sigma_i / (\phi_i^s)$ and *i* is not in summation here.

The other fictitious stress that is employed in this research is the fabric stress, which the is defined by the principal components of the stress tensor and fabric tensor as $\sigma_{ij}^f = \phi_{ik}\sigma_{kj}$. It is noted that *i* is not in summation here.

It is convenient to introduce the true stress invariants $\{p^*, q^*\}$ defined as $q^* = \sqrt{\frac{3}{2}s_{ij}^* s_{ij}^*}$ and $p^* = \sigma_{ii}^*/3$ with $s_{ij}^* = \sigma_{ij}^* - p^*\delta_{ij}$ in 3D cases. Similarly, for the true stress defined using the fabric tensor for the strong sub-network, the stress invariants are $q^{s*} = \sqrt{\frac{3}{2}s_{ij}^{s*} s_{ij}^{s*}}$ and $p^{s*} = \sigma_{ii}^{s*}/3$ with $s_{ij}^{s*} = \sigma_{ij}^{s*} - p^{s*}\delta_{ij}$.

4.3 Fabric evolution in 2D tests along proportional strain paths

As discussed before, the macroscopic variables of a granular material during

deformation can be obtained from microscopic variables via proper averaging method. This section examines the evolution of fabric tensors in different contact networks when a granular assembly is sheared along proportional strain paths using the results of DEM simulations presented in Chapter 3.

4.3.1 Fabric evolution in overall contact network

Fabric evolution in VED and VEI tests

According to Table 3-2, the VED and VEI tests correspond to volumetric dilation and isometric compression. Figure 4-3 presents the evolution of the fabric deviator $q_\phi = \phi_1 - \phi_2$ of the overall contact network in different tests. As shown in Figure 4-3 (a), the value of q_ϕ increased with the shear strain initially until it approached the peak value. Thereafter, q_ϕ decreased as shearing continuing and approaches a constant at large strain. This trend is similar to the evolution of the deviatoric stress as shown in Figure 3-7 (a). However, both the peak value and the ultimate value of q_ϕ at large shear strain depend on the imposed strain ratio $\mathfrak{R}$. In particular, the peak and ultimate values of q_ϕ increased as $\mathfrak{R}$ was decreased, implying that the contact orientations showed most strong directional preference to resist deformation in the VED tests ($0 < \mathfrak{R} < 1$ or $\vartheta < 0$), in which the specimen collapsed much easier than in other cases. The evolution of q_ϕ with the stress ratio (t/s) is plotted in Figure 4-3 (b), in which the deformation started from an initially isotropic stress state. Prior to the peak stress ratio, q_ϕ increased with the increase of t/s and the overall contact network resisted deformation by rearranging contact orientation with more contacts in the vertical direction. At the peak stress rate, the overall contact network reached its maximum bearing capacity and buckled. After the peak, a decrease of q_ϕ was

observed as t/s decreased and gradually approached the critical state. Before the peak stress ratio, the relation between q_ϕ and t/s was nonlinear, which is consistent with the conclusion of Mehrabadi and Nemat-Nasser (1983). Nevertheless, after the peak stress ratio, the variation of q_ϕ with t/s ratio can be described as a linear expression approximately, as shown in Figure 4-3.

In the VEI test $\Re = 1$, the volume of specimen was a constant during deformation since $\dot{\varepsilon}_1 = -\dot{\varepsilon}_2$ and the volumetric strain was $\varepsilon_v = 0$. The evolution of q_ϕ with the stress ratio (t/s) is similar to that from the VED tests, as shown in Figure 4-3.

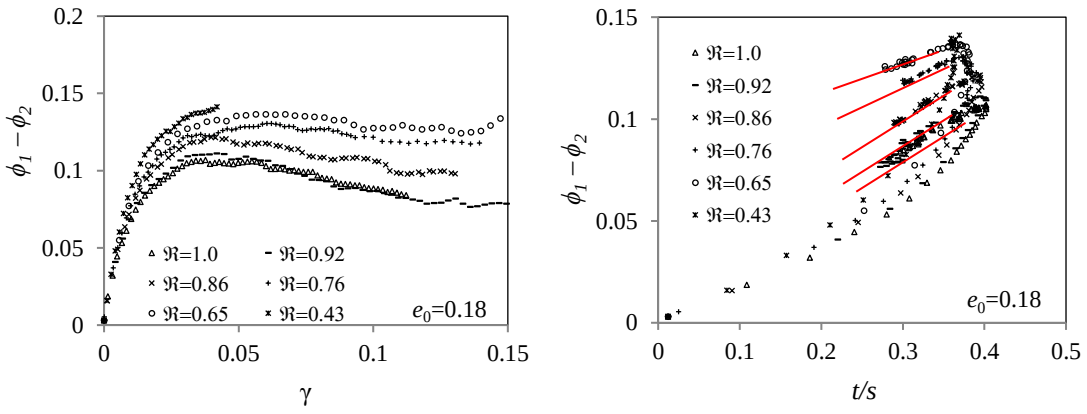

(a) (b)

Figure 4-3: Evolution of the fabric anisotropy in overall contact network with (a) shear strain and (b) stress ratio t/s in VED and VEI tests

Fabric evolution in VEC tests

As shown in Figure 4-4 (b), significant fabric anisotropy developed in the VED tests ($0 < \Re < 1$) since a rapid lateral extension caused a quick reduction of lateral constraint, which in turn resulted in relatively more contacts aligned in the vertical direction to resist deformation. Thereafter, failure of the overall contact network happened after

the fabric anisotropy approaching its maximum. The magnitude of fabric anisotropy in the VEC tests was lower than that in the VED and VEI tests owing to the smaller extension rate in the lateral direction ($\dot{\varepsilon}_2 = -\dot{\varepsilon}_1 / \Re, \Re > 1$) relative to the vertical compression rate $\dot{\varepsilon}_1$. With the increase of $\Re$, the horizontal extension rate, $|\dot{\varepsilon}_2|$, became smaller, which tended to produce relatively stable force-chains in the direction of σ_2. In other words, with an increase of the $\Re$ value, the force-chains in the lateral direction provided stronger support to the strong force-chains in the vertical direction. When the value of $\Re$ was large enough, the weak force-chains in the lateral direction were always stable during deformation and provided stronger support to the strong force-chains in the vertical directions. Correspondingly, the stress paths did not approach the peak state line, for example, in the test with strain path of $\Re \to +\infty$ in Figure 3-6.

Regarding the development of induced anisotropy, referring to Figure 4-4 (a), with the increasing of $\Re$, the fabric anisotropy decreased significantly, and q_ϕ may not have a peak value as $\Re > 32$, which implied that the contact network could resist external shearing steadily without much contact rearrangement. It should be noted that K_0-condition corresponds to $\Re \to \infty$.

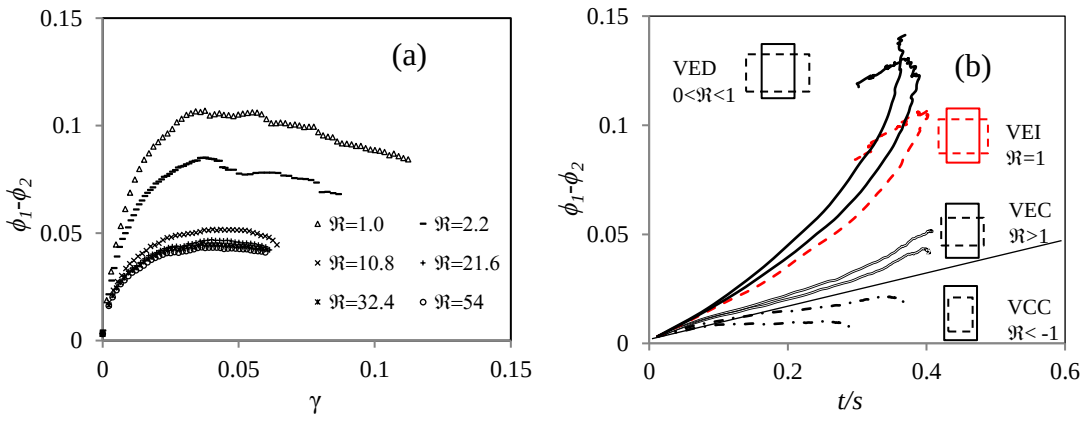

Figure 4-4: Evolution of fabric deviator for the overall contact network with (a) shear strain in VEC tests, and (b) t/s along different strain paths

Fabric evolution in VCC tests

In VCC tests, both $\dot{\varepsilon}_1$ and $\dot{\varepsilon}_2$ were positive (compression) with $\dot{\varepsilon}_1 > \dot{\varepsilon}_2 > 0$. When compared with other tests, the enhanced lateral constraint in VCC tests helped to build more contacts and increased the contact forces in the lateral direction. As a result, the directional variation of the contact distribution decreased, which resulted in a reduced magnitude of fabric anisotropy in the overall contact network; as can be observed in Figure 4-4 (b) and Figure 4-5.

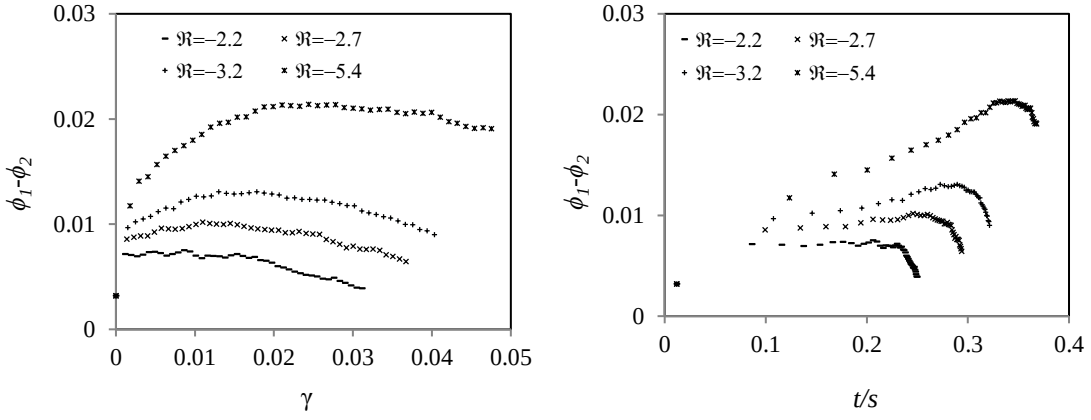

(a) (b)

Figure 4-5 Evolution of the fabric anisotropy in overall contact network with (a) shear strain, and (b) stress ratio t/s in VCC tests

Effect of stress on fabric evolution in overall contact network

To obtain a quantitative description of the evolution of fabric, a regression analysis of the results from the VED, VEI and some VEC tests was performed. As shown in Figure 4-6, prior to the peak stress state, the variation of q_ϕ with t/s and the imposed strain ratio can be described by

$$\phi_1 - \phi_2 = A(t/s)^n \tag{4-25}$$

where A and n are functions of the imposed strain ratio $\Re$ or ϑ. As shown in Figure

4-7, A and n can be reasonably expressed as $A=1.6-0.94\vartheta$ and $n=0.5-0.76\vartheta$. Eq. (4-25) plays the role of fabric evolution law that is important for a stress-strain model based on continuum mechanics.

In the post-peak loading stage, the variation of q_ϕ with the decrease of t/s can be described by a linear relation $q_\phi = q_\phi^{\max} + \kappa_p\left[t/s-(t/s)_{\max}\right]$ with $q_\phi^{\max} = A(t/s)_{\max}^n$, as shown in Figure 4-3 (b). The value of κ_p could be expressed as a function of the imposed strain ratio $\kappa_p = 0.50\vartheta + 0.24$; see Figure 4-7 (b).

The reason that the expression of Eq. (4-25) does not hold true for the post-peak deformation stage can be attributed to the different patterns of fabric evolution in the strong and weak sub-networks as well as the deformation instability. Owing to the rigid boundary conditions adopted in the DEM simulations, the post-peak deformation was still homogeneous without noticeable localized or diffused deformation patterns, and the deformation instability manifests itself as the collapse or buckling of force-chain segments.

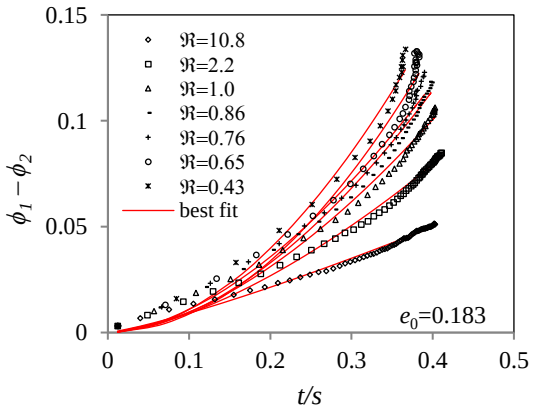

Figure 4-6: Evolution of the fabric deviator of the overall contact network with t/s and the best fit of pre-peak data in different tests

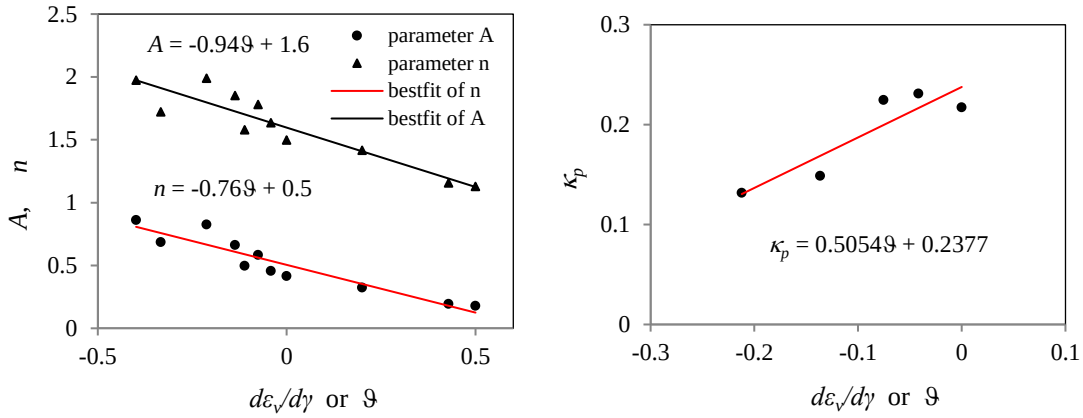

(a) (b)

Figure 4-7: Best fit of (a) the parameters A, n and (b) the parameter κ_p

4.3.2 Fabric evolution in strong sub-network

It seems that the fabric anisotropy in overall contact network alone cannot interpret the stress-strain response ideally. Therefore fabric of the strong network and its evolution were investigated for a better understanding of granular material's internal structure.

Fabric evolution in VED and VEI tests

Figure 4-8 presents the evolution of fabric anisotropy of the strong sub-network characterized by $q_\phi^s = \phi_1^s - \phi_2^s$ under different conditions, with ϕ_1^s and ϕ_2^s being the principal components of the fabric tensor defined for the strong sub-network. Figure 4-8 (a) shows the variation of q_ϕ^s with the t/s ratio in the VED and VEI tests with $\Re \in [0.43, 1.0]$. A unique relation between q_ϕ^s, or alternatively $(\phi_1^s - \phi_2^s)/(\phi_1^s + \phi_2^s)$, and t/s can be defined prior to the peak deviator stress ratio along different strain paths, which is different from the fabric evolution of the overall contact network presented in Figure 4-3(b). The maximum induced anisotropy $q_{\phi,peak}^s$ appeared simultaneously with $(t/s)_{\max}$ that corresponded to the peak friction angle. The

post-peak data were slightly scattered, however, they distributed in a narrow band that almost overlapped the pre-peak data. The following relation can be used to describe the variation of q_ϕ^s with the t/s ratio:

$$\frac{\phi_1^s - \phi_2^s}{\phi_1^s + \phi_2^s} = \kappa \frac{t}{s} \tag{4-26}$$

where κ is a constant. The best estimate of $\kappa = 1$ can be applied to different strain paths, as shown in Figure 4-8 (a).

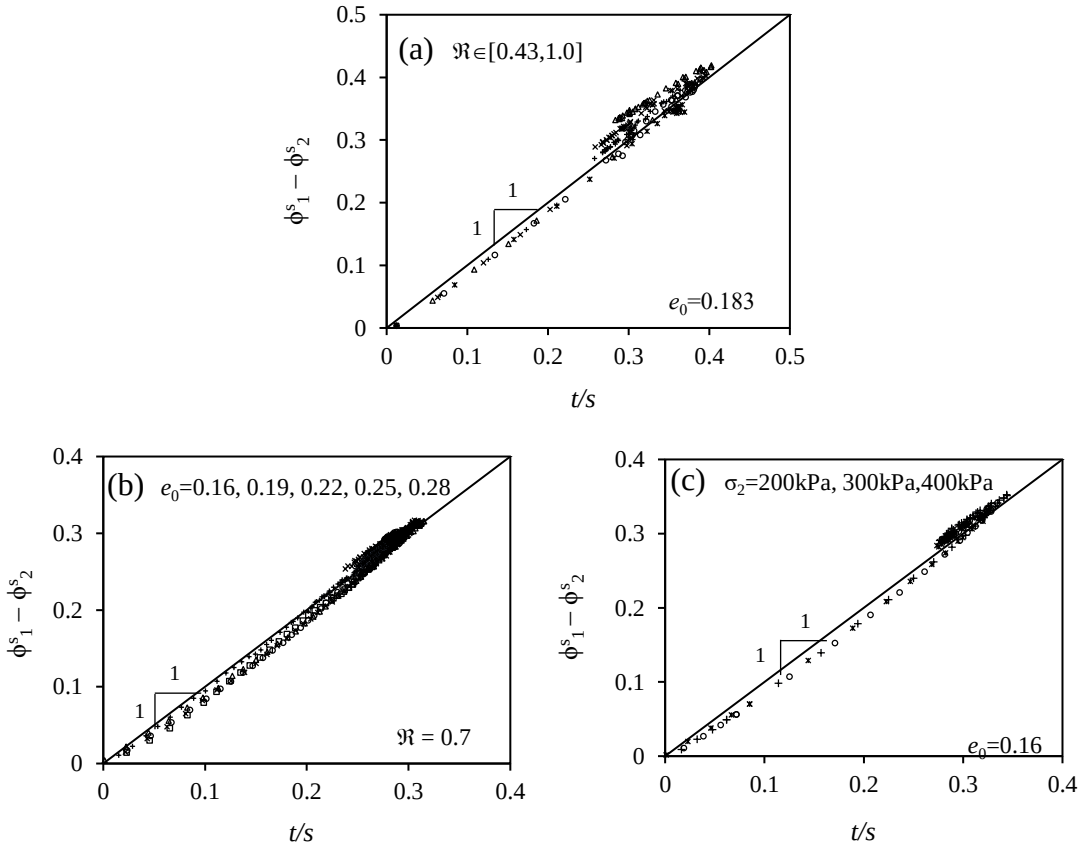

Figure 4-8: Evolution of the fabric deviator in the strong sub-network with stress ratio t/s (a) in the VED and VEI tests ($\vartheta \le 0$), (b) at different initial void ratios, and (c) under different confining pressures

Eq. (4-26) was verified by tests along imposed strain path $\Re = 0.7$ for

different initial void ratio in Figure 4-8 (b) and by conventional biaxial compression tests with constant σ_2 (VP200, VP300 and VP400) on specimens with initial void ratio being 0.16 in Figure 4-8 (c). In both cases, Eq. (4-26) can be used to describe the relation between t/s and $(\phi_1^s - \phi_2^s)$, regardless the initial void ratio of the specimens and the variation of the dilatancy rate $-d\varepsilon_v / d\gamma$ in the conventional biaxial compression tests. As such, one may conclude that Eq. (4-26) can be used to describe the evolution of fabric in the strong sub-network. With $\kappa = 1$ holding true for all cases, Eq. (4-26) can be alternatively expressed as $\phi_1^s : \phi_2^s = \sigma_1 : \sigma_2$.

Fabric evolution in VEC tests

When shearing took place along contraction strain paths in VEC tests with $\Re > 1$ (or $\vartheta > 0$), the $q_\phi^s \sim (t/s)$ curves were all in a narrow band around the line of $(\phi_1^s - \phi_2^s) = t/s$, as shown in Figure 4-9 (a). Similar to the development of anisotropy in the VED tests, a peak and a residual anisotropy were observed along strain paths with relatively small $\Re$ values; for example $\Re = 2.2$. Eq. (4-26) could be used to describe the prior peak $q_\phi^s \sim (t/s)$ relation. Moreover, the occurrence of the $(t/s)_{\max}$ and $q_{\phi,\max}^s$ implied that the maximum resistance to deformation of the strong sub-network was mobilized due to the intensive reduction of the lateral constraints.

However, when $\Re > 54$, the expansion of the specimen in the lateral direction was relatively small. As a result, the strong force-chain network was able to resist deformation without approaching its maximum capacity due to the strong support of the horizontal force-chains. Therefore, q_ϕ^s increased monotonically with the stress ratio (t/s) following Eq. (4-26). When compared with the scattered relation of

$q_\phi \sim t/s$ for the overall contact network shown in Figure 4-4, Figure 4-9 (a) suggested a strong influence of t/s on the internal structure of the strong sub-network in tests along contraction strain paths with $\Re > 1$. In addition, the ultimate fabric deviator $q^s_{\phi,ult}$ depended on the value of $\Re$ in these cases. $q^s_{\phi,ult}$ is higher than the critical value $q^s_{\phi,cr}$ in the VED and VEI tests.

Fabric evolution in VCC tests

For imposed contractant strain paths with $\vartheta > 0$ and $\Re < -1$ in the VCC tests, q^s_ϕ increased monotonically with t/s and the shear strain; as shown in Figure 4-9 (b) and (d). The ultimate fabric deviator $q^s_{\phi,ult}$ increased as the strain paths moves toward K_0-compression at $|\Re| \to \infty$. With an increase of the $|\Re|$ value, the volume contraction became dominant and the effect of shearing decreased. As a special case when $\Re = -1$, the specimen was subjected to hydrostatic compression. One expects smaller $q^s_{\phi,ult}$ values as $\Re$ increases, which is confirmed by the results in Figure 4-9 (b) and (d). With the decrease of $\Re$ value, the lateral constraint became weaker, and hence severe anisotropy developed in the strong sub-network.

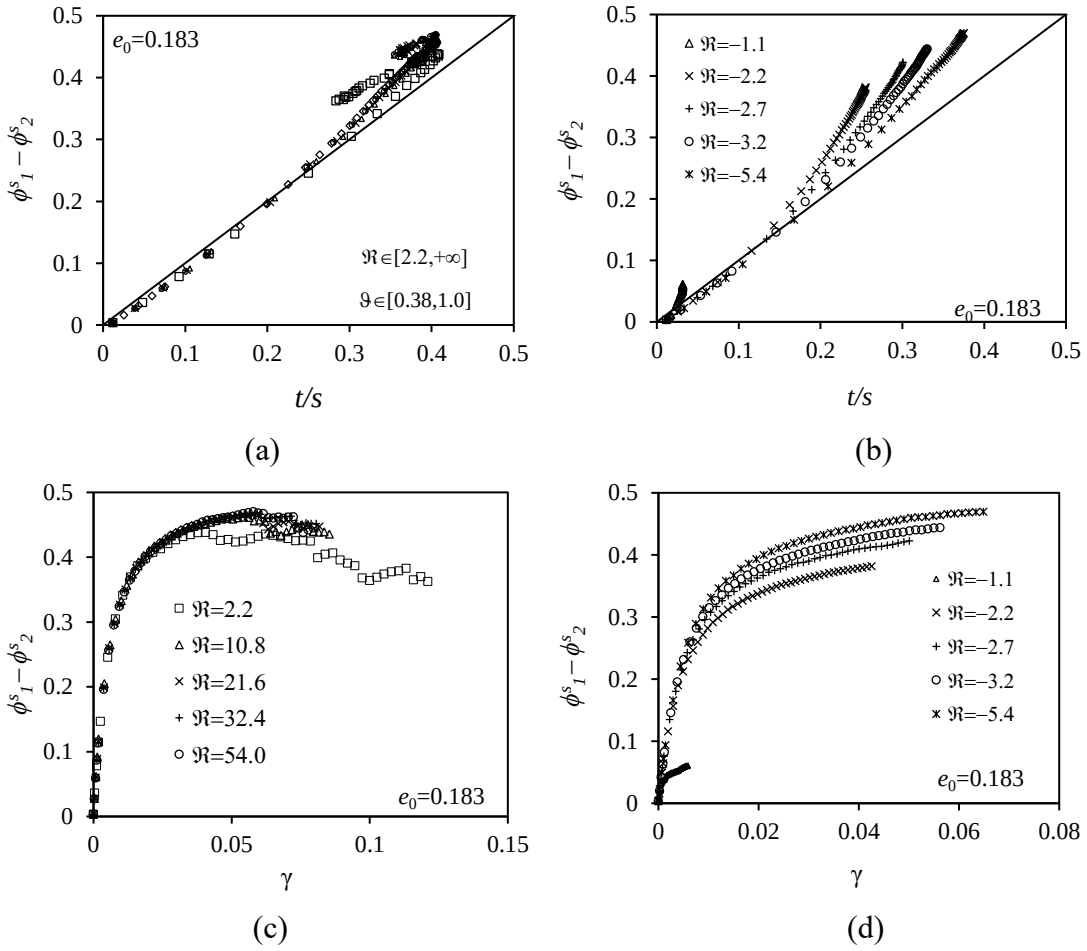

Figure 4-9: Evolution of fabric anisotropy in the strong sub-network with t/s in (a) VEC tests, (b) in VCC tests, (c) with the shear strain in VEC tests and (d) in VCC tests

4.3.3 Fabric evelotion in weak sub-network

Fabric evolution in VED and VEI tests

The evolution of anisotropy in the weak sub-network with the t/s ratio and shear strain in the VEI and VED tests with $0<\Re\leq 1$ are presented in Figure 4-10. Following an initial buildup of anisotropy with an increase of the t/s ratio and shear strain, the value of q_ϕ^w reached a maximum value and then decreased with continuous deformation; as shown in Figure 4-10. The initial buildup of q_ϕ^w along

dilatant strain paths showed a linear relation with t/s in the form of

$$\frac{\phi_1^w - \phi_2^w}{\phi_1^w + \phi_2^w} = \kappa^w \frac{t}{s} \tag{4-27}$$

in which κ^w was a coefficient that varied with the values of ϑ or $\Re$. As shown in Figure 4-11, κ^w varied in the ranges of 0.3 to 0.45 when the dilation rate increased from $\vartheta = -0.4$ ($\Re = 0.43$) to $\vartheta = 0$ ($\Re = 1.0$). The peak value of q_ϕ^w appeared much earlier than the maximum mobilized shear strength in Figure 3-7 (a).

The ultimate value of q_ϕ^w at large shear strain depended on the strain paths. As shown in Figure 4-10 (a), for tests along higher dilatant strain paths such as $\Re = 0.43, 0.65$, q_ϕ^w decreased to zero when t and s both approached zero, which corresponded to "liquefaction" of the samples. The weak sub-network collapsed since the horizontal extension was much larger than the vertical compression in these two tests. With an increase of $\Re$, the horizontal extension rate decreased and the weak sub-network were stable to provide support to the strong sub-network in the vertical direction. Correspondingly, both the peak and ultimate value of q_ϕ^w increased with the increasing of $\Re$. When $\Re = 1.0$, q_ϕ^w was almost a constant at large strain level; as shown in Figure 4-10 (a).

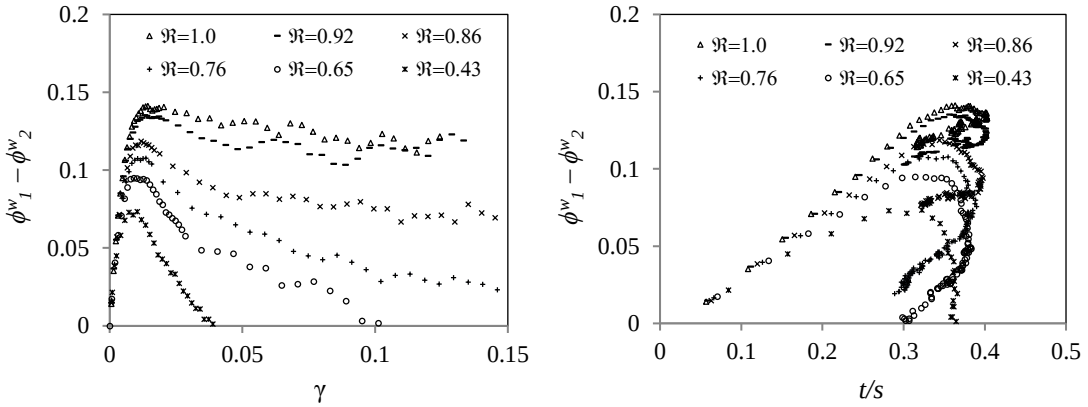

(a) (b)

Figure 4-10: Evolution of the fabric anisotropy in weak sub-network (a) with shear strain, and (b) with stress ratio t/s in the VED and VEI tests

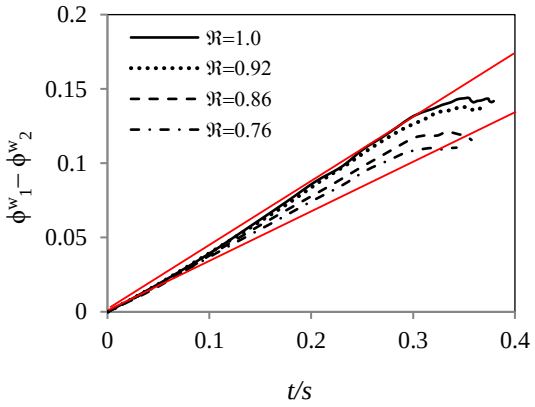

Figure 4-11: Linear relation between q^w_ϕ and t/s prior to the $q^w_{\phi,\max}$ in VED and VEI tests

Fabric evolution in VEC and VCC tests

In the VEC tests, the expansion rate of the specimen in the lateral direction ($\dot{\varepsilon}_2 < 0$) was smaller than the compression rate in the vertical direction ($\dot{\varepsilon}_1 > 0$). In the VCC tests, the specimen is compressed in both vertical and horizontal direction with $\dot{\varepsilon}_1 > \dot{\varepsilon}_2 > 0$ and $\Re < -1$. According to Figure 4-12 (a) and Figure 4-13 (a), q^w_ϕ

increased monotonically with the shear strain. At larger strain level, the value of q_{ϕ}^{w} increased with the increase of $\Re$ in VEC tests but decreased with the increase of the $\Re$ in VCC tests. For example, in the test with $\Re = -1.1$, the fabric anisotropy of the weak sub-network was the lowest among all tests.

Figure 4-12 (b) and Figure 4-13 (b) present the variation of q_{ϕ}^{w} with the t/s ratio in VEC tests and VCC tests, respectively. The induced anisotropy in the weak sub-network reached a much higher level as the t/s increased, as long as the strain paths were close to the K_0-compression. In the VCC tests, the q_{ϕ}^{w} increased monotonically with the stress ratio and could develop a much higher level if the stress paths were close to the K_0-compression. As a special case, no significant anisotropy was observed in the weak sub-network when a specimen was subjected to isotropic compression ($\Re = -1$). Only minor fabric anisotropy developed in the weak sub-network in the test with $\Re = -1.1$ when the lateral compression rate was slightly smaller than the vertical compression.

Figure 4-14 compares the evolution of the fabric anisotropy in different contact networks with shear strain in VED test ($\Re = 0.65$), VEI test ($\Re = 1.0$), VEC test ($\Re = 2.2$) and VCC test ($\Re = -2.2$). Significant anisotropy developed in the strong sub-network, with the degree of anisotropy much higher than those in overall contact network and weak sub-network in all tests. The evolution of fabric in the weak sub-network was significantly affected by the imposed strain paths, or the lateral constraint. When the value of $\Re$ decreased from $\Re = 0.65$ (Figure 4-14 a) to $\Re = -2.2$ (Figure 4-14 d), the lateral deformation of the specimen changed from extension to compression. With the increase of lateral constraint, strong anisotropy was developed in the weak sub-network, which was confined by the rose diagrams representing the directinal distribution of contact normals shown in Figure 4-15.

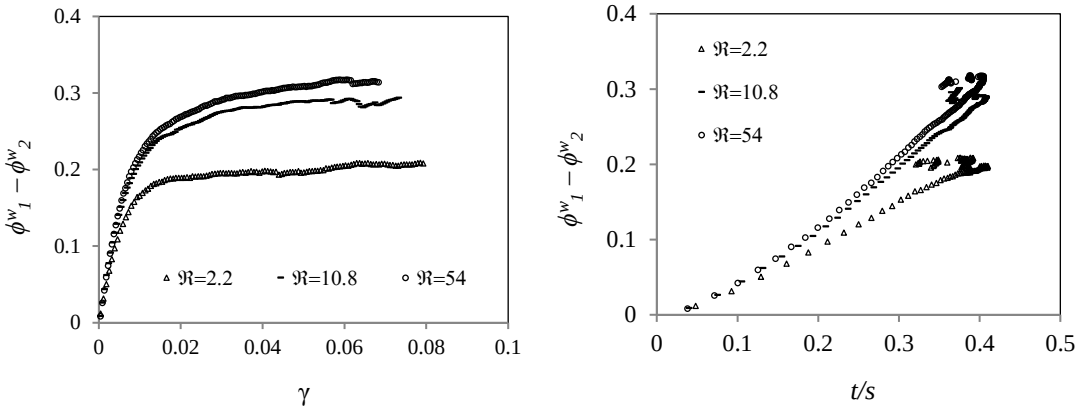

Figure 4-12: Evolution of the fabric anisotropy in the weak sub-network (a) with stress ratio t/s, and (b) shear strain in VEC tests

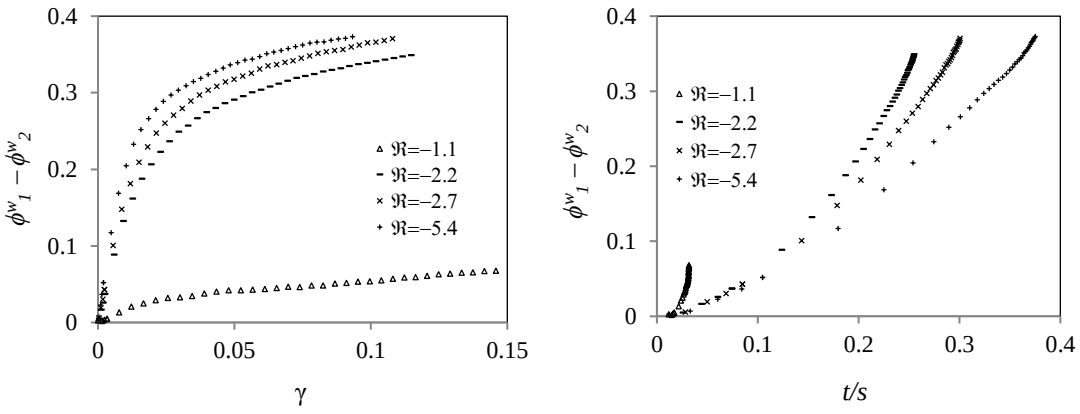

Figure 4-13: Evolution of fabric anisotropy in the weak sub-network (a) with shear strain, and (b) stress ratio t/s in VCC tests

According to Figure 4-15, the major principal direction of the fabric tensor of the strong sub-network was perpendicular to that in the weak sub-network during the shearing. Therefore, most contact normals in the strong sub-network were aligned in the vertical direction and the strong sub-network dominated the shear resistance during deformation. On the other hand, the contact normals in the weak sub-network

mostly orientated in the lateral direction and provided support for the strong sub-network. With a decrease of $\Re$, the contact normals in the weak sub-network tended to concentrate more in the lateral direction, which corresponded to an increased anisotropy of the weak sub-network. As shown in Figure 4-15, the directional distributions for the contact normal in the sub-network are much like peanuts which could not be exactly described using a second-rank Fourier expansion. Here an approximation is made in calculating the second-order fabric tensor for sub-networks.

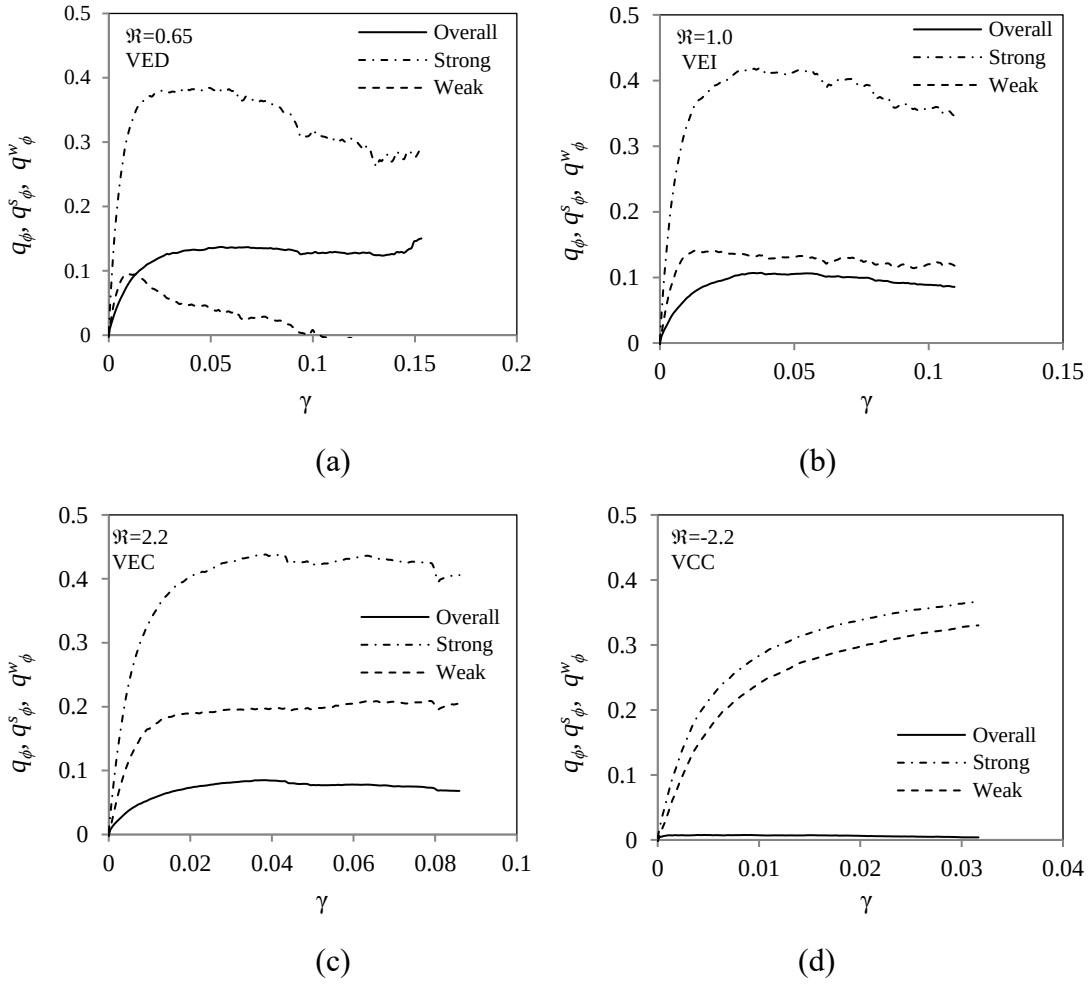

Figure 4-14: Evolution of the fabric anisotropy in overall contact network and sub-networks with shear strain in (a) VED tests, (b) VEI tests, (c) VEC tests and (d) VCC tests

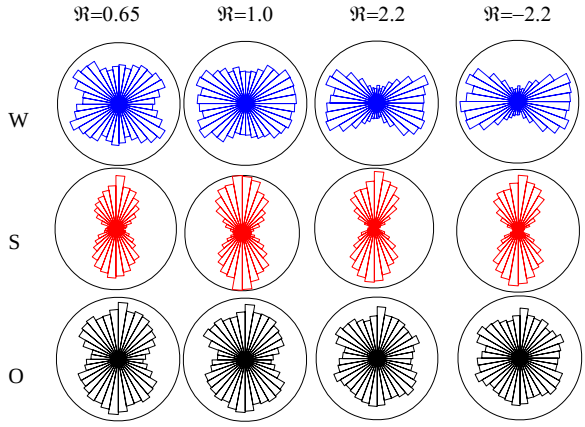

Figure 4-15: Histogram of the strong sub-network (S), the weak sub-network (W) and the overall contact network (O) when γ=3% in different tests

4.4 Fabric evolution in 2D simple shear tests

4.4.1 Fabric evolution in overall contact network

According to Figure 3-10, specimens in the simple shear tests were consolidated under different initial stress ratio $\delta = (\sigma_x - \sigma_y)/(\sigma_x + \sigma_y)$, which was equivalent to $\sigma_y / \sigma_x = (1-\delta)/(1+\delta)$. Once consolidated, the specimen was sheared under constant vertical confining pressure. Figure 4-16 presents the evolution of q_ϕ and t/s with shear strain under different isotropic consolidation stresses ($\delta = 0$). The specimens consolidated under hydrostatic pressure were almost isotropic initially. With the increase of shear strain, q_ϕ initially increased to a peak value and then approached a steady state. The variation of the q_ϕ with shear strain and its steady state value depend on the initial mean stress level; as shown in Figure 4-16(a). A higher degree of fabric anisotropy developed in tests with lower initial consolidation pressure. As shown in Figure 3-11 (c), under low confining pressure (i.e., $\sigma_y = 300$kPa), shearing

induced significant dilation of the specimen in the vertical direction. As a result, more contact normals tended to align around the horizontal direction, leading to higher degree of fabric anisotropy. Compared with the evolution of stress ratio with shear strain in Figure 4-16 (b), $(t/s)_{\max}$ appeared earlier ($\gamma \approx 0.1$) than that of the $q_{\phi,\max}$ which occurred at $\gamma \approx 0.2$. Figure 4-17 presents the evolution of q_ϕ with the stress ratio t/s for tests under different initial consolidation pressures. Prior to the peak value of $q_{\phi,\max}$, the fabric evolution with t/s could be approximately described by a unique curve in the form of $q_\phi = 0.005 + t/s\left(28.49 - 80.436\, t/s\right)$. After the peak, the evolution of the q_ϕ was dependent on the confining pressure. At the ultimate state (or critical state) of deformation, the value of q_ϕ depended on the confining pressure.

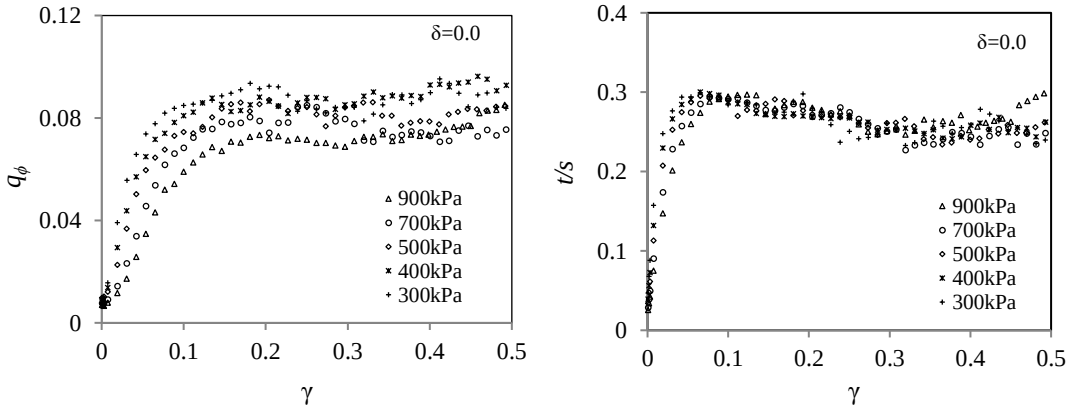

(a) (b)

Figure 4-16: Evolution of (a) fabric anisotropy in overall contact network and (b) t/s with shear strain in simple shear tests under different initial consolidation stresses with $\delta = 0$

Figure 4-18 displays the influence of initial stress ratio δ, which was defined as

$\delta = \frac{\sigma_x - \sigma_y}{\sigma_x + \sigma_y}$, on the evolution of q_ϕ with shear strain and stress ratio at initial consolidation pressure s_0=500kPa. As expected, "initial" or inherent anisotropy was observed in specimens under initial stresses with $\delta \neq 0$. In Figure 4-18 (a), the initial anisotropy was found to be $q_{\phi 0}$= 0.015, 0.02 and 0.03 for specimens with initial stress ratio δ = –0.1, -0.2 and -0.3, respectively. The initial value of q_ϕ increased with the value of $|\delta|$. As the shear strain increased, q_ϕ of all tests quickly increased to its ultimate value $q_\phi \approx 0.085$ at $\gamma \approx 20\%$. With further increase of shear strain, q_ϕ kept almost as constant until the critical state was approached. At the critical state, both the stress ratio (t/s) and q_ϕ approach constant values; as shown in Figure 4-18 (b). The ultimate value of q_ϕ was independent of the initial stress ratio δ (or the initial stress state) which is similar to the observation made by Ai *et al.* (2014). It should be noted, however, the ultimate value of q_ϕ was affected by the mean effective stress level as shown in Figure 4-16 (a).

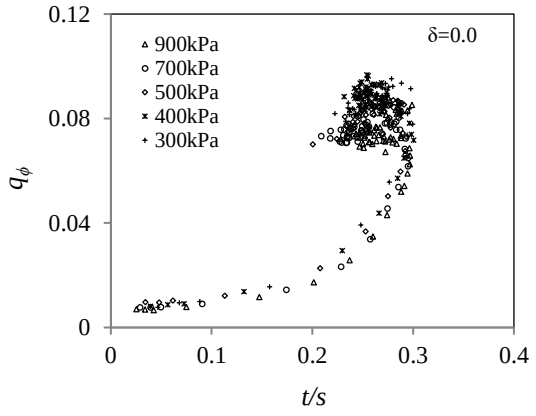

Figure 4-17: Evolution of q_ϕ with stress ratio t/s in simple shear tests under different initial consolidation pressures

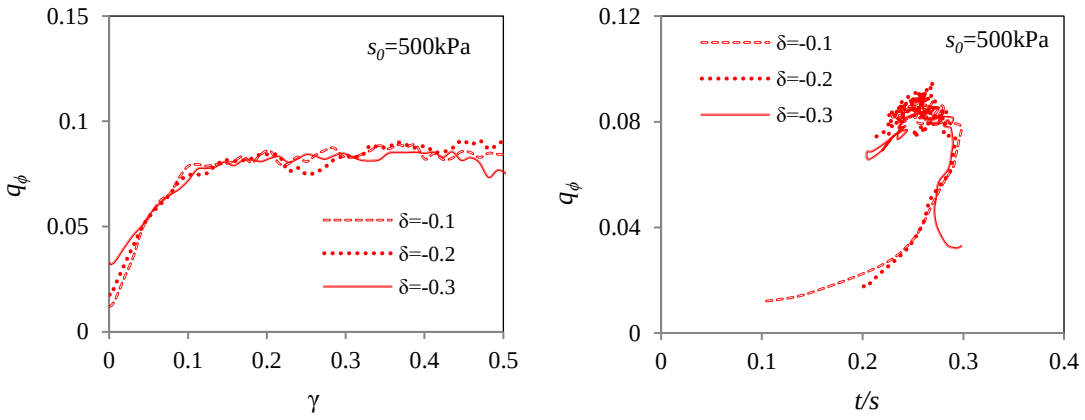

(a) (b)

Figure 4-18: Evolution of fabric anisotropy in overall contact network with (a) shear strain and (b) stress ratio in simple shear tests with different initial stress ratios δ and s_0=500 kPa

4.4.2 Fabric evolution in strong sub-network

For the specimens isotropically consolidated under hydrostatic pressure, the strong sub-network was nearly isotropic before shearing. The evolution of q_ϕ^s in simple shear tests under different confining pressures is illustrated in Figure 4-19. In general, the variation of q_ϕ^s with shear strain was similar to the evolution of stress ratio t/s presented in Figure 3-11. As shown in Figure 4-19 (b), the evolution of q_ϕ^s with respect to t/s showed that q_ϕ^s approached its peak simultaneously with $(t/s)_{max}$ and the critical fabric state was reached at large shear strains. Different from the highly non-linear relation between the q_ϕ and t/s for the whole contact network presented in Figure 4-17, a nearly linear relation could be established between q_ϕ^s and stress ratio t/s, as $q_\phi^s \approx t/s$, which was the same as Eq. (4-26) for 2D tests along proportional strain paths.

Figure 4-20 presents the evolution of q_ϕ^s in specimens initially consolidated at different stress ratio δ at s_0=500kPa. Referring to Figure 4-20 (a), a higher initial stress ratio resulted in stronger inherent anisotropy of the strong sub-network. As the shear strain increased, q_ϕ^s gradually approached a critical value, regardless of its initial value. Similar to the results obtained from tests with $\delta = 0$, the relation of q_ϕ^s with t/s could be considered as nearly linear, as shown in Figure 4-20 (b).

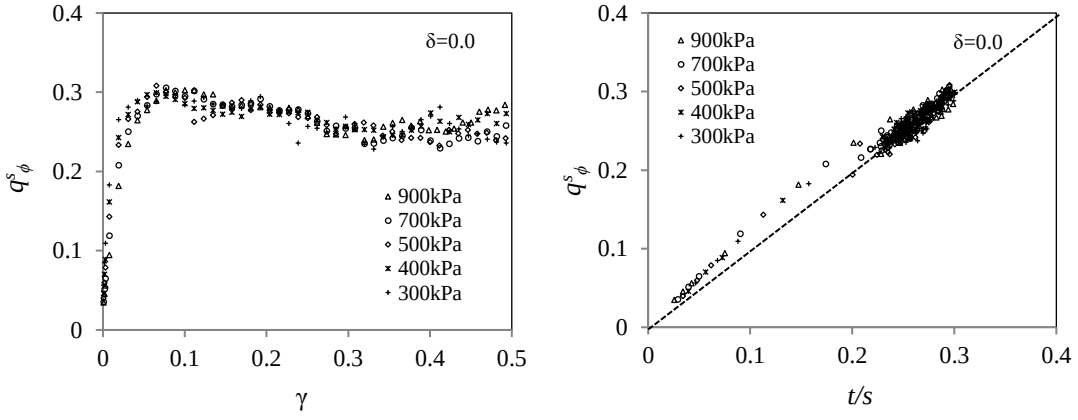

Figure 4-19: Evolution of fabric anisotropy in strong sub-network with (a) shear strain and (b) stress ratio in simple shear tests under different initial mean stresses with $\delta = 0$

4.4.3 Fabric evolution in weak sub-network

Figure 4-21 presents the evolution of q_ϕ^w with shear strain and stress ratio in simple shear tests under different confining pressures with $\delta = 0$. Similar to the biaxial tests along proportional strain paths, q_ϕ^w in the simple shear tests initially increased with shear strain until approaching its peak value, then decreased to an ultimate value as the shearing continued; as shown in Figure 4-21 (a). Higher peak value of q_ϕ^w was

observed when the initial consolidation stress increased. The variation of q_ϕ^w with t/s presented in Figure 4-21 (b) revealed that, prior to reaching its peak value, a unique relation between q_ϕ^w and t/s could be defined: $q_\phi^w = \Lambda(1-3\Lambda/4)$, $\Lambda = t/s$. As a first-order approximation, $q_\phi^w \approx t/s$ could be used. In the post-peak stage, q_ϕ^w gradually decreased with shear strain until approaching an ultimate constant, as shown in Figure 4-21 (a). The ultimate value of q_ϕ^w at large shear strain depended on the strain paths. For the test with higher initial consolidation pressure such as $s_0 = 900$ kPa, the ultimate value of q_ϕ^w was nearly 0.05. But for the test with $s_0 = 300$ kPa, the ultimate value of q_ϕ^w approached 0.02. The magnitude of fabric anisotropy was relatively small when compared with those in the whole contact network and strong sub-network. Therefore, at critical state, the weak sub-network was mostly isotropic.

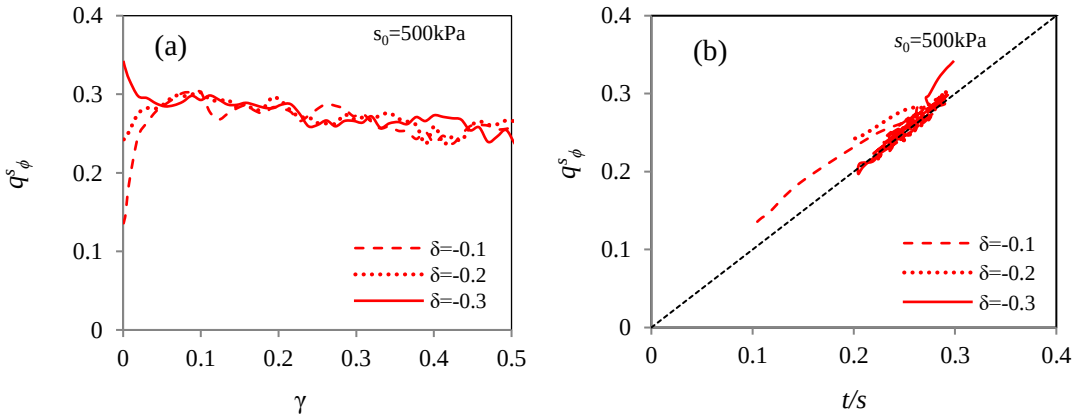

Figure 4-20: Evolution of fabric anisotropy in strong sub-network with (a) shear strain and (b) stress ratio in simple shear tests under different initial stress ratios at s_0=500kPa

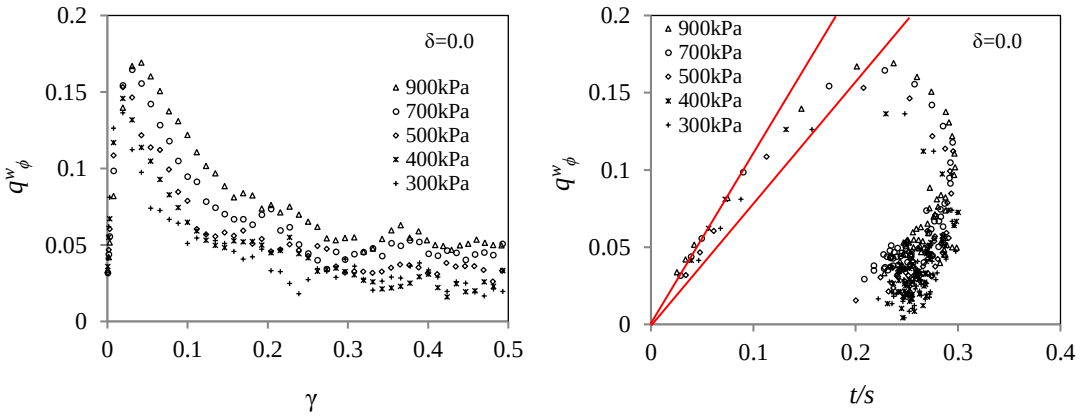

Figure 4-21: Evolution of fabric anisotropy in weak sub-network with (a) shear strain and (b) stress ratio in simple shear tests under different hydrostatic consolidation pressures

Figure 4-22 presents the evolution of fabric anisotropy of the weak sub-network in specimens consolidated under stress state with different δ values. The non-hydrostatic stress state of consolidation induced a certain level of initial anisotropy in the weak network. The higher the vertical stress, the more pronounced the initial anisotropy of the weak network. For the test with $\delta = -0.1$, the initial value of ϕ_q^w was relatively small. The evolution of ϕ_q^w was similar to that obtained in tests with $\delta = 0$. For tests with $\delta = -0.2$ and -0.3, the relatively high vertical stress induced strong inherent anisotropy of the weak sub-network after the consolidation. Upon shearing, the value of ϕ_q^w started to decrease immediately. In all case, the weak sub-network became almost isotropic with $\phi_q^w \approx 0.03$ at the ultimate state.

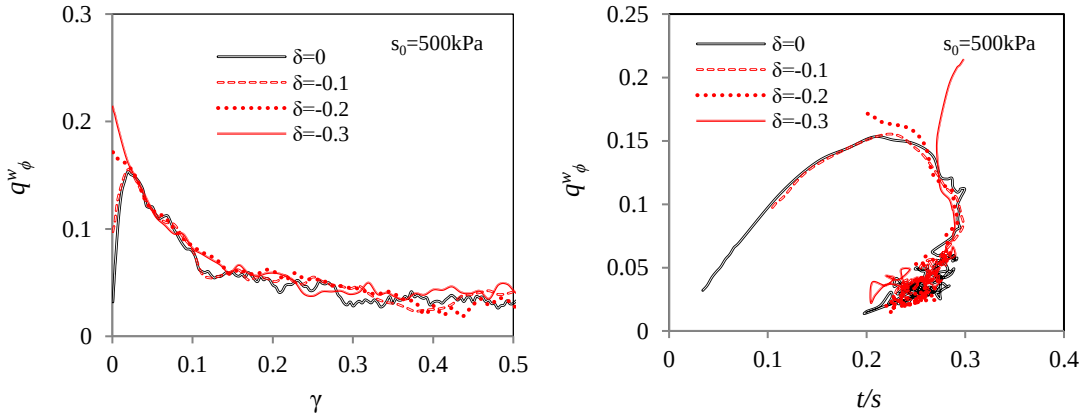

Figure 4-22: Evolution of fabric anisotropy for weak sub-network with (a) shear strain and (b) stress ratio at different δ values with $s_0 = 500$ kPa

4.5 Fabric evolution in 3D tests along radial stress paths on the π-plane

4.5.1 Fabric evolution in overall contact network

As discussed in Section 3.6, in 'true' triaxial tests, the three principal stress components were imposed by keeping the mean stress p and the intermediate stress coefficient b both constant. The deviator of fabric tensor, q_ϕ, was employed to characterize the degree of anisotropy of the overall contact network. Figure 4-23 summarizes the evolution of q_ϕ in the overall contact network with the stress ratio q/p along different stress paths at p=500 kPa. The evolution of q_ϕ was found to be stress path dependent. In particular, for the same stress ratio, shearing along the conventional axisymmetric compression ($b=1$ or $\bar{\theta}=-\pi/6$) tended to induce higher fabric anisotropy than axisymmetric extension ($b=0$ or $\bar{\theta}=\pi/6$). For a given b value, q_ϕ firstly increased with the stress ratio q/p until its peak value. Thereafter, q_ϕ and q/p decreased proportionally to their critical state values; as shown in Figure 4-23 (a).

In addition to the deviatoric stress ratio and the stress paths, the evolution of q_ϕ

was also affected by the mean stress level. As shown in Figure 4-23 (b), along the stress path ($b = 0$ or $\bar{\theta} = \pi / 6$) of axisymmetric extension, the induced degree of fabric anisotropy was more pronounced at lower mean stresses for the same q/p level. However, the peak values of q_ϕ and q/p were not sensitive to the variation of mean stresses.

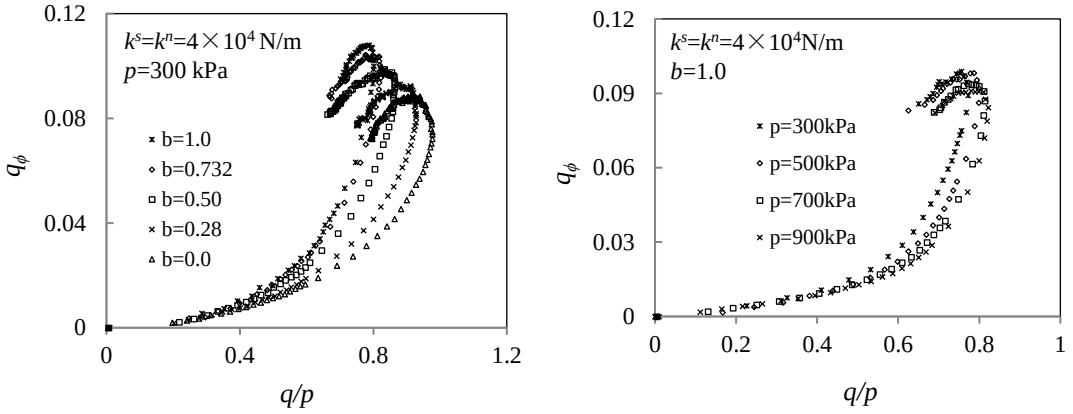

Figure 4-23: Comparison of fabric evolution with q/p: (a) p=300 kPa, $b = 0 \sim 1$; and (b) p=300-900 kPa, b=0: k^n=k^s=4×10^4 N/m

The fabric evolution in the overall contact network showed a power relation with the stress ratio before the peak stress state as shown in Figure 4-24. The evolution of q_ϕ highly depended on the stress path and was not sensitive to the mean stress level, as shown in Figure 4-24 (b). A regression analysis of the data indicated that, prior to the peak stress ratio, the relation between q_ϕ and q/p could be described by

$$q_\phi = B \ q / p \ ^z \tag{4-28}$$

where $B = 0.07 + 0.19b$ and $z = 3.4 + 0.99b$; as shown in Figure 4-25. It is noted

that Eq. (4-28) is similar to Eq. (4-25) for the evolution of q_ϕ in 2D tests along proportional strain paths.

During the post-peak deformation state, the variation of q_ϕ with the decrease of q/p can be described by a linear relation $q_\phi = q_\phi^{\max} + \kappa_p\left[q/p - (q/p)_{\max}\right]$ with $q_\phi^{\max} = B(q/p)_{\max}^{z}$, as shown in Figure 4-25 (b). The value of κ_p could be expressed as a function of the intermediate stress coefficient *b*, as $\kappa_p = 0.05b + 0.11$; see Figure 4-25 (b).

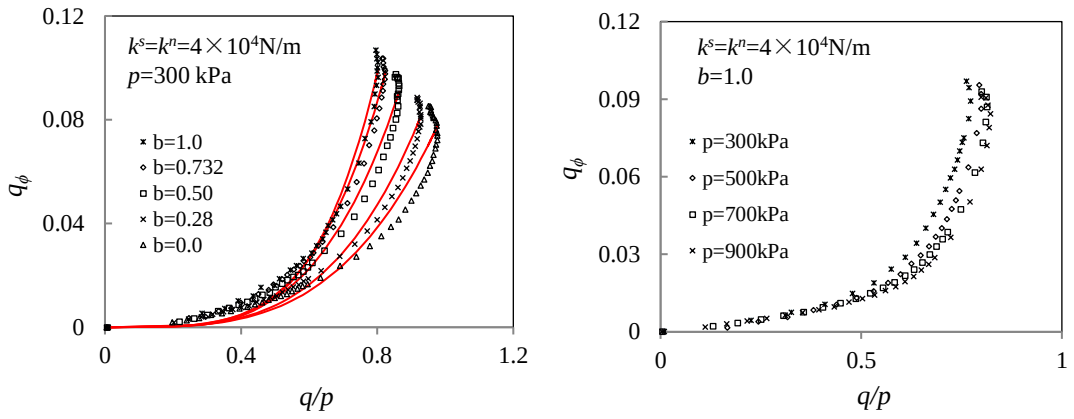

Figure 4-24: Evolution of q_ϕ with q/p before peak stress state: (a) *p*=300 kPa, $b = 0 \sim 1$; and (b) *p*=300-900 kPa, *b*=0: k^n=k^s=4 ×10^4 N/m

4.5.2 Fabric evolution in strong sub-network

Figure 4-26 presents the evolution of fabric anisotropy of the strong sub-network (q_ϕ^s) with the deviatoric strain and the stress ratio along stress paths of different b-values. In general, the variation of q_ϕ^s with the deviatoric strain ε_q was stress paths dependent, which was the same as the variation of q/p as presented in Figure 3-16

(b). In addition, the stronger anisotropy developed in the strong sub-network in the axisymmetric extension test (b=0, $\bar{\theta} = -\pi/6$) than that in the in axisymmetric compression test (b=1, $\bar{\theta} = \pi/6$), as shown in Figure 4-26 (a).

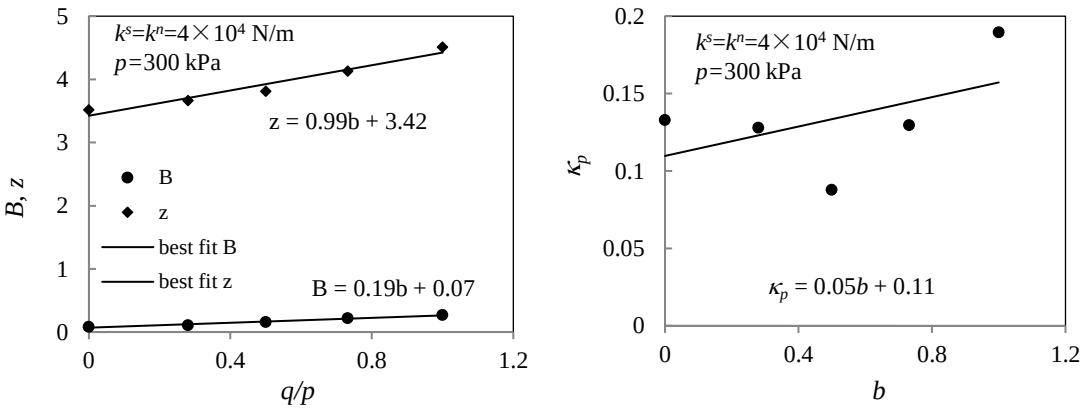

(a) (b)

Figure 4-25: Best fit for (a) B and z, and (b) κ_p

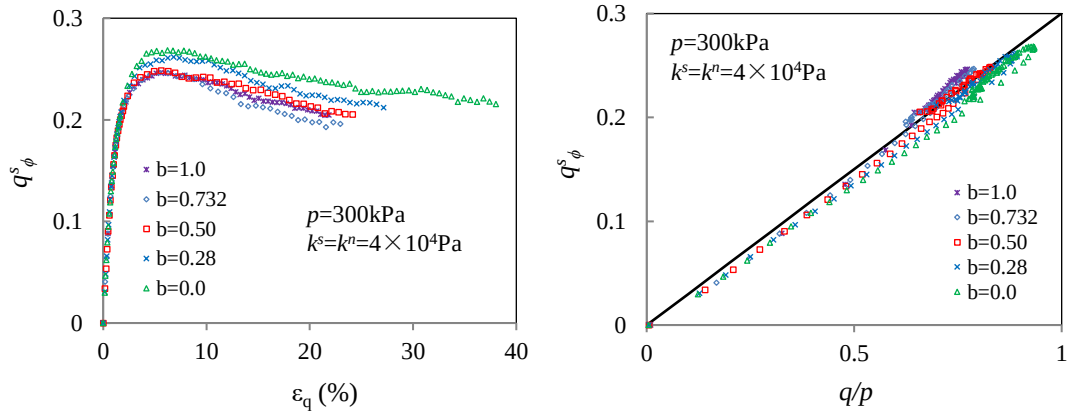

(a) (b)

Figure 4-26: Evolution of fabric anisotropy in the strong sub-network with (a) stress ratio and (b) deviatoric strain in 3D tests along radial stress paths on the π-plane with k^n=k^s=4 ×10^4 N/m

Figure 4-26 (b) presents the fabric evolution in the strong network characterized

by q_ϕ^s, against the q/p ratio under different conditions. Regarding the variation of q_ϕ^s with (q/p), a unique relation between q_ϕ^s and q/p can be defined for all cases as

$$q_\phi^s = \kappa^s \frac{q}{p} \tag{4-29}$$

with $\kappa^s = 1/3$ which was independent of the stress paths, the mean stress level and the inter-particle contact stiffness (see Figure 4-27). Since the mean of the fabric tensor is $p_\phi^s = 1/3$, Eq. (4-29) could be written as

$$\frac{q_\phi^s}{p_\phi^s} = \frac{q}{p} \tag{4-30}$$

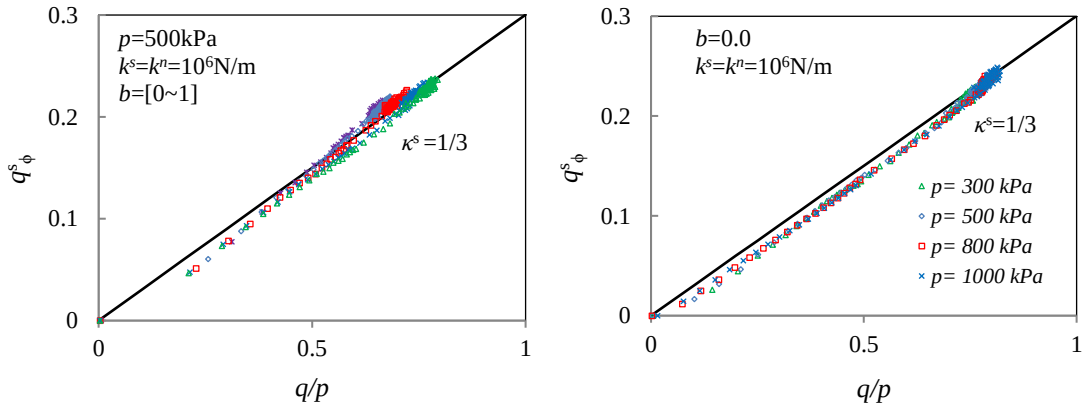

(a) (b)

Figure 4-27: A unique relation between the fabric deviator for strong sub-network and stress ratio q/p in 3D tests with k^n=k^s=10^6 N/m: (a) p=500 kPa, $b = 0 \sim 1$; and (b) p=300-1000 kPa, b=0.0

Comparing with the $q_\phi^s / p_\phi^s = t/s$ for 2D cases, we conclude that Eq.(30) is an unique stress-fabric relation for the strong sub-network for the granular assembly. It is

noted that Eq. (4-28) is applicable to the whole deformation process. In the post-peak deformation stage, q_ϕ^s decreased together with q/p as the shear strain continued increasing until the critical state was reached, as shown in Figure 4-26 (b).

4.5.3 Fabric evolution in weak sub-network

When k^n=k^s=4 ×10^4 N/m and p=300 kPa, the evolutions of the anisotropy of weak contact network with the q/p ratio and the deviatoric strain along different stress paths with a constant mean stress are presented in Figure 4-28. The weak fabric deviator q_ϕ^w initially increased with the deviatoric strain until approaching its peak value. For all stress paths, q_ϕ^w reached its maximum $q_{\phi,\max}^w$ at $\varepsilon_q = 1\%$ ~1.5%, much earlier than the occurrence of the peak stress ratio $(q/p)_{\max}$ and $q_{\phi,\max}^s$ at approximately $\varepsilon_q = 5.5\%$, as shown in Figure 3-16 (b) and Figure 4-26 (a). Comparing with Figure 4-26 (a), the values of $q_{\phi,\max}^w$ were much smaller than $q_{\phi,\max}^w$ at the same deformation state. As shown in Figure 4-28 (b), at low shear stress levels of $q/p < 0.5$, q_ϕ^w is linearly proportional to q/p for all stress paths, such that

$$q_\phi^w = \kappa^w \frac{q}{p} \tag{4-31}$$

with $\kappa^w = 0.187$. Comparing with Eq. (4-29), at a given q/p ratio, stronger anisotropic develops in the strong sub-network since $\kappa^w < \kappa^s$. After the peak, q_ϕ^w decreases as the deviatoric strain increases while the deviator stress ratio q/p keeps increasing until the peak state $(q/p)_{\max}$. At the critical stress state, q_ϕ^w arrives at its ultimate value close to zero, especially for the stress path of $b = 1.0$; as shown in

Figure 4-28 (b). Even though the critical state value of $(q_{\phi}^{w})_{cr}$ is small, the weak contact network can build up a certain level of anisotropy under axisymmetric compression ($b=0$). In particular, $q_{\phi,cr}^{w}=0.03$ at $b=0$ and $q_{\phi,cr}^{w}=0.01$ at $b=1$, respectively. However, it is reasonable to state that the weak contact network is nearly isotropic at the critical state, particularly when compared with the levels of fabric deviators in the strong and the whole contact network as presented in Figure 4-26 (a) and Figure 4-23 (a), respectively.

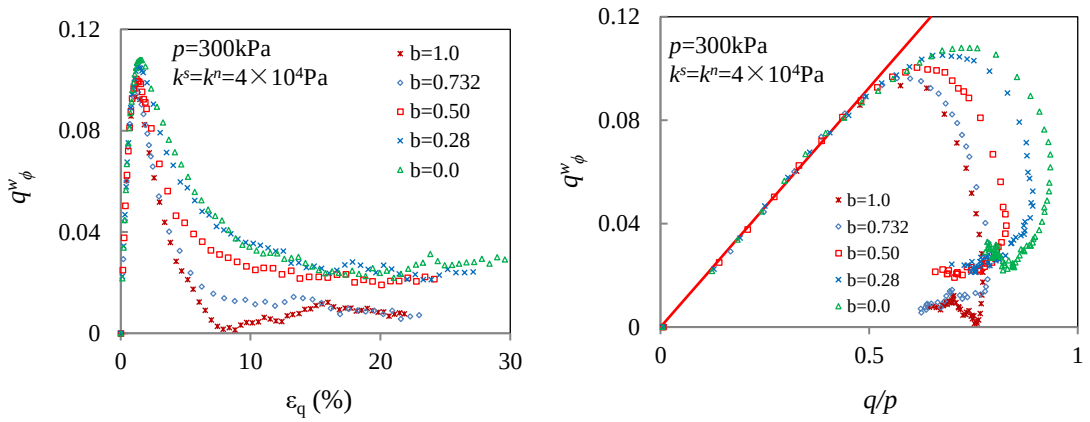

Figure 4-28: Evolution of fabric anisotropy in the weak sub-network along various stress paths: (a) q_{ϕ}^{w} *vs.* γ, and (b) q_{ϕ}^{w} *vs.* q/p : k^n=k^s=4 ×10^4 N/m, p=300 kPa

With regard to the evolution of fabric anisotropy in different contact networks, Figure 4-29 (a) compares the variation of q_{ϕ}, q_{ϕ}^{s} and q_{ϕ}^{w} with a deviatoric strain ε_q in axisymmetric compression test with b=1.0. At the very beginning, all contact networks were approximately isotropic. At small deviatoric strain, the induced anisotropy in the strong sub-network developed faster than those in the weak sub-network and the whole network. Thereafter q_{ϕ}^{w} approached its peak value (at A')

then declined gradually. Before the strain level at A', the relation between q_ϕ^s and q_ϕ^w was almost linear, as shown in Figure 4-29 (b). With the further increase of the deviatoric strain, q_ϕ^s approached its peak value at B', where the weak sub-network was nearly isotropic. After B', the q_ϕ^s began to decrease while q_ϕ continuously increased until its peak value at C'.

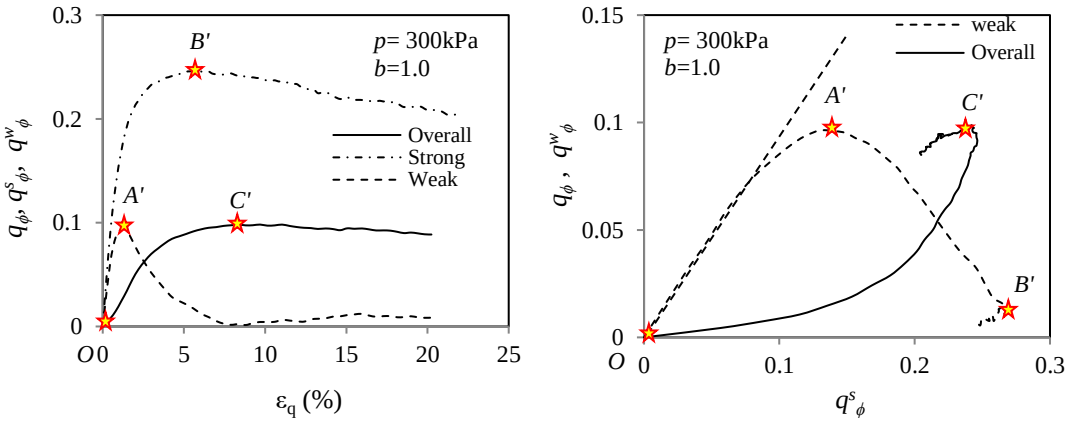

(a) (b)

Figure 4-29: Evolution fabric anisotropy in the whole, sub contact networks with deviatoric strain in tests along stress path (a) b=0.0 and (b) b=1.0, k^n=k^s=4 ×10^4 N/m

Figure 4-30 further compared the evolution of q_ϕ^w and q_ϕ^s with the rate of dilatancy quantified by $d\varepsilon_v / d\varepsilon_q$. At the initial deformation stage, both q_ϕ^w and q_ϕ^s increased almost linearly with $d\varepsilon_v / d\varepsilon_q$. $q_{\phi,\max}^w$ was achieved when deformation reached the maximum rate of compaction (A in Figure 4-30), then q_ϕ^w started to decrease while q_ϕ^s continued increasing together with the stress ratio q/p. When the maximum dilatancy rate was mobilized at B, both q_ϕ^s and q/p approached their

peak values simultaneously according to Eq. (4-29). At this time, q_ϕ^w reached a low level near its minimum. During the post-peak deformation process, q_ϕ^w stayed at its minimum while q_ϕ^s and q/p gradually decreased to their values at critical state.

One may interpret the increase of fabric deviator q_ϕ as a measure of strong anisotropy of internal structure or more biased arrangement of particles in preferential directions. A decreasing fabric deviator indicates degradation or collapse of the anisotropic internal structure. At the very beginning of shearing, owing to shear-induced compaction, both sub-networks (strong and weak) rearranged themselves to resist the shear stress. Following the occurrence of the maximum rate of volumetric compression rate, owing shear-induced dilation with the increase of shear strain, some contacts disappeared. The disappearing contacts were mostly in the weak sub-network and originally perpendicular to the major principal stress direction, which resulted in a decrease of q_ϕ^w. During this period of deformation, the strong force-chains still built up accompanied by an increase of q_ϕ^s and q/p. With the increase of volumetric dilation rate, continuous loading and weakening of the weak sub-network resulted in the local collapse of strong force-chains, which was initiated when q_ϕ^s and q/p reached their maximum values. The strong sub-network continued to collapse until a critical state at which the rate of volumetric strain became zero and the weak sub-network was practically isotropic; as shown in Figure 4-28.

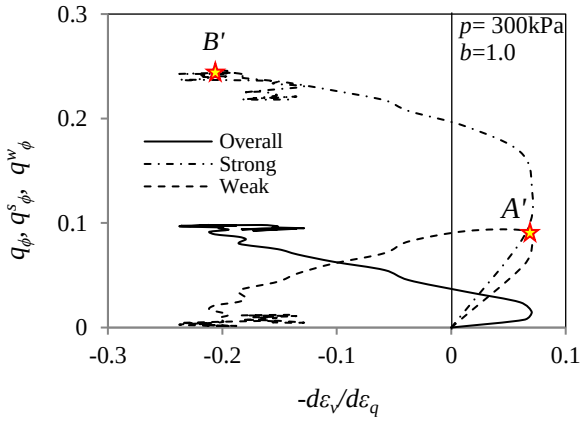

Figure 4-30: Evolution of fabric anisotropy in the whole and sub-networks with ratio of strain increment in tests along stress paths of b=1.0 and k^n=k^s=4 ×10^4 N/m

4.6 The upper limit of fabric anisotropy in 2D granular assembly

The fabric tensor, defined in strong sub-network in Eq. (4-10), can also be approximately expressed in the form of Eq. (4-5) as

$$\phi^s_{ij} = \int_0^{2\pi} E^s(\theta) n_i n_j d\theta \tag{4-32}$$

with the probability density function of contact normal distribution being (Radjai et al., 1998):

$$E^s(\theta) \approx \frac{1}{2\pi}\left[1 + a^s_c \cos 2\left(\theta - \theta^s_c\right)\right] \tag{4-33}$$

The parameters a^s_c and θ^s_c define the amplitude of anisotropy and its principal direction. Figure 4-31 shows the directional distribution of the contact normal of the strong sub-network at the peak stress state in an isochoric compression test, which corresponds to $\theta^s_c = \pi/2$. Given that $E^s(\theta) \geq 0$ must be satisfied in any direction, one has $a_c \leq 1$. It has been shown that $q^s_\phi = a^s_c/2$, which implies $q^c_\phi \leq 0.5$.

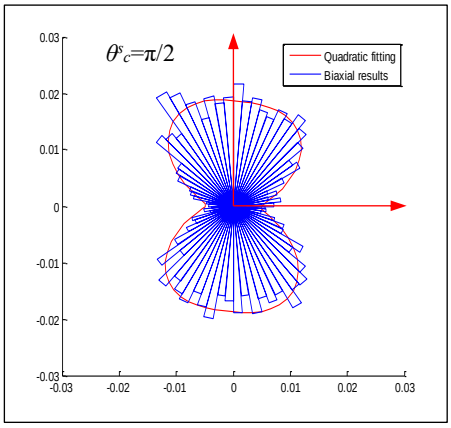

Figure 4-31: Sketch of the directional distribution of contact normal density for strong sub-network in VEI test when at the peak stress state ($\gamma = 3\%$)

The results of DEM simulations under various conditions have shown that q_ϕ^s is larger than both q_ϕ and q_ϕ^w. Therefore, the maximum value of the fabric deviator within strong sub-network satisfies $q_{\phi,\max}^s \le 0.5$.

Figure 4-32 (a) presents the variation of $q_{\phi,\max}^s$ with $\vartheta = d\varepsilon_v / d\gamma$ in 2D simulations for proportional strain paths tests and biaxial compression tests with constant confining pressure. In general, the data points can be divided into two sections by the K_0 state ($\Re \to \pm\infty$) where the value of fabric deviator within strong sub-network approached its maximum value. The right section corresponds to the VCC series ($\Re < -1$) in which the specimen had a compressive deformation in the directions of both σ_1 and σ_2. The $q_{\phi,\max}^s$ tended to decrease as $\vartheta = d\varepsilon_v / d\gamma$ increased in the right section, which was induced by increasing of the friction of strong contacts in the lateral direction due to the over-constraint imposed by deformation in the direction of σ_2. However, $q_{\phi,\max}^s$ increased with the increase of $\vartheta = d\varepsilon_v / d\gamma$ on the left section corresponding to VEC series tests, in which the

specimen was allowed to expand in σ_2 direction. $q^s_{\phi,\max} = 0.5$ was only approached when the specimen was subjected to K_0 compression as shown in Figure 4-32 (a). In biaxial tests with constant lateral stresses, the developed anisotropy was close to that along dilative strain paths with $\vartheta = -\sin\psi_{\max}$ in which $\psi_{\max}$ was the maximum dilatancy angle in conventional biaxial tests defined as $\sin\psi_{\max} = \tan\varpi_{\max} = -d\varepsilon_v / d\gamma$ (see Figure 4-32 b). The results of DEM simulations presented in Figure 4-32 confirm $q^s_{\phi,\max} \le 0.5$.

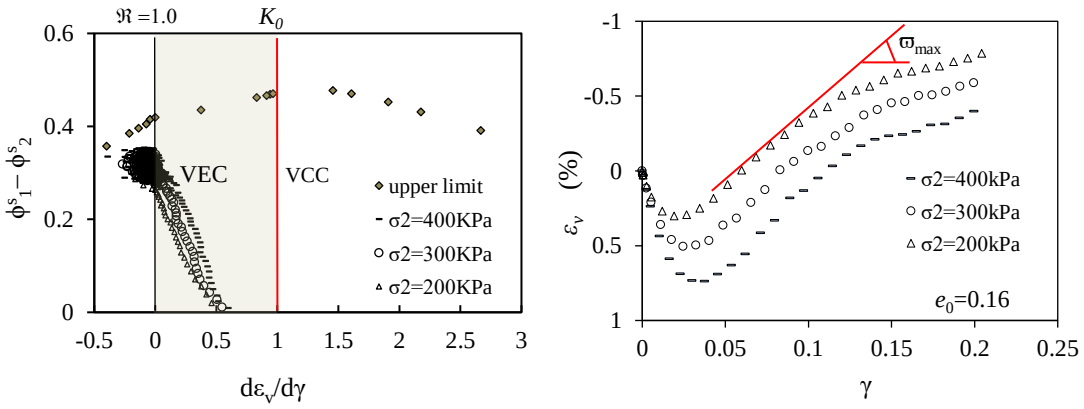

Figure 4-32: (a) The upper limits of fabric deviator in strong sub-network and (b) the volumetric strain variation in biaxial compression tests with constant confining pressure

4.7 Summary

This chapter focuses on the evolution of fabric in different contact networks during deformation in various simulated tests conducted in Chapter 3. With the fabric tensor being defined according to the directional distribution of contact normals, the fabric deviator was used as the measure of the fabric anisotropy. Based on the analyses for the results of DEM simulations, the following conclusions were obtained:

(1) The evolution of the fabric of the overall contact network depended on the stress path or the strain path. Owing to its dependency on deformation history, the fabric deviator of the overall contact network, q_ϕ, could not be expressed as a unique function of stress states.

(2) When a granular assembly was sheared along a selected proportional strain path or stress path, a power relation $q_\phi = A(t/s)^n \; or \; B(q/p)^z$ was found before the peak stress state with parameters of A, n and B, z depending on imposed dilatancy rate $-d\varepsilon_v / d\gamma$ and the intermediate stress ratio b; respectively.

(3) For an initially isotropic granular assembly subjected to shearing, a unique stress-fabric relation was found, which took the form $q_\phi^s / p_\phi^s = q/p$ for 3D stress conditions and $q_\phi^s / p_\phi^s = t/s$ for biaxial stress conditions. Alternatively, the stress-fabric relation for the strong sub-network can be expressed as $\phi_1^s : \phi_2^s \approx \sigma_1 : \sigma_2$ for 2D stress conditions.

(4) For the weak sub-network, the initial buildup of induced fabric anisotropy could be linearly related with the stress ratio under both two-dimensional tests and three-dimensional tests. The peak value of q_ϕ^w occurred much earlier than the peak stress ratio q/p or t/s. The evolution of q_ϕ^w was significantly affected by stress or strain paths. The anisotropy of the weak sub-network was always weaker than the strong sub-network. Moreover, at critical state, the weak sub-network tended to be isotropic.

Chapter 5 Induced Fabric at Critical State

5.1 Introduction

The critical state theory formulated by Roscoe *et al.* (1958) and Schofield and Wroth (1968) for soil mechanics assumes a unique ultimate state for soil under sustained shear. At critical state, the material deforms continuously under constant stresses with constant volume. This unique ultimate state in constitutive modeling of granular soils is described by the critical stress ratio M $(q/p')_c$ in the p'-q space together with a critical state line (CSL) defining in e-$\ln p'$ plane, where p', q and e are the mean effective stress, deviatoric stress, and void ratio, respectively. M is a material property which is independent of the initial state and the drainage condition but is affected by the history of deformation or stress paths. For example, under axisymmetric stress conditions, the value of M in triaxial compression is larger than that in triaxial extension. The necessary and sufficient conditions for the critical state are that $q/p' = M$ and $e = e_c = \hat{e}_c(p)$ with $\dot{q} = \dot{p} = 0$ are satisfied simultaneously. But the critical stress ratio may not unique. In the Lode system, the critical stress response surface is not a circle since M is stress path dependent.

The classical state theory does not make reference towards the fabric which depends on the connectivity of particles or the distribution of particle orientation, contact normals or branch vectors. It only includes a scalar measure, the void ratio, as an indirect measure of the particle arrangement. In other words, it is assumed that the critical state is independent of the fabric of the material. However, both DEM simulations and experimental studies reveal that granular material exhibit fabric anisotropy at their critical states, where the material is initially isotropic or with a certain level of inherent anisotropy (Been and Jefferies, 1985b; Li and Dafalias, 2011; Masson and Martinez, 2001; Nakata *et al.*, 1998; Thornton, 2000; Zhao and Guo,

2013). In addition, the induced fabric anisotropy at critical state also depends on the stress (Zhao and Guo 2013). On the constitutive modeling side, Li and Dafalias (2011) presented a critical-state based model, which considered the influence of the fabric during deformation and the fabric anisotropy at the critical state. Zhao and Guo (2013) proposed a unique relationship between the mean stress and a fabric anisotropy parameter K defined as the first joint invariant of the deviatoric stress tensor and deviatoric fabric tensor, which resulted in a unique curve in the *K*-*e*- p' space at the critical state.

In this chapter, the fabric-stress relation at critical state is explored using the obtained DEM simulations carried out in Chapter 3. The fabric tensor was calculated in both the overall contact network and sub-networks. The stress-fabric relations for different contact networks at the critical state were examined. The fabric response surfaces were identified at critical state for different contact networks.

5.2 Fabric anisotropy of the whole contact network at critical state

According to the findings from biaxial tests by Satake (1978, 1982) and Oda and Nemat-Nasser (1982), the relation between the principal components of induced fabric in the overall contact network and principal stresses can be expressed as

$$\phi_1 : \phi_2 = \sigma_1^m : \sigma_2^m \tag{5-1}$$

where m is a constant varying in the range of 0.4 to 0.6, ϕ_1, ϕ_2 and σ_1, σ_2 are the principal components of the fabric tensor and stress tensor, respectively. Maeda et al. (2006) conducted biaxial tests using DEM simulations and suggested that $m \approx 0.5$. For three-dimensional cases, Eq. (5-1) becomes

$$\phi_1 : \phi_2 : \phi_3 = \sigma_1^m : \sigma_2^m : \sigma_3^m \tag{5-2}$$

with the parameter *m* being approximately 0.5. This relation further coincides with the

spatially mobilized plane (SMP) and the concept of t_{ij} proposed by Chowdhury and Nakai (1998).

To obtain the relation between the principal components of fabric for the overall contact network and the principal stresses at the critical state, we define a new measure of stress as

$$\hat{\sigma}_i = (\sigma_i)^m \phi_i^{-1} \qquad \text{(i not in summation, and i =1, 2, 3)} \tag{5-3}$$

where m is constant. The mean and the deviator of $\hat{\sigma}_{ij}$ are $\hat{p} = \hat{\sigma}_i / 3$ and $\hat{q} = \sqrt{\frac{3}{2}\hat{s}_{ij}\hat{s}_{ij}}$ with $\hat{s}_{ij} = \hat{\sigma}_{ij} - \hat{p}\delta_{ij}$. When Eq. (5-2) holds true, one has $\hat{q} = 0$. Consequently, to examining the applicability of Eq. (5-2) and determine the deformation process at the critical state, one may explore the variation of $\hat{q}$ under various conditions. It should be noted that the true stress tensor defined in Eq. (4-24) is recovered from Eq. (5-2) when *m*=1.

Figure 5-1 presents the evolution of $\hat{q}/\hat{p}$ at different m values with the deviatoric strain along various stress paths in 3D tests with k^n=k^s= 1×10^6 N/m and *p*=500kPa. When m varied in the range of 0.35 to 0.5, for each individual stress path, $\hat{q}/\hat{p}$ approached a steady level when $\varepsilon_q > 10\%$ until the critical state. The minimum values of $\hat{q}/\hat{p} \approx 0.01$ was obtained at m=0.4, as shown in Figure 5-1 (b). As a result, it is plausible to the following relation at the critical state

$$\frac{(\sigma_1)^{0.4}}{\phi_1} = \frac{(\sigma_2)^{0.4}}{\phi_2} = \frac{(\sigma_3)^{0.4}}{\phi_3} \tag{5-4}$$

or

$$\phi_1 : \phi_2 : \phi_3 = (\sigma_1)^{0.4} : (\sigma_2)^{0.4} : (\sigma_3)^{0.4} \tag{5-5}$$

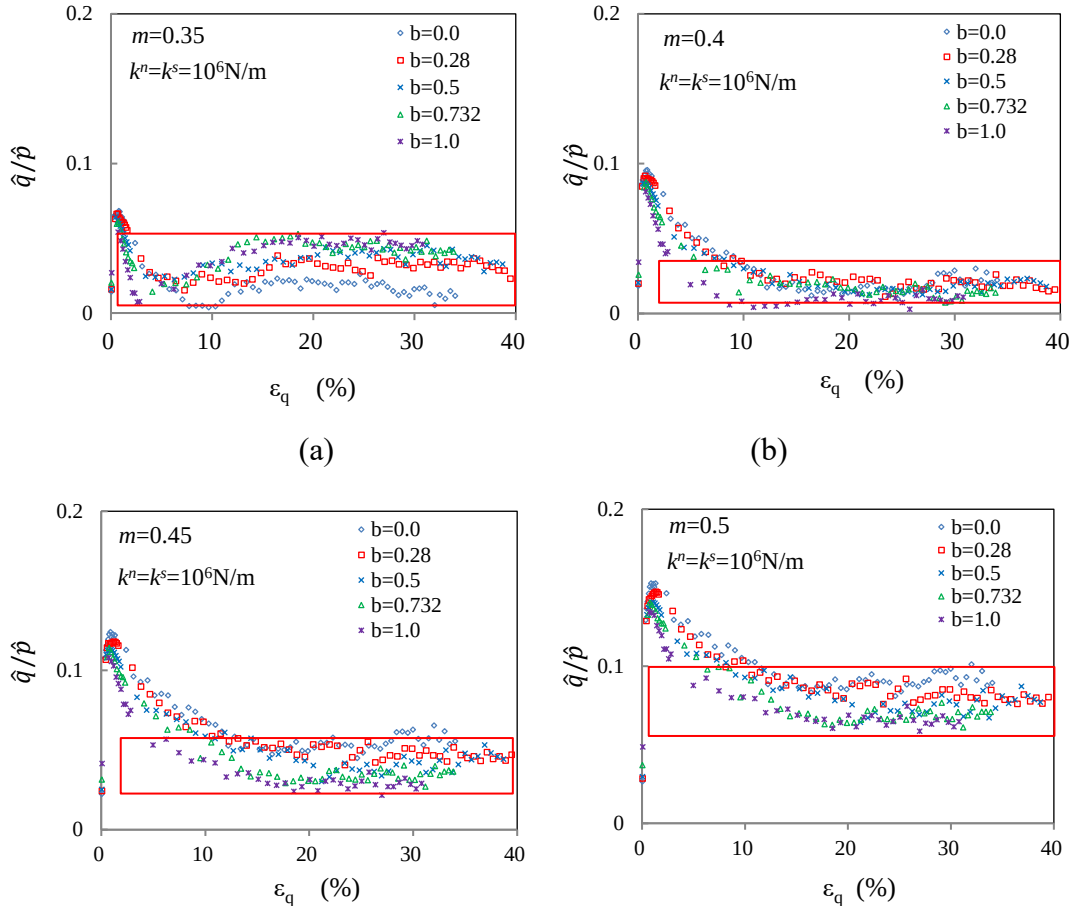

Figure 5-1: Evolution of $\hat{q}/\hat{p}$ with equivalent shear strain at various values of m: $k^n=k^s=1\times10^6$ N/m, p=500kPa

We next examine the dependency of m on the interaction at particle contacts. Figure 5-2 presents the variation of $\hat{q}/\hat{p}$ at different m-values in Eq. (5-3) when the contact stiffness $k^n=k^s=4\times10^4$ N/m. The minimum values of $(\hat{q}/\hat{p})_{\min}\approx0.01\sim0.03$ was obtained when m=0.3 at the ultimate deformation state; as shown in Figure 5-2 (b). In other words, at the critical state, the relation between the principal components for the stress and fabric for the overall contact network can be expressed as

$$\phi_1 : \phi_2 : \phi_3 = (\sigma_1)^{0.3} : (\sigma_2)^{0.3} : (\sigma_3)^{0.3} \tag{5-6}$$

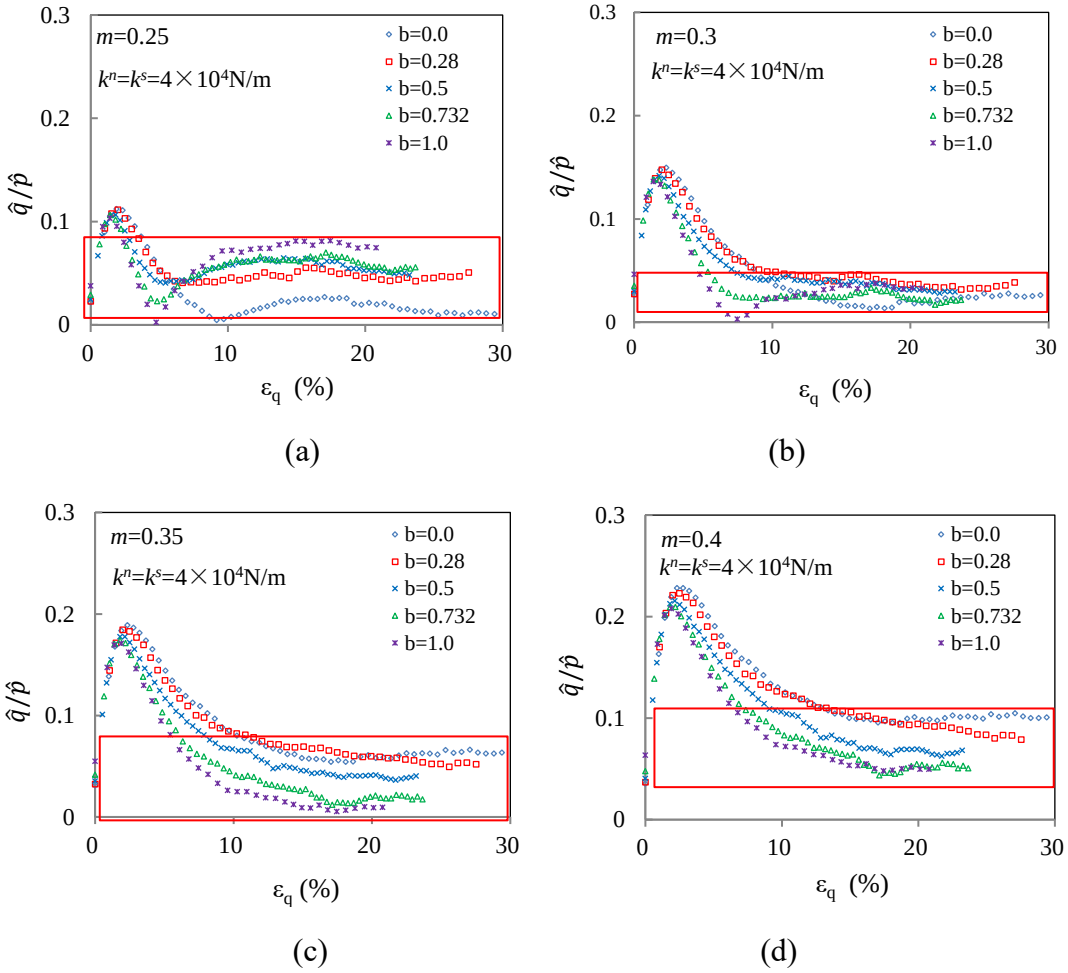

Figure 5-2: Evolution of $\hat{q}/\hat{p}$ with equivalent deviatoric strain at various values of m : k^n=k^s= 4×10^4 N/m, p=500kPa

As discussed previously, the principal components of the true stress tensor based on the fabric tensor of the strong sub-network are defined as $\sigma_{ij}^{s*} = \sigma_{ik}\left(\phi_{kj}^{s}\right)^{-1}$. When σ_{ij} and ϕ_{ij}^{s} are coaxial, the principal components of σ_{ij}^{s*} can be expressed as $\sigma_i^{s*} = \sigma_i (\phi_i^s)^{-1}$ (i is not in summation). Figure 5-3 and Figure 5-4 present the

variation of the true stress ratios q^*/p^* and q_s^*/p_s^* along different stress paths when k^n=k^s=1×10^6 N/m and k^n=k^s=4×10^4 N/m respectively. Comparing with the $q/p \sim \varepsilon_q$ curves in Figure 3-16 (b) and Figure 3-17 (b), the evolution of the deviatoric true stress ratios q^*/p^* with the deviatoric strain, as shown in Figure 5-3 (a) and Figure 5-4 (a) were very similar to that of q/p. For a given stress path, the values of q^*/p^* were smaller than q/p at the same deviatoric strain. The peak values of q^*/p^* were also lower than the peak q/p values of the same stress path. Moreover, ultimate values of q/p and q^*/p^* were stress paths dependent.

The variation of the true stress ratio q^{s*}/p^{s*} based on the fabric in the strong sub-network is plotted in Figure 5-3 (b) and Figure 5-4 (b). In general, the values of q^{s*}/p^{s*} were much smaller than q^*/p^* and q/p at the same deviatoric strain in tests with both high and low contact stiffness. At the critical state, regarding of the contact stiffness, the value of the true stress ratio q^{s*}/p^{s*} were very low (≤ 0.06). Therefore, one may assume $q^{s*}/p^{s*} \approx 0.0$, which yields the following relation between the principal components of stress and fabric tensors at the critical state:

$$\phi_1^s : \phi_2^s : \phi_3^s = \sigma_1 : \sigma_2 : \sigma_3 \tag{5-7}$$

The above relation can also be expressed as

$$\frac{q_\phi^s}{p_\phi^s} = \frac{q}{p}, \quad p_\phi^s = \frac{1}{3} \qquad \text{(3D)} \tag{5-8}$$

where q_ϕ^s, p_ϕ^s are the deviator and the mean of the fabric tensor for the strong sub-network. In general, Eqs. (5-7) and (5-8) hold true throughout the loading process can be used to describe the fabric evolution in the strong sub-network. It should be

noted that the Eq. (5-8) is identical to Eq. (4-28).

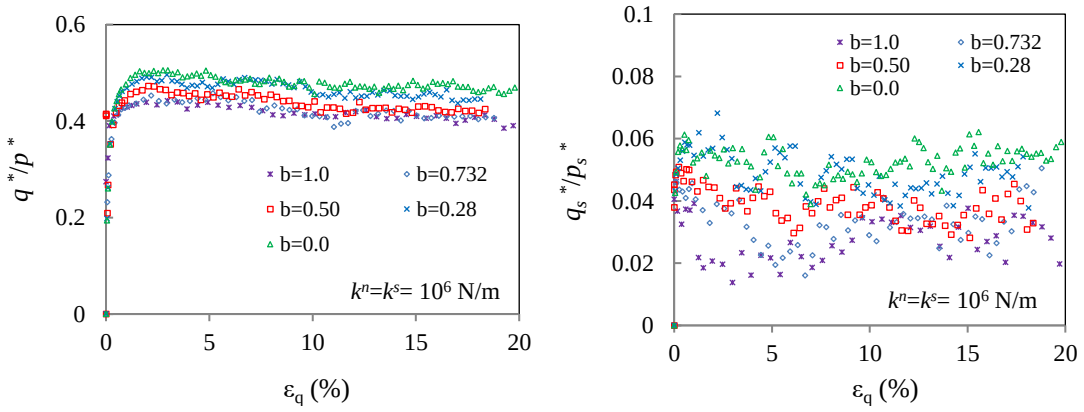

Figure 5-3: Evolution of true deviator stress ratio (a) q^*/p^* and (b) q^{s*}/p^{s*} with deviatoric strain: $k^n=k^s=1\times10^6$ N/m, p=500kPa

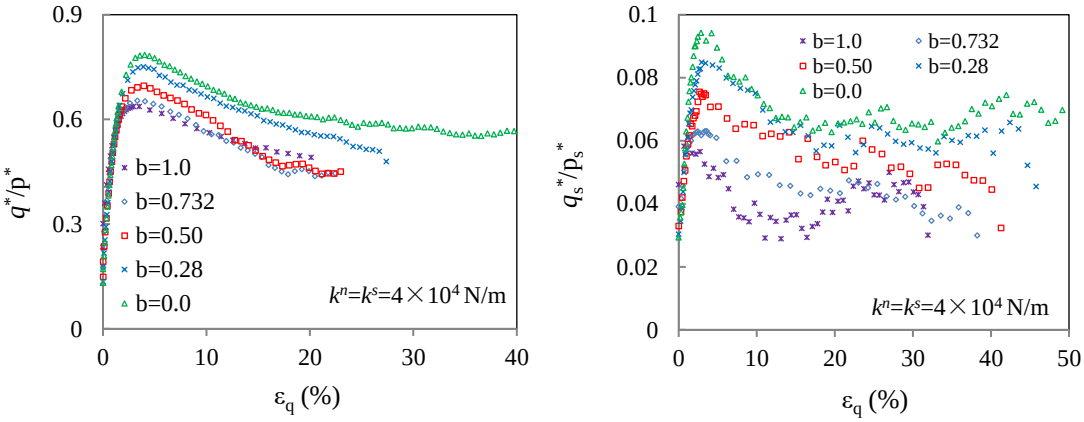

Figure 5-4: Evolution of true deviator stress ratio (a) q^*/p^* and (b) q^{s*}/p^{s*} with deviatoric strain: $k^n=k^s=4\times10^4$ N/m, p=500kPa

5.3 Limit stress surface at peak and critical states

This section discusses the stress surface in the Lode coordinate system at peak stress

state and the critical stress state. Figure 5-5 presents the Cauchy stress response envelopes at both the peak stress state and critical stress state at k^n=k^s=1×10^{6}N/m and p=500kPa. In general, the shape of the stress response surfaces is a rounded triangle on the π-plane, which can be reasonably expressed using the surfaces proposed by Lade and Duncan (1975) and Matsuoka and Nakai (1974) in the form of

$$\frac{I_1^3}{I_3} = \chi_{LD}, \qquad \frac{I_1 I_2}{I_3} = \chi_{MN} \tag{5-9}$$

where $I_1=\sigma_1+\sigma_2+\sigma_3$, $I_2=\sigma_1\sigma_2+\sigma_2\sigma_3+\sigma_3\sigma_1$ and $I_3=\sigma_1\sigma_2\sigma_3$ are the invariants of Cauchy stress (i.e., σ_{ij}), χ_{LD} and χ_{MN} are constants in the Lade-Duncan relation and the Matsuoka-Nakai relation, respectively. The agreement with the data set is excellent as shown in Figure 5-5 where the specific values of χ_{LD} and χ_{MN} used for the plots are $\chi_{LD}=31.5$ and $\chi_{MN}=10.11$ at the critical state and $\chi_{LD}=32.30$, $\chi_{MN}=10.15$ at the peak state for the specimen with contact stiffness k^n=k^s= 1×10^6 N/m and p=500kPa.

Eq. (5-5) was proposed as the failure criterions of granular material. For example, Davoudzadeh (1982) found that Lade surface could satisfactorily define the failure criterion of sand using experimental tests. The results from DEM simulation also had excellent agreements with Lade surface using spherical particles (Calvetti *et al.,* 2003; Thornton and Antony, 2000; Thornton and Zhang, 2010) and ellipsoids (Ng, 2001).

To examine the values of χ_{LD} and χ_{MN} at the peak states and the critical states, the variation of χ_{LD} and χ_{MN} with deviatoric strain during the deformation process is presented in Figure 5-6 under different conditions, which demonstrates that all data sets of different stress paths can be described by a unique curve, especially for the Lade's parameter. In general, either a Lade-Duncan relation or the Matsuoka-Nakai

relation can be used to reasonably describe Cauchy stress at the critical state.

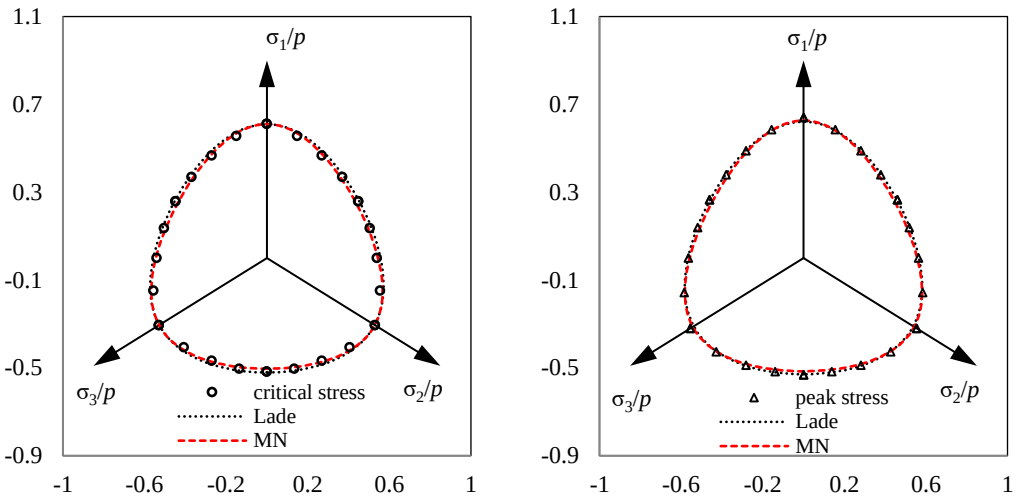

Figure 5-5: Stress envelops (a) at critical state and (b) at peak state: $k^n=k^s= 1\times10^6$ N/m and p=500kPa

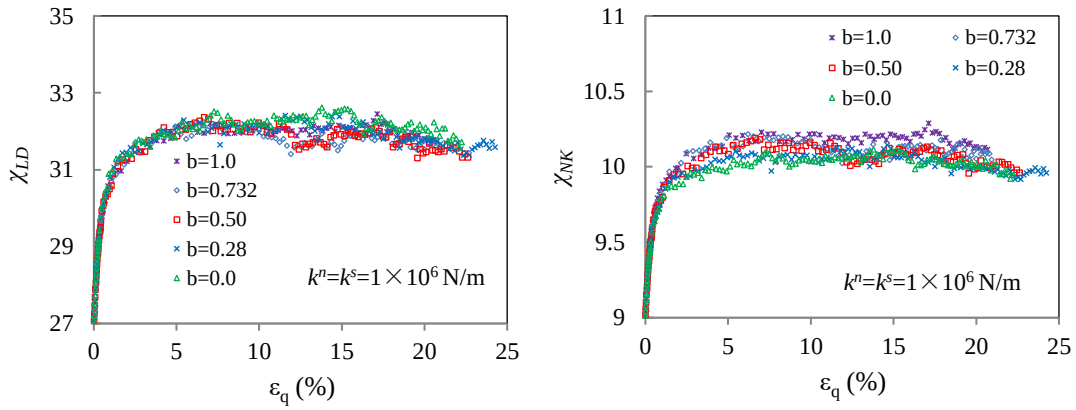

Figure 5-6: Evolution of the χ_{LD} and χ_{MN} for the Cauchy stress with shear strain under different stress paths: $k^n=k^s= 1\times10^6$ N/m and p=500kPa

The effect of the stress level and the contact stiffness on the stress surface at

critical state was also examined. Figure 5-7 presents the critical state stress surfaces on the π-plane at different mean effective stress levels when $k^n=k^s= 1\times10^6$ N/m and p=500 kPa to 1000 kPa. For the granular assembly and the adopted parameters of interaction between particles, the effect of the stress level on the critical stress surface can be neglected. Figure 5-8 compares the stress surfaces of the specimens with $k^n=k^s=1\times10^6$ N/m (dotted line) and $k^n=k^s=4\times10^4$ N/m (solid line) at the critical state. The fabric surface for the specimen with lower contact stiffness is slightly bigger than that with high contact stiffness at the critical state.

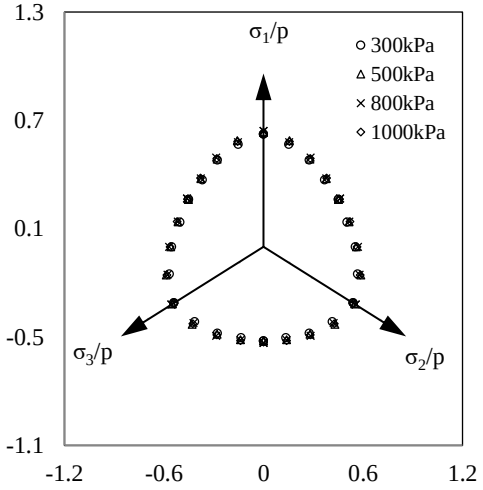

Figure 5-7: Influence of the mean stress level on the stress envelopes at critical state: $k^n=k^s=1\times10^6$ N/m

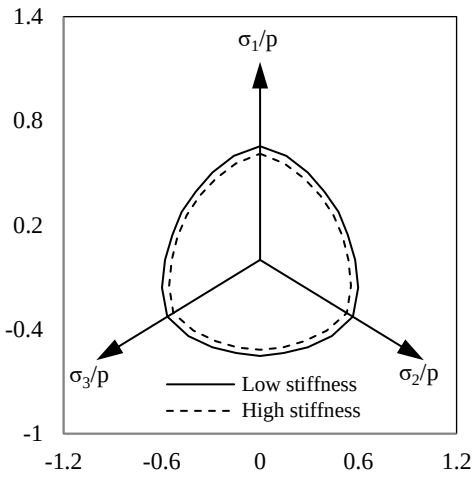

Figure 5-8: The stress envelopes at critical state for specimens with $k^n=k^s=1\times10^6$ N/m (dotted line) and $k^n=k^s=4\times10^4$ N/m (solid line)

Figure 5-9 presents the envelops of the true stress and the fabric stress at critical state, and the fittings using the Lade's surface and the Muskoka-Nakai's surface. It is recalled that the fabric stress is defined as $\sigma_{ij}^f = \phi_{ik}\sigma_{kj}$ in Chapter 4. The specific values of χ_{LD} and χ_{MN} were $\chi_{LD} = 28.8$, 37.5, $\chi_{MN} = 11.21$, 9.43 for the envelopes of σ_{ij}^* and σ_{ij}^f at the peak and critical states, respectively. The variation of χ_{LD} and χ_{MN} for the true stress and the fabric stress can be found in Figure 5-10 and Figure 5-11, respectively. In general, either a Lade-Duncan relation or the Matsuoka-Nakai relation can be used to describe the stress surface at the critical state.

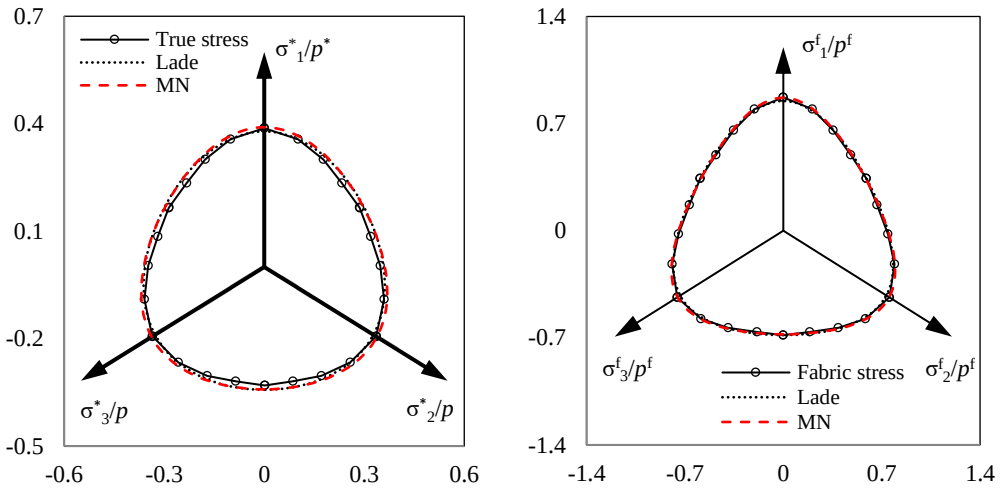

(a) (b)

Figure 5-9: Best fittings of (a) true stress envelops and (b) fabric surface at critical states using the Lade' surface and Matsuoka-Nakai's surface: k^n=k^s= 1×10^6 N/m and p=500kPa

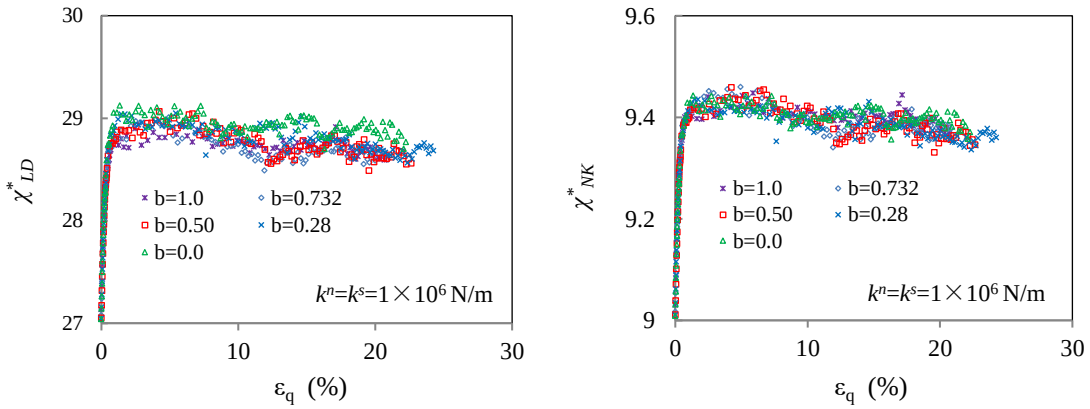

(a) (b)

Figure 5-10: Evolution of (a) χ^*_{LD} and (b) χ^*_{MN} of the true stresses with deviatoric strain: k^n=k^s= 1×10^6 N/m and p=500kPa

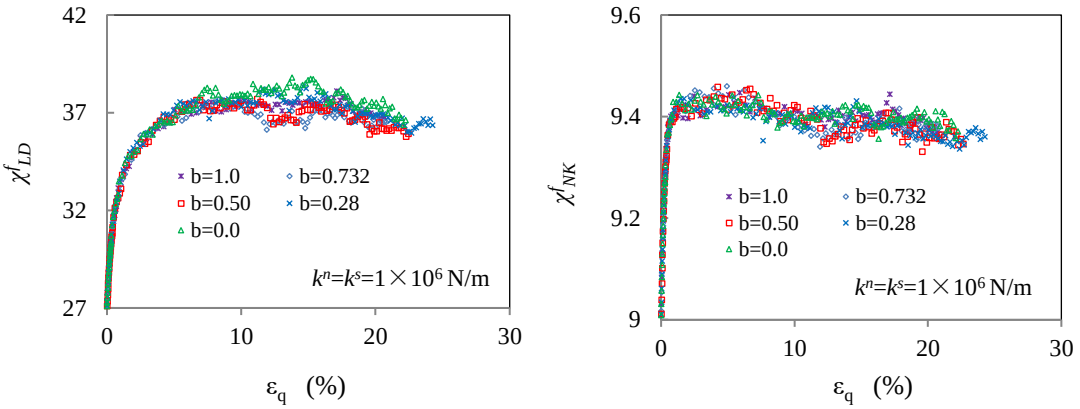

(a) (b)

Figure 5-11: Evolution of (a) χ^f_{LD} and (b) χ^f_{MN} of the fabric stresses with deviatoric strain: k^n=k^s= 1×10^6 N/m and p=500kPa

5.4 Limit fabric surface at critical states

In addition the evolution of fabric, it is equally important to evaluate the ultimate fabric at the critical deformation state. Similar to the stress envelop on the π-plane at critical state, the fabric states can also be defined as a surface using the Lode coordinates $r = \sqrt{2/3}q_\phi$ and $\bar{\theta}_\phi = -\frac{1}{3}\sin^{-1}\left(\frac{3\sqrt{3}J_{3\phi}}{2(J_{2\phi})^{3/2}}\right)$. Herein, $J_{2\phi}$ and $J_{3\phi}$ are the second and the third invariants of the deviatoric fabric tensor ($\phi_{ij} - \frac{1}{3}\delta_{ij}$), respectively. At critical stress state, the fabric surface for the overall contact network is plotted in Figure 5-12 (a), in which the surface took the shape of 'inverted' Lade's surface. For comparison purposes, Figure 5-12 (b) compares the 'inverted' Lade's surface for the fabric at critical state with other stress surfaces. It is observed that the critical state fabric surface was relatively smaller than any stress surfaces. According to Thornton and Zhang (2010), the 'inverted' Lade's surface for critical fabric state can be expressed as

$$\frac{I_{1\phi}^3}{2I_{1\phi}I_{2\phi}-3I_{3\phi}}=\eta^* \tag{5-10}$$

where η^* is a constant, $I_{1\phi}=\phi_1+\phi_2+\phi_3=1$, $I_{2\phi}=\phi_1\phi_2+\phi_1\phi_3+\phi_2\phi_3$ and $I_{3\phi}=\phi_1\phi_2\phi_3$ are the three invariants of the fabric tensor. Thornton and Zhang (2010) suggested $\eta^*=1.806$ for a dense polydisperse system of elastic spheres with the size ranging from 0.25mm to 0.33mm and inter-particle friction coefficient μ=0.5. Zhao and Guo (2013) found that the values of η^* at the critical state varied in a small range of $\eta^*=1.810\pm0.001$, marginally affected by the mean stress and the intermediate stress parameter b. Barreto and O'Sullivan (2012) showed that η^* at the peak stress state tended to increase with inter-particle friction coefficient μ following $\eta^*=(5.48/3)\mu^{0.0034}$.

The DEM simulation results obtained in this research showed that a modified expression of Eq. (5-10) in the following form

$$\frac{I_{1\phi}^3}{a^*I_{1\phi}I_{2\phi}-b^*I_{3\phi}}=\eta^* \tag{5-11}$$

can better describe the critical state fabric surface. In Eq. (5-11), a^*, b^* and η^* are constants. A regression analyses revealed that $b^*/a^*=1\sim1.5$. When a^*=2, b^*=3 and $a^*=b^*$=2, Eq. (5-11) had excellent agreement with the results of DEM simulations as shown in Figure 5-13. Moreover, the variation of η^* during deformation with the deviatoric strain could be described by a unique curve, which is independent of the stress paths with different intermediate stress coefficients. At critical states, when a^* =2, b^*=3 , the values of η^* varies in the range of $\eta_{cr}^*=1.809\pm0.001$, which is consistent with the findings by Zhao and Guo (2013). However, the results of DEM

simulation were also reproduced by $a^*=b^*=2$ with $\eta^*_{cr}=1.698\pm0.001$ for the critical state fabric surface. The evolution of the η^* with deviatoric strain presented in Figure 5-13 also implied that the fabric at the peak stress state may also be described by Eq. (5-11) with η^*_p which was slightly larger than η^*_{cr}.

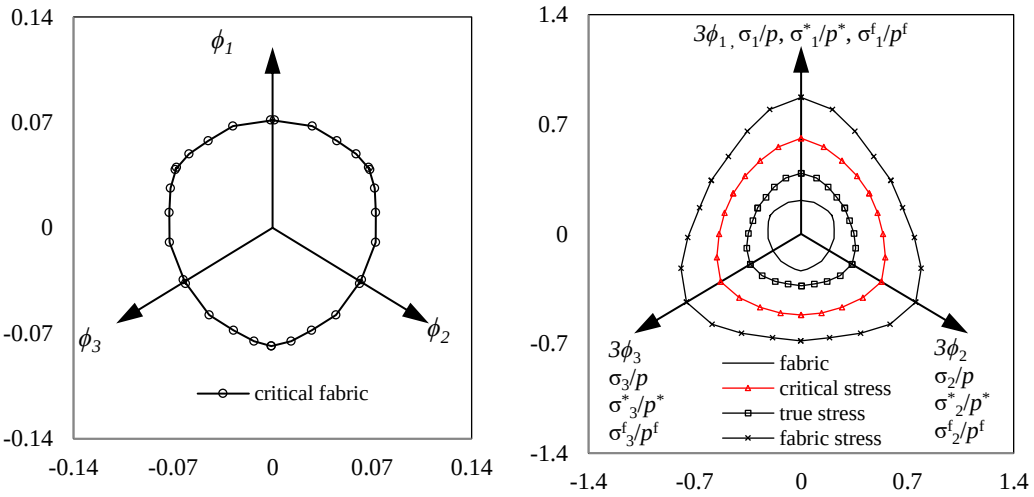

(a) (b)

Figure 5-12: (a) The fabric surface of the overall contact network at critical state and (b) comparison of critical fabric surface with different critical state stress: $k^n=k^s=1\times10^6$ N/m and p=500kPa,

Recalling Eq. (5-8), the principal component of the fabric tensor in the strong sub-network is proportional to principal stresses, $\phi^s_1:\phi^s_2:\phi^s_3=\sigma_1:\sigma_2:\sigma_3$, which indicated that the shape of the critical fabric surface for the strong sub-network has the same shape of the critical stress surface. As shown in Figure 5-14, the critical fabric surface for the strong sub-network is a rounded edge triangle that can be described using the Lade's surface. Recalling the findings in Chapter 4, the fabric anisotropy for the weak sub-network is much smaller than that of the strong and the overall contact

networks at critical state since the weak sub-network was nearly isotropic. As shown in Figure 5-14, the size of the fabric surface of the strong sub-network was bigger than that of the fabric surface of the weak sub-network, which is consistent with the findings in Chapter 4.

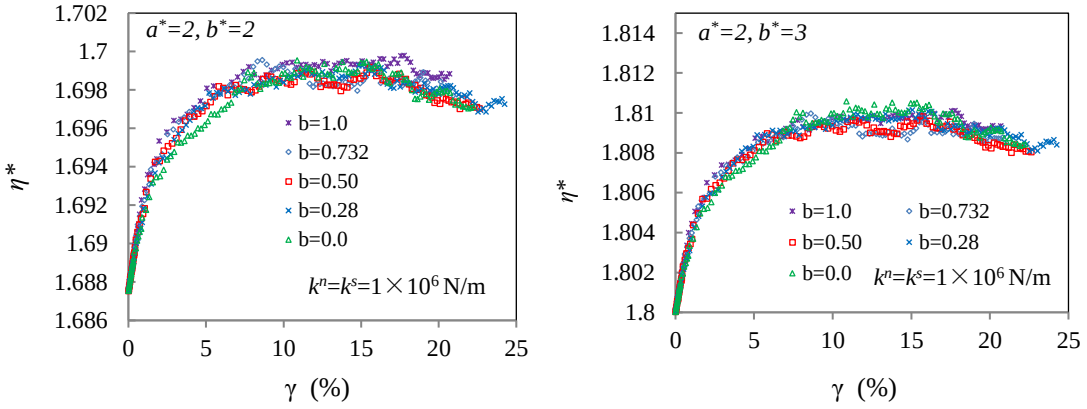

(a) (b)

Figure 5-13: Variation of η^* of surfaces against deviatoric strain when (a) $a^*=b^*=2$ and (b) $a^*=2$, $b^*=3$: $k^n=k^s=1\times10^6$ N/m and p=500kPa

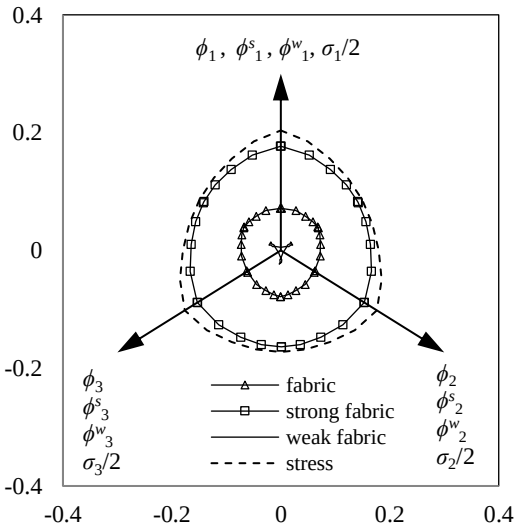

Figure 5-14: Fabric surfaces of different contact networks at critical state: $k^n=k^s=1\times10^6$ N/m and p=500kPa

5.5 Summary

A series of DEM simulations under general 3D stress conditions were carried out along different stress paths to investigate the state of fabric in different contact networks at the critical states. Base on the analyses of DEM simulation results, the following conclusions can be withdrawn:

(1) The stress-fabric relation for the overall contact network at critical state can be described using $\phi_1 : \phi_2 : \phi_3 = (\sigma_1)^m : (\sigma_2)^m : (\sigma_3)^m$ with m varying in the range of 0.4 ~ 0.3.

(2) For the strong contact sub-network, the evolution of its fabric components can be expressed as $\phi_1^s : \phi_2^s : \phi_3^s = \sigma_1 : \sigma_2 : \sigma_3$, which is applicable to the whole deformation process.

(3) The Cauchy stress envelopes at both the critical states and peak states can be described by the Lade's surface and the Matsuoka-Nakai's surface. The specific values of χ_{LD} and χ_{MN} used for the plots are $\chi_{LD} = 31.5$ and $\chi_{MN} = 10.11$, respectively. The surfaces of the true stresses and fabric stresses based on the fabric for the overall contact network also fit equations of the Lade's and Matsuoka-Nakai's surfaces satisfactorily.

(4) On the π-plane, the fabric envelopes for the overall contact network takes the shape of an inverted Lade's surface in the form of Eq. (5-11), in which η^* is approximately $\eta_{cr}^* = 1.809 \pm 0.001$ at the critical state when $a^* = 2.0$, $b^* = 3.0$ alternatively $\eta_{cr}^* = 1.698 \pm 0.001$ when $a^* = 2.0$ and $b^* = 2.0$.

(5) On the π-plane, the fabric envelope for the strong sub-network at critical state has the same shape as the Lade's surface.

Chapter 6 Coaxiality between Fabric and Stress

6.1 Introduction

In geotechnical engineering, the non-coaxiality refers to the principal axis of stress does not generally coincide with that of incremental strain, especially when the principal axis of stress rotates, for example in simple shear tests (Roscoe, 1970; Roscoe *et al.*, 1967). Experimental results showed that the initial anisotropy had a considerable effect on the degree of non-coaxiality during the rotation of principal stress orientation (Cai *et al.*, 2013; Miura *et al.*, 1986). Since the stress and deformation are originated from contact interaction and relative displacement on the microscopic scale, the non-coaxiality is inevitably related to the internal structure at the particle scale. The principal orientation of the fabric tensor is essential to understand the physical matter of the non-coaxiality between the direction of the principal stress and that of the strain increment.

Matsuoka *et al.* (1988) observed that the principal direction of fabric anisotropy rotates with rotation of the maximum shear stress during simple shear tests using initially isotropic assemblies of photo-elastic rods. Ai *et al.* (2014) observed that the orientation of the principal fabric for the overall contact network generally resembles that of the principal stress independent of the initial anisotropy. But they did not consider the fabric anisotropies for the sub-networks. Actually, not all contacts play the same role during the deformation of a granular assembly. According to Radjaï *et al.* (1998), the shear resistance is largely determined by the contribution of the strong force network. In Chapter 4, the mobilized shear stress ratio is proportional to the degree of fabric anisotropy of the strong sub-network in both 2D and 3D cases. Therefore, it is reasonable to assume that the principal direction of fabric for the strong sub-network might be coaxial with that of the principal stress.

The micromechanical analysis for the principal orientation of fabric yields to the stress-force-fabric relation. For a two-dimensional assembly of circular disks, the principal direction of fabric for the overall contact network is coaxial with principal direction of the stress according to the assumption made by Rothenburg and Selvadurai (1981) that the contact normal distribution is independent of those of contact forces. A similar conclusion was arrived by Hosseininia (2015) for randomly settled assemblies of circular or elongated particles. It is noted that the orientation of the principal stress did not rotate and the fabric anisotropy was computed for the overall contact network in their research.

Motivated by the observations above, this chapter attempts to investigate the non-coaxiality between the principal direction of stress tensor and that of the fabric tensor. A series of two-dimensional DEM simulations were conducted to investigate the stress-strain responses of granular materials including biaxial tests and simple shear tests. The internal structures of specimens were characterized by different particle contact networks, i.e., the strong-, weak- and overall contact networks. The non-coaxiality between stress and fabric tensors for different contact networks was determined from micromechanical analyses that yields the stress-force-fabric relation. The results showed that the orientation of stress tensor is always coaxial with that of the fabric tensor for strong sub-network instead of the fabric tensor for the overall contact network. The principal direction of the weak sub-network was always perpendicular to that of the strong sub-network except for tests with zero confining pressures, but not necessarily orthogonal to that of the overall contact network. The fabric anisotropy for the overall contact network could be interpreted as a combination of sub-network anisotropy weighted by the ratio of contact number in each sub-network over the total number of contacts.

6.2 Principal directions of the stress and fabric tensors

For a 2D granular assembly, the orientation of the stress tensor is quantified by the inclination angle of major principal stress with respect to the *x*-axis, as shown in Figure 6-1. Using a Mohr's circle, θ_σ can be determined as

$$\tan 2\theta_\sigma = \frac{2\sigma_{12}}{\sigma_{11} - \sigma_{22}} \tag{6-1}$$

According to this definition, θ_σ ranges within $\left[0^o, 180^o\right]$. Recalling Section 4.2, the stress components were explicitly derived from a microscopic scale, see Eq. (4-22) (a-c). Therefore, θ_σ can be expressed in term of the measures for the distribution of contact forces and contact normals as

$$\tan 2\theta_\sigma = \frac{a_c \sin 2\theta_c + a_n \sin 2\theta_n + a_t \sin 2\theta_t + a_n a_t (\sin 2\theta_t - \cos 2\theta_t)}{a_c \cos 2\theta_c + a_n \cos 2\theta_n + a_t \cos 2\theta_t} \tag{6-2}$$

By assuming that $\theta_c \approx \theta_n \approx \theta_t$ (Rothenburg and Bathurst, 1989), $\tan 2\theta_\sigma$ can be simplified as

$$\tan 2\theta_\sigma = \left(1 + \frac{a_n a_t}{a_c + a_n + a_t}\right) \tan 2\theta_c - \frac{a_n a_t}{a_c + a_n + a_t} \tag{6-3}$$

Given that a_n, a_t cannot be zero during a shearing process, $\theta_\sigma = \theta_c$ is possible only when $\theta_\sigma = \theta_c = \pi/2$, which implies that σ_1 is applied in the direction of the major principal fabric component.

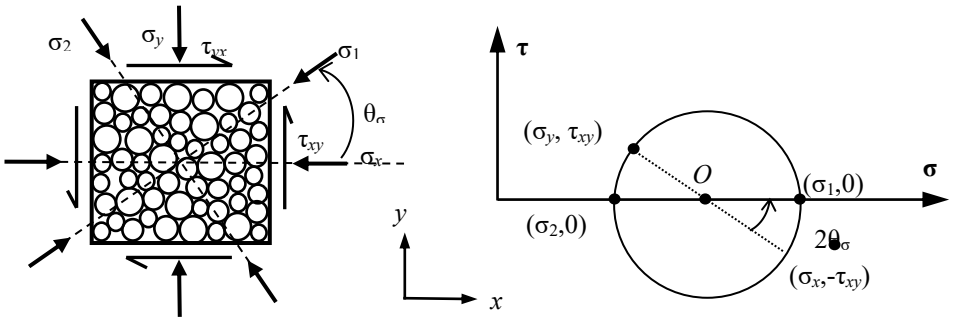

(a) (b)

Figure 6-1 (a) Sketches of principal stresses' orientations and (b) interpretation of the θ_σ in the Mohr's stress circle

Similar to the stress tensor in a two-dimensional case, the state of fabric can also be interpreted using the "Mohr's Circle" shown in Figure 6-2 (a) with the center and radius being $\frac{\phi_{xx}+\phi_{yy}}{2}$ and $\sqrt{(\frac{\phi_{xx}-\phi_{yy}}{2})^2+\phi_{xy}^2}$ respectively. The principal components of the fabric tensor are given as

$$\phi_{1,2}=\frac{\phi_{xx}+\phi_{yy}}{2}\pm\sqrt{(\frac{\phi_{xx}-\phi_{yy}}{2})^2+\phi_{xy}^2} \tag{6-4}$$

with the major principal direction being

$$\tan 2\theta_c=\frac{2\phi_{xy}}{\phi_{xx}-\phi_{yy}} \tag{6-5}$$

where θ_c designates the angle that defines the direction of the major principal component of fabric tensor, as shown in Figure 6-2 (a).

In the following sections, the evolution of fabric anisotropy and its orientation for different contact networks are investigated through 2D DEM simulations with fixed and rotation of the principal stress direction.

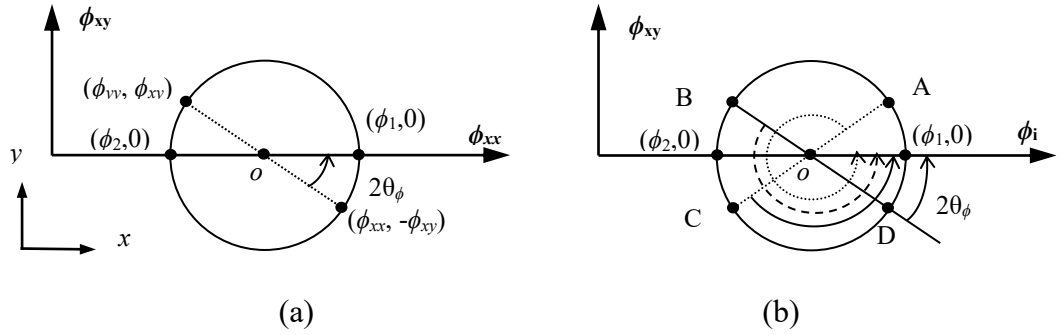

Figure 6-2: (a) Sketches of the transformation of fabric tensor; and (b) Definition of orientation of the major principal component of fabric tensor

6.3 Results from 2D tests along proportional strain paths

The degree of fabric anisotropy

Along different strain paths, the evolution of fabric anisotropy for the overall contact network, the strong and weak sub-networks with deviatoric strain was discussed in Section 4.3 corresponding to the VED, VEI and VEC tests. In this section, two types of loading paths were considered: highly dilatant path (e.g. $\Re = 0.5$) and contract strain path (e.g. $\Re = 10$). As shown in Figure 6-3, the evolution of q_ϕ for the overall contact network was affected significantly by the strain paths. The fabric deviator q_ϕ initially increased to its peak value with the increase of shear strain and then evolved individually without achieving a unique ultimate value as shearing continues. Both the peak value and ultimate value of q_ϕ were affected by the value of $\Re$ for each strain path. The peak value of q_ϕ decreases as the value of $\Re$ increases, with $q_{\phi,peak} = 0.125$ for the highly dilatant strain path at $\Re = 0.5$ and $q_{\phi,peak} = 0.047$ for the highly forced contraction strain path at $\Re = 10$. After the peak, two interesting phenomena were observed in Figure 6-3 (a). One is the sudden increase of fabric anisotropy in highly dilatant strain path test (i.e. $\Re = 0.5$), in

which catastrophic failure of the internal structure occurs when the shear resistance became zero due to diminishing constraint in the lateral direction at A, as shown in Figure 6-3 (b). The other is instantaneous isotropic fabric structure at D in tests along forced contraction strain paths. More specifically, as shown in Figure 6-3 (a), in the test along a highly forced contraction strain path with $\Re = 10$, after $q_{\phi,\max}$ point C, continuous shearing induced decrease of q_ϕ which became zero instantaneously at D. Since the stress path evolved blow the failure line on the t-s plane in Figure 6-3 (a), this decline of q_ϕ did not correspond to degradation or collapse of the overall contact network. But it indicates a significant change in the microstructure. With continuously shearing, regaining of the fabric anisotropy was observed after the decline of q_ϕ. The same phenomenon was observed in the test along forced constraction strain path corresponding to $\Re = 2$.

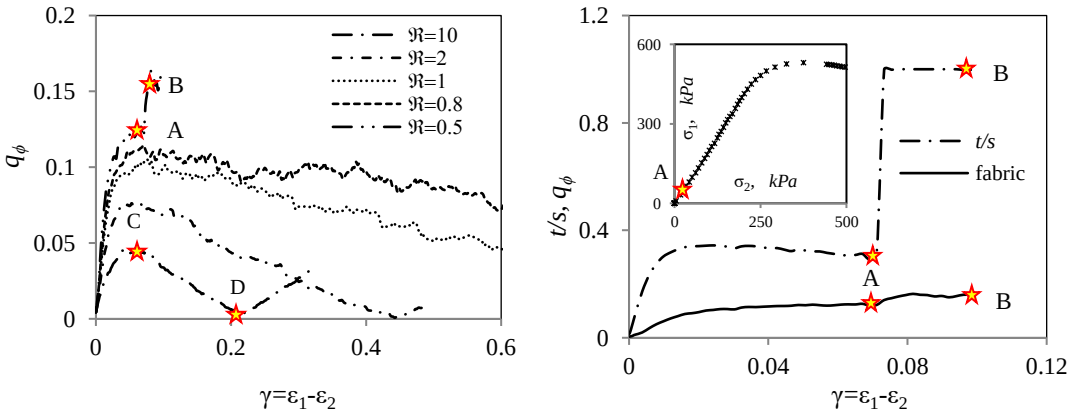

Figure 6-3: (a) Effect of strain paths on the evolution of fabric anisotropy for overall contact and (b) the fabric anisotropy before and after the catastrophic failure along strain path $\Re = 0.5$

In order to interpret these two phenomena microscopically, the evolution of the

fabric anisotropy for different contact networks were examined for tests along highly contractant strain path with $\Re = 10$ and highly dilatant strain path with $\Re = 0.5$. Figure 6-4 presents the evolution of fabric anisotropy in different contact networks in tests along those two paths. The polar diagram of contact normal distributions was plotted at selected deformation stages. As shown in Figure 6-4 (a), both overall contact network and sub-networks develop notable geometric anisotropy (q_ϕ, q_ϕ^s and q_ϕ^w), which initially increased with the shear strain. The peak value of q_ϕ (at C) accurred earlier than that of q_ϕ^s but later than that of q_ϕ^w. After the peaks q_ϕ^w experienced a short period of near constant value followed by a monotonic increase until the strain level corresponding to E where both q_ϕ^s and q_ϕ^w were almost equal. After the strain level at C, q_ϕ^s approached its peak value and then gradually decreased to an ultimate value with the increase of shear strain. The orientations of the principal fabric in strong and weak sub-networks were aligned in the vertical and horizontal directions, respectively. From C to D, the value of q_ϕ^w continuously increased while q_ϕ^s was almost constant, which in turn resulted in a decrease of the fabric anisotropy in the overall contact network. After the strain level at D where the overall contact network was instantaneously isotropic, q_ϕ^w continuously increased with q_ϕ^s decreasing with the shear strain, which resulted in an increase of q_ϕ and the orientation of principal fabric in the overall contact network rotates from the vertical to the horizontal.

For the test along highly dilatant strain path with $\Re = 0.5$, a significant post-peak decrease of q_ϕ^w took place, as shown in Figure 6-4 (b). The weak sub-network became nearly isotropic at A. Thereafter, the weak sub-network regained anisotropy quickly. The evolution of q_ϕ^s had the same trend as that of q_ϕ^w, but with less post-peak degradation and larger shear strain to mobilize the peak value of q_ϕ^s. The anisotropy of the overall contact network, however, increased monotonically with shear strain. It should be noted that both σ_1 and σ_2 were close to zero at A, as presented in Figure 6-3 (b). The principal fabric orientations for the overall contact network and the strong sub-network were in the vertical direction throughout the loading procedure. However, before and after A, the orientation of the principal fabric for the weak sub-network rotated from the horizontal direction to the vertical direction, as illustrated by the polar plots in Figure 6-4 (b). Microscopically, almost no contact could be stable in the horizontal direction due to the high extension rate after A. Therefore, most of the strong contacts and weak contacts were aligned with the vertical axis. The rearrangement of the contact sub-networks might cause the orientation of the major principal fabric component to rotate in either the overall contact network or the sub-networks. This will be further discussed later.

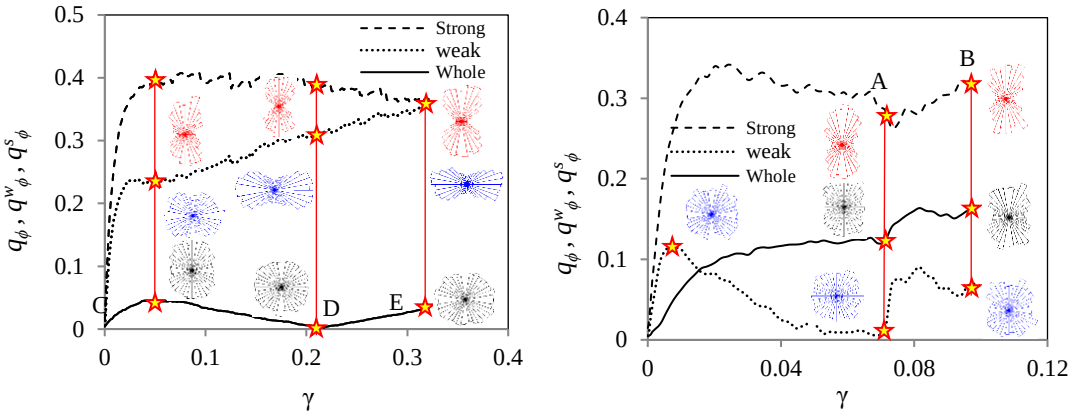

Figure 6-4: Evolution of fabric anisotropy with shear strain in different contact networks in tests along strain paths (a) $\Re = 10$ and (b) $\Re = 0.5$

The evolution of fabric anisotropy for the strong and weak sub-networks with shear strain is demonstrated in Figure 6-5. By comparing Figure 6-5 (a) with Figure 6-3 (a), one observed that $q^s_{\phi,\max}$ was much larger than that of the overall contact network. Along forced contraction strain paths ($\Re > 1$), the strong sub-network developed relatively higher geometric anisotropy than those along forced dilatant strain paths ($0 < \Re < 1$); see Figure 6-5 (a). This is also true for the weak force-chain networks, as shown by the evolution of q^w_ϕ with shear strain in Figure 6-5 (b). Generally, the trend of evolution of q^s_ϕ along different strain paths was mostly similar for different strain paths. Referring to biaxial tests along strain paths at $0 < \Re \le 1$ in Chapter 4, the evolution of q^s_ϕ could be related to the stress ratio t/s via $q^s_\phi = \kappa(t/s)$ with $\kappa \approx 1$, as shown in the inset of Figure 6-5 (a). However, the trend of the evolution of q^w_ϕ depended on the loading paths, as shown in Figure 6-5 (b). After an initial buildup, the value of q^w_ϕ approached a peak value that was followed by a decrease, then an increase again with the shear strain. The post-peak

reduction of q_ϕ^w varied with the strain paths. The lower the $\Re$ value, the more reduction of q_ϕ^w. In other words, a significant post-peak decrease of q_ϕ^w took place in tests along highly forced dilatant strain paths.

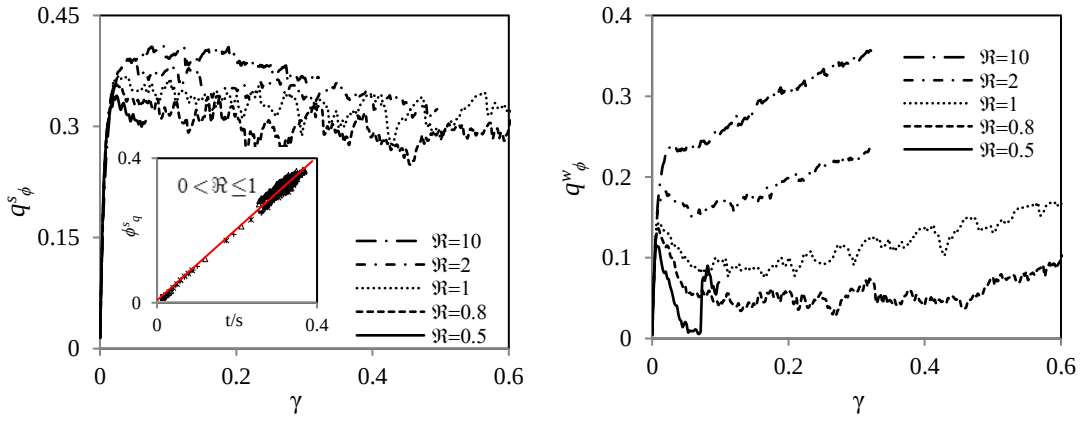

(a) (b)

Figure 6-5: Evolution of fabric anisotropy within strong sub-network (a), and weak sub-network (b) with shear strain

The major principal direction of fabric tensors

We next examine the major principal direction of fabric tensors for different contact networks as well as the principal directions of stress and strain increments. Figure 6-6 presents the evolution of the orientations of major principal stress and strain rate with the equivalent shear strain, in the test with $\Re = 1$ where $\theta_{d\varepsilon}$ is calculated using Eq. (3-17). Here, θ_σ and $\theta_{d\varepsilon}$ are the inclination angle of the major principal direction of σ_{ij} in terms of the tractions on the boundaries of the specimen and $\dot{\varepsilon}_{ij}$ with respect to the x-axis in the horizontal direction. As expected, for all strain paths investigated, the orientations of major principal strain increment, $\theta_{d\varepsilon}$, and major principal stress,

θ_σ, remained in the vertical direction, corresponding to $\theta_{d\varepsilon}=90°$ and $\theta_\sigma=90°$ once the deformation begins, as shown in Figure 6-6. The dotted line shows the orientation ($\overline{\theta}_\sigma$) of the major principal stress calculated from inter-particle contact forces and branch vectors. At small shear strain level (lower than 0.25%), $\overline{\theta}_\sigma$ initially started from $\overline{\theta}_\sigma=135°$ and rotated to the vertical direction of $\overline{\theta}_\sigma=90°$. The temporary non-coaxiality between σ_1 and $\dot{\varepsilon}_1$ reflected the influence of internal structure, which was not ideally isotropic initially. However, this deviation only exists at very low strain level and is negligible.

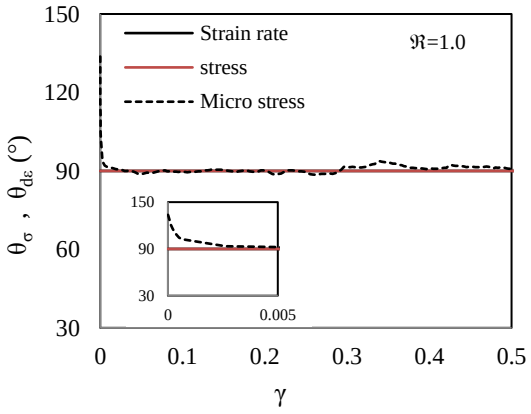

Figure 6-6: Evolution of orientations of the major principal stress and strain increment

For tests along forced dilatant strain paths with $0<\Re\leq 1$, the variations of major principal fabric orientations in different contact networks relative to the major principal stress direction, i.e., $(\theta_\sigma-\theta_c)$, $(\theta_\sigma-\theta_c^s)$ and $(\theta_\sigma-\theta_c^w)$, are plotted in Figure 6-7. Here, θ_σ is computed based on the inter-particle contact forces and contact normal direction. The maximum difference between θ_σ and θ_c was

approximately $8°$ at the beginning of loading but it decreased to $4°$ when $\gamma > 0.2\%$, as shown in Figure 6-7 (a). However, the fabric tensor for strong sub-network was practically coaxial with the stress tensor σ_{ij} and $|\theta_\sigma - \theta_c^s|_{\max} \approx 1.5°$ for different strain paths with $0 < \Re \leq 1$, as shown in Figure 6-7 (a). The major principal orientation of the stress tensor was always perpendicular to that of the fabric tensor for the weak sub-network, i.e., $|\theta_\sigma - \theta_c^w| = 90°$, as shown in Figure 6-7 (c). For the high dilatant strain path test, $(\theta_\sigma - \theta_c^w)$ became zero after A (see both Figure 6-7 and Figure 6-3). This is because most contacts were in the vertical direction at A with almost no confinement for contacts due to high dilatant rate in the horizontal direction. These results confirmed that the strong sub-network was coaxial with the stress tensor, while the weak sub-network was perpendicular to the strong sub-network or the major principal stress direction. This conclusion agrees with the directional distribution of contact normal in different networks presented in Figure 6-4.

For tests along the highly forced contraction strain paths with $\Re \geq 10$, the variations of $(\theta_\sigma - \theta_c)$, $(\theta_\sigma - \theta_c^s)$ and $(\theta_\sigma - \theta_c^w)$ with shear strain are presented in Figure 6-8. When $\gamma < 0.1$, the major principal orientation of fabric tensor ϕ_{ij} for the overall contact network was aligned with the orientation of the major principal stress. With an increase of the equivalent shear strain, the major principal orientation of ϕ_{ij} gradually rotated from the vertical direction to the horizontal axis. At D, the overall contact network became isotropic instantaneously (see Figure 6-4 a). Thereafter, the major principal direction of ϕ_{ij} was perpendicular to major principal stress direction. However, the major principal direction of fabric for the strong sub-network was coaxial with the direction of the major principal stress, as shown in Figure 6-8 (b). Similar to tests along dilatant strain paths, the direction of the major principal fabric

for weak sub-network was always perpendicular to the major principal direction of stress in tests along forced contraction strain paths; as shown in Figure 6-8 (c).

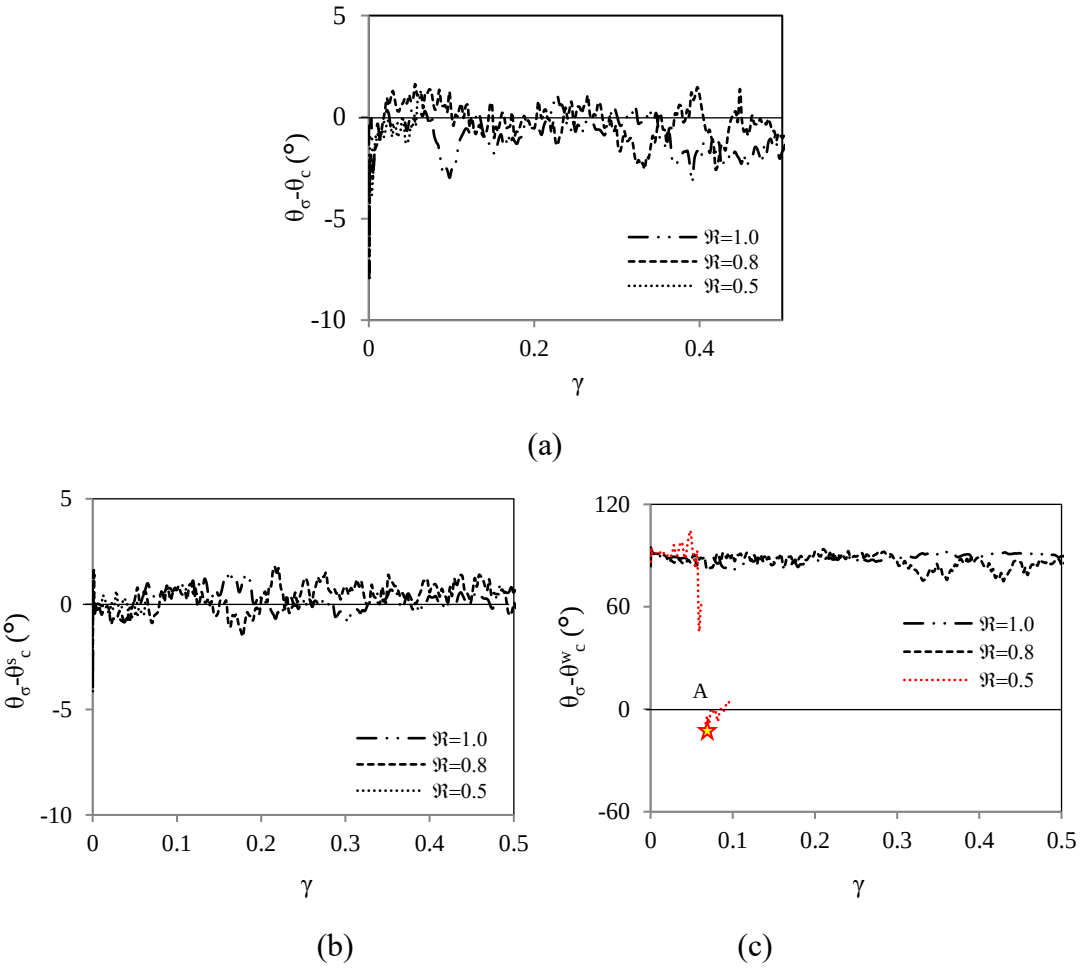

Figure 6-7: The non-coaxiality between the stress tensor and fabric tensor for the overall contact network (a), the strong sub-network (b) and the weak sub-network(c) in tests along strain paths $0 < \Re < 1$

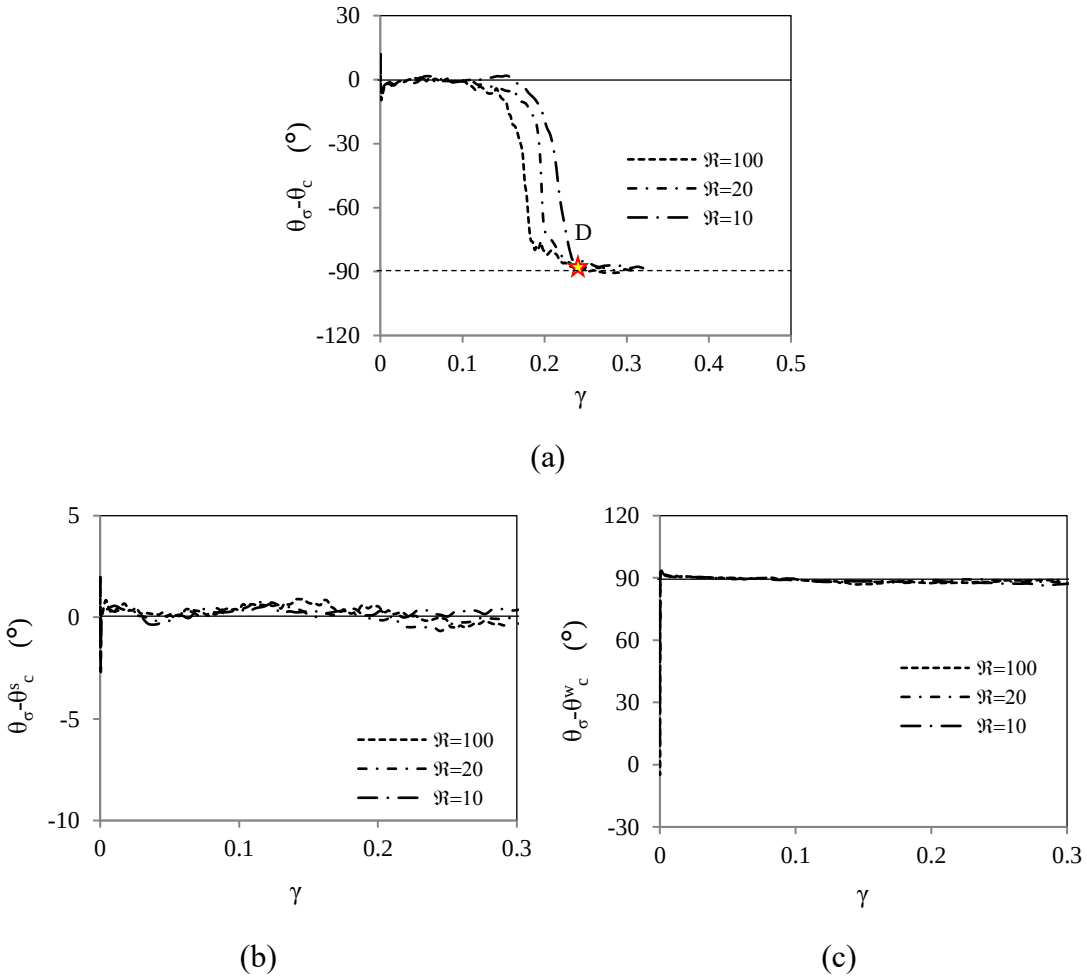

Figure 6-8: Differences between directions of stress tensor and fabric tensor for (a) the overall contact network, (b) the strong sub-network and (c) the weak sub-network along strain paths $\Re \geq 10$

The above analyses for the results of DEM simulations on biaxial tests along proportional strain paths showed that the evolution of fabric in different contact networks highly depended on the imposed strain paths and the corresponding stress states. In general, the major principal stress direction was always coaxial with the direction of the major component of fabric tensor for the strong sub-network even in highly contracted and dilatant tests. The orientations of the major principal component of fabric tensors in the strong and weak sub-networks were generally orthogonal to

each other, with the only exception in the test along strain path with $\Re = 0.5$ when the internal structure of the specimen collapsed and the stress components all approached zero. However, the major principal direction of fabric tensor for the overall contact network might be perpendicular or parallel to the major principal stress direction, depending on the applied strain paths.

The probability density function of contact normal distribution in the sub-networks can be written into second-order approximations as $E^{\dagger}(\theta) = \frac{1}{2\pi}\left[1 + a_c^{\dagger}\cos 2(\theta - \theta_c^{\dagger})\right]$ with † = "s" or "w" representing the strong sub-network or the weak sub-network, respectively. By defining $\alpha = N_c^s / N_c$, the fabric anisotropy within the overall contact network can be expressed in terms of that in sub-networks as

$$a_c \cos 2\theta_c = \alpha a_c^s \cos 2\theta_c^s + (1-\alpha) a_c^w \cos 2\theta_c^w \tag{6-6}$$

where ($\theta_c, \theta_c^s, \theta_c^w$) and ($a_c, a_c^s, a_c^w$) are the direction and degree of fabric anisotropy for the whole, the strong and the weak sub-networks respectively. Herein, the ratio α evolves during deformation. By applying $|\theta_c^s - \theta_c^w| = 90°$ and $a_c = 2q_\phi$, Eq. (6-6) can be alternatively written as

$$q_\phi \cos 2\theta_c = \left[\alpha q_\phi^s - (1-\alpha) q_\phi^w\right] \cos 2\theta_c^s \tag{6-7}$$

The relation reveals that q_ϕ and θ_c for the overall contact network depends on the directions and degrees of anisotropy in the sub-networks as well as the normalized contact number $\alpha = N_c^s / N_c$. Herein, θ_c is not necessarily identical to θ_c^s; as shown in Figure 6-8 (a) for tests along highly contracted strain paths. For most cases, $\theta_c \approx \theta_c^s$, Eq. (6-7) can be approximately expressed as

$$q_\phi = \alpha q_\phi^s - (1-\alpha) q_\phi^w \tag{6-8}$$

Eq. (6-8) is applicable to tests along dilatant strain paths when the stress paths on the *s-t* plane approach both the peak and critical state lines, as shown in Figure 6-9.

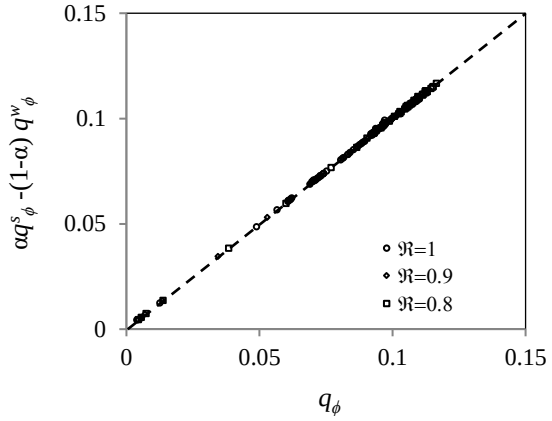

Figure 6-9: Correspondence between q_ϕ and $\alpha q_\phi^s - (1-\alpha) q_\phi^w$ in biaxial tests along proportional strain paths with $0.8 \le \Re \le 1$

6.4 Results from simple shear tests

Stress-strain responses

In this section, we discuss the coaxiality between the major principal directions of the stress and fabric tensors in simple shear tests described in Section 3.5. For convenience and completeness of discussion, the stress-strain responses in simple shear tests are discussed below which is a repeat of Section 3.5. Figure 6-10 presents the stress-strain curves and volume change responses for simple shear tests at the same initial mean stress of $(\sigma_{x0} + \sigma_{y0})/2 = 500$ kPa but different initial stress ratio δ defined as $\delta = \left(\sigma_{x0} - \sigma_{y0}\right) \Big/ \left(\sigma_{x0} + \sigma_{y0}\right)$. The peak and frictional angles obtained from simple shear tests were $\varphi_{peak} = 18°$ and $\varphi_{cv} = 15°$, respectively, which are lower than those obtained from biaxial tests that yielded $\varphi_{peak} = 21°$ and $\varphi_{cv} = 17°$ using the same specimen. The difference might result from the method by which the shear is

applied via the discrete wall system.

Owing to the constraint of $\varepsilon_x = 0$ and the constant vertical stress during shearing, the horizontal stress σ_x is expected to vary with the shear strain and the applied vertical stress. As a result, the stress path on the *t*-*s* plane and the volume change curves are affected by the initial stress state characterized by δ. As shown in Figure 6-10 (a), the mean stress during shearing increases with the decrease of δ at the same t/s ratio. In addition, more contraction and hence less dilation is observed in tests under larger vertical stress, for example, when $\delta = -0.3$, as shown in Figure 6-10 (b).

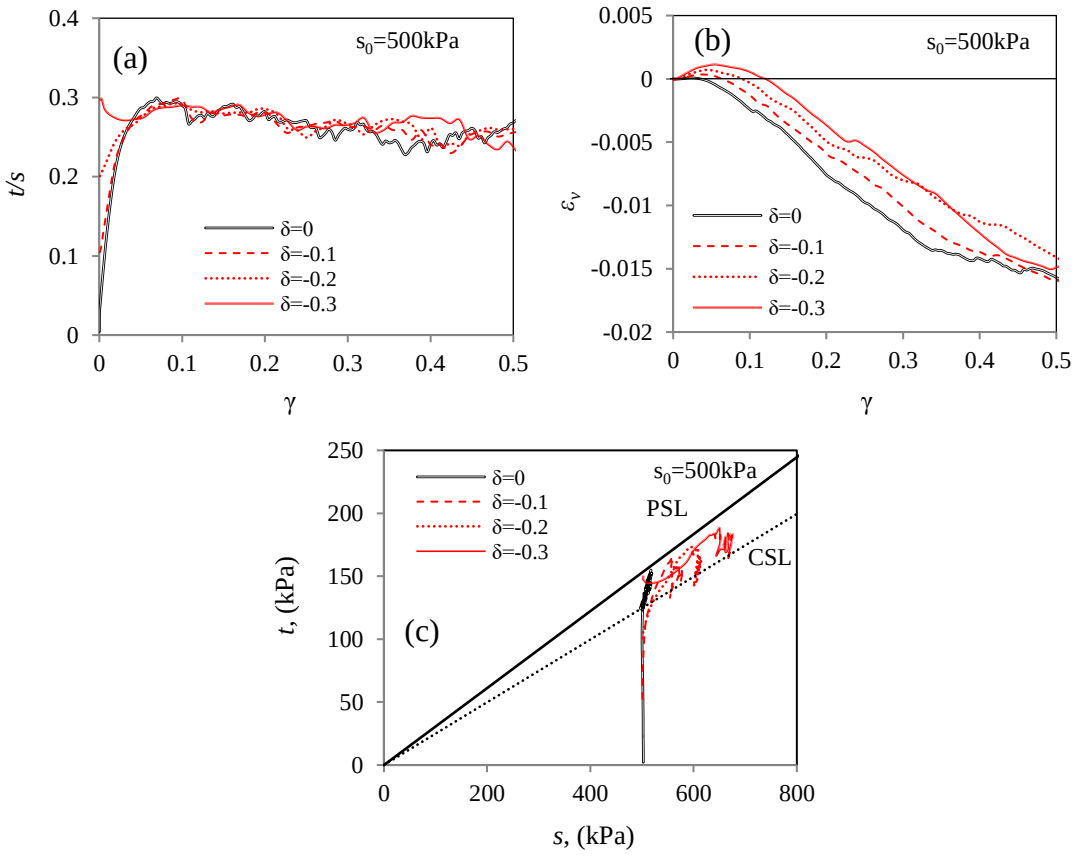

Figure 6-10: Evolution of (a) stress ratio, (b) volumetric strain with shear strain and (c) stress paths under different initial consolidation stress ratio δ: s_0=500 kPa

Figure 6-11 presents the evolution of σ_x/σ_y and τ_{xy}/σ_y with shear strain in tests starting at different initial stress states. It should be noted that in each test, the vertical stress σ_y was kept as a constant. According to Figure 6-11 (a), regardless of the initial stress ratio, σ_x/σ_y approached to 1.0 with the increase of shear strain. At the critical state, the specimen was subjected to pure shear with $\sigma_x = \sigma_y$. The τ_{xy}/σ_y vs. shear strain curves in Figure 6-11 (b) revealed that the mobilized friction angle of the horizontal plane at the peak and the critical states were practically identical to those determined from the t/s ratio.

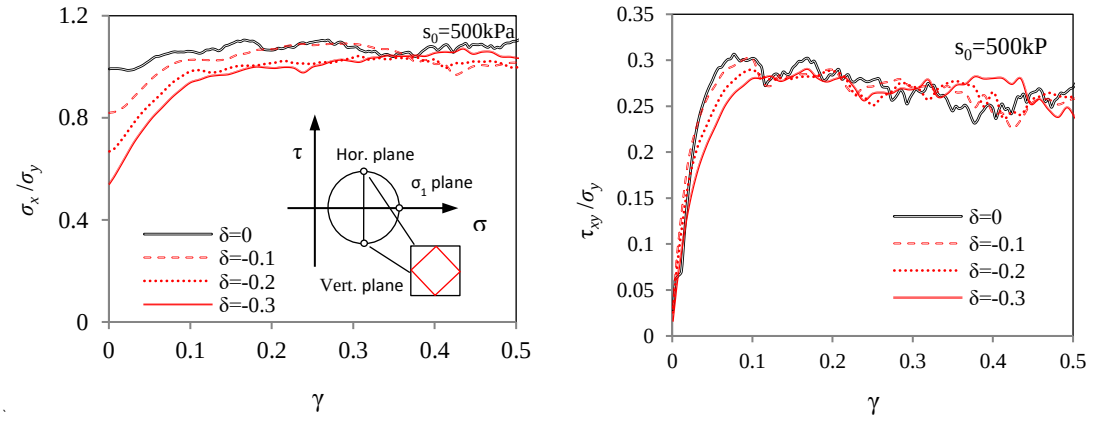

(a) (b)

Figure 6-11: Evolution of (a) stress ratio σ_x/σ_y with shear strain and (b) the variation of shear stress ratio τ_{xy}/σ_y with shear strain under different initial consolidation stress ratio δ: s_0=500kPa

Non-coaxiality between stress and strain increment

As expected, the major principal stress orientation rotated during simple shear tests, as shown in Figure 6-12 (a). In all tests, the major principal stress direction initiated from

$\theta_\sigma = 90°$ (vertical direction). Thereafter, as the shear strain increased, the major principal stress direction rotated and gradually approached $\theta_\sigma = 135°$ when the critical stress state was reached, as shown in Figure 6-10 (a). At the critical state, the horizontal stress equaled the vertical stress ($\sigma_y = \sigma_x$), which implied that the specimen was under pure shear, as demonstrated in the inset of Figure 6-11 (a). The rate of principal stress rotation in terms of the shear strain was affected by the initial stress state. A higher vertical stress (e.g. when $\delta = -0.3$) induced a slower rate of rotation of the major principal stress orientation.

In contrast, the inclination angle of the major principal strain rate, $\theta_{d\varepsilon}$, varied in the range of 134° to 136.7° upon shearing until to the critical state, see Figure 6-12 (b). In general, $\theta_{d\varepsilon}$ varied within a small range of $135° \pm 3°$ in all tests and was nearly independent of the initial stress ratio. Recalling Eq. (3-17), since $\dot{\varepsilon}_x = 0$ and $\dot{\gamma} = const.$ in all simple shear tests, $\theta_{d\varepsilon}$ was determined via $\tan 2\theta_{d\varepsilon} = -\dot{\gamma} / \dot{\varepsilon}_y$, which implies $\theta_{d\varepsilon} = 135°$ when $\dot{\varepsilon}_y = 0$. During the shearing process, $(\theta_{d\varepsilon} - 135°)$ reflected the rate of shear-induced contraction or dilation and could be used as a measure of dilatancy.

Figure 6-12 (c) presents the variation of $(\theta_{d\varepsilon} - \theta_\sigma)$ with the shear strain. An immediate conclusion was that the value of $(\theta_{d\varepsilon} - \theta_\sigma)$ decreased quickly from its initial value ($\approx 45°$) as the shear strain increased and gradually approached its ultimate value $(\theta_{d\varepsilon} - \theta_\sigma) = 0°$ at the critical state. The decrease rate of $(\theta_{d\varepsilon} - \theta_\sigma)$

with shear strain was affected by the initial stress ratio or the vertical stress. In particular, with an increase of shear strain, $(\theta_{d\varepsilon}-\theta_{\sigma})$ gradually decreased, accompanied by shear-induced dilation. $(\theta_{d\varepsilon}-\theta_{\sigma})_{\min}$ appeared when the maximum dilation was mobilized. Theoretically, the coaxiality of the major principal stress and strain rate under simple shear conditions requires that $\frac{\dot{\varepsilon}_x-\dot{\varepsilon}_y}{\sigma_x-\sigma_y}=\frac{\dot{\varepsilon}_{xy}}{\tau_{xy}}=\frac{\dot{\gamma}}{2\tau_{xy}}$, which can be satisfied only at the critical state.

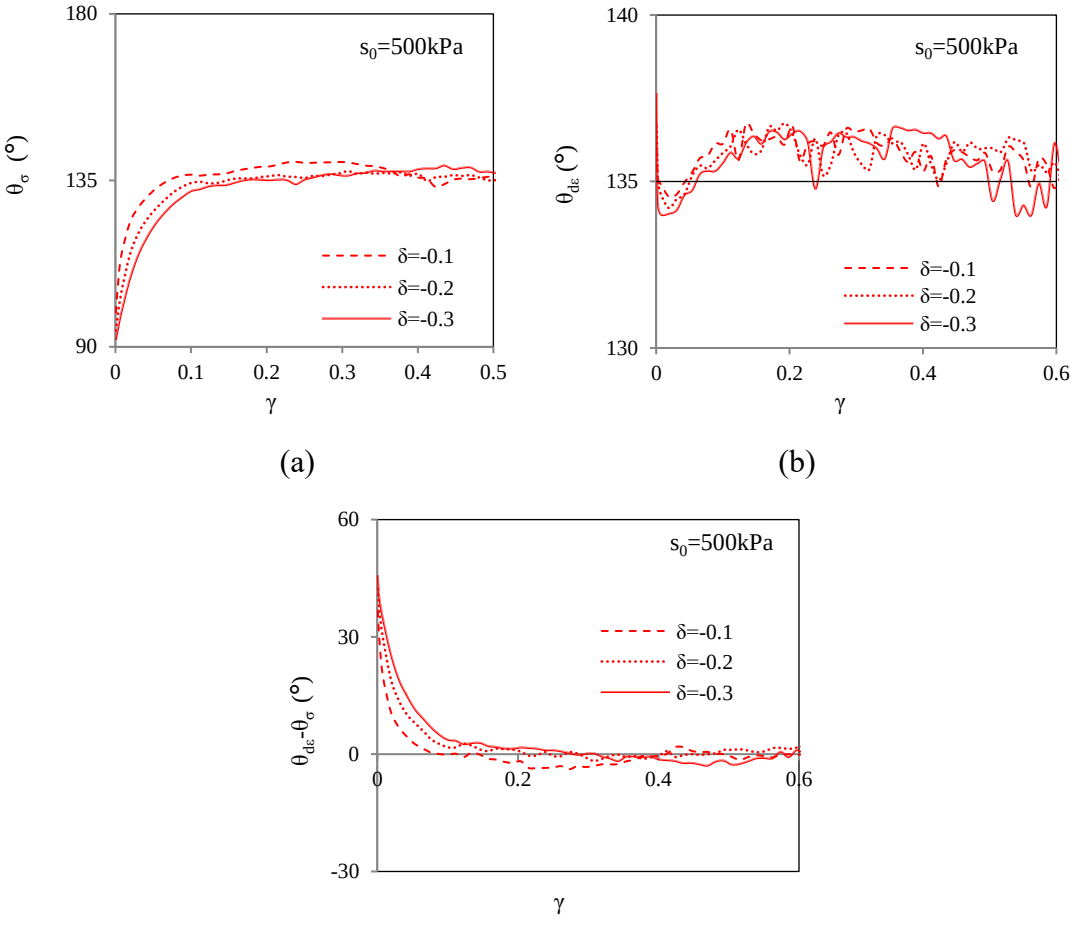

Figure 6-12: Evolution orientations of major principal (a) stress and (b) strain increment with shear strain; (c) the variation of $\theta_{d\varepsilon}$-θ_{σ} with shear strain under different initial consolidation stress ratio δ: s_0=500kPa

Non-coaxiality between stress and fabric tensors

We next examine the non-coaxiality between the major principal stress and the major principal fabric components for different contact networks during simple shear tests. Figure 6-13 plots the variations of $\theta_\sigma - \theta_c$, $\theta_\sigma - \theta_c^s$ and $\theta_\sigma - \theta_c^w$ with respect to shear strain for different initial stress ratio $\delta = 0 \sim -0.3$ at $s_0 = 500\,\text{kPa}$. According to the results in Figure 6-13(a), even though the specimens are nearly isotropic initially, noticeable differences between θ_σ and θ_c are observed at $\gamma < 20\%$. The maximum magnitudes of non-coaxiality, with $\left(\theta_\sigma - \theta_c\right)_{\max} \approx 5°$, occurred at the shear strain corresponding to the maximum volume compaction approximately (see Figure 6-10 b). With an increase of shear strain, the orientations of the major principal stress and the principal fabric component gradually approach to each other. Even though there are some fluctuations in the data, it is plausible to conclude that $(\theta_\sigma - \theta_c) \to 0°$ when $\gamma > 25\%$. Regarding the direction of the major principal component of fabric tensor for the strong sub-network, one observed $\left|\theta_\sigma - \theta_c^s\right| < 2°$ (see Figure 6-13 b), which confirms that orientation of the major principal fabric for the strong sub-network closely followed that of the major principal stress during simple shear tests. At the same time, the major principal component of fabric tensor for the weak sub-network always made an angle of $90°$ relative to the direction of major principal stress with $\left|\theta_\sigma - \theta_c^w\right| = 90° \pm 5°$. The large oscillation of data when $\gamma > 35\%$ was likely owing to the numerical error when the weak sub-network approached isotropy

(see Figure 4-22 c). These results demonstrated that, regardless of the initial stress states, the major principal fabric component in the strong sub-network was always coaxial with the major principal stress and perpendicular to the direction of the major principal fabric component for the weak sub-network.

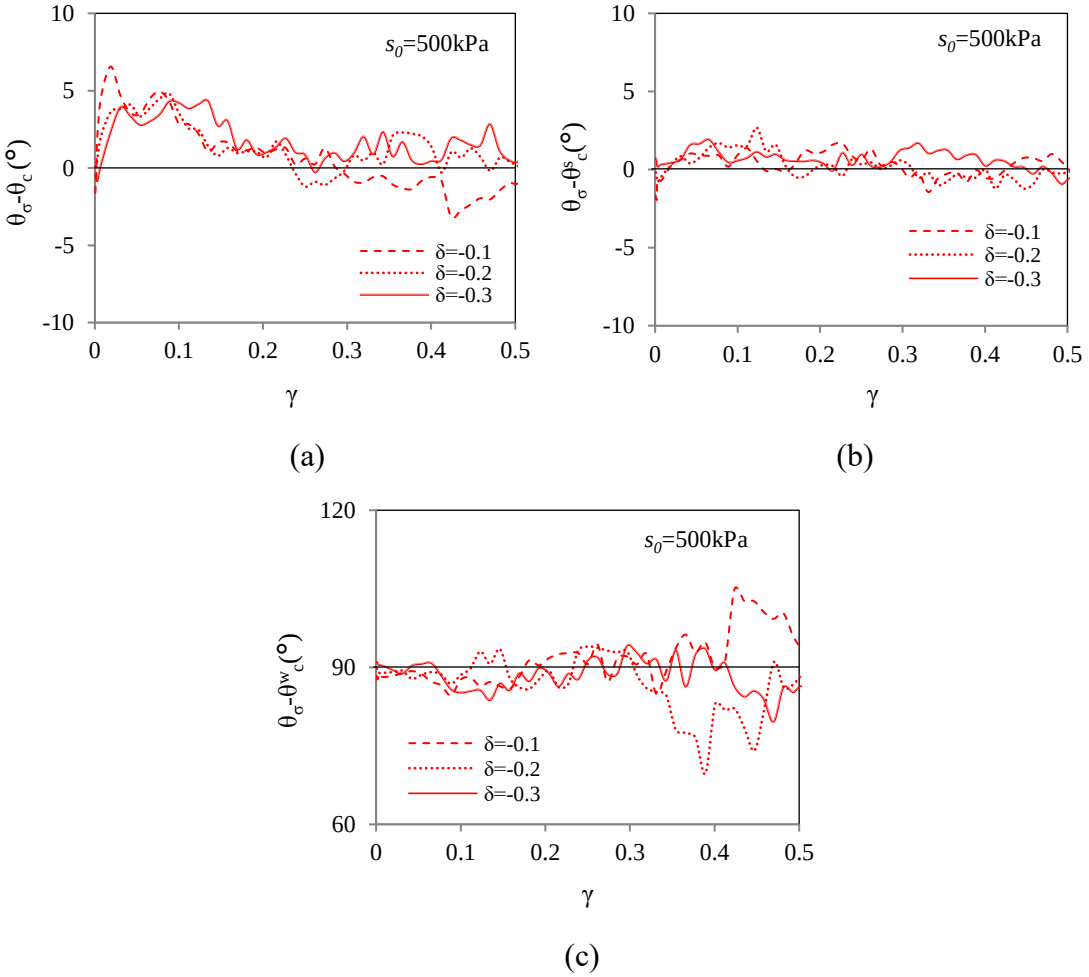

Figure 6-13: Evolution of non-coaxiality between the orientations of major principal stress and the major principal fabric for (a) the overall contact network; (b) the strong sub-network and (c) the weak sub-network: s_0=500kPa

6.5 Results from 3D tests with radial stress paths on the π-plane

Details about 3D tests along radial stress path on the π-plane were described in Section 3.6. In this series of tests, the Lode angle or the intermediate principal stress coefficient b is kept as a constant, as shown in Figure 6-14 (a). For each stress paths with constant Lode angle, the corresponding fabric trajectories on the π-plane are plotted in Figure 6-14 (b). It is noted that the directions of the fabric increments did not necessarily coincide with that of the stress increments even for initially isotropic granular materials. On the π-plane, the Lode angle of the Cauchy stress tensor was defined in Eq. (3-18). Similarly, the Lode angles for the fabric tensors can be expressed as

$$\theta_c = \tan^{-1}\left[\frac{2\phi_2 - 3\phi_1 + \phi_3}{\sqrt{3}\left(\phi_1 - \phi_3\right)}\right] \quad \theta_c^s = \tan^{-1}\left[\frac{2\phi_2^s - 3\phi_1^s + \phi_3^s}{\sqrt{3}\left(\phi_1^s - \phi_3^s\right)}\right] \tag{6-9}$$

for the overall contact network and the strong sub-network, respectively.

As demonstrated in Figure 6-14 (c), the non-coaxiality between the stress and fabric tensors can be measured by $\Delta\theta = \theta_\sigma - \theta_c$ and $\Delta\theta^s = \theta_\sigma - \theta_c^s$ for the overall contact network and the strong sub-network respectively.

Figure 6-15 presents the variations of $\Delta\theta$ and $\Delta\theta^s$ with shear strain for tests along various stress paths with selected b values. The following observations were obtained:

(a) Along stress paths of axisymmetric compression (b=0) and extension (b=1), the stress tensor could be considered as coaxial with the fabric tensors for both the whole contact network and the strong sub-network, with the maximum value of $\Delta\theta$ and $\Delta\theta^s$ being approximately 5° and 1°, respectively.

(b) For non-axisymmetric stress conditions along stress paths with $0 < b < 1$, the stress tensor for the strong sub-network was nearly coaxial with the stress

tensor, with the maximum value of $\Delta\theta^s$ being around $\pm 5°$; as shown in Figure 6-15 (b).

(c) However, non-coaxiality was observed between ϕ_{ij} of the whole contact network and the stress tensor, with $\Delta\theta_{max} = 18°$, as shown in Figure 6-15 (a).

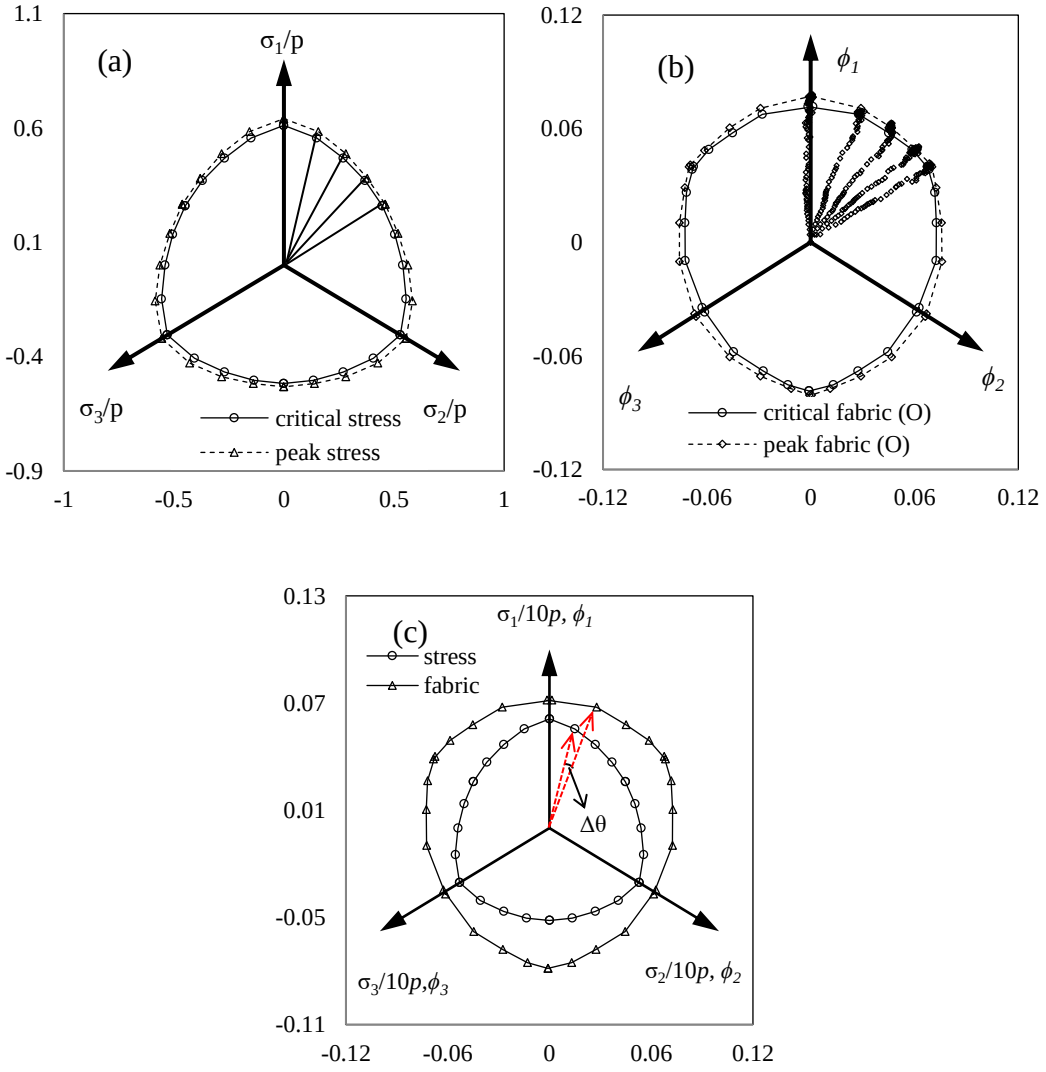

Figure 6-14: Trajectories of (a) stress paths and (b) associated fabric paths along different *b* values on the π-plane; (c) sketch of $|\theta_\sigma - \theta_c|$ on the π-plane: k^n=k^s= 4×10^4 N/m, *p*=300 kPa

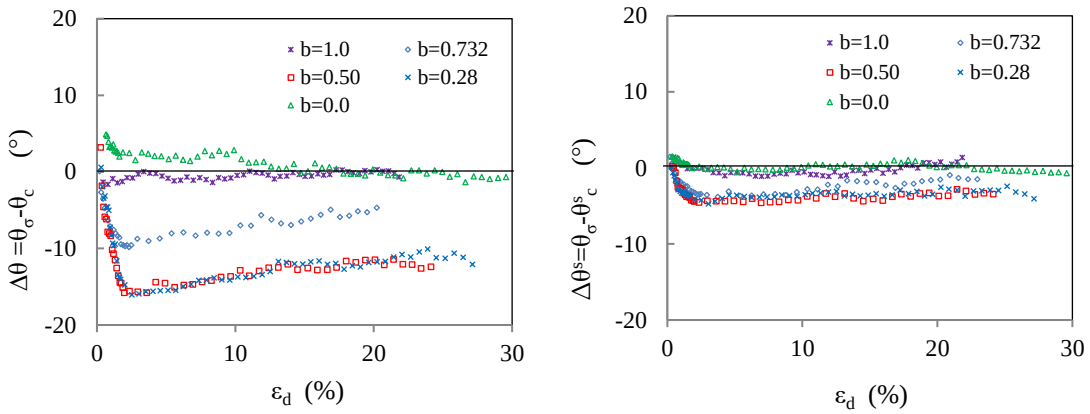

Figure 6-15: The evolution of magnitudes of non-coaxiality between (a) the stress tensor and the fabric tensor for the overall contact network, (b) the fabric tensor for strong contact network with deviatoric strain: k^n=k^s= 4×10^4 N/m, p=300 kPa

In general, the results clearly demonstrated that, regardless of the initial stress states, the major principal fabric component in the strong sub-network was always coaxial with the major principal stress and perpendicular to the direction of the major principal fabric component for the weak sub-network.

6.6 Fabric evolution law

As discussed above, the stress-induced fabric relation for the strong contact network can be addressed as $\phi_1^s:\phi_2^s=\sigma_1:\sigma_2$ and $\phi_1^s:\phi_2^s:\phi_3^s=\sigma_1:\sigma_2:\sigma_3$ for 2D and 3D stress conditions, respectively, no matter whether the principal stress orientation rotates or not. Hence, one can obtain that

$$\bar{\mathbf{J}}^s=\hbar\bar{\boldsymbol{\sigma}} \tag{6-10}$$

where $\bar{\mathbf{J}}^s$ and $\bar{\boldsymbol{\sigma}}$ are the diagonal matrices of the principal stresses and fabric components for the strong sub-network; the parameter $\hbar$ depends on the stress state and loading path. According to the matrix transformation, the stress and fabric can be

expressed in term of transformation matrixes T and Q.

$$\bar{\mathbf{J}}^{\mathbf{s}} = \mathbf{T}^T \mathbf{J}^{\mathbf{s}} \mathbf{T} \qquad \bar{\boldsymbol{\sigma}} = \mathbf{Q}^T \boldsymbol{\sigma} \mathbf{Q} \tag{6-11}$$

It is noted that $\mathbf{T}^{-1} = \mathbf{T}^T$ and $\mathbf{Q}^{-1} = \mathbf{Q}^T$. By substituting Eq. (6-11) into Eq. (6-10), it comes that

$$\mathbf{T}^T \mathbf{J}^{\mathbf{s}} \mathbf{T} = \hbar \mathbf{Q}^T \boldsymbol{\sigma} \mathbf{Q} \tag{6-12}$$

Since the stress tensor and fabric tensor are coaxial with each other, we can easily address that $\mathbf{T} = \mathbf{Q}$. Hence, the stress- fabric relation can be expressed as

$$\mathbf{J}^{\mathbf{s}} = \hbar \boldsymbol{\sigma} \quad \text{or} \quad \phi_{ij}^s = \hbar \sigma_{ij} \tag{6-13}$$

Since $\theta_\sigma - \theta_c^s$ always holds true and θ_c^w is perpendicular to the θ_σ in most cases. Therefore, it is reasonable to obtain the relation of $\left|\theta_c^s - \theta_c^w\right| = 90^\circ$ conditionally. Micromechanically, behaving as the confining pressure, the weak sub-network provide supports for the strong contact which contributes to the majority of the shear stress. This finding is identical with the conclusion made by Radjaï *et al.* (1998). Even though θ_c^s is more precise in describing the orientation of the stress than the θ_c, it is still reasonable to conclude that $\left|\theta_c - \theta_c^w\right| \approx 90^\circ$ conditionally. This is consistent with the finding made by Radjaï *et al.* (1998).

According to Radjaï *et al.* (1998), most of contact slidings happen within the weak sub-network. In other word, the whole dissipation by friction occurs at contacts bearing a force lower than the average force. Almost all contacts with a force larger than the average, corresponding to the bulking chains, are non-sliding. Therefore, intensive rearrangement of the weak sub-network plays a critical role in supporting the strong sub-network on the orthotropic plane. Furthermore, the role of the weak sub-network on the macro-instability and energy dissipation will be discussed later on.

6.7 Summary

In this study, the coaxiality between the principal stress orientation and the direction of the principal fabric component was investigated via a series of DEM simulations, which involved loading under constant principal stress orientation and continuous rotation of the principal stress direction. The evolution of fabric tensors was examined for both the overall contact network as well as the strong and the weak sub-networks.

The major principal direction of the fabric of the strong sub-network is always coaxial with the major principal stress orientation. The major principal direction of the fabric of the weak sub-network is always perpendicular to that of the strong sub-network, regardless of where the principal stress rotates or not. The major principal orientation of the fabric of the overall contact network, however, may not be in line with the major principal stress direction, even for the isotropic granular assembly subjected to biaxial compression tests with fixed principal stress directions.

For the loading in which the critical stress could be approached, the direction of the fabric of the overall contact network is nearly coaxial with that of the strong sub-network. Correspondingly, the fabric anisotropy within overall contact network is expressed in terms of those in sub-networks as $\phi_q = \alpha\phi_q^s - (1-\alpha)\phi_q^w$ with α is the ratio of strong contact number in the overall contact network.

The evolution of fabric tensor in strong sub-network is uniquely related to the applied stress by $\phi_1^s : \phi_2^s = \sigma_1 : \sigma_2$ and $\phi_1^s : \phi_2^s : \phi_3^s = \sigma_1 : \sigma_2 : \sigma_3$ for 2D and 3D stress conditions respectively. The stress-fabric relation can be further described as $\phi_{ij}^s = \hbar\sigma_{ij}$, with the parameter $\hbar$ depending on stress state and loading condition. The evolution of the fabric anisotropy in the weak and the overall contact network, however, can not be described as a function of the applied stress only.

Chapter 7 Micromechanical Interpretation of Material's Instability

7.1 Introduction

In mechanical terms, stability is obtained if a small stress increment yields a small strain increment, while instability is defined as a behaviour in which large plastic strains develop rapidly due to inability of the material to sustain a given stress or load. Hill (1958) and Drucker (1957) demonstrated a sufficient condition of the stability using the second-order work, respectively. For any $\left(\mathrm{d}\sigma_{ij},\mathrm{d}\varepsilon_{ij}\right)$ linked by their constitutive relation, a material is stable when $\mathrm{d}^2W>0$. Correspondingly, the material may be unstable when $\mathrm{d}^2W\le 0$. It is essential to note that the second-order work criterion by itself does not provide a sufficient condition for failure. For a granular material, owing to the non-symmetry of the constitutive tensor related to shear-induced dilation, $\mathrm{d}^2W\le 0$ may take place before the occurrence of failure at the maximum shear resistance (Nicot *et al.*, 2014). When the second-order work vanishes along a loading path, the material may become unstable with a bifurcation in deformation mode or transformation from a quasi-static regime towards a dynamic regime (Nicot *et al.*, 2014).

Physically, the deformation becomes unstable when an initially homogeneous deformation field (called 'trivial') ceases to be unique and stable, evolving into an inhomogeneous alternative deformation pattern. Since the deformation of a granular material is generally associated with the movement of individual particles, the transition from homogeneous to inhomogeneous deformation pattern implies a change of the material's internal structure. In other words, the vanishing of the second-order

work may be triggered by the change of the internal structure.

It is not a trivial task to understand micro-structural mechanisms that govern the vanishing of the second-order work. According to the micromechanics of granular materials, the stresses and strains can be related to the contact force and relative displacement, respectively. Hence, the second-order work and the failure criteria may be determined within the framework of the granular micro-mechanics. It has been revealed that the origin of material instabilities as a macro-scale phenomenon could be directly related to the constitutive nature of the local contact model at particle contacts (Nicot and Darve, 2006). In addition, Nicot *et al.* (2007) observe that changes in the fabric of the medium, associated with rearrangements caused by sliding and rolling, caused nonequivalence between the microscopic and macroscopic second-order works.

This chapter will focus on the variation of fabric in different contact networks and its relation to the vanishing of the macroscopic second-order work, which makes it possible to interpret the origin of material instability from a microscopic point of view.

7.2 Second-order work criteria for material stability

Drucker (1957) presented a fundamental definition of a stable inelastic (elastic-visco-plastic) material that "the work done by external agency on the change in displacement it produces must be positive". For a non-viscous and time-independent material this criterion is written as:

$$\mathrm{d}^2W_p = \dot{\sigma}_{ij}\dot{\varepsilon}_{ij}^p \geq 0\,,\ \ \mathrm{d}W_p - \mathrm{d}W_p^* = \left(\dot{\sigma}_{ij} - \dot{\sigma}_{ij}^*\right)\dot{\varepsilon}_{ij}^p \geq 0 \tag{7-1}$$

where σ_{ij} is a stress state located on the yield surface, σ_{ij}^* represents a state located within the yield surface, and $\dot{\sigma}_{ij}$ is a stress increment initiated on the yield surface causing the plastic strain increment $\dot{\varepsilon}_{ij}^p$. The first inequality, which is referred to as

the stability in the small, defines stable behaviour of material deformation. If it is not fulfilled for any $\dot{\sigma}_{ij}$, then the material may be unstable. Otherwise, the material will be unconditionally stable (Lade et al., 1988). The second one, which is referred to as the stability in the large, requires the yield surface to be convex.

Hill (1958) extended Drucker's postulate to the second increment of total work. For a solid volume V in the steady state, suppose that a part of the boundary is fixed and other part of the boundary is only under action of dead loading, Hill (1958) demonstrated that this system was stable if every $\left(\mathrm{d}\sigma_{ij},\mathrm{d}\varepsilon_{ij}\right)$ admitted by the constitutive relation satisfied that

$$W_2 = \int_V \mathrm{d}\sigma_{ij}\mathrm{d}\varepsilon_{ij}\mathrm{d}V \tag{7-2}$$

Eq. (7-2) presents a sufficient condition of the stability in the large or global scale. At the material point or on the small scale, the local form of the condition of material stability can be expressed as

$$\mathrm{d}^2W = \mathrm{d}\sigma_{ij}\mathrm{d}\varepsilon_{ij} > 0 \tag{7-3}$$

For a non-associated material such as a granular material, the global condition holds true when the local condition is satisfied at every point of volume V. It is noted that a positive second-order work constitutes a sufficient, but not necessary, the condition of stability.

7.3 Fabric evolution and instability in 2D tests along proportional strain paths

Attempts have been made to investigate material instability in granular assemblies on the microscopic scale in terms of the microstructure of the overall contact network; see, e.g., Wan *et al.* (2007), Nicot and Darve (2006, 2005) and Nicot *et al.* (2015). The following analyses, however, will focus on the variation of fabric in different contact networks when the macroscopic second-order work vanishes.

Following the stability analysis for sand tested along proportional strain paths undertaken by Wan *et al.* (2007), Darve and Laouafa (2000) and Wan *et al.* (2005), the second-order work under biaxial stress conditions can also be expressed via

$$\mathrm{d}^2W = \left(\mathrm{d}\sigma_1 - \frac{\mathrm{d}\sigma_2}{\Re} \right) \mathrm{d}\varepsilon_1 = \mathrm{d}\left(\sigma_1 - \frac{\sigma_2}{\Re} \right) \mathrm{d}\varepsilon_1 \tag{7-4}$$

with $\Re = -\dot{\varepsilon}_1 / \dot{\varepsilon}_2$ as defined previously. With the strain increment $\mathrm{d}\varepsilon_1$ being non-negative, the condition of zero second-order work is satisfied when $\mathrm{d}\left(\sigma_1 - \sigma_2 / \Re \right) = 0$, for which

$$\left(\sigma_1 - \frac{\sigma_2}{\Re} \right) = \max \tag{7-5}$$

The above equation implies that instability starts at the peak point of the curve obtained by plotting $\sigma_1 - \sigma_2 / \Re$ versus the axial strain ε_1.

Figure 7-1 presents the variation of $\sigma_1 - \sigma_2 / \Re$ with the axial strain along different proportional strain paths. The peak points corresponding to the onset of deformation instability according to Eq. (7-5) can be easily identified in VED tests ($0 < \Re < 1$). For the VEC ($\Re > 1$) and VCC ($\Re < -1$) tests, however, the value of $\left(\sigma_1 - \sigma_2 / \Re \right)$ in each individual test tended to increase monotonically with ε_1, indicating that the deformation is always stable.

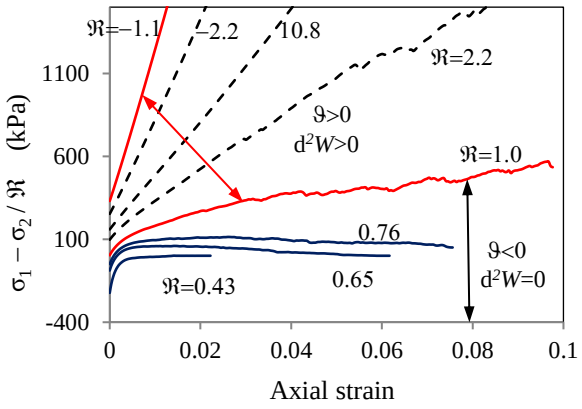

Figure 7-1: Variation of $(\sigma_1-\sigma_2/\Re)$ with axial strain

Figure 7-2 presents the variation of the second-order work d^2W as well as the fabric deviator for different contact networks in the VED tests with $\Re=0.43\sim0.86$. As shown in Figure 7-2 (a), in the test with $\Re=0.43$, d^2W was initially positive and gradually decreased with increasing shear strain and approaches zero value when the shear strain $\gamma=0.018$. Herein, γ is defined as $\gamma=\varepsilon_1-\varepsilon_2$. At this strain level, $q_\phi^s=\phi_1^s-\phi_2^s$ for the strong sub-network was at its peak value while $q_\phi^w=\phi_1^w-\phi_2^w$ in the weak sub-network is decreasing, as shown in Figure 7-2 (a). With further increase in the shear strain, the second-order work remained at d^2W=0, while the weak sub-network gradually evolved to an isotropic state in which $q_\phi^w=0$. The strong sub-network and the whole contact network, however, both showed significant anisotropy.

Similar curves have been observed in Figure 7-2 (b) with $\Re=0.65$. It is noted that the stress paths for $\Re=0.43$ and $\Re=0.65$ developed strain softening of shear resistance in Figure 7-2 (e) and d^2W=0 occurred at points marked the star after the peak deviatoric stresses. After the onset of the zero second-order work, the stresses quickly reduced toward zero and the material underwent instability. When $\Re=0.76$ and 0.86, d^2W=0 occurred slightly after the peak of deviatoric stress ratio $(t/s)_{max}$, as

shown in Figure 7-2 (e). Then, the stress paths stretched from the peak state line towards the critical state line after the onset of $d^2W=0$, which indicated that material instability happened after the failure state being approached. According to Figure 7-2 (c) and (d), the second-order work vanished slightly after the peak of the fabric deviator for the strong contact network. Generally, in all tests, the onset of the zero second-order work did accompany the highest magnitude of the fabric anisotropy for the strong sub-network.

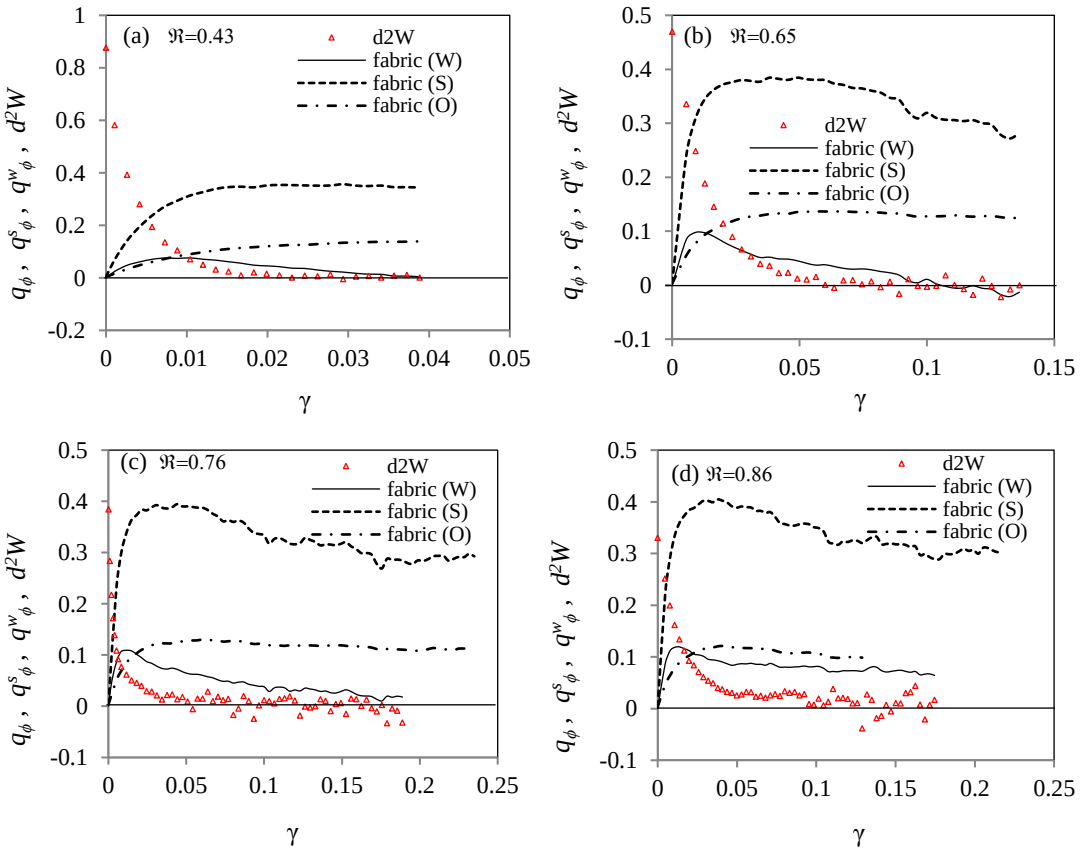

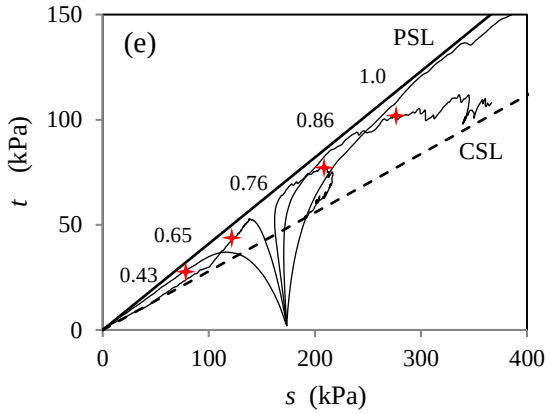

Figure 7-2: Variation of the fabric anisotropy in different contact networks and second-order work in VED tests (a) $\Re = 0.43$, (b) $\Re = 0.65$, (c) $\Re = 0.76$ and (d) $\Re = 0.86$; (e) the stress state corresponding to vanish of the second-order work in the stress paths (star marks)

Figure 7-3 presents the variations of $q_\phi^s = \phi_1^s - \phi_2^s$ and $q_\phi^w = \phi_1^w - \phi_2^w$ with $(\sigma_1 - \sigma_2/\Re)$ in VED and VEI tests with $\Re = 0.43 \sim 1.0$. In particular, Figure 7-3 (a). shows the variation of q_ϕ^s with $(\sigma_1 - \sigma_2/\Re)$. The thicker dotted segment on each curve represents states of unstable deformation. An immediate observation is that the strong sub-network was responsible for deformation instability since the peak fabric deviator of the strong sub-network was reached when $d^2W=0$. More specifically, for high dilation rate with $\Re = 0.43 \sim 0.65$, $q_\phi^s = \phi_1^s - \phi_2^s$ increased initially with $(\sigma_1 - \sigma_2/\Re)$, both reaching their maximum simultaneously, see Figure 7-3(a). For lower rates of dilation with $\Re = 0.76 \sim 0.86$, q_ϕ^s and $(\sigma_1 - \sigma_2/\Re)$ reached their maximum at the same time approximately. However, degradation of strong sub-network with reduced degree of anisotropy took place following the onset of deformation instability, as shown in Figure 7-1. In the VEI test, a peak value of q_ϕ^s developed during deformation process which was always stable according to Figure

7-1 since $(\sigma_1-\sigma_2/\Re)$ increased monotonically. These observations indicate that the onset of deformation instability was accompanied by a degradation or progressive collapse of the strong sub-network. However, degradation of the strong sub-network does not guarantee unstable deformation. In other words, degradation of strong sub-network is a necessary but not sufficient condition for deformation instability.

Figure 7-3 (b) displays the evolution of weak sub-network anisotropy with $(\sigma_1-\sigma_2/\Re)$. For dilation rates in the range of $\Re=0.43\sim0.86$, the highest value of $q_\phi^w=\phi_1^w-\phi_2^w$ was not associated with $(\sigma_1-\sigma_2/\Re)_{\max}$ that was achieved after the peak of q_ϕ^w. In all cases, a significant decrease of q_ϕ^w took place when deformation became unstable. In other words, degradation of the weak sub-network was initiated before deformation became unstable. For the VEI test ($\Re=1$), deformation was always stable and therefore no degradation of q_ϕ^w occurred.

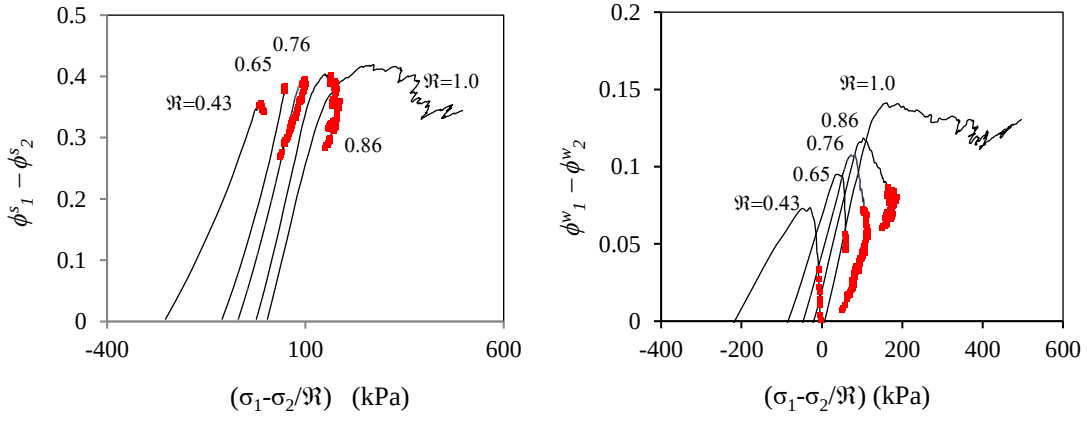

(a) (b)

Figure 7-3: (a) Evolution of deviator fabric of strong contact sub-network and (b) weak contact sub-network with $(\sigma_1-\sigma_2/\Re)$ along various strain paths

As shown in Figure 7-1, the second-order work was always positive in the VEC

and VCC tests. Figure 7-4 and Figure 7-5 compare the evolution of the fabric anisotropy for different contact networks and the variation of the second-order work for VEC ($\Re > 1$) and VCC tests ($\Re < -1$), respectively. When $\Re = 2.2$, both q_ϕ^w and q_ϕ^s initially increased with the shear strain and approached its peak at $\gamma = 0.05$. At the same time, d^2W decreased from its initial positive value continuously until a positive constant at approximately $\gamma = 0.05$. Thereafter, both q_ϕ^w and q_ϕ^s gradually decreased. The decrease of the fabric anisotropy does not represent the collapse of the internal structure since the second-order work was always positive. In other words, the specimen may not collapse since it underwent volumetric contraction. When $\Re = 10.8$, q_ϕ^w increased monotonically and the peak value of q_ϕ corresponding to a positive constant of the second-order work at $\gamma = 0.06$, as shown in Figure 7-4 (b). In the VCC tests, starting from its initial positive value d^2W increased monotonically with the shear strain, as shown in Figure 7-5. Correspondingly, the fabric anisotropy for different contact networks continuously increased upon loading without approaching a peak value.

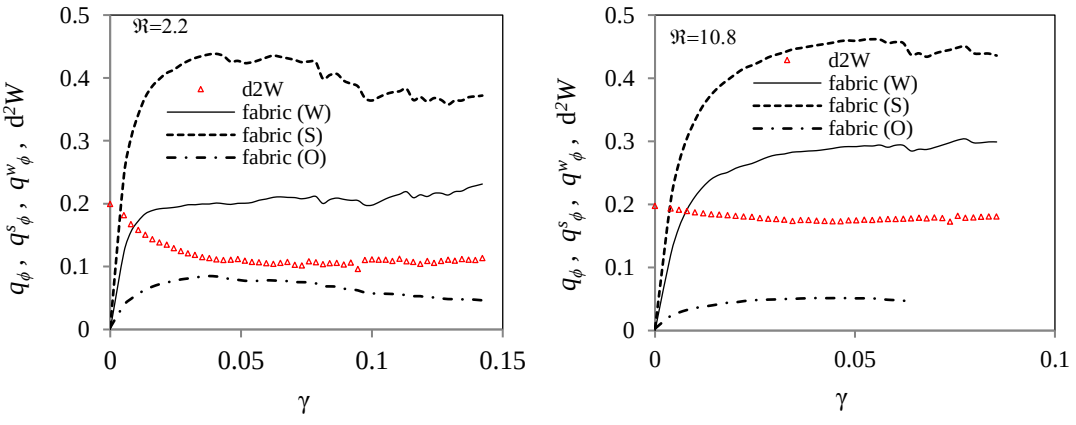

(a) (b)

Figure 7-4: Variation of the fabric anisotropy in different contact networks and second-order work with the shear strain in VEC tests (a) $\Re = 2.2$ and (b) $\Re = 10.8$

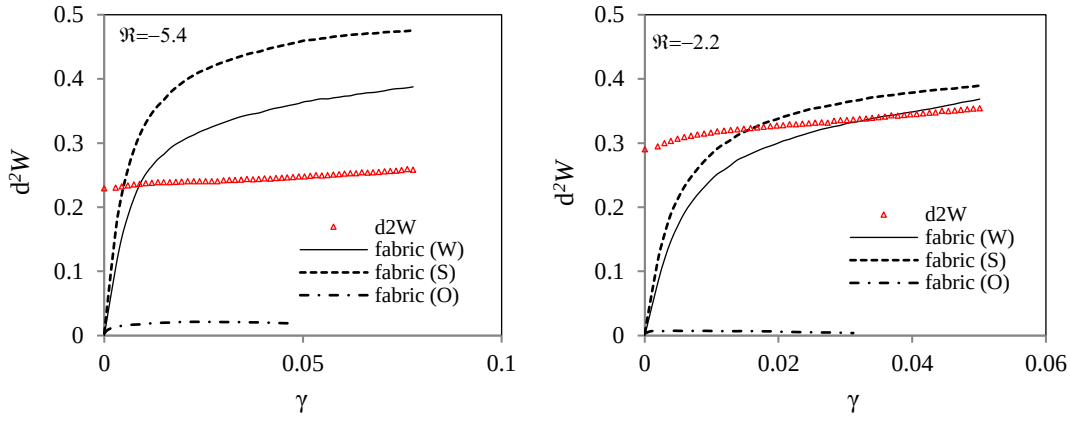

Figure 7-5: Variation of the fabric anisotropy in different contact networks and second-order work with the shear strain in VCC tests (a) $\Re = -5.4$ and (b) $\Re = -2.2$

Based on the discussion about the results presented above, one may conclude that the degradation of strong sub-network (i.e., the decrease of q_ϕ^s) is a necessary but not a sufficient condition of deformation instability. In other words, deformation instability is accompanied by strong network degradation but not opposite. On the other hand, a decrease of q_ϕ^w or collapse of the weak sub-network is an indicator of deformation instability in tests along all imposed strain paths.

7.4 Micro-interpretation of second-order work

7.4.1 Estimate of relative particle displacements

Based on different assumptions, various approaches have been proposed to correlate the average relative displacement between particles and the (macroscopic) strain tensor. When adopting the Voigt hypothesis and assuming the existence of a mean field of displacement, Liao *et al.* (1997) presented a relation between the relative incremental displacement du_i between two particles in contact and the incremental

strain tensor $d\varepsilon_{ij}$ as

$$\mathrm{d}u_i = \mathrm{d}\varepsilon_{ij} l_j \tag{7-6}$$

where l_j is the branch vector connecting the centroids of the two particles. When introducing the average length $\hat{l}_0$ of the branch vectors, l_j can be expressed as $l_j = \hat{l}_0 n_j$, with n_j being a unit vector in the direction of the branch vector. For spherical particles, n_j is the same as the unit vector of the contact normal. It follows that (Nicot and Darve, 2006, 2005):

$$\mathrm{d}u_i = \hat{l}_0 \mathrm{d}\varepsilon_{ij} n_j \tag{7-7}$$

The relative displacement can be further decomposed into a normal component (du^n) and a tangential component (du^t), with

$$\mathrm{d}\boldsymbol{u} = \mathrm{d}u^n \boldsymbol{n} + \mathrm{d}u^t \boldsymbol{t}; \quad \mathrm{d}u^n = \mathrm{d}u_i n_i; \quad \mathrm{d}u^t = \mathrm{d}u_i t_i \tag{7-8}$$

in which $\boldsymbol{n}$ and $\boldsymbol{t}$ are unit vectors normal to and parallel to the contact plane, respectively. As shown in Figure 4-1, in a polar coordinate system of 3D, $\boldsymbol{n} = (\cos\theta, \sin\theta\cos\varphi, \sin\theta\sin\varphi)^T$, $\boldsymbol{t} = (\sin\theta, -\cos\theta\cos\varphi, \cos\theta\sin\varphi)^T$, with $\theta \subset [0, \pi]$ and $\varphi \subset [0, 2\pi]$. For 2D cases, $\boldsymbol{n}$ and $\boldsymbol{t}$ are expressed as $\boldsymbol{n} = (\cos\theta, \sin\theta)^T$ and $\boldsymbol{t} = (-\sin\theta, \cos\theta)^T$, respectively (as shown in Figure 4-1 b).

7.4.2 Micro and macro-level second-order works

Consider a representative volume element around a point in a granular assembly, the macroscopic stress tensor at this point can be computed from the local contact forces and branch vectors using the generalized homogenization method. For a given density function $E(\theta, \varphi)$ describing the directional distribution of the contact normal, the macroscopic stress tensor can be determined as

$$\sigma_{ij} = \frac{N_c \widehat{l}_0}{V} \iint_{\Omega} E(\theta,\varphi) f_i(\theta,\varphi) n_j d\Omega \tag{7-9}$$

where $d\Omega = \sin\varphi d\theta d\varphi$ and Ω is the solid angle corresponding to $\boldsymbol{n}$, N_c is the total number of contacts in the granular assembly. Based on the experimental results obtained by Field (1963), Nicot and Darve (2006) proposed an expression for N_c as

$$N_c = 12 N_p \frac{\rho_0}{\rho_g} \frac{1}{1-\varepsilon_{kk}} \tag{7-10}$$

in which ρ_0 and N_p are the initial density and the number of particles with the density of ρ_g in the granular assembly. Given the initial volume V_0 of the granular assembly, the present volume is

$$V = V_0 (1-\varepsilon_{kk}) \tag{7-11}$$

in which ε_{kk} is the current volumetric strain of the granular assembly (or the specimen).

By substituting Eqs. (7-10), (7-11) into Eq. (7-9), the expression of σ_{ij} becomes

$$\sigma_{ij} = \upsilon \iint_{\Omega} \frac{E(\theta,\varphi) f_i(\theta,\varphi) \widehat{l}_0 n_j}{(1-\varepsilon_{kk})^2} \sin\theta \mathrm{d}\theta \mathrm{d}\varphi \tag{7-12}$$

with $\upsilon = 12 N_g \frac{\rho_0}{\rho_g} \frac{1}{V_0}$, which is a constant independent of the timescale. When considering the normal and the tangential components of the contact force with $f_i = f^n n_i + f^t t_i$, the stress tensor can be decomposed into two parts: the stress component σ_{ij}^n associated with the normal contact force f^n and the component σ_{ij}^t associated with the tangential contact force f^t so that

$$\sigma_{ij} = \sigma_{ij}^n + \sigma_{ij}^t \tag{7-13}$$

where

$$\sigma_{ij}^{n} = \upsilon \iint_{\Omega} \frac{E(\theta,\varphi)}{\left(1-\varepsilon_{kk}\right)^{2}} f^{n} \hat{l}_0 n_i n_j \sin\theta \mathrm{d}\theta \mathrm{d}\varphi$$

$$\sigma_{ij}^{n} = \upsilon \iint_{\Omega} \frac{E(\theta,\varphi)}{\left(1-\varepsilon_{kk}\right)^{2}} f^{t} \hat{l}_0 t_i n_j \sin\theta \mathrm{d}\theta \mathrm{d}\varphi$$

As a result, the stress increment can be estimated as

$$\mathrm{d}\sigma_{ij} = \mathrm{d}\sigma_{ij}^{n} + \mathrm{d}\sigma_{ij}^{t} \tag{7-14}$$

with

$$\mathrm{d}\sigma_{ij}^{n} = \upsilon \iint_{\Omega} \mathrm{d}\left[\frac{E(\theta,\varphi) f^{n}}{\left(1-\varepsilon_{kk}\right)^{2}}\right] \hat{l}_0 n_i n_j \sin\theta \mathrm{d}\theta \mathrm{d}\varphi$$

and $\mathrm{d}\sigma_{ij}^{t} = \upsilon \iint_{\Omega} \mathrm{d}\left[\frac{E(\theta,\varphi) f^{t}}{\left(1-\varepsilon_{kk}\right)^{2}}\right] \hat{l}_0 t_i n_j \sin\theta \mathrm{d}\theta \mathrm{d}\varphi$. Thus, the second-order work is decomposed into two parts:

$$\mathrm{d}^2 W = \mathrm{d}\sigma_{ij}\mathrm{d}\varepsilon_{ij} = \left(\mathrm{d}^2 W\right)_{\mathrm{I}} + \left(\mathrm{d}^2 W\right)_{\mathrm{II}} \tag{7-15}$$

in which

$$\left(\mathrm{d}^2 W\right)_{\mathrm{I}} = \mathrm{d}\sigma_{ij}^{n}\mathrm{d}\varepsilon_{ij} = \upsilon \iint_{\Omega} \mathrm{d}\left[\frac{E(\theta,\varphi) f^{n}}{\left(1-\varepsilon_{kk}\right)^{2}}\right] \mathrm{d}\varepsilon_{ij} \hat{l}_0 n_i n_j \sin\theta \mathrm{d}\theta \mathrm{d}\varphi$$

$$\left(\mathrm{d}^2 W\right)_{\mathrm{II}} = \mathrm{d}\sigma_{ij}^{t}\mathrm{d}\varepsilon_{ij} = \upsilon \iint_{\Omega} \mathrm{d}\left[\frac{E(\theta,\varphi) f^{t}}{\left(1-\varepsilon_{kk}\right)^{2}}\right] \mathrm{d}\varepsilon_{ij} \hat{l}_0 t_i n_j \sin\theta \mathrm{d}\theta \mathrm{d}\varphi$$

Recalling Eqs. (7-7) and (7-15) the two parts of the second-order work can be expressed as:

$$\left(\mathrm{d}^2 W\right)_{\mathrm{I}} = \upsilon \iint_{\Omega} \mathrm{d}\left[\frac{E(\theta,\varphi) f^{n}}{\left(1-\varepsilon_{kk}\right)^{2}}\right] \mathrm{d}u^{n} \sin\theta \mathrm{d}\theta \mathrm{d}\varphi \tag{7-16}$$

$$\left(\mathrm{d}^2 W\right)_{\mathrm{II}} = \upsilon \iint_{\Omega} \mathrm{d}\left[\frac{E(\theta,\varphi) f^{t}}{\left(1-\varepsilon_{kk}\right)^{2}}\right] \mathrm{d}u^{t} \sin\theta \mathrm{d}\theta \mathrm{d}\varphi \tag{7-17}$$

On the other hand, the contact force increments and the relative incremental

displacements can be related through contact law. For $\mathrm{d}f^n$ and $\mathrm{d}u^n$, we have $\mathrm{d}f^n = k^n \mathrm{d}u^n$. For the tangential forces and the relative tangential displacements, depending on whether relative sliding occurs or not, the relation between $\mathrm{d}f^t$ and $\mathrm{d}u^t$ can be expressed as $\mathrm{d}f^t = k^t \mathrm{d}u^t$ for elastic contact, or else $\mathrm{d}u^t = \dfrac{\mathrm{d}f^t - \mu k^n \mathrm{d}u^n}{k^s}$ for sliding contacts with μ being the interparticle friction coefficient. Therefore, the expressions for $\left(\mathrm{d}^2W\right)_{\mathrm{I}}$ and $\left(\mathrm{d}^2W\right)_{\mathrm{II}}$ in Eqs. (7-12) and (7-13) can be rewritten as

$$\left(\mathrm{d}^2W\right)_{\mathrm{I}} = \upsilon \iint_{\Omega} \left\{ \begin{array}{l} \dfrac{f^n \mathrm{d}E(\theta,\varphi)}{\left(1-\varepsilon_{kk}\right)^2} + \dfrac{E(\theta,\varphi)\mathrm{d}f^n}{\left(1-\varepsilon_{kk}\right)^2} \\ +\ldots+\dfrac{2f^n E(\theta,\varphi)\mathrm{d}\varepsilon_{kk}}{\left(1-\varepsilon_{kk}\right)^3} \end{array} \right\} \mathrm{d}u^n \sin\theta \mathrm{d}\theta \mathrm{d}\varphi \tag{7-18}$$

$$\left(\mathrm{d}^2W\right)_{\mathrm{II}} = \upsilon \iint_{\Omega} \left\{ \begin{array}{l} \dfrac{f^t \mathrm{d}E(\theta,\varphi)}{\left(1-\varepsilon_{kk}\right)^2} + \dfrac{E(\theta,\varphi)\mathrm{d}f^t}{\left(1-\varepsilon_{kk}\right)^2} \\ +\ldots+\dfrac{2f^t E(\theta,\varphi)\mathrm{d}\varepsilon_{kk}}{\left(1-\varepsilon_{kk}\right)^3} \end{array} \right\} \mathrm{d}u^t \sin\theta \mathrm{d}\theta \mathrm{d}\varphi \tag{7-19}$$

Following Nicot and Darve (2006), d^2W can be divided into three terms as $\mathrm{d}^2W = (\mathrm{d}^2W)^{fabric} + (\mathrm{d}^2W)^{micro} + (\mathrm{d}^2W)^{volume}$. The term $(\mathrm{d}^2W)^{micro}$ can be interpreted as the summation of the average of the local directional second-order work in each contact direction. The term $(\mathrm{d}^2W)^{volume}$ accounts for the volume change of the granular assembly and the term $(\mathrm{d}^2W)^{fabric}$ is the second-order work related to the change of fabric. Similarly, $\left(\mathrm{d}^2W\right)_{\mathrm{I}}$ and $\left(\mathrm{d}^2W\right)_{\mathrm{II}}$ can be decomposed into these three components, which yield

$$(\mathrm{d}^2W)^{fabric} = (\mathrm{d}^2W)_{\mathrm{I}}^{fabric} + (\mathrm{d}^2W)_{\mathrm{II}}^{fabric} \tag{7-20}$$

$$(\mathrm{d}^2W)^{micro} = (\mathrm{d}^2W)_{I}^{micro} + (\mathrm{d}^2W)_{\mathrm{II}}^{micro} \tag{7-21}$$

$$(\mathrm{d}^2W)^{volume} = (\mathrm{d}^2W)_{I}^{volume} + (\mathrm{d}^2W)_{\mathrm{II}}^{volume} \tag{7-22}$$

with

$$(\mathrm{d}^2W)_{\mathrm{I}}^{fabric} = \frac{\upsilon}{k^n}\iint_{\Omega}\frac{\mathrm{d}E(\theta,\varphi)f^n}{(1-\varepsilon_{kk})^2}\mathrm{d}f^n\sin\theta d\theta d\varphi \tag{7-23}$$

$$(\mathrm{d}^2W)_{\mathrm{I}}^{micro} = \frac{\upsilon}{k^n}\iint_{\Omega}\frac{E(\theta,\varphi)\mathrm{d}f^n}{(1-\varepsilon_{kk})^2}\mathrm{d}f^n\sin\theta d\theta d\varphi \tag{7-24}$$

$$(\mathrm{d}^2W)_{\mathrm{I}}^{volume} = \frac{2\upsilon}{k^n}\iint_{\Omega}\frac{E(\theta,\varphi)f^n\mathrm{d}\varepsilon_{kk}}{(1-\varepsilon_{kk})^3}\mathrm{d}f^n\sin\theta d\theta d\varphi \tag{7-25}$$

$$(\mathrm{d}^2W)_{\mathrm{II}}^{fabric} = \upsilon\iint_{\Omega}\frac{\mathrm{d}E(\theta,\varphi)f^t}{(1-\varepsilon_{kk})^2}\mathrm{d}u^t\sin\theta d\theta d\varphi \tag{7-26}$$

$$(\mathrm{d}^2W)_{\mathrm{II}}^{micro} = \upsilon\iint_{\Omega}\frac{E(\theta,\varphi)\mathrm{d}f^t}{(1-\varepsilon_{kk})^2}\mathrm{d}u^t\sin\theta d\theta d\varphi \tag{7-27}$$

$$(\mathrm{d}^2W)_{\mathrm{II}}^{volume} = 2\upsilon\iint_{\Omega}\frac{E(\theta,\varphi)f^t\mathrm{d}\varepsilon_{kk}}{(1-\varepsilon_{kk})^3}\mathrm{d}u^t\sin\theta d\theta d\varphi \tag{7-28}$$

Similar expressions can be obtained for d^2W and its components associated with different mechanisms.

7.4.3 Analysis of second-order work in 2D tests along controlled strain paths

As illustrated in Figure 3-4 (b), in a biaxial test along a proportional strain path, the constant strain increment ratio $\Re = -\dot{\varepsilon}_{11}/\dot{\varepsilon}_{22}$ was achieved by controlling the movement of the vertical and horizontal walls. According to this definition, $\dot{\varepsilon}_{11}$ is the vertical strain rate. Nevertheless, the inclination angle of contact normal is defined according to the horizontal axis. Therefore, we rotate the coordinate system by 90° and the strain rate tensor becomes

$$\mathrm{d}\varepsilon_{ij} = \begin{bmatrix} -C/\Re & 0 \\ 0 & C \end{bmatrix} \tag{7-29}$$

where C is the constant strain rate in the horizenta direction. The relative normal and tangential displacements between two particles with the contact normal

$\boldsymbol{n} = (\cos\theta, \sin\theta)^T$ can be estimated as

$$\mathrm{d}u_n = \mathrm{d}\varepsilon_{ij} n_i n_j = C(\sin\theta)^2 - \frac{C}{\Re}(\cos\theta)^2 \,;\, \mathrm{d}u_t = \mathrm{d}\varepsilon_{ij} t_i n_j = \frac{1}{2}(C + \frac{C}{\Re})\sin 2\theta \quad (7\text{-}30)$$

Recalling Eq. (4-5), the probability density function of the contact normal is $E(\theta) = \frac{1}{2\pi}\left[1 + a_c \cos 2(\theta - \theta_c)\right]$. The directional variations of the normal and tangential contact forces can be expressed as (Rothenburg and Selvadurai, 1981)

$$f^n(\theta) = f_0^n\left[1 + a_n \cos 2(\theta - \theta_n)\right], \quad f^t(\theta) = f_0^n a_t \sin(\theta - \theta_t) \quad (7\text{-}31)$$

where f_0^n is the directional mean normal contact force which equals the mean normal contact force only when the contact normals in all directions are uniformly distributed, a_c, a_n and a_t define the degree of anisotropies in the distributions of the contact normal, the normal contact force $f^n(\theta)$ and tangential contact force $f^t(\theta)$, respectively. θ_c, θ_n and θ_t represent the major principal directions of the directional distribution of contact normals, normal contact forces and tangential contact forces. Following Rothenburg and Bathurst (1989), we assume that $\theta_n = \theta_c = \theta_t$. As discussed in Chapter 6, in biaxial tests along proportional strain paths, we may assume $\theta_n = \theta_c = \theta_t = \pi/2$. As a result, the second-order work components $(\mathrm{d}^2W)_{\mathrm{I}}$ and $(\mathrm{d}^2W)_{\mathrm{II}}$, which are associated with the normal and tangential contact forces respectively in Eqs.(7-18) and (7-19), are expressed as

$$(\mathrm{d}^2W)_{\mathrm{I}} = \frac{C\upsilon\hat{l}_0}{2}\int_{[0,2\pi]} \mathrm{d}\left[\frac{E(\theta) f^n(\theta)}{(1-\varepsilon_{kk})^2}\right]\left[\left(1 - \frac{1}{\Re}\right) - \left(1 + \frac{1}{\Re}\right)\cos 2\theta\right] d\theta \quad (7\text{-}32)$$

and

$$(\mathrm{d}^2W)_{\Pi} = \frac{1}{2}\upsilon\hat{l}_0\left(C + \frac{C}{\Re}\right)\int_{[0,2\pi]} \mathrm{d}\left[\frac{E(\theta) f^t(\theta)}{(1-\varepsilon_{kk})^2}\right]\sin 2\theta d\theta \quad (7\text{-}33)$$

After some algebraic manipulations, the different terms of $(\mathrm{d}^2W)_{\mathrm{I}}$ and $(\mathrm{d}^2W)_{\Pi}$ are

determined as

$$(\mathrm{d}^2W)_{\mathrm{I}}^{fabric} = \frac{\upsilon l_0 C f_0^n \mathrm{d}a_c \left[(1+\frac{1}{\Re}) + a_n(1-\frac{1}{\Re}) \right]}{4(1-\varepsilon_{kk})^2} \tag{7-34}$$

$$(\mathrm{d}^2W)_{\mathrm{I}}^{micro} = \frac{\upsilon \hat{l}_0 C \left[\begin{array}{l} \mathrm{d}f_0^n[(1-\frac{1}{\Re})(2+a_c a_n) + (a_c+a_n)(1+\frac{1}{\Re})] \\ +\ldots + f_0^n \mathrm{d}a_n[a_c(1-\frac{1}{\Re}) + (1+\frac{1}{\Re})] \end{array} \right]}{4(1-\varepsilon_{kk})^2} \tag{7-35}$$

$$(\mathrm{d}^2W)_{\mathrm{I}}^{volume} = \frac{\upsilon \hat{l}_0 C f_0^n \mathrm{d}\varepsilon_{kk} \left[(1-\frac{1}{\Re})(2+a_c a_n) + (a_c+a_n)(1+\frac{1}{\Re}) \right]}{2(1-\varepsilon_{kk})^3} \tag{7-36}$$

$$(\mathrm{d}^2W)_{\Pi}^{fabric} = 0 \tag{7-37}$$

$$(\mathrm{d}^2W)_{\Pi}^{micro} = \frac{\upsilon \hat{l}_0 C (1+\frac{1}{\Re})(a_t \mathrm{d}f_0^n + f_0^n \mathrm{d}a_t)}{4(1-\varepsilon_{kk})^2} \tag{7-38}$$

$$(\mathrm{d}^2W)_{\Pi}^{volume} = \frac{\upsilon \hat{l}_0 C (1+\frac{1}{\Re}) f_0^n a_t \mathrm{d}\varepsilon_{kk}}{2(1-\varepsilon_{kk})^3} \tag{7-39}$$

which yield the three components of d^2W associated with different mechanisms:

$$(\mathrm{d}^2W)^{fabric} = \frac{\upsilon l_0 C f_0^n \mathrm{d}a_c}{4(1-\varepsilon_{kk})^2} \left[(1+a_n) + \frac{1}{\Re}(1-a_n) \right] \tag{7-40}$$

$$(\mathrm{d}^2W)^{micro} = \frac{\upsilon \hat{l}_0 C (1+\frac{1}{\Re})}{4(1-\varepsilon_{kk})^2} \left[\begin{array}{l} \left[\frac{\Re-1}{\Re+1}(2+a_c a_n) + (a_c+a_n+a_t) \right] \mathrm{d}f_0^n \\ +\ldots + f_0^n \left[a_c \frac{\Re-1}{\Re+1} + 1 \right] \mathrm{d}a_n + f_0^n \mathrm{d}a_t \end{array} \right] \tag{7-41}$$

$$(\mathrm{d}^2W)^{volume} = \frac{\upsilon \hat{l}_0 C f_0^n \mathrm{d}\varepsilon_{kk}}{2(1-\varepsilon_{kk})^3} \left[\left(1-\frac{1}{\Re}\right)(2+a_c a_n) + (a_c+a_n+a_t)\left(1+\frac{1}{\Re}\right) \right] \tag{7-42}$$

Recalling Eqs. (4-22) (a-c), the mean stress and the stress deviator are determined as

$$t = \frac{\sigma_{11}-\sigma_{22}}{2} = \frac{\upsilon \hat{l}_0 f_0^n (a_c+a_n+a_t)}{4(1-\varepsilon_{kk})^2}, s = \frac{\sigma_{11}+\sigma_{22}}{2} = \frac{\upsilon \hat{l}_0 f_0^n (2+a_c a_n)}{4(1-\varepsilon_{kk})^2} \tag{7-43}$$

Eqs. (7-40) and (7-42) can be rewritten as

$$(\mathrm{d}^2W)^{fabric} = \frac{Cs}{2-a_c a_n}\left[(1+a_n)+\frac{1}{\Re}(1-a_n)\right]\mathrm{d}a_c \tag{7-44}$$

$$(\mathrm{d}^2W)^{volume} = \frac{2sC\mathrm{d}\varepsilon_{kk}}{1-\varepsilon_{kk}}\left(1+\frac{1}{\Re}\right)\left(\frac{\Re-1}{\Re+1}+\sin\phi\right) = \frac{2sC\mathrm{d}\varepsilon_{kk}}{1-\varepsilon_{kk}}\left(1+\frac{1}{\Re}\right)(\sin\phi+\vartheta) \tag{7-45}$$

By applying Eq. (7-43), the local second-order work $(\mathrm{d}^2W)^{micro}$ becomes

$$(\mathrm{d}^2W)^{micro} = C(1+\frac{1}{\Re})\left\{\left(\frac{\Re-1}{\Re+1}s+t\right)\frac{\mathrm{d}f_0^n}{f_0^n}+\frac{s}{2+a_c a_n}\left[\left(a_c\frac{\Re-1}{\Re+1}+1\right)\mathrm{d}a_n+\mathrm{d}a_t\right]\right\} \tag{7-46}$$

By assuming that $1-\varepsilon_{kk}\approx 1$ and $2+a_c a_n \approx 2$, hence $\mathrm{d}s/s \approx \mathrm{d}f_0^n/f_0^n$. Then, Eq. (7-41) can be simplified as

$$(\mathrm{d}^2W)^{micro} \approx C(1+1/\Re)\left\{(\sin\phi+\vartheta)\mathrm{d}s+\frac{s}{2}(1+\vartheta a_c+\xi)\mathrm{d}a_n\right\} \tag{7-47}$$

in which $\vartheta=(\Re-1)/(\Re+1)$, $\xi=\mathrm{d}a_t/\mathrm{d}a_n$. It should be noted that the above analysis is limited to the case when the major principal stress and the major principal fabric are coaxial with $\theta_\sigma=\theta_c=\pi/2$. According to Chapter 6, this assumption holds true for the VED test, all VED tests and VEC tests with $1<\Re<10.8$.

Base on Eqs. (7-47), (7-44) and (7-45), for tests along proportional strain paths with $\Re>0$, the following conclusions can be obtained:

(1) $(\mathrm{d}^2W)^{fabric}$ is always positive when $\mathrm{d}a_c>0$.

(2) may be positive or negative depending on the imposed strain rate. According to Eq. (7-45), $(\mathrm{d}^2W)^{volume}>0$ when $\mathrm{d}\varepsilon_{kk}<0$ & $t/s+\vartheta<0$ corresponding to $0<\Re<\frac{1-t/s}{1+t/s}$, or when $\mathrm{d}\varepsilon_{kk}>0$ & $t/s+\vartheta>0$ corresponding to $\Re>1$. In other words, global volumetric dilation does not guarantee $(\mathrm{d}^2W)^{volume}<0$, for

example, $(\mathrm{d}^2W)^{volume} < 0$ when $\frac{1-t/s}{1+t/s} < \Re < 1$.

(3) The average local second-order work $(\mathrm{d}^2W)^{micro}$ is significantly affected by the distribution of the normal contact forces. A decrease of a_n tends to reduce $(\mathrm{d}^2W)^{micro}$ and results in the vanishing of $(\mathrm{d}^2W)^{micro}$. Since a_n is closely related to the strong force chain network, the decrease of a_n implies the degradation of the strong network during shearing. This is consistent with the observation obtained from Figure 7-3 (a) that the onset of deformation instability is accompanied by a degradation or progressive collapse of strong sub-network. However, degradation of strong sub-network does not guarantee macroscopic unstable deformation owing to the contribution of $(\mathrm{d}^2W)^{fabric}$ or $(\mathrm{d}^2W)^{micro}$ to the overall second-order work d^2W.

As a special case, for the isochoric compression test in which $\Re = 1$ and $\mathrm{d}\varepsilon_{kk} = 0$, the Eqs. (7-40) to (7-42) are simplified as

$$(\mathrm{d}^2W)^{fabric} = \frac{\upsilon l_0 C f_0^n \mathrm{d}a_c}{2} \tag{7-48}$$

$$(\mathrm{d}^2W)^{micro} = \frac{\upsilon \hat{l}_0 C\left[\mathrm{d}f_0^n(a_c + a_n + a_t) + f_0^n(\mathrm{d}a_n + \mathrm{d}a_t)\right]}{2} \tag{7-49}$$

$$(\mathrm{d}^2W)^{volume} = 0 \tag{7-50}$$

It follows that

$$\mathrm{d}^2W = (\mathrm{d}^2W)^{fabric} + (\mathrm{d}^2W)^{micro} = \frac{1}{2}\upsilon \hat{l}_0 C\mathrm{d}\left[f_0^n(a_c + a_n + a_t)\right] = 2C\mathrm{d}t \tag{7-51}$$

Eq. (7-51) is identical to the macro-level expression of d^2W:

$$\mathrm{d}^2W = \mathrm{d}\sigma_{ij}\mathrm{d}\varepsilon_{ij} = \mathrm{d}s\mathrm{d}\varepsilon_v + \mathrm{d}t\mathrm{d}\gamma = 2C\mathrm{d}t \tag{7-52}$$

In previous chapters, the relation between the fabric anisotropy factor a_c and the

fabric deviator q_ϕ was obtained as $a_c = 2q_\phi$. Eqs. (7-48) to (7-51) show that $\mathrm{d}^2W = 0$ and $(\mathrm{d}^2W)^{micro} = 0$ do not necessarily take place at the same time. Depending on how the fabric tensor evolves during shearing, it is possible that the specimen is locally stable but macroscopically unstable owing to the fabric change or vice versa. More specifically, when $(\mathrm{d}^2W)^{micro} = 0$ while $\mathrm{d}q_\phi = 0$, the macro-level second-order work will still be positive. On the other side, when degradation of the fabric occurs, $\mathrm{d}^2W = 0$ is possible when $(\mathrm{d}^2W)^{micro} > 0$.

It is noted that all terms of second-order work calculated from DEM simulation results of 2D tests along proportional strain paths were normalized using the unit time or the constant vertical strain ratio as

$$\left(d^2W\right)^F = \frac{\left(d^2W\right)^{fabric}}{\Delta t}, \left(d^2W\right)^M = \frac{\left(d^2W\right)^{micro}}{\Delta t}, \left(d^2W\right)^V = \frac{\left(d^2W\right)^{volume}}{\Delta t} \qquad (7\text{-}53)$$

where $\Delta t = \frac{\Delta \varepsilon_1}{C}$ and C is the constant vertical strain rate. For convenience, we make $\left(d^2W\right)^{fabric} = \left(d^2W\right)^F$, $\left(d^2W\right)^{micro} = \left(d^2W\right)^M$ and $\left(d^2W\right)^{volume} = \left(d^2W\right)^V$ in the following discussions. Figure 7-6 (a) presents the evolution of d^2W together with its components $(\mathrm{d}^2W)^{micro}$, $(\mathrm{d}^2W)^{fabric}$ and $(\mathrm{d}^2W)^{volume}$ obtained from the DEM simulation for the test with $\Re = 1.0$. d^2W was mostly contributed by the average of the local second-order work, which was approximately 80% of d^2W. $(\mathrm{d}^2W)^{fabric}$ was approximately 20% of d^2W and could not be neglected. Figure 7-6 (b) presents the evolutions of $(\mathrm{d}^2W)^{fabric}$ and a_c with the shear strain, which confirmed the relation in Eq. (7-48) and $(\mathrm{d}^2W)^{fabric}$ vanished when a_c reached its peak value. Even though d^2W was initially larger than $(\mathrm{d}^2W)^{micro}$, the decrease of $(\mathrm{d}^2W)^{fabric}$ resulted in vanishing of d^2W prior to $(\mathrm{d}^2W)^{micro}$, as can be observed from Figure 7-6

(a).

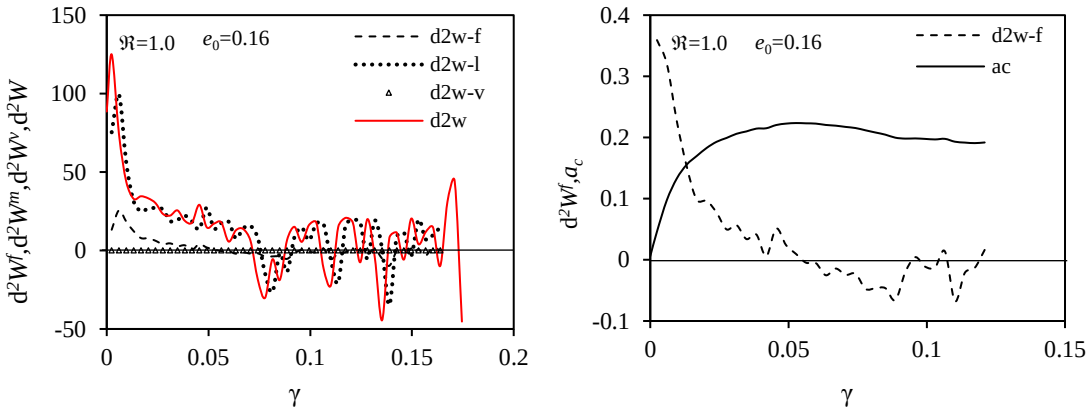

(a) (b)

Figure 7-6: (a) Evolution of the second-order work and its three components associated with the shear strain; (b) Evolution of $(\mathrm{d}^2W)^{fabric}$ and a_c with the shear strain in VEI test: $\Re = 1.0$, e_0=0.16

For tests along the strain path with $\Re = 10$, the evolution of the second-order work computed from the micromechanical analysis using the DEM simulation results is presented in Figure 7-7 (a). In this case, the specimen was sheared along a forced contraction strain path with $\vartheta > 0$. Consequently, the second-order work induced by volume change, $(\mathrm{d}^2W)^{volume}$, was always positive according to Eq. (7-42). However, $(\mathrm{d}^2W)^{fabric}$ initially increased and then vanished at approximately $\gamma = 0.05$ where da_c approached zero and a_c approached its maximum value. After that, a_c decreased and $(\mathrm{d}^2W)^{fabric}$ became negative, as shown in Figure 7-7(b). $(\mathrm{d}^2W)^{fabric}$ formed only a small fraction of d^2W (less than approximately 3%). Owing to the continuous increase in $(\mathrm{d}^2W)^{volume}$ and the volume compaction of the specimen, the deformation of the specimen was always stable with $\mathrm{d}^2W > (\mathrm{d}^2W)^{fabric} > 0$ even

though $(\mathrm{d}^2W)^{fabric}$ vanished at $\gamma = 0.05$. The results are consistent with that in Figure 7-4 in which a decrease in $a_c (= 2q_\phi)$ did not induce deformation instability.

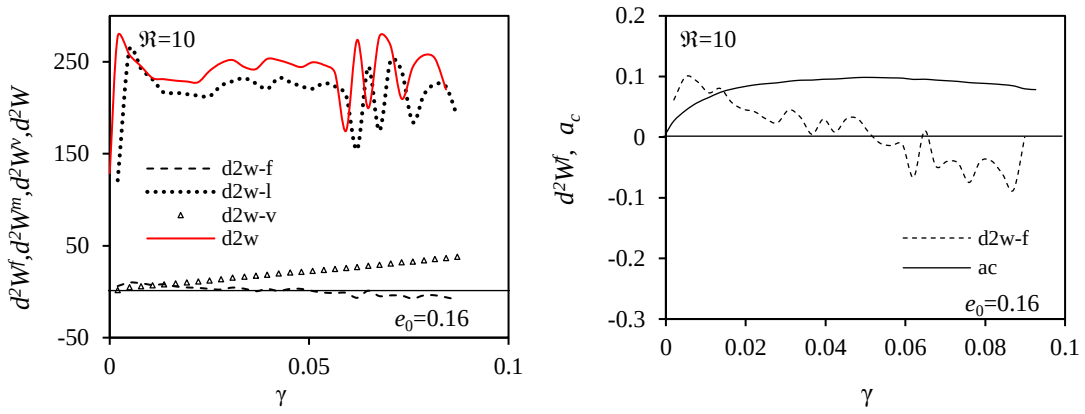

(a) (b)

Figure 7-7: (a) Evolution of the second-order work and its three components with the shear strain; (b) evolution of $(\mathrm{d}^2W)^{fabric}$ and a_c with the shear strain in VEC test: $\Re = 10$, e_0=0.16

For tests along strain paths with $0 < \Re < 1$, the term $(1+a_n)+(1-a_n)/\Re$ in Eq. (7-42) was always positive, which implies that $(\mathrm{d}^2W)^{fabric}$ can be negative only when $\mathrm{d}a_c$. As shown in Figure 7-8, when $\Re = 0.5$, $(\mathrm{d}^2W)^{fabric}$ initially increased to its peak then decreased gradually with the shear strain. $(\mathrm{d}^2W)^{fabric}$ vanished when the peak fabric deviator was approached. In this case, even though d^2W was initially larger than $(\mathrm{d}^2W)^{micro}$, the decrease of $(\mathrm{d}^2W)^{fabric}$ resulted in vanishing of d^2W, $(\mathrm{d}^2W)^{micro}$, and $(\mathrm{d}^2W)^{fabric}$ at the same time; as can be observed from Figure 7-8 (a).

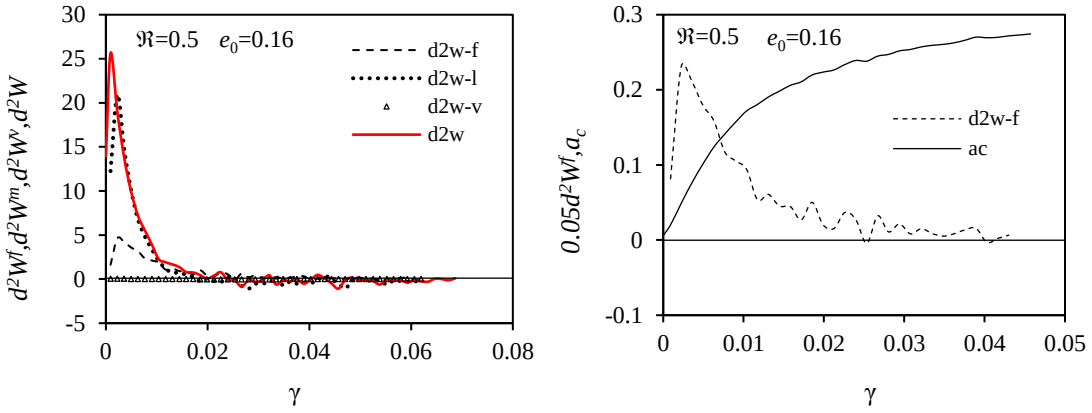

(a) (b)

Figure 7-8: (a) Evolution of the second-order work and its three components with the shear strain; (b) evolution of $(\mathrm{d}^2W)^{fabric}$ and a_c with the shear strain in VED test: $\Re = 0.5$, e_0=0.16

7.5 Fabric evolution and instability in 3D tests

To better understand the evolution of the second-order work and fabric evolution under general 3D stress conditions, a series of DEM simulations were carried out along radial stress paths on the π-plane with the mean effective stress $p = 300kPa$ at select b coefficient, which corresponds to a constant Lode angle on the π-plane. In these simulations, the specimens were isotropically consolidated and the values of the normal and tangential stiffness were k^n=k^s = 4×10^{4}N/m. Figure 7-9 presents the evolution of the second-order work and fabric anisotropy in different contact networks. The results of the triaxial compression test (b=0) are presented in Figure 7-9 (a). With the increase of the deviatoric strain ε_q, q_ϕ^w, q_ϕ^s and q_ϕ all increased initially. However, q_ϕ^w quickly increased to its peak value at $\varepsilon_q = 0.019$ while q_ϕ^s and q_ϕ were still increasing. With further increase of ε_q, q_ϕ^s and q_ϕ continued to increase but q_ϕ^w decreased, indicating a degradation of the weak force chain network. During

this process, the second-order work d^2W continuously decreased. When q_ϕ^s approached its maximum at $\varepsilon_q = 0.093$, $\mathrm{d}^2W \to 0$ simultaneously. At this moment, the value of q_ϕ was still increasing. The second-order work was positive at the peak value of q_ϕ^w in all tests with various stress paths. With further increase of shear strain, d^2W stayed at very small value around zero, while q_ϕ^w and q_ϕ^s continuously decreased with q_ϕ increasing until a steady state was reached. At this steady state, the value of q_ϕ^w was close to zero, implying that the weak force chain network was nearly isotropic. For other stress paths with different *b*-values, q_ϕ^w, q_ϕ^s, q_ϕ and d^2W varied following the same trends.

In the 3D tests along radial stress paths on the π-plane, we normalized the second-order work using the the constant vertical strain ratio ($\mathrm{d}\varepsilon_1$) as

$$d^2W = \frac{d\sigma_{ij} d\varepsilon_{ij}}{\left(d\varepsilon_1\right)^2} \tag{7-54}$$

Figure 7-10 summarizes the relation between d^2W and the degree of fabric anisotropy in the strong and weak sub-networks respectively along stress paths with different *b*-values. As shown in Figure 7-10 (a), regardless of the *b*-value, d^2W decreased monotonically while q_ϕ^s of the strong network increased. The results clearly showed that the second-order work vanished when $q_\phi^s \to q_{\phi,\max}^s$. The results in Figure 7-10 (a) confirmed that q_ϕ^w reached a peak value prior to the vanishing of d^2W in all simulations. Then q_ϕ^w decreased quickly to a near-zero value when $\mathrm{d}^2W \to 0$.

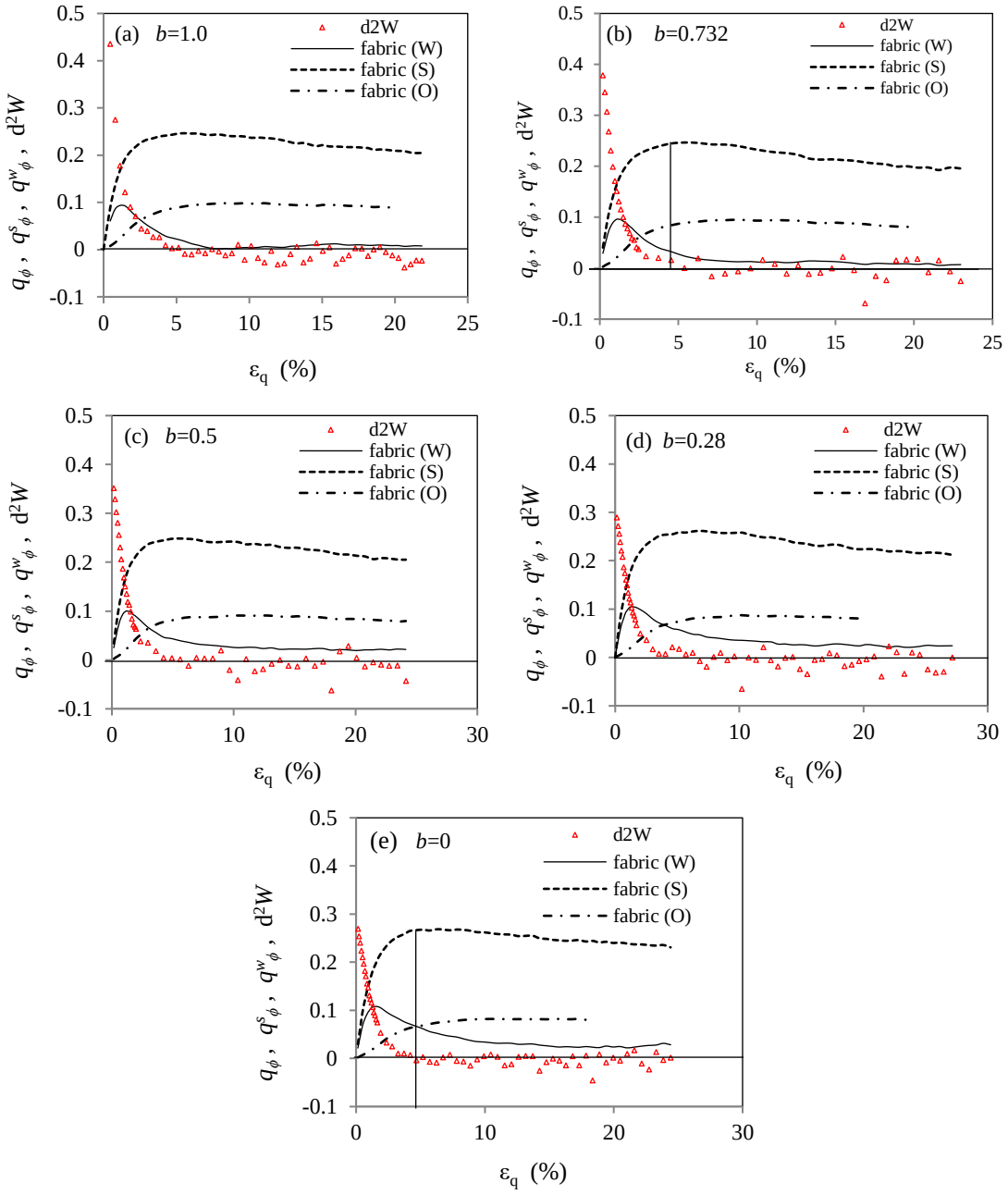

Figure 7-9: Variation of fabric anisotropy in different contact networks and d^2W in 3D tests along stress paths with constant *b*-value: *p*=300 kPa, $k^n=k^s= 4\times10^4$N/m

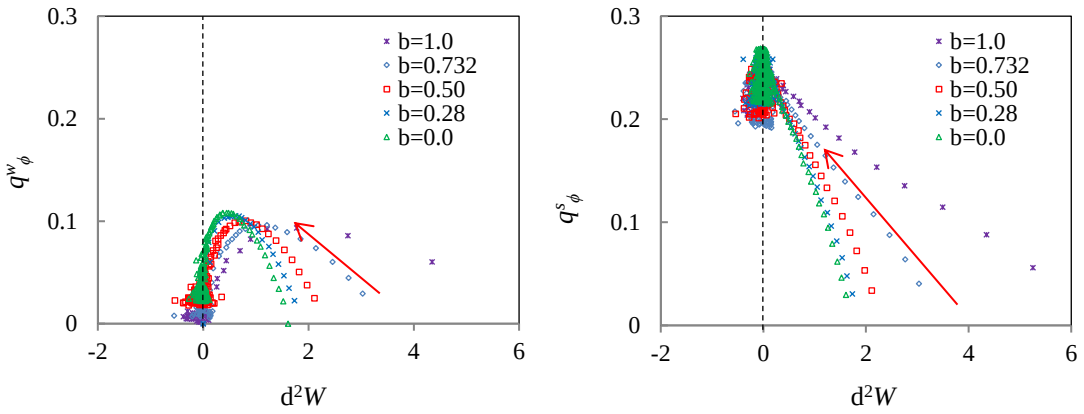

Figure 7-10: Variation of fabric anisotropy of (a) the strong sub-network, and (b) the weak sub-network with d^2W in 3D tests along different stress paths: p=300kPa and k^n=k^s= 4×10^{4}N/m

In conclusion, the results obtained from DEM simulations along radial stress paths on the π-plane confirm the finding from 2D DEM simulations for tests along proportional strain paths. More specifically, the degradation of strong sub-network (i.e., the decrease of q^s_ϕ) is a necessary but not a sufficient condition of instability, while a degradation of the weak sub-network is the indicator of deformation instability. The fabric evolution plays an important role in composing the second-order work. Thus the vanishing of directional average local second-order work does not mean the macroscopic instability. Moreover, the evolution of the fabric anisotropies in sub-network works can be used to characterize the vanishing of the second-order work macroscopically.

7.6 Summary

The instability of a granular material might be initiated from the variation of its internal structure. The fabric tensor, characterizing the geometric arrangement of the

microstructure, should be involved in the macroscopic instability of granular materials. In this chapter, the evolution of fabric in different contact networks was investigated to identify potential relations between fabric and the material instability in Hill's sense. The DEM simulations for granular materials along proportional strain paths under 2D conditions and radial stress paths on the π-plane under 3D stress conditions revealed that the degradation of strong sub-network is a necessary but not a sufficient condition of instability, while the degradation of the weak sub-network is the indicator of deformation instability in tests along all imposed strain paths.

In addition to DEM simulations, this chapter provided a micro-interpretation for the vanishing of the second-second order work. The macroscopic second-order work can be decomposed into three terms: the average of the local directional second-order work associated with inter-particle contact forces and relation displacements, the term accounts for the volume change of the granular assembly and the term related to the change of fabric. It was shown that vanishing of the macro-level second-order work was dependent on the fabric degradation of the granular assembly, particularly the strong force chain network.

Physically, the strong sub-network dominants the shear resistance and the weak sub-network provides supports to the strong contacts. The results from 2D tests along proportional strain paths indicated that the fabric anisotropies for sub-networks can be used to identify the vanishing of macroscopic second-order work. Moreover, the degradation of strong sub-network (i.e., the decrease of q_{ϕ}^{s}) is found to be a necessary but not a sufficient condition of instability. In other words, deformation instability is accompanied by strong network degradation but not opposite. On the other hand, a decrease of q_{ϕ}^{w} or the degradation of weak sub-network is the indicator of deformation instability in tests along all imposed strain paths.

Chapter 8 Conclusions and Discussions

8.1 Main contributions

In this research, the focus was placed on the behaviour of granular materials subjected to quasi-static shear in terms of the fabric evolution including the magnitude and direction of anisotropy for different contact networks. Both statistical and micromechanical approaches were adopted to obtain the macroscopic properties, such as the fabric tensor, Cauchy stress tensor and the second-order work, in terms of the micro-scale variables. A series of DEM simulations were conducted to simulate laboratory tests along fixed loading paths; for example, 2D tests along proportional strain paths, 2D simple shear tests and 3D tests along radial stress paths on the π-plane. The following conclusions can be addressed based on the research accomplished within this thesis.

(1) Using statistic approach, the fabric-stress relation is obtained and equivalent to the stress-force-fabric function presented by other researchers. The relation between the orientations of the major principal stress and the major principal fabric component is presented in Eq. (6-2).

(2) DEM results show that the induced fabric anisotropy within overall contact network can be related with the deviatoric stress ratio q/p (in 3D) or t/s (in 2D) through $q_\phi = A(t/s)^n$ or $q_\phi = B(q/p)^z$ before the peak stress state with parameters of A and n depending on the stress paths and the parameters of B and z depending on the strain increment rate.

(3) After the peak stress state, the stress-fabric relation (in 3D) for the overall contact network can be described using $\phi_1 : \phi_2 : \phi_3 = (\sigma_1)^m : (\sigma_2)^m : (\sigma_3)^m$, where m ranges within 0.3~0.4. The shape of the fabric response envelope for the overall

contact network is that of a small inverted Lade's surface at critical state in Eq.(5-11). The ratio of the parameters b^*/a^* ranges from 1.0 to 1.2.

(4) For the strong sub-network, the stress-fabric relation yields to $\phi_1^s:\phi_2^s:\phi_3^s=\sigma_1:\sigma_2:\sigma_3$ or $\phi_1^s:\phi_2^s=\sigma_1:\sigma_2$ throughout the loading process in 3D or 2D cases along general loading conditions. This relation is independent of the stress or strain paths, the friction coefficient, the contact stiffness. At critical state, the fabric response envelopes for the strong sub-network shows similar shape with the Lade's surface and is much larger than that of the fabric for the overall contact network.

(5) The macro second-order work can be interpreted into three parts: directional average second-order work from the contact plane, a part induced by the fabric evolution and a part induced by the volumetric change. The second-order work induced by the fabric evolution cannot be neglected. Moreover, a decrease of q_ϕ^w or the degradation of weak sub-network is the indicator of deformation instability. The degradation of strong sub-network (i.e., the decrease of q_ϕ^s) is a necessary but not a sufficient condition of instability.

(6) The orientation of the major principal stress is always coaxial with that of the fabric for strong sub-network which is perpendicular to the direction of the major principal component of the fabric tensor for the weak sub-network. The fabric anisotropy within overall contact network is expressed in terms of those in sub-networks as $q_\phi=\alpha q_\phi^s-(1-\alpha)q_\phi^w$ with α is the ratio of strong contact number in the overall contact network.

(7) It is notable that the direction of the principal fabric tensor in the overall contact network may rotate 90° in tests along forced high contraction strain paths, which implies that the degree of induced fabric anisotropy in overall contact network may become isotropic instantaneously when the principal direction of fabric tensor

rotates. However, the orientation of the major principal fabric in strong sub-network is always coaxial with the major principal stress direction regardless of the major principal stress rotating or not. Moreover, $\left|\theta_c^s - \theta_c^w\right| = 90°$ indicates that the weak sub-network provide supports for the strong contact which contributes to the majority of the shear stress since $\left|\theta_\sigma - \theta_c^s\right| \approx 0°$.

8.2 Future works

Once the evolution of the microstructure has been quantified, the macro response of the granular material can be interpreted micromechanically. Moreover, the fabric evolution can be added into the modeling under continuum framework. Some other interesting studies could be further explored within the scope of this thesis. The following works will be considered in the future.

(1) Verification of the fabric-stress evolution law

In order to verify the fabric-stress relation, irregular shape particles and rolling resistance should be properly considered in DEM simulations. Moreover, this relation can also be verified by results of laboratory tests using photo-elastic material.

(2) A unique critical fabric for granular material

At critical state, the induced fabric anisotropy is relatively high and varies with the loading path. The critical state theory does involve a local level parameter, the void ratio which quantifies the void cell system of granular material according to (Li and Li, 2009). However, the fabric structure or the solid cell system is found to be critical for the stress-strain behavior of the granular material. Therefore, the unique critical state needs to consider the fabric anisotropy based on the contact normals.

(3) Continuum model with a consideration of fabric evolution

Employing the fabric evolution law into the continuum modeling of the granular material is critical for better understanding the macro behavior of sand. One approach

is adding the fabric to the yielding surface and the plastic potential function.

(4) Hydro-DEM coupling

The real granular material shows multiphase, such as the air, solid, water. For simplicity, both the solid skeleton and the pore water can be considered. The coupling procedure can be computed as a DEM implementation plus a computational fluid dynamics.

Bibliography

Ai, J., Langston, P.A., Yu, H.S., 2014a. Discrete Element Modeling of Material Non-coaxiality in Simple Shear Flows. Int. J. Numer. Anal. Methods Geomech. 38(6), 615–635. https://doi.org/10.1002/nag.2230

Ai, J., Langston, P.A., Yu, H.S., 2014b. Discrete element modeling of material non-coaxiality in simple shear flows. Int. J. Numer. Anal. Methods Geomech. 38(6), 615–635.

Antony, S.J., Momoh, R.O., Kuhn, M.R., 2004. Micromechanical modelling of oval particulates subjected to bi-axial compression. Comput. Mater. Sci. 29(4), 494–498. https://doi.org/10.1016/j.commatsci.2003.12.007

Arthur, J.R.F., Chua, K.S., Dunstan, T., 1977. Induced anisotropy in a sand. Geotechnique 27(1), 13–30.

Azéma, E., Radjaï, F., 2012. Force chains and contact network topology in sheared packings of elongated particles. Phys. Rev. E - Stat. Nonlinear, Soft Matter Phys. 85(3). https://doi.org/10.1103/PhysRevE.85.031303

Bagi, K., 1996. Stress and strain in granular assemblies. Mech. Mater. 22(3), 165–177. https://doi.org/10.1016/0167-6636(95)00044-5

Bardet, J.P., 1998. Introduction to computational granular mechanics, in: Behaviour of Granular Materials. Springer, pp. 99–169.

Barreto, D., O'Sullivan, C., 2012. The influence of inter-particle friction and the intermediate stress ratio on soil response under generalised stress conditions. Granul. Matter 14(4), 505–521. https://doi.org/10.1007/s10035-012-0354-z

Bathurst, R.J., 1985. A study of stress and anisotropy in idealized granular assemblies. Qween's University.

Bathurst, R.J., Rothenburg, L., 1992. Micromechanical features of granular assemblies with planar elliptical particles. Géotechnique 42(1), 79–95. https://doi.org/10.1680/geot.1992.42.1.79

Bathurst, R.J., Rothenburg, L., 1988. Micromechanical aspects of isotropic granular assemblies with linear contact interactions. J. Appl. Mech. 55(1), 17–23. https://doi.org/10.1115/1.3173626

Been, K., Jefferies, M.G., 1985a. A state parameter for sands. Géotechnique 35(2), 99–112. https://doi.org/10.1680/geot.1985.35.2.99

Been, K., Jefferies, M.G., 1985b. A state parameter for sands. Géotechnique 35(2), 99–112. https://doi.org/10.1680/geot.1985.35.2.99

Belheine, N., Plassiard, J.-P., Donze, F.-V., Darve, F., Seridi, A., 2009. Numerical simulation of drained triaxial test using 3D discrete element modeling. Comput. Geotech. 36, 320–331. https://doi.org/10.1016/j.compgeo.2008.02.003

Brewer, R., 1964. Fabric and Mineral Analysis of Soils. John Wiley, New York.

Cai, Y., Yu, H.-S., Wanatowski, D., Li, X., 2013. Noncoaxial behavior of sand under

various stress paths. J. Geotech. Geoenvironmental Eng. 139(8), 1381–1395. https://doi.org/10.1061/(ASCE)GT.1943-5606.0000854

Calvetti, F., Viggiani, G., Tamagnini, C., 2003. A numerical Investigation of the Incremental Behaviour of Granular Soils. Riv. Ital. di Geotec. (37), 11–29.

Castro, G., 1969. Liquefaction of sands, Harvard Soil Mechanics Series No. 81. Harvard University.

Chang, C., Gao, J., 1996. Kinematic and static hypotheses for constitutive modelling of granulates considering particle rotation. Acta Mech. 115, 213–229. https://doi.org/10.1007/BF01187439

Chang, C.S., 1993. Micromechanical modeling of deformation and failure for granulates with frictional contacts. Mech. Mater. 16(1–2), 13–24. https://doi.org/10.1016/0167-6636(93)90023-K

Chang, C.S., Liao, C.L., 1990. Constitutive relation for a particulate medium with the effect of particle rotation. Int. J. Solids Struct. 26(4), 437–453. https://doi.org/10.1016/0020-7683(90)90067-6

Chang, C.S., Ma, L., 1991. A micromechanical-based micropolar theory for deformation of granular solids. Int. J. Solids Struct. 28(1), 67–86. https://doi.org/10.1016/0020-7683(91)90048-K

Chang, C.S., Yin, Z.Y., Hicher, P.Y., 2011. Micromechanical analysis for interparticle and assembly instability of sand. J. Eng. Mech. 137(3), 155–168. https://doi.org/Doi 10.1061/(Asce)Em.1943-7889.0000204

Chantawarungal, K., 1993. Numerical simulations of three dimensional granular assemblies. University of Waterloo.

Cheng, Y.., Nakata, Y., Bolton, M.D., 2003. Discrete element simulation of crushable soil. Géotechnique 53(7), 633–641. https://doi.org/10.1680/geot.2003.53.7.633

Chowdhury, E.Q., Nakai, T., 1998. Consequences of the t(ij)-concept and a new modeling approach. Comput. Geotech. 23(3), 131–164. https://doi.org/10.1016/S0266-352X(98)00017-2

Christoffersen, J., Mehrabadi, M.M., Nemat-Nasser, S., 1981. A micromechanical description of granular material behavior. J. Appl. Mech. Trans. ASME 48(2), 339–344. https://doi.org/10.1115/1.3157619

Chu, J., Lo, S. -C. R., Lee, I.K., 1993. Instability of Granular Soils under Strain Path Testing. J. Geotech. Eng. 119(5), 874–892. https://doi.org/10.1061/(ASCE)0733-9410(1993)119:5(874)

Collins, I.F., Muhunthan, B., 2003. On the relationship between stress–dilatancy, anisotropy, and plastic dissipation for granular materials. Géotechnique 53(7), 611–618. https://doi.org/10.1680/geot.2003.53.7.611

Cui, L., O'Sullivan, C., 2006. Exploring the macro- and micro-scale response of an idealised granular material in the direct shear apparatus. Géotechnique 56(7), 455–468. https://doi.org/10.1680/geot.2006.56.7.455

Cundall, P.A., 2004. PFC2D user's manual (Version 3.1). Minnesota Itasca Consult. Gr. Inc 325.

Cundall, P.A., 1987. Discrete Element Models of Rock and Soil Structure. Anal. Comput. methods Eng. rock Mech. 126–163.

Cundall, P.A., 1971. A computer model for simulating progressive large-scale movements in blocky rock systems, in: Proocedings of the Symposio of the International Society of Rock Mechanics, Nancy 2. p. No. 8.

Cundall, P.A., Strack, O.D.L., 1979. A discrete numerical model for granular assemblies. Géotechnique 29(1), 47–65. https://doi.org/10.1680/geot.1979.29.1.47

Dabeet, A., Wijewickreme, D., Byrne, P., 2015. Evaluation of stress strain non-uniformities in the laboratory direct simple shear test specimens using 3D discrete element analysis. Geomech. Geoengin. 10(4), 249–260. https://doi.org/10.1080/17486025.2014.979889

Dafalias, Y.F., 1986. An anisotropic critical state soil plasticity model. Mech. Res. Commun. 13(6), 341–347.

Dafalias, Y.F., Li, X.S., 2004. A constitutive framework for anisotropic sand including non-proportional loading. Géotechnique 54(1), 41–55. https://doi.org/10.1680/geot.2004.54.1.41

Daouadji, A., Hicher, P.Y., Jrad, M., Sukumaran, B., Belouettar, S., 2013. Experimental and numerical investigation of diffuse instability in granular materials using a microstructural model under various loading paths. Geotechnique 63(5), 368–381. https://doi.org/10.1680/geot.10.P.121

Darve, F., Laouafa, F., 2000. Instabilities in granular materials and application to landslides. Mech. Cohesive-Frictional Mater. 5(8), 627–652. https://doi.org/10.1002/1099-1484(200011)5:8<627::AID-CFM109>3.0.CO;2-F

David, C.T., García-Rojo, R., Hermann, H.J., Luding, S., 2007. Powder flow testing with 2D and 3D biaxial and triaxial simulations. Part. Part. Syst. Charact. 24(1), 29–33. https://doi.org/10.1002/ppsc.200601052

Davoudzadeh, F., 1982. Responses of Sand to Three Independently Controlled Principal Stresses. University of London.

Drescher, A., de Josselin de Jong, G., 1972. Photoelastic verification of a mechanical model for the flow of a granular material. J. Mech. Phys. Solids 20(5), 337–340. https://doi.org/10.1016/0022-5096(72)90029-4

Drucker, D.C., 1957. A definition of stable inelastic material. J. Appl. Mech. 26(1), 101–106. https://doi.org/10.2307/1146143

Emeriault, F., Cambou, B., 1996. Micromechanical modelling of anisotropic non-linear elasticity of granular medium. Int. J. Solids Struct. 33(18), 2591–2607. https://doi.org/10.1016/0020-7683(95)00170-0

Emeriault, F., Chang, C.S., 1997. Interparticle forces and displacements in granular

materials. Comput. Geotech. 20(3–4), 223–244. https://doi.org/10.1016/S0266-352X(97)00004-9

Favier, J.F., Abbaspour-Fard, M.H., Kremmer, M., Raji, A.O., 1999. Shape representation of axi-symmetrical, non-spherical particles in discrete element simulation using multi-element model particles. Eng. Comput. 16(4), 467–480. https://doi.org/10.1108/02644409910271894

Field, W.G., 1963. Toward the statistical definition of a granular mass, in: Proc. 4th A. and N. Z. Conf. On Soil Mech. pp. 143–148.

Fu, P., Dafalias, Y.F., 2015. Relationship between void- and contact normal-based fabric tensors for 2D idealized granular materials. Int. J. Solids Struct. 63, 68–81. https://doi.org/10.1016/j.ijsolstr.2015.02.041

Fu, P., Dafalias, Y.F., 2011. Fabric evolution within shear bands of granular materials and its relation to critical state theory. Int. J. Numer. Anal. Methods Geomech. 35(18), 1918–1948. https://doi.org/10.1002/nag.988

Fu, P., Walton, O.R., Harvey, J.T., 2012. Polyarc discrete element for efficiently simulating arbitrarily shaped 2D particles. Int. J. Numer. Methods Eng. 89(5), 599–617.

Gao, Z., Zhao, J., 2017. A non-coaxial critical-state model for sand accounting for fabric anisotropy and fabric evolution. Int. J. Solids Struct. 106–107, 200–212. https://doi.org/10.1016/j.ijsolstr.2016.11.019

Gao, Z., Zhao, J., 2013. Strain localization and fabric evolution in sand. Int. J. Solids Struct. 50(22–23), 3634–3648. https://doi.org/10.1016/j.ijsolstr.2013.07.005

Gao, Z., Zhao, J., Li, X.S., Dafalias, Y.F., 2014. A critical state sand plasticity model accounting for fabric evolution. Int. J. Numer. Anal. Methods Geomech. 38(4), 370–390. https://doi.org/10.1002/nag.2211

García, X., Medina, E., 2008. Strong-weak network anisotropy switching and hysteresis in three-dimensional granular materials. Phys. Rev. E - Stat. Nonlinear, Soft Matter Phys. 78(2). https://doi.org/10.1103/PhysRevE.78.021305

Goddard, J.D., 1999. Granular dilatancy and plasticity of glassy lubricants. Ind. Eng. Chem. Res. (38), 820–822.

Goldenberg, C., Goldhirsch, I., 2005. Friction Enhances Elasticity in Granular Solids. Nature 435(7039), 188–191.

Guo, P., Su, X., 2007. Effect of dilatancy on instability, pre-instability strain softening of sand along proportional strain paths. Soils Found. 47(4), 757–770.

Gutierrez, M., Ishihara, K., 2000. Non-coaxiality and energy dissipation in granular materials. Soils Found. 40(2), 49–59.

Gutierrezl, M., Lshiharam, K., Towhata, L., 1991. Flow theory for sand during rotation of principal stress direction. SOILS Found. 31(4), 121–132. https://doi.org/10.1248/cpb.37.3229

Hardin, B.O., 1989. Low-Stress Dilation Test. J. Geotech. Eng. 115(6), 769–787.

https://doi.org/10.1061/(ASCE)0733-9410(1989)115

Hertz, H., 1882. Über die Berührung fester elastischer Körper. J. für die reine und Angew. Math. 92, 156–171.

Hicher, P.Y., Chang, C.S., 2005. Evaluation of two homogenization techniques for modeling the elastic behavior of granular materials. J. Eng. Mech. 131(11), 1184–1194. https://doi.org/Doi 10.1061/(Asce)0733-9399(2005)131:11(1184)

Hight, D.W., Gens, A., Symes, M.J., 1983. The development of a new hollow cylinder apparatus for investigating the effects of principal stress rotation in soils. Geotechnique 33(4), 355–383.

Hill, R., 1958. A general theory of uniqueness and stability in elastic-plastic solids. J. Mech. Phys. Solids 6(3), 236–249. https://doi.org/10.1016/0022-5096(58)90029-2

Hill, R., 1950. The mathematical theory of plasticity. Oxford university press.

Hosseininia, E.S., 2015. A micromechanical study on the stress rotation in granular materials due to fabric evolution. Powder Technol. (283), 462–474. https://doi.org/10.1016/j.powtec.2015.06.013

Huang, X., Hanley, K.J., O'Sullivan, C., Kwok, C.Y., 2014. Exploring the influence of interparticle friction on critical state behaviour using DEM. Int. J. Numer. Anal. Methods Geomech. 38(12), 1276–1297. https://doi.org/10.1002/nag.2259

Ishibashi, I., Capar, O.F., 2003. Anisotropy and its Relation to Liquefaction Resistance of Granular Material. Soils Found. 43(5), 149–159. https://doi.org/10.3208/sandf.43.5_149

Ishihara, K., 1983. Soil response in cyclic loading induced by earthquakes traffic and waves, in: 7th Asian Reg. Conf. Soil Mech. Found. Eng. pp. 42–46.

Iwashita, K., Oda, M., 1998. Rolling resistance at contacts in simulation of shear band development by DEM. J. Eng. Mech. 124(3), 285–292. https://doi.org/10.1061/(ASCE)0733-9399(1998)124:3(285)

Jenkins, J.T., 1987. Volume change in small strain axisymmetric deformations of a granular material, in: Micromechanics of Granular Materials. pp. 245–252.

Jenkins, J.T., Strack, O.D.L., 1993. Mean-field inelastic behavior of random arrays of identical spheres. Mech. Mater. 16(1–2), 25–33. https://doi.org/10.1016/0167-6636(93)90024-L

Jiang, M., Yu, H., Harris, D., 2006. Kinematic variables bridging discrete and continuum granular mechanics. Mech. Res. Commun. 33(5), 651–666. https://doi.org/10.1016/j.mechrescom.2005.06.013

Joer, H., Lanier, J., Flavigny, E., 1992. "1γ2ε": A new shear apparatus to study the behavior of granular materials. ASTM Geotech. Test. J. 15(2), 129–137. https://doi.org/10.1520/GTJ10235J

Johnson, K.L., 1985. Contact Mechanics. Cambridge University Press, Cambridge.

Konishi, J., Naruse, F., 1988. A note on the fabric in terms of voids, in:

Micromechanics of Granular Materials. pp. 39–46.

Kruyt, N.P., 2016. On weak and strong contact force networks in granular materials. Int. J. Solids Struct. 92–93, 135–140. https://doi.org/10.1016/j.ijsolstr.2016.02.039

Kruyt, N.P., 2012. Micromechanical study of fabric evolution in quasi-static deformation of granular materials. Mech. Mater. 44, 120–129. https://doi.org/10.1016/j.mechmat.2011.07.008

Kruyt, N.P., Rothenburg, L., 2016. A micromechanical study of dilatancy of granular materials. J. Mech. Phys. Solids 95, 411–427.

Kruyt, N.P., Rothenburg, L., 2014. On micromechanical characteristics of the critical state of two-dimensional granular materials. Acta Mech. 225(8), 2301–2318. https://doi.org/10.1007/s00707-014-1128-y

Kuhn, M.R., 1999. Structured deformation in granular materials. Mech. Mater. 31(6), 407–429. https://doi.org/10.1016/S0167-6636(99)00010-1

Kuhn, M.R., Sun, W.C., Wang, Q., 2015. Stress-induced anisotropy in granular materials: fabric, stiffness, and permeability. Acta Geotech. 10(4), 399–419. https://doi.org/10.1007/s11440-015-0397-5

Kuo, C.Y., Frost, J.D., Chameau, J.L.A., 1998. Image analysis determination of stereology based fabric tensors. Geotechnique 48(4), 515–525. https://doi.org/10.1680/geot.1998.48.4.515

Lade, P. V., 2002. Instability, shear banding, and failure in granular materials. Int. J. Solids Struct. 39(13–14), 3337–3357. https://doi.org/10.1016/S0020-7683(02)00157-9

Lade, P. V., 1988. Effects of voids and volume changes on the behaviour of frictional materials. Int. J. Numer. Anal. Methods Geomech. 12(4), 351–370. https://doi.org/10.1002/nag.1610120402

Lade, P. V., Duncan, J.M., 1975. Elastoplastic stress-strain theory for cohesionless soil. J. Geotech. Geoenvironmental Eng. (101).

Lade, P. V, 2008. Failure criterion for cross-anisotropic soils. J. Geotech. Geoenvironmental Eng. 134(1), 117–124. https://doi.org/10.1061/(ASCE)1090-0241(2008)134:1(117)

Lade, P. V, Nelson, R.B., Ito, Y.M., 1988. Instability of Granular Materials with Nonassociated Flow. J. Eng. Mech. 114(12), 2173–2191. https://doi.org/10.1061/(ASCE)0733-9399(1988)114:12(2173)

Li, X., Li, X.S., 2009. Micro-macro quantification of the internal structure of granular materials. J. Eng. Mech. 135(7), 641–656. https://doi.org/10.1061/(ASCE)0733-9399(2009)135:7(641)#sthash.BYUK4rSK.dpuf

Li, X., Yu, H.S., 2013. On the stress-force-fabric relationship for granular materials. Int. J. Solids Struct. 50(9), 1285–1302.

https://doi.org/10.1016/j.ijsolstr.2012.12.023

Li, X., Yu, H.S., 2011. Applicability of stress–force–fabric relationship for non-proportional loading. Comput. Struct. 89(11), 1094–1102. https://doi.org/10.1016/j.compstruc.2010.12.004

Li, X., Yu, H.S., 2009. Influence of loading direction on the behavior of anisotropic granular materials. Int. J. Eng. Sci. 47(11–12), 1284–1296. https://doi.org/10.1016/j.ijengsci.2009.03.001

Li, X.S., Dafalias, Y.F., 2011. Anisotropic critical state theory: role of fabric. J. Eng. Mech. 138(3), 263–275. https://doi.org/10.1061/(ASCE)EM.1943-7889.0000324

Li, X.S., Dafalias, Y.F., 2002. Constitutive modeling of inherently anisotropic sand behavior. J. Geotech. Geoenvironmental Eng. 128(10), 868–880. https://doi.org/10.1061/(ASCE)1090-0241(2002)128:10(868)

Liao, C.L., Chang, T.P., Young, D.H., Chang, C.S., 1997. Stress-strain relationship for granular materials based on the hypothesis of best fit. Int. J. Solids Struct. 34(31–32), 4087–4100. https://doi.org/10.1016/S0020-7683(97)00015-2

Lin, X., Ng, T., 1995. Contact detection algorithms for three-dimensional ellipsoids in discrete element modelling. Int. J. Numer. Anal. Methods Geomech. 19(9), 653–659.

Liu, S.H., Matsuoka, H., 2003. Microscopic interpretation on a stress-dilatancy relationship of granular materials. Soils Found. 43(3), 73–84.

Maeda, K., Hirabayashi, H., Ohmura, A., 2006. Micromechanical influence of grain properties on deformation-failure behaviors of granular media by DEM, in: Geomechanics and Geotechnics of Particulate Media. pp. 173–179.

Masson, S., Martinez, J., 2001. Micromechanical Analysis of the Shear Behavior of a Granular Material. J. Eng. Mech. 127(10), 1007–1016. https://doi.org/10.1061/(ASCE)0733-9399(2001)127:10(1007)

Matiotti, R., Ibraim, E., Doanh, T., 1995. NUMERICAL MODELS IN GEOMECHANICS, G. N. Pande and S. Pietruszczak (Editors).

Matsuoka, H., 1974. Dilatancy characteristics of soil. Soils Found. 14(3), 13–24.

Matsuoka, H., Nakai, T., 1974. stress-deformation and strength characteristics of soil under three different principal stresses. Proc. JSCE (232), 59–70.

Matsuoka, H., Sakakibara, K., Suzuki, Y., 1988. A constitutive model for granular materials evaluating principal stress rotation, in: Micromechanics of Granular Materials. pp. 287–296.

Mehrabadi, M.M., Nemat-Nasser, S., 1983. Stress, dilatancy and fabric in granular materials. Mech. Mater. 2(2), 155–161. https://doi.org/10.1016/0167-6636(83)90034-0

Mehrabadi, M.M., Nemat-Nasser, S., Oda, M., 1982. On statistical description of stress and fabric in granular materials. Int. J. Numer. Anal. Methods Geomech. 6(1), 95–108. https://doi.org/10.1002/nag.1610060107

Mindlin, R.D., 1949. Compliance of elastic bodies in contact. J. Appl. Mech. https://doi.org/10.1007/978-1-4613-8865-4_24

Mindlin, R.D., Deresiewicz, H., 1953. Elastic spheres in contact under varying oblique forces. Am. Soc. Mech. Eng. -- Trans. -- J. Appl. Mech.

Misra, A., Poorsolhjouy, P., 2015. Micro-macro scale instability in 2D regular granular assemblies. Contin. Mech. Thermodyn. 27(1–2), 63–82. https://doi.org/10.1007/s00161-013-0330-9

Miura, Ki., Miura, S., Toki, S., 1986. Deformation Behavior of Anisotropy Dense Sand under principal Stress Axes Rotation. Soils Found. 26(1), 36–52. https://doi.org/http://doi.org/10.3208/sandf1972.26.36

Modaressi, H., Laloui, L., Aubry, D., 1994. Thermodynamical approach for CamClay-family models with Roscoe-type dilatancy rules. Int. J. Numer. Anal. Methods Geomech. 18(2), 133–138. https://doi.org/10.1002/nag.1610180206

Mohamed, A., Gutierrez, M., 2010. Comprehensive study of the effects of rolling resistance on the stress–strain and strain localization behavior of granular materials. Granul. Matter 12(5), 3527–3271. https://doi.org/10.1007/s10035-010-0211-x

Nakata, Y., Hyodo, M., Murata, H., Yasufuku, N., 1998. Flow deformation of sands subjected to principal stress rotation. Soils Found. 38(2), 115–128.

NAKATA, Y., HYODO, M., MURATA, H., YASUFUKU, N., 1998. Flow Deformation of Sands Subjected to Principal Stress Rotation. SOILS Found. 38(2), 115–128. https://doi.org/10.3208/sandf.38.2_115

Nemat-Nasser, S., 1999. Averaging theorems in finite deformation plasticity. Mech. Mater. 31(8), 493–523. https://doi.org/10.1016/S0167-6636(98)00073-8

Nemat-Nasser, S., Lori, M., Datta, S.K., 1996. Micromechanics: Overall Properties of Heterogeneous Materials. J. Appl. Mech. 63, 561. https://doi.org/10.1115/1.2788912

Ng, T., 2001. Fabric evolution of ellipsoidal arrays with different particle shapes. J. Eng. Mech. 127(10), 994–999. https://doi.org/10.1061/(ASCE)0733-9399(2001)127:10(994)

Ng, T.-T., 2009. Discrete element method simulations of the critical state of a granular material. Int. J. Geomech. 9(5), 209–216.

Ng, T.-T., Lin, X., 1997. A three-dimensional discrete element model using arrays of ellipsoids. Géotechnique 47(2), 319–329. https://doi.org/10.1680/geot.1997.47.2.319

Nguyen, N.S., Magoariec, H., Cambou, B., Danescu, A., 2009. Analysis of structure and strain at the meso-scale in 2D granular materials. Int. J. Solids Struct. 46(17), 3257–3271. https://doi.org/10.1016/j.ijsolstr.2009.04.019

Nicot, F., 2004. From constitutive modelling of a snow cover to the design of flexible protective structures Part I—Mechanical modelling. Int. J. Solids Struct. 41(11),

3317–3337.

Nicot, F., 2003. Constitutive modelling of a snow cover with a change in scale. Eur. J. Mech. 22(3), 325–340.

Nicot, F., Daouadji, A., Hadda, N., Jrad, M., Darve, F., 2013. Granular media failure along triaxial proportional strain paths. Eur. J. Environ. Civ. Eng. 17(9), 777–790. https://doi.org/10.1080/19648189.2013.819301

Nicot, F., Darve, F., 2009. A unified framework for failure in geomaterials, in: In Proceedings of the 1st International Symposium on Computational Geomechanics. pp. 158–168.

Nicot, F., Darve, F., 2006. Micro-mechanical investigation of material instability in granular assemblies. Int. J. Solids Struct. 43(11–12), 3569–3595. https://doi.org/10.1016/j.ijsolstr.2005.07.008

Nicot, F., Darve, F., 2005. A multi-scale approach to granular materials. Mech. Mater. 37, 980–1006. https://doi.org/10.1016/j.mechmat.2004.11.002

Nicot, F., Hadda, N., Darve, F., 2013. Second-order work analysis for granular materials using a multiscale approach. Int. J. Numer. Anal. Methods Geomech. 37(17), 2987–3007. https://doi.org/10.1002/nag.2175

Nicot, F., Hadda, N., Sibille, L., Radjaï, F., Hicher, P.Y., Darve, F., 2014. Some micromechanical aspects of failure in granular materials based on second-order work. Comptes Rendus - Mec. https://doi.org/10.1016/j.crme.2014.01.006

Nicot, F., Sibille, L., Donze, F., Darve, F., 2007. From microscopic to macroscopic second-order work in granular assemblies. Mech. Mater. 39(7), 664–684. https://doi.org/10.1016/j.mechmat.2006.10.003

Nicot, F., Sibille, L., Hicher, P.Y., 2015. Micro-macro analysis of granular material behavior along proportional strain paths. Contin. Mech. Thermodyn. 27(1–2), 173–193. https://doi.org/10.1007/s00161-014-0347-8

O'Sullivan, C., 2011. Particulate Discrete Element Modelling: A Geomechanics Perspective. Taylor & Francis, New York.

O'Sullivan, C., 2002. The application of discrete element modelling to finite deformation problems in geomechanics. University of California, Berkeley.

O'Sullivan, C., Bray, J.D., Riemer, M., 2002. Influence of Particle Shape and Surface Friction Variability on Response of Rod-Shaped Particulate Media. J. Eng. Mech. 128(11), 1182–1192. https://doi.org/10.1061/(ASCE)0733-9399(2002)128:11(1182)

O'Sullivan, C., O'Neill, S., Cui, L., 2007. An analysis of the triaxial apparatus using a mixed boundary three-dimensional discrete element model. Géotechnique 57(10), 831–844. https://doi.org/10.1680/geot.2007.57.10.831

Oda, M., 1999. An introduction Mechanics of granular materials. Balkma.

Oda, M., 1993. Inherent and induced anisotropy in plasticity theory of granular soils. Mech. Mater. 16(1–2), 35–45. https://doi.org/10.1016/0167-6636(93)90025-M

Oda, M., 1982. Fabric tensor for discontinuous geological materials. Soils Found. 22(4), 96–108. https://doi.org/10.3208/sandf1972.22.4_96

Oda, M., 1972. Initial Fabrics and Their Relations to Mechanical Properties of Granular Material. Soils Found. 12(1), 17–36. https://doi.org/10.3208/sandf1960.12.17

Oda, M., 1972. The Mechanism of Fabric Changes During Compressional Deformation of Sand. Soils Found. 12(2), 1–18. https://doi.org/10.3208/sandf.47.887

Oda, M., Iwashita, K., 2000. Study on couple stress and shear band development in granular media based on numerical simulation analyses. Int. J. Eng. Sci. 38(15), 1713–1740. https://doi.org/10.1016/S0020-7225(99)00132-9

Oda, M., Konishi, J., 1974. Microscopic Deformation Mechanism Of Granular Material In Simple Shear. Soils Found. 14(4), 25–38. https://doi.org/10.3208/sandf1972.14.4_25

Oda, M., Konishi, J., Nemat-Nasser, S., 1982. Experimental micromechanical evaluation of strength of granular materials: Effects of particle rolling. Mech. Mater. 1(4), 269–283. https://doi.org/10.1016/0167-6636(82)90027-8

Oda, M., Nakayama, H., 1988. Introduction of Inherent Anisotropy of Soils in the Yield Function, in: Studies in Applied Mechanics. pp. 81–90. https://doi.org/10.1016/B978-0-444-70523-5.50017-5

Oda, M., Nemat-Nasser, S., 1982. A statistical study of fabric in a random assembly of spherical granules. Int. J. Numer. Anal. methods Geomech. 6(1), 77–94.

Oda, M., Nemat-Nasser, S., Konishi, J., 1985. Stress-induced anisotropy in granular masses. Soils Found. 25(3), 85–97. https://doi.org/10.3208/sandf1972.25.3_85

Ohkawa, H., Kuwano, J., Nakada, T., Tachibana, S., 2011. Yielding characteristic and non-coaxiality of Toyoura sand on p′-constant shear stress plane. Soils Found. 51(1), 179–190.

Ouadfel, H., Rothenburg, L., 2001. `Stress-force-fabric' relationship for assemblies of ellipsoids. Mech. Mater. 33(4), 201–221. https://doi.org/10.1016/S0167-6636(00)00057-0

Peters, J.F., Muthuswamy, M., Wibowo, J., Tordesillas, A., 2005. Characterization of force chains in granular material. Phys. Rev. E - Stat. Nonlinear, Soft Matter Phys. 72(4). https://doi.org/10.1103/PhysRevE.72.041307

Potyondy, D.O., Cundall, P.A., 2004. A bonded-particle model for rock. Int. J. Rock Mech. Min. Sci. 41(8 SPEC.ISS.), 1329–1364. https://doi.org/10.1016/j.ijrmms.2004.09.011

Powrie, W., Ni, Q., Harkness, R.M., Zhang, X., 2005. Numerical modelling of plane strain tests on sands using a particulate approach. Géotechnique 55(4), 297–306.

Pradel, D., Ishihara, K., Gutierrez, M., 1990. Yielding and flow of sand under principal stress axes rotation. Soils Found. 30(1), 87–99.

https://doi.org/10.3208/sandf1972.30.87

Prunier, F., Laouafa, F., Lignon, S., Darve, F., 2009. Bifurcation modeling in geomaterials: From the second-order work criterion to spectral analyses. Int. J. Numer. Anal. Methods Geomech. 33(9), 1169–1202. https://doi.org/10.1002/nag.762

Radjaï, F., Delenne, J.Y., Azéma, E., Roux, S., 2012. Fabric evolution and accessible geometrical states in granular materials. Granul. Matter 14(2), 259–264. https://doi.org/10.1007/s10035-012-0321-8

Radjaï, F., Jean, M., Moreau, J.-J., Roux, S., 1996. Force distributions in dense two-dimensional granular systems. Phys. Rev. Lett. 77(2), 274–277. https://doi.org/10.1103/PhysRevLett.77.274

Radjai, F., Wolf, D., Jean, M., Moreau, J.-J., 1998. Bimodal character of stress transmission in granular packings. Phys. Rev. Lett. 80(1), 61–64. https://doi.org/10.1103/PhysRevLett.80.61

Reynolds, O., 1885. LVII. On the dilatancy of media composed of rigid particles in contact. With experimental illustrations. London, Edinburgh, Dublin Philos. Mag. J. Sci. 20(127), 469–481.

Riemer, M.F., Seed, R.B., 1997. Factors affecting apparent position of steady-state line. J. Geotech. Geoenvironmental Eng. 123(3), 281–288. https://doi.org/10.1061/(ASCE)1090-0241(1997)123:3(281)

Roscoe, K.H., 1970. The Influence of Strains in Soil Mechanics. Géotechnique 20(2), 129–170. https://doi.org/10.1680/geot.1970.20.2.129

Roscoe, K.H., Bassett, R.H., Cole, E.R., 1967. Principal axes observed during simple shear of a sand, in: Proc. Geotech. Conf. pp. 231–237.

Roscoe, K.H., Schofield, A.N., Wroth, C.P., 1958. On The Yielding of Soils. Géotechnique 8(1), 22–53. https://doi.org/10.1680/geot.1958.8.1.22

Roscoe, K.H., Schofield, a. N., Thurairajah, a., 1963. Yielding of clays in states wetter than critical. Géotechnique 13(3), 211–240. https://doi.org/10.1680/geot.1963.13.3.211

Rothenburg, L., 1980. Micromechanics of Idealized Granular Systems.

Rothenburg, L., Bathurst, R.J., 1991. Numerical simulation of idealized granular assemblies with plane elliptical particles. Comput. Geotech. 11(4), 315–329. https://doi.org/10.1016/0266-352X(91)90015-8

Rothenburg, L., Bathurst, R.J., 1989. Analytical study of induced anisotropy granular materials in idealized. Geotechnique 39(4), 601–614.

Rothenburg, L., Kruyt, N.P., 2004. Critical state and evolution of coordination number in simulated granular materials. Int. J. Solids Struct. 41(21), 5763–5774. https://doi.org/10.1016/j.ijsolstr.2004.06.001

Rothenburg, L., Selvadurai, A.P.S., 1981. A micromechanical definition of the Cauchy stress tensor for particulate media. Mech. Struct. media 469–486.

Rowe, P.W., 1962. The Stress-Dilatancy Relation for Static Equilibrium of an Assembly of Particles in Contact. Proc. R. Soc. A Math. Phys. Eng. Sci. 269(1339), 500–527. https://doi.org/10.1098/rspa.1962.0193

Satake, M., 1987. Graph-theoretical approach to the mechanics of granular materials, in: Spencer, A.J.M. (Ed.), Continuum Models of Discrete Systems. Taylor & Francis, Boston, pp. 163–172.

Satake, M., 1984. Anisotropy in groundand soil materials. Tsuchito Kiso 32(11).

Satake, M., 1982. Fabric tensor in granular materials. Deltf Universtiy.

Satake, M., 1978. Constitution of mechanics of granular materials through the graph theory. Contin. Mech. Stat. approaches Mech. Granul. Mater. 47–62.

Schofield, A., Wroth, P., 1968. Critical State Soil Mechanics. Soil Use Manag. 25(3), 128–105. https://doi.org/10.1111/j.1475-2743.1987.tb00718.x

Sibille, L., Nicot, F., Donzé, F. V., Darve, F., 2007. Material instability in granular assemblies from fundamentally different models. Int. J. Numer. Anal. Methods Geomech. 31(3), 457–481. https://doi.org/10.1002/nag.591

Soga, K., Yimsiri, S., 2010. DEM analysis of soil fabric effects on behaviour of sand. Géotechnique 60(6), 483–495. https://doi.org/10.1680/geot.2010.60.6.483

Subhash, G., Nemat-Nasser, S., Mehrabadi, M.M., Shodj, H.M., 1991. Experimental investigation of fabric-stress relations in granular materials. Mech. Mater. 11(2), 87–106. https://doi.org/10.1016/0167-6636(91)90010-W

Suiker, A.S.J., Chang, C.S., 2004. Modeling failure and deformation of an assembly of spheres with frictional contacts. J. Eng. Mech. 130(3), 283–293.

Taylor, D.W., 1948. Fundamentals of soil mechanics, Wiley. ed. New York.

Thornton, C., 2000. Numerical simulations of deviatoric shear deformation of granular media. Géotechnique 50(1), 43–53. https://doi.org/10.1680/geot.2000.50.1.43

Thornton, C., Antony, S.J., 2000. Quasi-static shear deformation of a soft particle system. Powder Technol. 109(1–3), 179–191. https://doi.org/10.1016/S0032-5910(99)00235-1

Thornton, C., Antony, S.J., 1998. Quasi-static deformation of particulate media. Philos. Trans. R. Soc. A Math. Phys. Eng. Sci. 356(1747), 2763–2782. https://doi.org/10.1098/rsta.1998.0296

Thornton, C., Zhang, L., 2010. On the evolution of stress and microstructure during general 3D deviatoric straining of granular media. Géotechnique 60(5), 333–341. https://doi.org/10.1680/geot.2010.60.5.333

Thornton, C., Zhang, L., 2006. A numerical examination of shear banding and simple shear non-coaxial flow rules. Philos. Mag. 86(21–22), 3425–3452. https://doi.org/10.1080/14786430500197868

Ting, J.M., 1992. A robust algorithm for ellipse-based discrete element modelling of granular materials. Comput. Geotech. 13(3), 175–186. https://doi.org/10.1016/0266-352X(92)90003-C

Tokue, T., 1979. Deformation behaviours of dry sand under cyclic loading and a stress-dilatancy model. Soils Found. 19(2), 63–78.

Tsuchikura, T., Satake, M., 1998. Statistical measure tensors and their application to computer simulation analysis of biaxial compression test, in: Engineering Mechanics: A Force for 21st Century. pp. 1732–1735.

Ueng, T.-S., Lee, C.-J., 1990. Deformation behavior of sand under shear—particulate approach. J. Geotech. Eng. 116(11), 1625–1640.

Vaid, Y.P., Chern, J.C., 1985. Cyclic and monotonic undrained response of saturated sands, in: Advances in the Art of Testing Soils under Cyclic Conditions. ASCE, pp. 120–147.

Vaid, Y.P., Sivathayalan, S., 1996. Static and cyclic liquefaction potential of Fraser Delta sand in simple shear and triaxial tests. Can. Geotech. J. 33(2), 281–289. https://doi.org/10.1139/t96-007

Voivret, C., Radjaï, F., Delenne, J.Y., El Youssoufi, M.S., 2009. Multiscale force networks in highly polydisperse granular media. Phys. Rev. Lett. 102(17). https://doi.org/10.1103/PhysRevLett.102.178001

Vu-Quoc, L., Zhang, X., Walton, O.R., 2000. A 3-D discrete-element method for dry granular flows of ellipsoidal particles. Comput. Methods Appl. Mech. Eng. 187(3–4), 483–528. https://doi.org/10.1016/S0045-7825(99)00337-0

Walton, K., 1987. The effective elastic moduli of a random packing of spheres. J. Mech. Phys. Solids 35(2), 213–226. https://doi.org/10.1016/0022-5096(87)90036-6

Wan, R., Al-Mamun, M., Guo, P., 2007. Experimental investigation of instabilities of granular materials in relation to dilatancy and fabric issues, in: In Bifurcations, Instabilities, Degradation in Geomechanics. Springer, Berlin Heidelberg, pp. 71–93.

Wan, R., Pouragha, M., 2015. Fabric and connectivity as field descriptors for deformations in granular media. Contin. Mech. Thermodyn. 27(1–2), 243–259. https://doi.org/10.1007/s00161-014-0370-9

Wan, R.G., Al-Mamun, M., Guo, P.J., 2005. How do fabric and dilatancy affect the strength of granular materials, in: Proceedings of the International Conference on Soil Mechanics and Geotechnical Engineering. pp. 863–875.

Wan, R.G., Guo, P.J., 2004. Stress Dilatancy and Fabric Dependencies on Sand Behavior. J. Eng. Mech. 130(6), 635–645. https://doi.org/10.1061/(ASCE)0733-9399(2004)130:6(635)

Wan, R.G., Guo, P.J., 1998. A simple constitutive model for granular soils: Modified stress-dilatancy approach. Comput. Geotech. 22(2), 109–133. https://doi.org/10.1016/S0266-352X(98)00004-4

Wong, R.K.S., Arthur, J.R.F., 1986. Sand sheared by stresses with cyclic variations in direction. Géotechnique 36(2), 215–226.

https://doi.org/10.1680/geot.1986.36.2.215

Yang, Z.X., Li, X.S., Yang, J., 2007. Undrained anisotropy and rotational shear in granular soil. Géotechnique 57(4), 371–384. https://doi.org/10.1680/geot.2007.57.4.371

Yin, Z.Y., Chang, C.S., 2013. Stress-dilatancy behavior for sand under loading and unloading conditions. Int. J. Numer. Anal. Methods Geomech. 37(8), 855–870. https://doi.org/10.1002/nag.1125

Yoshimine, M., Ishihara, K., Vargas, W., 1998. Effects of principal stress direction and intermediate principal stress on undrained shear behavior of sand. SOILS Found. 38(3), 179–188. https://doi.org/10.3208/sandf.38.3_179

Yu, H.S., 2008. Non-coaxial theories of plasticity for granular materials. Proc. 12th Int. Conf. IACMAG (1988), 1–6.

Zhao, J., Guo, N., 2014. Rotational resistance and shear-induced anisotropy in granular media. Acta Mech. Solida Sin. 27(1), 1–14. https://doi.org/10.1016/S0894-9166(14)60012-4

Zhao, J., Guo, N., 2013. Unique critical state characteristics in granular media considering fabric anisotropy. Géotechnique 63(8), 695–704. https://doi.org/10.1680/geot.12.P.040

Zhu, H., Nicot, F., Darve, F., 2016. Meso-structure evolution in a 2D granular material during biaxial loading. Granul. Matter 18(1), 1–12. https://doi.org/10.1007/s10035-016-0608-2

Appendix

A-1 2D-sample.dat

```
;fname: 2D-sample.dat      Creation and packing of particles – 2D sample
new
SET random ; reset random-number generator
SET disk on ; treat balls as disks of unit thickness
def make_walls ; create walls with overhang of extend
   extend = 0.5
   _x0 = -extend*width
   _y0 = 0.0
   _x1 = width*(1.0 + extend)
   _y1 = 0.0
   command
      wall id=1 kn=w_stiff nodes (_x0,_y0) (_x1,_y1)
   end_command
   _x0 = width
   _y0 = -extend*height
   _x1 = width
   _y1 = height*(1.0 + extend)
   command
      wall id=2 kn=w_stiff nodes (_x0,_y0) (_x1,_y1)
   end_command
   _x0 = width*(1.0 + extend)
   _y0 = height
   _x1 = -extend*width
   _y1 = height
   command
```

```
      wall id=3 kn=w_stiff nodes (_x0,_y0) (_x1,_y1)
   end_command
   _x0 = 0.0
   _y0 = height*(1.0 + extend)
   _x1 = 0.0
   _y1 = -extend*height
   command
      wall id=4 kn=w_stiff nodes (_x0,_y0) (_x1,_y1)
   end_command
end
def assemble ; assemble sample
   s_stiff = 0.0 ;initial stiffnesses
   n_stiff = 1e8
   w_stiff = 1e8
   tot_vol = height * width * 1.0
   rbar = 0.5 * (rlo + rhi)
   num = int((1.0 - poros) * tot_vol/(pi * rbar^2))
   mult = 2.0                                    ; initial radius multiplication factor
   rlo_0 = rlo / mult
   rhi_0 = rhi / mult
   make_walls
   command
         gen id=1,15000 rad=rlo_0,rhi_0 x=0,width y=0,height
         prop dens=2000 ks=s_stiff kn=n_stiff
      end_command
   command
            gen id=15001, 21000 rad=rlo_0,rhi_0 x=0,width y=0,height
```

```
            prop dens=2000 ks=s_stiff kn=n_stiff
    end_command
    command
            gen id=21001, num rad=rlo_0,rhi_0 x=0,width y=0,height
            prop dens=2000 ks=s_stiff kn=n_stiff
    end_command
    ii = out(string(num)+'particles were created')
    sum = 0.0 ; get actual porosity
    bp = ball_head
    loop while bp # null
      sum = sum + pi * b_rad(bp)^2
      bp = b_next(bp)
    end_loop
    pmeas = 1.0 - sum / tot_vol
    mult = sqrt((1.0-poros)/(1.0-pmeas))
    command
      ini rad mul mult
      cycle 1000
      prop ks=1e8 fric 0.5
      cycle 500
    end_command
end
def cws                                          ;change lateral wall stiffnesses
    command
      wall id 2 kn=w_stiff
      wall id 4 kn=w_stiff
      wall id 1 kn=w_stiff
```

```
      wall id 3 kn=w_stiff
   end_command
end
macro zero 'ini xvel 0 yvel 0 spin 0'
SET height=4.0 width=2 rlo=0.008 rhi=0.01 poros= 0.160
assemble
SET w_stiff= 1e7                                ;make lateral wall stiffness=0.1 of ball
stiffness
cws
cyc 5000
zero
solve    av=0.0001 max=0.0001
zero
plot create assembly
plot add ball lorange wall black
save 2D_ass.SAV
return
```

A-2 2D-stress.dat

```
;fname: 2D-stress.DAT      Preparation for upcoming tests. Define output variables
 set log off
 res 2D_ass.SAV                                 ;restore compacted assembly
def get_coor
   count_1= 0
   bp=ball_head
   loop while bp # null
   count_1 = count_1+1
```

```
    bp=b_next(bp)
    endloop
    count_2= 0
    cp=contact_head
    loop while cp # null
        b1=c_ball1(cp)
        b2=c_ball2(cp)
    if pointer_type(b2) # 101
        count_2 = count_2+1
    endif
    cp=c_next(cp)
    endloop
    count_1 = count_1*1.1
    count_2 = count_2*1.1
    co_nu    = count_2/count_1
end
def get_ss                                          ;determine average stress and
strain at walls
    get_coor
    xdif = w_x(wadd2) - w_x(wadd4)
    ydif = w_y(wadd3) - w_y(wadd1)
    new_xwidth = width + xdif
    new_height = height+ ydif
    volume = new_xwidth*new_height
    wsxx = 0.5 * (w_xfob(wadd4)- w_xfob(wadd2)) / (new_height * 1.0)
    wsyy = 0.5 * (w_yfob(wadd1)- w_yfob(wadd3)) / (new_xwidth * 1.0)
    wexx = xdif/(width*1.0)
```

```
    weyy = ydif/(height*1.0)
    wevol= wexx + weyy
    dest = weyy - wexx
if co_nu_0 > 1.0
    r_co = (co_nu-co_nu_0)/co_nu_0
else
    r_co = 0.0
endif
cp=contact_head
    sum_fx  = 0.0
    sum_fy  = 0.0
    sum_fxy = 0.0
    sum_fyx = 0.0
loop while cp # null
      b1 = c_ball1(cp)
      b2 = c_ball2(cp)
      nforce=c_nforce(cp)
if pointer_type(b2) # 101
    x_dif=b_x(b2)-b_x(b1)
    y_dif=b_y(b2)-b_y(b1)
    vel_x=c_xun(cp)
    vel_y=c_yun(cp)
    delta_fx  = nforce*vel_x*x_dif
    delta_fy  = nforce*vel_y*y_dif
    delta_fxy = nforce*vel_x*y_dif
    delta_fyx = nforce*vel_y*x_dif
    sum_fx  = sum_fx  + delta_fx
```

```
    sum_fy    = sum_fy    + delta_fy
    sum_fxy = sum_fxy + delta_fxy
    sum_fyx = sum_fyx + delta_fyx
endif
cp=c_next(cp)
endloop
    wsxx_1 = sum_fx/volume
    wsyy_1 = sum_fy/volume
    wsxy_1 = sum_fxy/volume
    wsyx_1 = sum_fyx/volume
end
def get_gain                    ;determine servo gain parameters for x and y
    alpha = 0.5                 ;relaxation factor
    count = 0
    avg_stiff = 0
    cp = contact_head           ;find avg.number of contacts on x-walls
    loop while cp # null
        if c_ball1(cp) = wadd2
            count = count + 1
            avg_stiff = avg_stiff + c_kn(cp)
        end_if
        if c_ball1(cp) = wadd4
            count = count + 1
            avg_stiff = avg_stiff + c_kn(cp)
        end_if
        if c_ball2(cp) = wadd2
            count = count+1
```

```
        avg_stiff = avg_stiff + c_kn(cp)
      end_if
      if c_ball2(cp) = wadd4
        count = count+1
        avg_stiff = avg_stiff + c_kn(cp)
      end_if
      cp = c_next(cp)
    end_loop
    nxcount = count/2.0
    avg_stiff = avg_stiff/count
    gx = alpha*(height*1.0)/(avg_stiff*nxcount*tdel)
    count = 0
    avg_stiff = 0
    cp = contact_head                    ;find avg. number of contacts on y-walls the
averaged lateral force
    loop while cp # null
      if c_ball1(cp) = wadd1
        count = count + 1
        avg_stiff = avg_stiff + c_kn(cp)
      end_if
      if c_ball1(cp) = wadd3
        count = count + 1
        avg_stiff = avg_stiff + c_kn(cp)
      end_if
      if c_ball2(cp) = wadd1
        count = count + 1
        avg_stiff = avg_stiff + c_kn(cp)
```

```
        end_if
        if c_ball2(cp) = wadd3
            count = count + 1
            avg_stiff = avg_stiff + c_kn(cp)
        end_if
        cp = c_next(cp)
    end_loop
    nycount = count/2.0
    avg_stiff = avg_stiff/count
    gy = alpha*(width*1.0)/(avg_stiff*nycount*tdel)
end
def servo
    while_stepping
    if x_servo = 1
        udx = gx*(wsxx-sxxreq)
        w_xvel(wadd4) = udx
        w_xvel(wadd2) = -udx
    endif
    if y_servo = 1                          ;switch stress servo on or off
        udy = gy*(wsyy-syyreq)
        w_yvel(wadd1) = udy
        w_yvel(wadd3) = -udy
    end_if
end
def iterate
    loop while 1 # 0
        if abs((wsxx-sxxreq)/sxxreq)<sig_tol then
```

```
        if abs((wsyy-syyreq)/syyreq)<sig_tol then
          exit
        end_if
      end_if
      command
        cycle 500
      end_command
    end_loop
end
def out_detail
new_xwidth_0=new_xwidth
new_height_0=new_height
get_poros
oo=out(string(pmeas1)+'is the porosity      '+string(new_xwidth_0)+' is the new
width      '+string(new_height_0)+'is the new height        ')
end
def wall_addr
   wadd1 = find_wall(1)
   wadd2 = find_wall(2)
   wadd3 = find_wall(3)
   wadd4 = find_wall(4)
end
wall_addr
zero
SET sxxreq=-2e5 syyreq=-2e5 sig_tol=1e-6 y_servo=1 x_servo = 1
iterate                                    ;get all stresses to requested state
SET width=new_xwidth        height=new_height
```

```
out_detail
zero
……
sav 2D_stress.SAV        ;get the required stress states and ready for the intializtion
return
```

A-3 2D-preload.dat

```
;fname: 2D-preload.DAT      Preparation for upcoming tests. Define output variables
  set log off
  res bt_stre.SAV
def get_fabric
        fs_x_x = 0.0
        fs_x_y = 0.0
        fs_y_x = 0.0
        fs_y_y = 0.0
        ns_c    = 0
        fw_x_x = 0.0
        fw_x_y = 0.0
        fw_y_x = 0.0
        fw_y_y = 0.0
        nw_c    = 0
        f_x_x = 0.0
        f_x_y = 0.0
        f_y_x = 0.0
        f_y_y = 0.0
        f_x_x = f_x_x/n_c
        f_x_y = f_x_y/n_c
```

```
        f_y_x = f_y_x/n_c
        f_y_y = f_y_y/n_c
        fs_x_x = fs_x_x/ns_c
        fs_x_y = fs_x_y/ns_c
        fs_y_x = fs_y_x/ns_c
        fs_y_y = fs_y_y/ns_c
        fw_x_x = fw_x_x/nw_c
        fw_x_y = fw_x_y/nw_c
        fw_y_x = fw_y_x/nw_c
        fw_y_y = fw_y_y/nw_c
end
def set_ini ;set initial strains
    get_ss
    weyy_0    = weyy
    wexx_0    = wexx
    wevol_0 = wevol
    co_nu_0 = co_nu
    dest_0    = dest
end
def get_average_f
      n_avg_s=0.0
      n_c=0
      n_c_f=0.0
    _cp=contact_head
loop while _cp # null
    b2=c_ball2(_cp)
    nforce=c_nforce(_cp)
```

```
    if nforce>1e-6
    if pointer_type(b2) # 101
        n_c=n_c+1
        n_c_f = n_c_f +c_nforce(_cp)
    end_if
    end_if
       _cp=c_next(_cp)
endloop
        n_avg_s = n_c_f/n_c
end
def conf            ;variables for histories
    get_ss
    get_fabric
    degree_f
    get_poros
    avxy_1 = wsxx_1
    devi_1 = wsyy_1-avxy_1
    conf_1 = avxy_1
    avxy = wsxx
    devi = wsyy - avxy            ;deviatoric stress
    conf = avxy                    ;confining stress
    deax = weyy - weyy_0          ;axial strain
    dela = wexx - wexx_0          ;lateral strain
    devol= wevol- wevol_0         ;volumetric strain
    dest = dest - dest_0          ;deviatoric strain
    coor_r= r_co
    stress_s=-(avxy+wsyy)/2
```

```
   stress_t=-(wsyy-avxy)/2
end
def accel_platens                ; Accelerates the platens to achieve vel of _vfinal in
_nsteps; using _nchunks
     conf
   _niter = _nsteps / _nchunks
   loop _chnk (1,_nchunks)
      if _close = 1 then
         _vel_1 = _chnk*(_vfinal/_nchunks)
      else
         _vel_1 = -_chnk*(_vfinal/_nchunks)
      end_if
       _mvel_1 = -_vel_1
       _vel_2    = _vel_1*new_xwidth_0/(n_rate*new_height_0)
       _mvel_2 = -_vel_1*new_xwidth_0/(n_rate*new_height_0)
      command
         wall id 1 yvel= _vel_1
         wall id 3 yvel= _mvel_1
         wall id 2 xvel= _vel_2
         wall id 4 xvel= _mvel_2
         cycle _niter
      end_command
   end_loop
end
def degree_f
array degree (4, 80000)
array average_n(36,1)            ;y vector for an
```

```
array average_t(36,1)             ;y vector for at
array x_a_n(36,2)                  ;x matrix for an
array x_a_t(36,2)                 ;x matrix for at
array average_ns(36,1)             ;y vector for asn
array average_ts(36,1)            ;y vector for ast
array average_nw(36,1)             ;y vector for awn
array average_tw(36,1)             ;y vector for awt
sum_avg_ns=0.0
sum_avg_nw=0.0
sum_avg_n=0.0
loop i (1, 80000)
        degree (1, i)=0.0
        degree (2, i)=0.0
        degree (3, i)=0.0
        degree (4, i)=0.0
endloop
count= 0
va1 = 1.0
va2 = 0.0
cp = contact_head
loop while cp # null
    b1 = c_ball1(cp)
    b2 = c_ball2(cp)
    nforce=c_nforce(cp)
    sforce=c_sforce(cp)
    if nforce>1e-6
    if pointer_type(b2) # 101
```

```
count = count+1
vb1 = b_x(b2)-b_x(b1)
vb2 = b_y(b2)-b_y(b1)
maga_a = sqrt(va1*va1+va2*va2)
maga_b = sqrt(vb1*vb1+vb2*vb2)
na1= va1/maga_a
na2= va2/maga_a
nb1= vb1/maga_b
nb2= vb2/maga_b
cc= na1*nb2-na2*nb1                    ;cross product
bb= nb1*na1+nb2*na2                    ;dot product
dthet = atan2(abs(cc),abs(bb))
if sforce > 1e-7
    sthet= dthet+0.5*pi
else
     sthet=1.5*pi+dthet
endif
        if cc>0.0
            if bb<0.0
                dthet = pi-dthet
                 if sforce > 1e-7
                     sthet= dthet+0.5*pi
                 else
                      sthet=dthet-0.5*pi
                  endif
              endif
          else
```

```
                    if bb>0.0
                        dthet = 2*pi-dthet
                        if sforce > 1e-7
                            sthet= dthet-1.5*pi
                        else
                            sthet=dthet-0.5*pi
                        endif
                    else
                        dthet = pi+dthet
                        if sforce > 1e-7
                            sthet= dthet+0.5*pi
                        else
                            sthet=dthet-0.5*pi
                        endif
                    endif
                endif
        degree (1,count) = dthet
        degree (2,count) = c_nforce(cp)
        degree (3,count) = sthet
        degree (4,count) = sforce
    endif
    endif
cp=c_next(cp)
endloop
loop i (1,36)
  detal_n1=(i-1)*pi/18
  detal_n2=i*pi/18
```

```
  count_n=0
  sum_n=0.0
  sum_t=0.0
  count_ns=0
  sum_ns=0.0
  sum_ts=0.0
  count_nw=0
  sum_nw=0.0
  sum_tw=0.0
get_average_f
n_avg_ff = n_avg_s
  x_a_n(i,1)= cos(2*detal_n2)
  x_a_n(i,2)= sin(2*detal_n2)
  x_a_t(i,1)= sin(2*detal_n2)
  x_a_t(i,2)=-cos(2*detal_n2)
  array x_mat(36,2)
  array y_mat(36,1)
  loop j (1, count)
     if degree (1,j)>detal_n1
     …….
    endif
    endloop
       average_n(i,1)=sum_n/count_n
       average_t(i,1)=sum_t/count_n
       average_ns(i,1)=sum_ns/count_ns
       average_ts(i,1)=sum_ts/count_ns
       average_nw(i,1)=sum_nw/count_nw
```

```
      average_tw(i,1)=sum_tw/count_nw
endloop
loop k (1,36)
   if average_n(k,1)>1e-5
      sum_avg_n=sum_avg_n+average_n(k,1)
   endif
      if average_ns(k,1)>1e-5
      sum_avg_ns=sum_avg_ns+average_ns(k,1)
   endif
      if average_nw(k,1)>1e-5
         sum_avg_nw=sum_avg_nw+average_nw(k,1)
   endif
endloop
sum_avg_n=sum_avg_n/36
sum_avg_ns=sum_avg_ns/36
sum_avg_nw=sum_avg_nw/36
loop k (1,36)
     average_n(k,1)=average_n(k,1)/sum_avg_n-1          ; y function for an
     average_t(k,1)=-average_t(k,1)/sum_avg_n           ; y function for at
     average_ns(k,1)=average_ns(k,1)/sum_avg_ns-1
     average_ts(k,1)=-average_ts(k,1)/sum_avg_ns
     average_nw(k,1)=average_nw(k,1)/sum_avg_nw-1
     average_tw(k,1)=-average_tw(k,1)/sum_avg_nw
endloop
loop m (1,36)
     x_mat(m,1)= x_a_n(m,1)              ;x function for an
     x_mat(m,2)= x_a_n(m,2)              ;x function for an
```

```
    y_mat(m,1)= average_n(m,1)          ;y function for an
endloop
find_roots
b_1_an= return_a
b_2_an= return_b
a_nn=sqrt(b_1_an^2+b_2_an^2)
thet_n=atan2(abs(b_2_an),abs(b_1_an))
if b_1_an >0
    if b_2_an >0
        thet_n=thet_n;
    else
        thet_n=2*pi-thet_n;
    endif
else
   if b_2_an >0
       thet_n=pi-thet_n;
   else
       thet_n=pi+thet_n;
   endif
endif
a_n_theta=thet_n/2
loop m (1,36)
    x_mat(m,1)= x_a_t(m,1)              ;x function for at
    x_mat(m,2)= x_a_t(m,2)              ;x function for at
    y_mat(m,1)=average_t(m,1)           ;y function for at
endloop
find_roots
```

```
b_1_at=return_a
b_2_at=return_b
a_tt =sqrt(b_1_at^2+b_2_at^2)
thet_t=atan2(abs(b_2_at),abs(b_1_at))
if b_1_at >0
    if b_2_at >0
        thet_t=thet_t;
    else
        thet_t=2*pi-thet_t;
    endif
else
   if b_2_at >0
       thet_t=pi-thet_t;
   else
       thet_t=pi+thet_t;
   endif
endif
a_t_theta=thet_t/2
loop m (1,36)
    x_mat(m,1)= x_a_n(m,1)              ;x function for ans
    x_mat(m,2)= x_a_n(m,2)              ;x function for ans
    y_mat(m,1)= average_ns(m,1)         ;y function for ans
endloop
find_roots
a_nns =sqrt(b_1_ans^2+b_2_ans^2)
thet_ns=atan2(abs(b_2_ans),abs(b_1_ans))
if b_1_ans >0
```

```
    if b_2_ans >0
        thet_ns=thet_ns;
    else
        thet_ns=2*pi-thet_ns;
    endif
else
   if b_2_ans >0
       thet_ns=pi-thet_ns;
   else
       thet_ns=pi+thet_ns;
   endif
endif
a_ns_theta=thet_ns/2
loop m (1,36)
    x_mat(m,1)= x_a_t(m,1)              ;x function for at
    x_mat(m,2)= x_a_t(m,2)              ;x function for at
    y_mat(m,1)=average_ts(m,1)           ;y function for at
endloop
find_roots
b_1_ats=return_a
b_2_ats=return_b
a_tts = sqrt(b_1_ats^2+b_2_ats^2)
thet_ts= atan2(abs(b_2_ats),abs(b_1_ats))
if b_1_ats >0
    if b_2_ats >0
        thet_ts=thet_ts;
    else
```

```
        thet_ts=2*pi-thet_ts;
    endif
else
   if b_2_ats >0
       thet_ts=pi-thet_ts;
   else
       thet_ts=pi+thet_ts;
   endif
endif
a_ts_theta=thet_ts/2
loop m (1,36)
    x_mat(m,1)= x_a_n(m,1)                ;x function for ans
    x_mat(m,2)= x_a_n(m,2)                ;x function for ans
    y_mat(m,1)= average_nw(m,1)           ;y function for ans
endloop
find_roots
a_nnw =sqrt(b_1_anw^2+b_2_anw^2)
thet_nw =atan2(abs(b_2_anw),abs(b_1_anw))
if b_1_anw >0
    if b_2_anw >0
        thet_nw=thet_nw;
    else
        thet_nw=2*pi-thet_nw;
    endif
else
   if b_2_anw >0
       thet_nw=pi-thet_nw;
```

```
   else
       thet_nw=pi+thet_nw;
   endif
endif
a_nw_theta=thet_nw/2
loop m (1,36)
     x_mat(m,1)= x_a_t(m,1)                ;x function for at
     x_mat(m,2)= x_a_t(m,2)                ;x function for at
     y_mat(m,1)=average_tw(m,1)             ;y function for at
endloop
find_roots
b_1_atw=return_a
b_2_atw=return_b
a_ttw = sqrt(b_1_atw^2+b_2_atw^2)
thet_tw = atan2(abs(b_2_atw),abs(b_1_atw))
if b_1_atw >0
     if b_2_atw >0
          thet_tw=thet_tw;
     else
          thet_tw=2*pi-thet_tw;
     endif
else
   if b_2_atw >0
       thet_tw=pi-thet_tw;
   else
       thet_tw=pi+thet_tw;
   endif
```

```
endif
a_tw_theta=thet_tw/2
end
def out_put_f
    degree_f
loop n (1,count)
    de_gress= degree(1,n)
    de_force= degree(2,n)
    de_sgress=degree(3,n)
    de_sforce=degree(4,n)
    oo=out(string(de_gress)+'          '+string(de_force)+'
'+string(de_sgress)+'          '+string(de_sforce))
endloop
end
def out_put_c
array coornumber (1, 10)
loop i (1, 10)
    coornumber (1, i) = 0
endloop
max_co = -10
……..
end
wall_addr
zero
set_ini
history id=1 conf
history id=2 devi
```

```
history id=3 deax
…….
SET hist_rep=500
del ball range x -10 -1
del ball range x    5    20
zero
sav 2D_init.SAV                                    ;ready implosed strain tests
return
```

This is the end.